

# Molecular Simulations of Charge Transport for Energy Storage and Conversion Applications

Thesis by  
Jeongmin Kim

In Partial Fulfillment of the Requirements for the  
Degree of  
Doctor of Philosophy

The logo for the California Institute of Technology (Caltech), featuring the word "Caltech" in a bold, orange, sans-serif font.

CALIFORNIA INSTITUTE OF TECHNOLOGY  
Pasadena, California

2022  
Defended July 30, 2021

© 2022

Jeongmin Kim

ORCID: 0000-0002-7405-8200

All rights reserved

## ACKNOWLEDGEMENTS

I would like first to thank my advisor, Professor Thomas F. Miller III. His guidance, support, encouragement, and patience have helped me become a scientist and an independent researcher. The opportunities he has given are invaluable to shape and broaden my scientific view and enhance my problem-solving skills.

I would also like to thank my thesis committee: Professor Zhen-Gang Wang, Professor Kimberly See, and Dr. Simon Jones. I have learned a lot from them through classes, collaborations, and questions that helped me think about bigger pictures of my research.

I think this thesis could not have been done without fruitful collaborations. I have always felt that I am lucky to have wonderful collaborators. It has been a great pleasure to working with all of you. I am grateful to the team Geiger at Northwestern: Professor Franz M. Geiger, Emily Ma, and Rico Xi. I have learned a lot from working with them and from their enthusiasm and tireless effort.

I also want to thank Dr. Simon Jones, Professor Robert Grubbs, Professor Julia Greer, Steve, Fernando, and Willie for the exciting opportunities. I thank the entire SCALAR team. I want to particularly thank Professor Rachael Segalman, Professor Ram Seshadri, Dakota, Gordon, and Ioan. Thank you all for your valuable scientific discussions.

I also thank all the members of the Miller group: Priscilla, Brett, Matthew Z, Xuecheng, Jorge, Dan, Feizhi, Michiel, Matt, Sherry, Roman, Marta, James, Jiace, Zhuoran, Doris, Leanne, Sebastian, Tamara, Emiliano, Saleh, Varun, Philip, Xing-long, Ralph, and Mike. I have always been motivated by their hard work and group meeting talk that shows challenging and intriguing problems. I especially thank Steve for his mentorship and friendship. It was great working with you, Steve.

Last but of course not least, I truly appreciate my parents and little brother. They are always there for me. I could not have made it this far without their help.

## ABSTRACT

Molecular simulation plays a variety of roles in accelerating the development of energy materials, from providing a fundamental understanding of molecular processes to predicting their performance spanning a wide range of chemical space. In this thesis, we present molecular simulation studies of charge transport both in bulk energy materials and at their interfaces to provide molecular principles for advanced rechargeable batteries in part I and electricity generation using a metal nanofilm from water motion in part II.

In part I, we discuss ion transport and interfacial electron transfer in polymeric battery materials, both of which are closely associated with battery operation. As a bulk electrolyte and a solid electrolyte interphase (SEI), polymeric materials often benefit rechargeable batteries, allowing for enhanced safety and increased energy density. Firstly, we propose a unique mechanism of lithium-ion transport in polymer-based electrolytes, including conjugated polymers with an imidazolium sidechain and polyborane-based single-ion conductors, which utilizes the formation of a percolating ion network to facilitate lithium ion transport. Secondly, we discuss interfacial ion solvation structure and dynamics that are closely related to interfacial electron-transfer kinetics. Simulations provide molecular insights into how a functional SEI passivates a metal electrode, thereby accelerating materials discovery such as an artificial SEI of self-assembled monolayers.

In part II, we present molecular principles of energy conversion from a flow of ionic solution to electricity using metal nanolayers. The energy conversion emerges at a water-solid interface and requires a boundary of an electrical double layer at which ion adsorption and desorption occur along with the flow. We discuss charge induction mechanisms related to a heterolayered structure of a metal nanolayer and investigate factors that affect energy conversion efficiency in two different modes of operation, namely a flow cell and a wavetank.

## PUBLISHED CONTENT AND CONTRIBUTIONS

- [1] Jeongmin Kim, Brett M. Savoie, and Thomas F. Miller III. “Interfacial electron transfer and ion solvation in the solid electrolyte interphase.” In: *The Journal of Physical Chemistry C* 125.8 (2021), pp. 4614–4622. DOI: 10.1021/acs.jpcc.0c11194.  
The author participated in designing of the research, conducting simulations, discussing the results, and preparing a draft.
- [2] Emily Ma et al. “A new imaginary term in the 2nd order nonlinear susceptibility from charged interfaces.” In: *The Journal of Physical Chemistry Letters* 12.24 (2021), pp. 5649–5659. DOI: 10.1021/acs.jpcllett.1c01103.  
The author participated in conducting computations, discussing the computation results, and preparing a draft.
- [3] Emily Ma et al. “Stern and diffuse layer interactions during ionic strength cycling.” In: *The Journal of Physical Chemistry C* 125.32 (2021), pp. 18002–18014. DOI: 10.1021/acs.jpcc.1c04836.  
The author participated in conducting simulations, discussing the results, and preparing a draft.
- [4] Dakota Rawlings et al. “Li<sup>+</sup> and oxidant addition to control ionic and electronic conduction in ionic liquid functionalized conjugated polymers.” In: *Chemistry of Materials* (2021). DOI: 10.1021/acs.chemmater.1c01811.  
The author participated in conducting simulations of amorphous polymers, discussing the results of ion solvation and transport in the polymers, and preparing a draft.
- [5] Shichuan<sup>†</sup> Xi et al. “Energy conversion via metal nanolayers in a wavetank.” In: *in preparation* (2021).  
The author participated in designing the research, conducting simulations, discussing the results, and preparing a draft.
- [6] Qingmin Xu et al. *Solid electrolyte interphase (SEI) application on anode of fluoride ion/shuttle batteries*. US Patent App. 16/702,327. June 2020. URL: <https://patents.google.com/patent/US20200185776A1/en>.  
The author participated in conducting simulations, discussing the simulation results, and preparing the simulation part of the Patent.
- [7] Mavis D. Boamah et al. “Energy conversion via metal nanolayers.” In: *Proceedings of the National Academy of Sciences* 116.33 (2019), pp. 16210–16215. DOI: 10.1073/pnas.1906601116.  
The author participated in conducting simulations, discussing the results, and preparing a draft.
- [8] Victoria K. Davis et al. “Fluoride-ion solvation in non-aqueous electrolyte solutions.” In: *Materials Chemistry Frontiers* 3.12 (2019), pp. 2721–2727.

DOI: 10.1039/C9QM00512A.

The author participated in conducting simulations, discussing the results of ion solvation and transport in mixtures, and preparing a draft.

## TABLE OF CONTENTS

Acknowledgements . . . . .	iii
Abstract . . . . .	iv
Published Content and Contributions . . . . .	v
Table of Contents . . . . .	vi
List of Illustrations . . . . .	ix
List of Tables . . . . .	xxi
Chapter I: Brief Overview and Motivation . . . . .	1
Chapter II: Introduction . . . . .	6
Part I. Ion Solvation and Transport at Bulk and Electrified Interfaces for Energy Storage Applications . . . . .	9
Chapter III: Facilitated Lithium-Ion Transport in Ionic Liquid Functionalized Conjugated Polymers at High Salt Concentrations . . . . .	10
3.1 Abstract . . . . .	10
3.2 Introduction . . . . .	10
3.3 Computational Methods . . . . .	12
3.4 Results and Discussion . . . . .	15
3.5 Conclusion . . . . .	22
3.6 Appendix . . . . .	23
Chapter IV: Lithium-Ion Transport in Polyborane-based electrolytes . . . . .	25
4.1 Abstract . . . . .	25
4.2 Introduction . . . . .	26
4.3 Simulation Model and Method . . . . .	28
4.4 Results and Discussion . . . . .	29
4.5 Conclusion . . . . .	36
Chapter V: Interfacial Ion Solvation and Electron Transfer in Solid Electrolyte Interphase . . . . .	37
5.1 Abstract . . . . .	37
5.2 Introduction . . . . .	37
5.3 Methods and Calculation Details . . . . .	39
5.4 Results and Discussion . . . . .	44
5.5 Conclusions . . . . .	52
5.6 Appendix . . . . .	53
Chapter VI: Design Rules for Passivating Self-Assembled Monolayers to a Metal Electrode from Fluoride-Ion Solvation Structure and Dynamics . . . . .	59
6.1 Abstract . . . . .	59
6.2 Introduction . . . . .	59
6.3 Methods and Calculation Details . . . . .	62
6.4 Results and Discussion . . . . .	66
6.5 Summary and Conclusions . . . . .	73

6.6 Appendix . . . . .	74
Part II. Energy Transduction of Water Kinetic Energy to Electricity using Metal Nanolayers . . . . .	82
Chapter VII: Generating Electricity Using Metal Nanolayers from a Flow of Alternating Salinity Gradients . . . . .	83
7.1 Abstract . . . . .	83
7.2 Introduction . . . . .	83
7.3 Simulation Method . . . . .	85
7.4 Design Rules Found in Experiments . . . . .	87
7.5 Computational Results and Discussion . . . . .	89
7.6 Conclusion . . . . .	95
7.7 Appendix . . . . .	96
Chapter VIII: Energy Conversion using Metal Nanolayers in a Wave Tank . .	101
8.1 Abstract . . . . .	101
8.2 Introduction . . . . .	101
8.3 Calculation Methods . . . . .	103
8.4 Results and Discussion . . . . .	106
8.5 Conclusion . . . . .	115
8.6 Appendix . . . . .	117
Chapter IX: Coupled and Decoupled Dynamics of Stern and Diffuse Layers at Aqueous Oxide Interfaces . . . . .	119
9.1 Abstract . . . . .	119
9.2 Introduction . . . . .	119
9.3 Simulation Method and Calculation of SHG Responses . . . . .	121
9.4 Results and Discussion . . . . .	127
9.5 Conclusion . . . . .	135
9.6 Appendix . . . . .	136
Bibliography . . . . .	141

## LIST OF ILLUSTRATIONS

<i>Number</i>	<i>Page</i>
3.1 MD snapshots for the crystalline polymers at $r = 0.2$ (left) and $r = 0.8$ (right). The color code is as follows: red spheres represent Li cations; blue spheres represent $\text{BF}_4$ anions; yellow surfaces represent imidazolium nitrogen atoms; grey spheres represent sulfur atoms of thiophene rings; and green lines connect neighboring Li and $\text{BF}_4$ within 4 Å. . . . .	13
3.2 Chemical structure and structural characterization of P3HT-IM. (a) Schematic structure of the thiophene-based conjugated polymeric ionic liquid used in this study. (b) Azimuthally integrated GIWAXS patterns for neat P3HT-IM. (c) Illustration of the polymer model used in MD simulations. (d) MD snapshot of the simulation box used for the crystalline polymer. . . . .	16
3.3 Experimental results for the P3HT-IM polymers upon $\text{LiBF}_4$ salt addition. (a) Integrated GIWAXS patterns for neat P3HT-IM and P3HT-IM with added $\text{LiBF}_4$ salt at $r = 1$ , where $r$ is the ratio of the moles of salt to the moles of monomer. (b) Ionic conductivity as a function of lithium salt addition at room temperature. . . . .	17
3.4 MD simulation results for the ion solvation environment [112] in crystalline P3HT-IM polymers at different salt concentrations at 300 K. (a) Snapshots of representative $\text{BF}_4^-$ solvation environments in P3HT-IM and (b) their abundance as a function of salt concentration. (c) Snapshots of representative $\text{Li}^+$ solvation environments in P3HT-IM and (d) their abundance as a function of salt concentration. . . . .	18

3.5	Simulation results for ion solvation in the amorphous (a-b) and crystalline (c-d) P3HT-IM polymers at 400 K. (a,c) Dispersed localized ion pairs of $\text{Li}^+$ and $\text{BF}_4^-$ at low salt concentration ( $r = 0.2$ ) (b,d) Percolating network of $\text{Li}^+$ and $\text{BF}_4^-$ at high salt concentration ( $r = 0.8$ ). (e) Probability, $P_{perc}$ , that the largest ionic network in the amorphous P3HT-IM polymer percolates the simulation box at several salt concentrations. The color code in (a-d) is as follows: red spheres represent $\text{Li}^+$ ; blue spheres represent $\text{BF}_4^-$ ; and yellow surfaces represent imidazolium groups; green lines connect neighboring $\text{Li}^+$ within 4 Å.	20
3.6	Simulation results for ion network and transport in both amorphous and crystalline P3HT-IM polymers at 400 K. Li- $\text{BF}_4$ contact duration in (a) amorphous and (b) crystalline polymers. (c) Calculated diffusion coefficients for $\text{Li}^+$ and $\text{BF}_4^-$ as a function of salt concentration in the amorphous (solid symbols) and crystalline polymer (open symbols).	21
3.7	Li solvation by $\text{BF}_4$ in the amorphous polymers as a function of interatomic distance between Li and B.	23
3.8	Mean-square displacement of ions in the amorphous (left column) and the crystalline (right column) polymers at several salt concentrations.	24
3.9	Charge mean-squared displacement, $\Sigma_{GK}(t)$ , in the amorphous (left) and the crystalline (right) polymers.	24
4.1	Mechanism for synthesis of polyborane-based electrolytes.	28
4.2	EIS-measured ionic conductivity ( $\sigma$ ) of poly-b9BBN at $R_{salt}=[9\text{BBN}]/[\text{BuLi}]=8$ at various temperatures. Inset displays chemical details of poly-9BBN before the reaction with BuLi. Experiments were conducted by Fernando Villafuerte.	29

4.3	Lithium ion solvation in bulk Poly-b2EtB. Left panel: a simulation snapshot at $R_{salt}=[2EtB]/[BuLi]=8$ . The color code is the following: Yellow spheres represent lithium ions; red sticks represent ethyl side chains for a butylated boron moiety; and pink sticks represent butyl side chains for a butylated boron moiety. Here, all the other atoms of polymer backbone and neutral boron moieties are not drawn for the clarity. Right panel: Cumulative distribution of hydrogens for a lithium ion. Blue line is for hydrogens of the carbon of a butyl side chain next to a butylated boron. Red line is for hydrogens of the carbon of a ethyl side chain next to a butylated boron. Green line is for hydrogens of the end carbon of a ethyl side chain of a butylated boron. . . . .	31
4.4	Ion transport in Poly-b2EtB. (a) Volume-corrected collective charge mean-square displacement, $\Sigma(t)$ , as a function of time, $t$ . The ratio is the molar ratio of 2EtB to BuLi, so the increasing ratio decreases the lithium concentration. (b) Mean-square displacement (MSD) of lithium ion. (c) MSD of carbon in a butyl moiety. (d) Lithium-boron contact duration, $H_{ca}(t)$ . . . . .	32
4.5	Ion aggregates at various salt concentrations, where $R=[2EtB]/[BuLi]$ . The color code is the same as in Fig. 4.3. . . . .	34
4.6	Effect of THF co-solvent on ion conductivity of poly-b2EtB at $R_{salt}=8$ with various equivalent concentration of THF to BuLi. (a) Volume-corrected collective charge mean-square displacement, $\Sigma(t)$ , as a function of time, $t$ . The ratio is the molar ratio of 2EtB to BuLi, so the increasing ratio decreases the lithium concentration. (b) Mean-square displacement (MSD) of carbon in a butyl moiety. (c) Lithium-boron contact duration, $H_{ca}(t)$ . . . . .	35
5.1	Chemical structures of the ethereal molecular electrolytes (DME and G4) and polymer electrolytes (PEO and P(2EO-MO)). . . . .	38

5.2	Simulation snapshot and electrode-charge polarization. (a) A simulation snapshot including PEO, $\text{Li}^+$ ions, $\text{TFSI}^-$ ions, $\text{Li}^0$ atoms, and model electrodes. The grey strand represents a single PEO chain. Purple spheres represent $\text{Li}^+$ ions while yellow ones do neutral $\text{Li}^0$ atoms. $\text{TFSI}^-$ ions are drawn in green. The two slabs are pristine, polarizable model electrodes held with the bias potential $\Delta\Psi = 0$ V. Color for the electrode atoms is associated with their induced charges between -0.01 (blue) and +0.01 (red). (b) Electrode-charge polarization on the innermost layer of the anode in (a). . . . .	39
5.3	Lithium-ion coordination environment at infinite dilution. Index of oxygens of (a) bulk PEO and (b) bulk P(2EO-MO) that forms the first solvation shell of a representative lithium-ion. Root-mean-square-deviation of the indices (i.e., index RMSD) of the oxygens of (c) PEO and (d) P(2EO-MO). PEO exhibits primarily intra-segmental solvation of the lithium ion, whereas P(2EO-MO) exhibits greater inter-segmental character. . . . .	45
5.4	Cumulative (a) and radial (b) $\text{Li}^+$ -oxygen distribution functions for the bulk electrolytes. Solid lines represent oxygen atoms of the electrolyte, and dotted lines represent oxygen atoms of $\text{TFSI}^-$ anion in each electrolyte. . . . .	47
5.5	The normalized local density (Eq. 5.7) of the ions and electrolytes as a function of distance, $d$ from the anode at various bias potentials, $\Delta\Psi$ . The columns of panels correspond to the various considered electrolytes. Row (a-d) presents the distribution for the $\text{Li}^+$ ions; Row (e-h) presents the distribution for ether oxygen of the electrolyte; Row (i-l) presents the distribution for $\text{TFSI}^-$ ions. In panels (i-l), solid lines represent oxygen atoms of $\text{TFSI}^-$ anion, and dotted lines represent a nitrogen atom of $\text{TFSI}^-$ anion. In all panels, the black vertical line indicates the location of the electrolyte-exposed layer of the anode. . . . .	48
5.6	Fraction of $\text{Li}^+$ ion solvation motifs, in bulk and at the anode interface with zero bias. . . . .	49
5.7	Distribution of induced charge per atom of the anode, for the various electrolytes and bias potentials. (a) PEO. (b) P(2EO-MO). (c) DME. (d) G4. Solid lines represent Gaussian fits. (E) Normalized local density of $\text{Li}^+$ ions on a log-linear scale at $\Delta\Psi = 4$ V. . . . .	50

- 5.8 Lithium electroreduction in PEO at the anode interface. (a-c) Probability distributions  $P(\Delta E)$  of the vertical energy gap  $\Delta E$ , and (d-f) their associated free energy curves for both the  $\text{Li}^+$  and  $\text{Li}^0$  in PEO. Results are shown for various bias potentials. Solid lines in (d-f) are parabolic curves using linear-response assumptions in Eq. 5.5. . . . 52
- 5.9 Mean electric potential across the simulation cell for the various electrolytes and bias potentials. In all panels, the black vertical line indicates the location of the electrolyte-exposed layer of the anode. . . 54
- 5.10 Spatially-resolved lithium-ion solvation motif at the anode interface. A top panel is for the first layer of interfacial lithium-ions, and a bottom panel is for the second layer of interfacial lithium-ions. For PEO and P(2EO-MO), the first layer is a region of  $d \in (2, 7)$ , and the second layer is a region of  $d \in [7, 11)$ . For G4, the first layer is a region of  $d \in (2, 4.5)$ , and the second layer is a region of  $d \in [4.5, 7)$ . The distance ( $d$ ) is from the anode in unit of Å. . . . . 55
- 5.11 Lithium electroreduction in P(2EO-MO) at the anode interface. (a-c) Probability distributions  $P(\Delta E)$  of the vertical energy gap  $\Delta E$ , and (d-f) their associated free energy curves for both the  $\text{Li}^+$  and  $\text{Li}^0$  in P(2EO-MO). Results are shown for various bias potentials. Solid lines in (d-f) are parabolic curves using linear-response assumptions in Eq. 5.5. . . . . 56
- 5.12 Lithium electroreduction in G4 at the anode interface. (a-c) Probability distributions  $P(\Delta E)$  of the vertical energy gap  $\Delta E$ , and (d-f) their associated free energy curves for both the  $\text{Li}^+$  and  $\text{Li}^0$  in G4. Results are shown for various bias potentials. Solid lines in (d-f) are parabolic curves using linear-response assumptions in Eq. 5.5. . . . 57
- 5.13 Lithium electroreduction in DME at the anode interface. (a-c) Probability distributions  $P(\Delta E)$  of the vertical energy gap  $\Delta E$ , and (d-f) their associated free energy curves for both the  $\text{Li}^+$  and  $\text{Li}^0$  in DME. Results are shown for various bias potentials. Solid lines in (d-f) are parabolic curves using linear-response assumptions in Eq. 5.5. . . . 58

6.1	Simulation snapshot and electrode-charge polarization. (a) A simulation snapshot including a BTFE-like SAM layer, $\text{Np}_2\text{F}$ salt, BTFE solvent, and model electrodes. Yellow spheres represent $\text{F}^-$ ions and $\text{Np}_2^+$ ions are drawn in orange. BTFE solvents are drawn in grey. Two slabs are pristine, polarizable model electrodes (purple spheres for the anode and pink ones for the cathode) held with a bias potential $\Delta\Psi = 4$ V. Color for electrode atoms is associated with their induced charges between $-0.05$ e (red) and $+0.05$ e (blue). (b) Electrode-charge polarization on the innermost layer of the anode in (a). . . . .	62
6.2	Local density of electrolyte atoms as a function of the distance from an anode with bias potential ( $\Delta\Psi = 4$ V) for various SAM layers. In each panel, the grey box indicates the 1.2 nm thick SAM region. . . . .	66
6.3	Fluoride-ion SAM density with bias potential ( $\Delta\Psi = 4$ V) for various SAM layers. (a) Potential of mean force ( $\beta W(d)$ ) associated with fluoride-ion SAM density, where $\beta = 1/k_B T$ . (b) Cumulative average ( $\rho_{ca}$ ) of $\text{F}^-$ density as a function of the distance ( $d$ ) from the anode surface. . . . .	67
6.4	Statistics of $\text{F}^-$ SAM density on the anode with bias potential ( $\Delta\Psi = 4$ V) for various SAM layers at two different coverage densities ( $\sigma_{SAM}$ ). (a,c) Cumulative average of $\text{F}^-$ density as a function of the distance, $d$ , from the anode surface. (b,d) The average distance of $\text{F}^-$ from the anode. . . . .	68
6.5	Statistics of $\text{F}^-$ SAM intercalation on the anode for BTFE-like and PVDF-like SAM layers with various bias potentials, $\Delta\Psi$ . (a) Average $\text{F}^-$ SAM density. (b) The average distance of $\text{F}^-$ from the anode. . . . .	69
6.6	$\text{F}^-$ density in a BTFE-like SAM layer as a function of time ( $t$ ) after bias potential is reversed (from $\Delta\Psi = 4$ V to $\Delta\Psi = -4$ V). Top panel: SAM intercalation. Bottom panel: SAM de-intercalation. In both panels, black dotted lines represent the results from different initial configurations, and colored lines are the averaged density over the initial configurations. Cyan lines are the fit using the Eq. 6.6. . . . .	70
6.7	Average time (Eq. 6.6) of $\text{F}^-$ SAM intercalation (top) and de-intercalation (bottom) in various SAM layers. . . . .	72

6.8	Kinetics of the electrode polarization during $F^-$ SAM (de-)intercalation. (a) Time-dependent charge polarization of each electrode during $F^-$ SAM (de-)intercalation in Fig. 6.6. (b) Relaxation time (Eq. 6.7) of the electrode polarization for $F^-$ SAM intercalation (top) and de-intercalation (bottom) in various SAM layers. . . . .	75
6.9	Fluoride-ion solvation sites in a BTFE-like SAM layer on a metal electrode. . . . .	76
6.10	Experimental results for ionic conductivity of $Np_1F$ (0.75 M) in BTFE:co-solvent mixtures. Asterisks indicate that a color change was observed during the experiment, suggesting reaction of $F^-$ with the co-solvent. . . . .	76
6.11	Ion transport in BTFE:co-solvent mixtures. (a) Correlation in displacement between $Np_1^+$ and $F^-$ , $z_i z_j \langle [r_i(t) - r_i(0)][r_j(t) - r_j(0)] \rangle / V$ , where $i$ indicates $Np_1^+$ , $j$ indicates $F^-$ , and $V$ is the volume of simulation box. (b) Volume-corrected charge MSD on a log-log scale, the slope of which indicates calculated ion conductivity. . . . .	77
6.12	Mean-square displacement of (a) $F^-$ , (b) $Np_1^+$ , and (c) BTFE in a mixture with a co-solvent or neat BTFE solution. . . . .	78

- 7.1 Experimental results of energy conversion using metal nanolayers with a flow of alternating salinity. (a) Photographs of iron and aluminum nanolayers with indicated thicknesses on microscope glass slides over the Northwestern University seal. (b) Current induced in a 10 nm Fe:FeOx nanolayer ( $3 \times 1 \text{ in}^2$ ) when flowing deionized (DI) water at pH 5.8 for 20 sec (blue segment), followed by 20 sec flow of 1 M NaCl held at pH 7 (green segment), and six subsequent replicates, all at a constant flow rate of  $20 \text{ mL min}^{-1}$ . (c) Average current densities measured as a function of aqueous flow velocity using 10 nm thin nanolayers of Fe:FeOx (blue-filled circles), Ni:NiOx (purple-filled circles), V:VOx (red-filled circles), Al:AlOx (grey-filled circles), and Cr:CrOx (orange-filled circles) while alternating deionized water (pH=5.8) and 0.6 M NaCl solution (pH~7) segments every 20 sec, and current density obtained for  $30 \mu\text{L}$  drops falling with a  $0.1$  to  $0.2 \text{ cm}^2$  contact area onto a 10 nm thick Fe:FeOx nanolayer deposited onto a  $1 \times 3 \text{ in}^2$  glass substrate while alternating the drop salinity between deionized water and 0.6 M at a drop rate of  $2 \text{ mL min}^{-1}$  and an incident angle of  $160^\circ$  (vertical blue bar). Error bars on point estimates shown are for 1 standard deviation from 7 or 8 replicate measurements per flow rate. (d) Current density recorded for Fe:FeOx nanolayers varying in total thickness obtained with a flow velocity of  $0.74 \text{ cm s}^{-1}$  while alternating deionized water and 0.6 M NaCl solution segments every 20 sec. . . . . 88

- 7.2 Model of charge mobility in nanoconfined, insulator-terminated metal conductor. (a) Atom probe tomography reconstruction of the heterostructured Fe:FeOx nanolayer (Center). Iron oxide and iron metal shown separately on top (red) and bottom (blue), respectively. (b) All-atom representation of the heterostructured nanolayer, including the metal conductor (gray) and a nonpolarizable oxide overlayer and with columnar subsurface heterostructure (pink); a single-probe Na<sup>+</sup> cation is shown at a distance of 1.6 Å from the nanolayer. (c) Induced charge distribution,  $Q(x)$ , by the Na<sup>+</sup> cation at 4 different lateral positions relative to the position of the nonpolarizable heterostructure as in Fig. 7.6. (d) Ion–nanolayer Coulomb interaction as a function of function of lateral ion position, for various widths,  $d$ , of the nonpolarizable heterostructure;  $\Delta E_{coul}$  is the difference in the ion–nanolayer Coulomb interaction for the nanolayer systems with and without the subsurface heterostructure. (e) MD simulation snapshot for alternating regions of ionized (0.43 M NaCl) water/DI water in contact with the nanolayer with columnar heterostructure ( $d = 1.3$  nm). The nanolayer is shown as in b, but with the instantaneous charge polarization of metal conductor atoms also indicated (range =  $[-0.005 e$  (blue),  $+0.005 e$  (red)]). Vertical dotted lines indicate semipermeable boundaries for the ions to preserve the salinity boundaries. (f) For the simulation cell shown in e, the time-averaged induced charge distribution,  $Q(x)$  (black), as well as the 0.5-ns block averages of the same quantity. (g) Comparison of the time-averaged induced charge distribution for the system with (black) and without (red) nonpolarizable heterostructure. . . . . 97
- 7.3 Illustration of energy conversion mechanism (a) and its equivalent circuit (b). See the text for details. . . . . 98
- 7.4 Scalability of energy conversion using metal nanolayers (a) with multiple droplets of same size, and (b) with breaking a large droplet into smaller ones. . . . . 98
- 7.5 Salinity boundary dynamics. (a) Induced charge distribution ( $-\delta Q(x, t)$ ) as a function of time ( $t$ ) after a water flow starts to cover a model nanolayer from  $x = 0$ . (b) Calculated time-dependent current output,  $I(t)$  with various relaxation times ( $\tau_k$ ) of the salinity gradient dynamics. Here,  $k_0 = 10$ . . . . . 99

7.6	For various positions of a single monocation, the distribution of induced charge in the metallic portion of the nanolayer, $Q(x, z)$ , integrated over the y-coordinate of the simulation cell. Nonpolarizable oxide atoms are indicated in pink. The position of the monocation is indicated with the black circle, illustrating various displacements with respect to the position of the subsurface heterostructure. . . . .	100
8.1	Schematic illustration of our experimental setup (left panel), including (i) water pump, (ii) column post to hold samples, metal nanolayer, (iii) deposited on its substrate (iv), and (v) picoammeter/Multimeter for electrical measurements. Green arrows indicate the direction of wave motion. Figure not drawn to scale. Right panel: calculated two-dimensional electrostatic potential inside a metal underlayer, $\Psi(x, y)$ (Eq. 8.10), with the preferential adsorption of (top) $\text{Na}^+$ ions ( $Q_{ion} = +10 \text{ mC m}^{-2}$ ), and (bottom) $\text{Cl}^-$ ions ( $Q_{ion} = -10 \text{ mC m}^{-2}$ ). . . . .	106
8.2	Electrical outputs in experiment and in computation. (a) Electrical outputs via a 10 nm Ni nanolayer on glass connected in series to a 100 $\Omega$ external resistor in our Instant Ocean wavetank. The wet area is 2.5 x 6.4 $\text{cm}^2$ . (b) Calculated electrical outputs (Eq. 8.4- 8.5) for a 10 nm Ni nanolayer connected in series to a 100 $\Omega$ external resistor using a model wave, $F(t)$ (Eq. 8.1 with $b = 2$ ). The same wet area is used as in (a). (c) Microscopic depiction of waving potential during the wetting stage of a wave event. The colorbar represents the potential gradient along a model metal nanolayer. . . . .	108
8.3	Ohmic contact in 10 nm thick Ni nanolayers with a wetted area of 2.5 x 6.4 $\text{cm}^2$ . (a) Linear relationship between peak current and peak voltage with variable external resistors. (b) Peak current, peak voltage, and peak power generated with variable external resistors. . . . .	109
8.4	Energy conversion via Ni nanolayers of various thicknesses with a wet area of 2.5 x 6.4 $\text{cm}^2$ . . . . .	110
8.5	Energy conversion via 10 nm thick Ni nanolayers of various sizes in experiment (left column) and in theory (right column). (a) The width of the nanolayers is fixed at 6.4 cm. (b) The height of the nanolayers is fixed at 2.5 cm. (c) Scalability depending on the location of electric pickups. . . . .	112
8.6	Energy conversion via 10 nm thick nanolayers of various metal elements with a wet area of 2.5 x 6.4 $\text{cm}^2$ . . . . .	114

8.7	Energy conversion via 10 nm thick Ni nanolayers on various substrates with a wet area of $2.5 \times 6.4 \text{ cm}^2$ . . . . .	115
8.8	Current (top) and voltage (bottom) recorded during wave action for 10nm thin nickel nanolayers on glass. Circles represent peaks picked from the time series. The cyan region is a buffer zone to exclude small irregularities in periodic signals and ensure the peaks are appropriately included. The peak finding method employed here infrequently misses peaks and rarely finds slightly false peaks for both current and voltage. However, we have sampled enough peaks for statistical analysis on both of the electrical outputs. . . . .	117
8.9	Triplicate electrical outputs of 10 nm Ni nanolayers in our Instant Ocean wavetank deposited via PVD in the same batch on glass substrate. The wet area is $2.5 \times 6.4 \text{ cm}^2$ . . . . .	118
9.1	A simulation snapshot with 0.1 M NaCl with $\sigma_0 = -0.04 \text{ C m}^{-2}$ . The inert layers are grey spheres, on top of which are hydroxyl groups (red and white spheres). Water molecules are in blue. Yellow and green spheres are $\text{Na}^+$ and $\text{Cl}^-$ ions, respectively. . . . .	121
9.2	Second-order nonlinear susceptibility of a single SiOH group, $\chi_{\text{SiOH}}^{(2)}$ , as a function of the tilt angle, $\theta_0$ . . . . .	126
9.3	Heterodyne-detected SHG measurements on abrupt salinity transitions. (a-b) Point estimates of $\chi^{(2)}$ (orange) and $\Phi(0)_{\text{tot}}$ (blue) obtained from the experimentally determined SHG signal and SHG phase for ionic strength conditions indicated. (c) Correlation plot of $\chi^{(2)}$ and $\Phi(0)_{\text{tot}}$ for 0.1 M to 10 $\mu\text{M}$ jump (light green) and 0.1 M to 1 mM NaCl (dark green). Portion shown is for forward (high to low [salt]) jumps only, the results for the return jumps are omitted. . . .	128
9.4	Atomistic simulation model and interfacial ion distribution. (Top left) Atomistic models used in our analysis. (Top right) Calculated distributions of $\text{Na}^+$ ion at the silica surface for the four situations examined. (Bottom) Angle:distance probability density plots at zero NaCl concentration for the contact ion (left) and solvent-separated (right) ion pairs. See text for details. . . . .	130

- 9.5 Second-order nonlinear susceptibility estimates computed for the various models and scenarios examined as a function of distance from the interface (Left and Center). First and third moments of the water orientation angle and water oxygen density as a function of distance from the interface (Right) for the various models and scenarios examined. . . . . 131
- 9.6 Comparison between experiment and simulation. (Left)  $\chi_{tot}^{(2)} : \Phi(0)_{tot}$  correlation plot after normalization and referencing overlaying the experimental (green circles) and model-computed (blue circles) results. (Right) Same data but showing only the positively signed portion on the ordinate. Thicker the blue circles indicate higher charge density in the model (-0.02, -0.04, and -0.08 C m<sup>-2</sup>). Blue lines show the  $\chi_{water}^{(2)}$  results only. See text for details. . . . . 134
- 9.7 Calculated electric field for model silica:water interfaces. (a, b) Electrostatic field across the fused silica:water interface from finite element calculations. The silica contains 100 ppm of charged impurities and the aqueous phase is at 0.1 M [NaCl]. The relative permittivity in the aqueous phase is 78. (c, d) Height vs. position profiles from several atomic force microscopy lines scans across the flat side of our fused silica hemispheres, primitive cell used for finite element calculations shown in black box nested in between its periodic images, and electrostatic field across an atomically smooth (black line) and rough (purple line for L=H=1 nm features, blue line for L=H=2 nm features) fused silica:water interface. Horizontal dashed line depicts the E-field value used for the 1-nm wide rough region. The relative permittivity of the aqueous phase is 78. The surface charge density is -0.015 C m<sup>-2</sup>. . . . . 137
- 9.8 Finite element calculation model for a corrugated oxide:water interface. The rough oxide:water interface is modeled using a nanoscale dendrite of height (H) and length (L), represented by the yellow region. Bright green elements are the dendrite corners where the oxide:water boundary is along both the x- and y-axes. . . . . 139

## LIST OF TABLES

<i>Number</i>	<i>Page</i>
3.1 Computed ion-transport coefficients in the P3HT-IM polymers at various $r$ ([LiBF <sub>4</sub> ]/[monomer]) at 400 K. Diffusion coefficients ( $D$ ) are in unites of Å <sup>2</sup> /ns. Ionic conductivities ( $\sigma$ ) are in unites of S/m. Statistical errors of the final digit are indicated in parentheses. . . . .	22
4.1 Fitting results of ionic conductivity ( $\sigma$ ) in Fig. 4.2 using the Arrhenius relation: $\sigma(T) = \sigma_0 \exp(-E_a/RT)$ . $R^2$ is the coefficient of determination. . . . .	30
5.1 Fraction of lithium-ion solvation motifs in bulk electrolytes at finite concentration. Statistical errors of the final digit are indicated in parentheses. <sup>a</sup> The remaining fraction is associated with multi-chain solvation more than two. . . . .	46
6.1 Four SAM molecules considered in this study. <sup>a</sup> E represents an electrode surface. <sup>b</sup> CH <sub>2</sub> moiety is present next to CF <sub>2</sub> without an oxygen atom. . . . .	62
6.2 Ion SAM molar density at various bias potentials ( $\Psi$ ). Excess charge molar density is the difference between ion molar density with the charge considered. Statistical errors of the final digit are indicated in parentheses. . . . .	69
6.3 Diffusion constants (Å <sup>2</sup> /ns), ion dissociation, and F <sup>-</sup> solvation sheath composition, (BTFE) <sub>X</sub> -(co-solvent) <sub>Y</sub> -(Np <sub>1</sub> <sup>+</sup> ) <sub>Z</sub> , in 0.75 M Np <sub>1</sub> F electrolytes determined from all-atom simulations. Statistical errors of the final digit are indicated in parentheses. . . . .	77
7.1 Lennard-Jones parameters for water, ions, and nanolayer atom. . . . .	86
9.1 Lennard-Jones parameters and atomic charge of water, ions, and model silica atoms. . . . .	123
9.2 Electric potentials and second-order susceptibilities at various surface-charge densities ( $\sigma_0$ ) and NaCl concentrations (0.1 M or 0 M). Three different conditions for interfacial Na <sup>+</sup> ions are investigated: CIP represents contact pairs of SiO <sup>-</sup> . . . Na <sup>+</sup> , SSIP represents solvent-separated contact pairs of SiO <sup>-</sup> and Na <sup>+</sup> , NIP represents the case of no interfacial Na <sup>+</sup> . . . . .	133

*Chapter 1***BRIEF OVERVIEW AND MOTIVATION**

This thesis is a result of pursuing fundamental understandings of molecular processes using simulations in collaboration with experiments to provide design rules for energy storage and conversion materials to accelerate their discovery and development. To meet the energy demand of the modern lifestyle while reducing the use of fossil fuel and thereby reducing greenhouse gas emissions and air pollution, we need to harvest clean, renewable energies as much as possible such as solar, wind, and hydro energy [75]. The intermittent nature of renewable energy sources requires a large-scale energy storage system that operates in a safe way [154]. Furthermore, battery technology is at the heart of our modern life, from small personal electronics to electric transportation [179]. Herein, for developing advanced rechargeable batteries, we discuss the necessity of solid polymer electrolytes that effectively transport ions and a polymeric thin film layer that provides enhanced stability of a battery interface. Regarding clean energy harvesting, we discuss an emerging technique called "hydrovoltaics" to generate electricity from water kinetic energy, utilizing a water-solid interface instead of a turbine.

Stabilizing their interfacial is a great challenge to build better rechargeable batteries for large-scale energy grid systems and electric vehicles [175, 197, 122, 54, 182, 178, 105, 53]. In commercially widely used lithium-ion batteries, liquid electrolytes shuttle ions between a carbon anode and a metal oxide cathode, while electrons are transferred through an external wire. While a liquid electrolyte efficiently transports the ions with an excellent ion solubility, electrolyte decomposition at the electrode interface could lead to significantly limited lifespans, severe safety concerns, or battery failures if not controlled. Further, lithium electrodeposition also sometimes becomes dendritic, which could short-circuit a battery, penetrating a separator. The interfacial safety issues become even more severe with a lithium metal anode; despite its lightweight and high reactivity, its practical use is quite limited due to the thermal runaway, and the dendrite formation [197, 105]. Therefore, the ultimate design principle for the electrolyte is an effective ion conductor with tremendous interfacial stability not to compromise the electrochemical performance or safety.

One of the ways to provide enhanced interfacial stability is to replace the liquid

electrolyte with solid-state polymeric materials [105, 216, 196]. We note that this thesis does not include the discussion of solid-state inorganic materials. The solid polymer electrolytes (SPEs) have been known to be effective in suppressing the dendritic growth of lithium deposits with high modulus and good adhesion. Their easy processing also enables higher energy density with the decreased package volume. However, the major downside of SPEs is that their ion conductivity is more than two orders of magnitude lower than their liquid counterparts; the practically useful ionic conductivities (on the order of  $1 \text{ mS cm}^{-1}$ ) are obtained only at elevated temperatures [144, 116]. Thus, designing fast ion-conducting SPEs is a grand challenge for building better batteries.

One of the best-performing SPEs is polyethylene oxide (PEO) since its development in the 1970s [143, 145, 144, 116]. In a molecular picture, electron-rich oxygen provides local regions for metal ions to sit on, which is a major driving force of lithium salt solubility in this low dielectric polymer. Strong ion-polymer interaction strongly couples ion transport to polymer segmental relaxation, resulting in slower cation transport than anion. Further, physical crosslinks between cations and PEO chains severely limit the number of available free cations, hindering the leading to the maximum ion conductivity at a pretty low salt concentration.

An excellent polymeric ionic-conductor should be flexible with reduced glass transition temperature and decreased crystallinity to facilitate intersegmental ion hopping [216, 196]. SPEs also need to simultaneously facilitate ion-pair dissociation and exhibit minimal resistance to ion motion. However, in the most liquid and solid electrolytes, free ion concentration and ion mobility compete with each other, which challenges the development of a better SPE. For example, on the one hand, ion mobility is likely to be enhanced with a chemical moiety to decrease ion-polymer interaction, yet salt solubility should be severely decreased. On the other hand, the number of free ions could be increased with a chemical moiety to increase ion-polymer interaction, yet the ion mobility should be significantly decreased.

This thesis firstly presents a salt-concentrating approach as an effective design strategy for polymer-based electrolytes. In essence, we suggest a structure-dynamics relationship to support an enhanced ionic conductivity in concentrated regimes; spatially extended ionic aggregates could provide continuous pathways for ions to travel efficiently.

Developing a better battery requires molecular understandings of ion solvation and transport at an electrified interface. The battery interface is quite complex due to

the presence of a thin film called a solid electrolyte interphase (SEI) that forms due to immediate and spontaneous electrolyte degradations [132, 29, 5, 142, 184, 24]. An SEI is structurally and chemically heterogeneous, including organic, inorganic, and even polymeric components; the heterogeneities further complicate interfacial molecular processes by increasing the complexity of the ion-transport and electron-leakage pathways, potentially resulting in an unstable battery interface. A functional SEI should passivate an electrode by conducting active species yet blocking electron conduction. As a result, further detrimental side reactions and the dendrite formation could be alleviated.

A useful SEI should also regularize lithium electroplating, mitigating dendrite growth [105]. All the five steps in lithium electroreduction affect the final morphology of lithium deposit: bulk ion transfer, desolvation of the ions at the battery interface, surface adsorption, charge transfer, and surface diffusion to the deposition site [105]. For instance, limited bulk lithium transfer could break electrical neutrality, building a local space charge at an anode interface that potentially leads to the dendritic growth of lithium deposits. As it is discussed above, the dendrite growth worsens at a metallic anode, and regularizing lithium plating is a key challenge to revive a lithium metal anode.

This thesis secondly discusses the molecular processes at a metal anode interface, including a thin polymeric SEI layer that forms from electrolyte decomposition and an artificial organic SEI layer from deposition of sacrificial additives. One of the merits of our interface simulation studies is that the image-charge effect is included by using a polarizable metal electrode, which significantly affects ion adsorption behaviors and ion-ion interaction in the vicinity of a metal electrode. Factors that govern lithium electroreduction at the metal/SEI are investigated to provide fundamental understanding of how polymeric materials could benefit the battery interface, mitigating the dendrite growth and design rules for sacrificial additives to form a functionally useful SEI.

In regards to energy conversion, we are interested in harvesting hydro energy that has a vast potential to provide clean electricity; for instance, more than 50 percent of the U.S. population lives within 50 miles of coastlines [1]. Water is an abundant energy source, covering  $\sim 70\%$  of the Earth's surface, whose energy evolves into a rich variety of forms that dominate the energy transfer occurring in various natural phenomena through the hydrological cycle on Earth [213, 214]. According to the Energy Department, wave energy resources along U.S. coastlines range between

approximately 900 and 1,230 terawatt-hours (TWh) per year [1]; one TWh per year can power approximately 90,000 homes.

Converting hydro energy to electricity goes back to the late nineteenth century [186, 213]. Quincke found that electricity is generated when a pressure gradient drives a flow of aqueous electrolytes through a narrow channel. Energy harvesting is a result of direct interaction between water and solid, transporting preferentially populated ions at the interface. For instance, most oxides are negatively charged, so they preferentially populate cations over anions at their surface in order to balance charge neutrality [109]. The aqueous region where the local charge neutrality is broken is called an electrical double layer (EDL). Thus, cations (in this example) are favorably transferred along with a pressure gradient, which will drive an electrode reaction due to the ion concentration gradient, if an external wire is connected. If not, a potential gradient is built across the channel to balance the concentration gradient, called streaming potential. Thus, this classical electrokinetic effect converts water kinetic energy to electricity, utilizing an EDL at a water-solid interface. However, its practical application is quite limited due to the low energy conversion efficiency of the streaming potential (only around  $\sim 3\%$  in practice and  $\sim 12\%$  in theory) [70, 181].

Recently, many other ways, similar to classical electrokinetics, have been developed to harvest hydro energy to generate electric energy, utilizing a solid surface in contact with water to generate electricity instead of a turbine [174, 213]. The advantages of these emerging techniques called "hydrovoltaic" technology include their relatively high conversion efficiency (reported up to 30%) and their operation in various modes [128, 130]. Successful hydrovoltaic materials include low-dimensional nanometer-thin carbon materials such as graphene and doped graphenes [206, 205, 202, 176] and silicon-based semiconducting nanofilms [128, 130].

Hydrovoltaics requires an EDL boundary, while both classical electrokinetics and the newly developed methods utilize an EDL at a solid-water interface [213]. One example is a moving droplet of ionic water in contact with a graphene substrate [205]. In this case, a water-air boundary corresponds to an EDL boundary. Electricity generation is not free since no energy is harvested when the droplet is still. Once the droplet moves, the interfacial ions adsorb and desorb at the EDL boundaries along with the moving droplet, which is a vital process in hydrovoltaics. Furthermore, a hydrovoltaic material should conduct electrons, while classical electrokinetics only need a solid substrate for ion adsorption. The adsorbed cations polarize the

graphene, inducing electrons at the interface to be transferred along with the flow. In this regard, we need to investigate molecular processes at a solid-water interface to advance our understanding of the electricity generation mechanisms and enhance the transduction efficiency.

This thesis presents electricity generation using our newly developed metal nanolayers as a the hydrovoltaic material, which exhibits the transduction as effective as previous successful (semi-)conducting materials. Our combined efforts of theory and experiment have been devoted to unveiling the energy conversion mechanisms in various operating modes and rationalizing design rules found in experiments by connecting microscopic variables at a molecular level to macroscopic outputs at a device level.

*Chapter 2*

## INTRODUCTION

Molecular simulation is a powerful tool to build and advance our understanding of molecular processes of energy materials and even predict their performance spanning a wide range of chemical space. This thesis utilizes molecular simulations to build molecular principles of charge transport in energy materials, thereby accelerating their development for storage and conversion applications.

Part I focuses on simulations of lithium-ion transport in bulk polymer-based electrolytes, factors for electron transfer kinetics at thin polymeric film/metal interfaces, and fluoride-ion solvation structure and dynamics in a self-assembled monolayer at a metal anode.

We begin by discussing lithium-ion transport mechanisms in solvent-free polymer-based electrolytes. In Chapter 3, we suggest a unique lithium-ion transport mechanism associated with the morphological feature of ion aggregates in a model mixed polymeric conductor with an ionic liquid pendant. The solvent-free polymer is a positively charged single-ion conductor with an imidazolium pendant. Ions in such a mixed conductor diffuse in an ordered region, which is complicated by the presence of the ordered region that is responsible for electron or hole transport. We found simulations support experimental results that ionic conductivity of the mixed conductor monotonically increases up to exceptionally high salt concentrations. We rationalized this intriguing result by connecting ion transport mechanism and the morphology of ion aggregates: A percolating ion network facilitates lithium-ion transport by providing connected pathways to travel, whose formation is stabilized by the presence of the charged imidazolium pendant.

In Chapter 4, we continue to discuss the connection between the formation of a spatially extended ion aggregate and enhanced lithium-ion transport in recently developed polyborane-based electrolytes. The polyborane single-ion conductor has a negatively charged borane moiety that electrostatically attracts lithium ions, forming ion aggregates. We found that at high butyllithium concentrations, a percolating ion network facilitates lithium-ion transport via local reorganization of the borane sites, while lithium diffusion is localized in small ion clusters at low concentrations.

We then discuss ion solvation and transport in a solid electrolyte interphase (SEI)

at electrified interfaces. As it is well known, enhancing interfacial stability is a key challenge in the development of next-generation rechargeable batteries for large-scale energy grid systems and for electrical vehicles [175, 197, 122, 182, 178, 105, 53, 59]. A functional SEI stabilizes the electrochemical interface by allowing for facile ion transport, yet blocking electron transport. One of the computational novelties in this thesis is that a polarizable metal electrode is incorporated in our models to investigate the effect of applied potential with the image-charge interaction included.

In Chapter 5, we investigate factors that affect interfacial electron-transfer kinetics, including lithium-ion solvation structures and solvent reorganization as a function of applied electrode potential, at an SEI/metal interface. Linear ether homopolymers are studied as a chemically and structurally well-defined proxy for polymeric SEIs, along with the ethereal molecular solvents. Interfacial ion solvation at the metal anode is strikingly dependent on chain connectivity, solvation environment, and the magnitude of the applied electrode potential, resulting in very different electron-transfer kinetics for lithium electroreduction. Nevertheless, the linear-response assumptions of the Marcus theory for electron transfer are found to be robust in both polymeric and molecular SEIs.

In Chapter 6, we suggest design rules for a self-assembled monolayer (SAM) layer as an artificial SEI to passivate a metal anode by investigating fluoride-ion solvation structure and dynamics. The molecular recipe for sacrificial additives for the SAM layer includes great film formation ability, high fluoride-ion solubility, poor solvent penetration, and fast (de-)fluorination. The static results of atomic-resolution simulations suggest that both fluorinated and  $\alpha$ -CH<sub>2</sub> moieties are necessary for a functional SAM molecule, as in bis(2,2,2-trifluoroethyl) ether solvent that enables facile fluoride-ion shuttle at room temperature. We found the structure-dynamics relationship in fluoride-ion SAM solvation, connecting the kinetics with several distinct fluoride-ion SAM solvation states. Further, a sizable free-energy barrier at a SAM/electrolyte boundary suggests that a better choice of its end group of a SAM molecule, which faces towards the boundary, could enhance the fluoride-ion shuttle across the SAM.

Part II focuses on simulations of molecular principles for energy conversion processes from water kinetic energy to electricity using metal nanolayers. Such "hydrovoltaic" energy conversion is primarily enabled by ion adsorption and desorption in an electrical double layer at a liquid-solid interface, subsequently inducing electrons

in a solid substrate [213].

In Chapter 7, we discuss molecular processes of electrical current generation using metal nanolayers with a flow of alternating salinity gradients, including charge induction, salinity boundary dynamics, and functional mechanisms. The metal nanolayers are heterostructured [43, 14] with a metal covered by a few nanometers thin thermal oxide over-layer, both of which are involved in the energy conversion process. The interface of the heterostructure is even dendritic, implying potential complications in further optimizations. Experiments suggested additional design rules for functional nanolayers: (i) a redox-active oxide overlayer, and (ii) a nanometer-thin metal layer below, whose thickness is comparable to electron mean-free path. We present simulation approaches to rationalize the design rules observed in experiments by providing molecular understanding, constructing connections between microscopic variables to device-level observables.

In Chapter 8, we continue to discuss electricity generation mechanisms of the metal nanolayers that operate in a wavetank filled with ocean water mimic. We suggest a mechanism that involves a momentary non-equilibrium state at an air:water:oxide junction to generate a potential difference across a metal nanolayer. With a combined effort of experiment and computation, the scalability of the energy conversion is investigated with the nanofilm's thickness and its footprint based on predictions from the waving potential model. Additional factors, including metal elements and substrate, are also investigated to optimize energy conversion efficiency. With their scalable nature and ease of making, the metal nanolayers are appealing as cost-effective alternatives for real-life applications in harvesting ocean wave energy.

Lastly, in Chapter 9, we discuss molecular insights from atomistic simulations into the structure and dynamics of electrical double layers (EDLs). In particular, their responses to an abrupt salinity transition of ionic solutions over fused silica at constant bulk solution pH are investigated. The response of Stern and diffuse layers, disentangled using heterodyne-detected second harmonic generation (HD-SHG) measurements, is found not necessarily concerted, but depends on how big the ionic strength jump is. Simulation suggests that specific interaction between sodium ions and the silica surface plays a prominent role in decoupled kinetics of two EDL layers, recapitulating the results of HD-SHG. Molecular understandings of the responses at electrified interfaces to external stimuli will advance materials design for energy transducers such as metal nanolayers.

PART I. ION SOLVATION AND TRANSPORT AT BULK AND  
ELECTRIFIED INTERFACES FOR ENERGY STORAGE  
APPLICATIONS

## FACILITATED LITHIUM-ION TRANSPORT IN IONIC LIQUID FUNCTIONALIZED CONJUGATED POLYMERS AT HIGH SALT CONCENTRATIONS

### 3.1 Abstract

This chapter discusses the ionic conduction of model mixed polymeric conductors in which ionic liquid groups are tethered to an electron-conducting conjugated polymer backbone. Ion transport in such a mixed-conducting material is complicated by the presence of both ordered and disordered regions that follow distinct materials design rules. The model conjugated polymeric ionic liquid, poly3-[6'-(N-methylimidazolium)hexyl]thiopheneBF<sub>4</sub><sup>-</sup> (P3HT-IM) is capable of dissolving Li<sup>+</sup> salt up to a concentration of  $r = 1$  [moles of salt]/[moles of monomer]. Surprisingly, the polymer displays a monotonic increase in ionic conductivity with salt concentration, reaching a maximum ionic conductivity of  $10^{-5}$  S cm<sup>-1</sup> at the highest concentration of  $r = 1$ . We propose a lithium-ion conduction mechanism that utilizes an ionic network of which the imidazolium side chains promote formation using all-atom molecular dynamics simulations. The percolated ion network facilitates ion transport, decoupled from polymer segmental dynamics up to unusually high salt concentrations. The result suggests that the morphological features of ion aggregates and ion conduction is crucial to determine ion conductivity at high salt concentrations, which needs to be considered in the design of such a mixed-conducting polymer.

Data and content in this chapter have been published as Ref. [146]. The author participated in conducting simulations of amorphous polymers, discussing the results of ion solvation and transport in the polymers, and preparing a draft.

### 3.2 Introduction

Simultaneous ion and electron conduction is essential in all electrochemical devices and is particularly important for applications in energy storage, and conversion [152, 131]. The rational design of mixed conducting organic materials is challenging because ion and electron conducting materials follow different design rules. Ion transport in polymers is generally correlated to segmental motion and is optimized in polar rubbery materials [145, 143, 169, 17], while electron transport often re-

lies on structural alignment in highly ordered polymeric systems [152, 131, 124]. Conjugated polymers are particularly promising in the field of mixed conductors because their electronic, ionic, and structural properties can be readily tuned through conventional synthetic design strategies [159, 52, 160].

Incorporating ion-conducting moieties into conjugated polymers serves as a route to provide conduction pathways for both ions and electrons. Optimizing ionic and electronic conduction in conjugated polymers requires a system with both highly ordered and polar domains with high segmental mobility. Conjugated polymers with oligoethylene glycol side chains have shown both high ionic conductivity ( $\approx 10^{-4}$  S cm $^{-1}$ ) upon lithium salt addition and evidence of long-range order [161]. The addition of ionic moieties, such as sulfonate groups, to a conjugated polymer backbone promotes ion transport and ion injection in electrochemical devices [25].

Ionic liquid moieties can be tethered to a conjugated polymer backbone to enable ion conduction without the presence of a solvent, which is particularly important for solvent-free electrochemical devices [159, 34, 156, 160]. Mixed conducting conjugated materials are commonly employed as protective coatings and binders for cathode materials in batteries due to their easy processability and facile ion and electron transport in the presence of liquid electrolyte [90, 36]. However, increasing interest in solvent-free battery construction has created a demand for materials that can conduct both ions and electrons without the presence of a solvent. Conjugated polymers with ionic liquid-like side chains have considerable promise in the field of solvent-free mixed conduction. Large, polarizable ionic side-chain moieties serve to weaken ionic associations and increase ion dynamics without the presence of a solvent, while the conjugated backbone imparts electron conductivity [160]. Polythiophenes with imidazolium side chains have shown intrinsic ionic conductivity up to  $10^{-4}$  S cm $^{-1}$  in the neat state, while also showing evidence of significant long-range order in scattering studies [138, 139].

Ion conductivity in polymer electrolytes is dependent on the concentration and mobility of ions, which are related to the polarity and the segmental dynamics of the polymer [145, 143, 52, 169, 17]. For a given concentration of added salt, the mobile ion concentration depends on the extent of salt dissociation, which is affected by the local dielectric environment, the interactions between anions and cations, and interactions between the polymer and the ions [160]. Introducing of highly polar functional groups or increasing the size and polarizability of ionic groups serves to increase the dielectric constant, weaken electrostatic interactions, and promote ion

dissociation [159, 156, 65]. Additionally, the mobility of ions generally depends on the dynamics of the polymer system as solvation sites rearrange to create a conduction pathway [145, 143, 190]. For polymers above their glass transition temperature ( $T_g$ ), the ionic mobility is often tied to the segmental dynamics of the polymer, which is related to the distance from  $T_g$ . However, ion dynamics are also affected by the nature of ion-ion and polymer-ion associations, where ion solvation sites and ion coordinating groups, which help ions dissociate, can slow ion dynamics.

Ion aggregation counterintuitively can lead to higher ionic conductivity if aggregates percolate through the material [212, 30, 18, 126, 20]. Ion transport in many polymeric systems can be characterized by transport through a transient network of solvation sites, where the mobility of ions is partly connected to the density and connectivity of solvation sites. Local ion transport in aggregated domains is postulated to be higher in some systems due to the proximity of solvation sites. In this case, the ionic mobility is related to the extent to which aggregates form continuous domains through the material.

This chapter presents ionic transport mechanisms in a semicrystalline polythiophene-based system with ionic side chains, enabling simultaneous ionic and electronic conduction through the addition of salt. Surprisingly, the polymer solvates added salt up to a concentration of  $r = 1$  [mole of salt]/[mole of monomer], and displays a monotonic increase in conductivity with salt concentration. MD simulations suggest that a percolating network of solvation sites forms at high concentrations, facilitating lithium-ion conduction over a wide range of salt concentrations. This unique ion conduction mechanism provides a guiding principle to optimize such a mixed-conducting polymer further.

### **3.3 Computational Methods**

#### **Molecular dynamics simulations**

All-atom molecular dynamics simulations were carried out to provide molecular-level mechanistic insights into ion solvation and ion transport. Simulations for P3HT polymers with charged imidazolium side chains were carried out in both crystalline and amorphous phases. Initial configurations of crystalline polymers were generated by stacking 16 straight polymer chains into two separate adjacent stackings (8x2 grid), where each chain consisted of 10 monomers. A  $\text{BF}_4^-$  counterion was added in the proximity of each imidazolium moiety to balance the positive charge.

Additionally, an equal number of  $\text{Li}^+$  and  $\text{BF}_4^-$  ions was added in random positions in the simulation box to study the effects of salt concentration. The Li-free polymer ( $r = 0$ ) was equilibrated for 5 ns. The additional salt was added in gradually, 32 ion pairs at a time ( $r = 0.2$ ), and at every stage the simulation was equilibrated for an additional 1 ns. Amorphous polymers at each salt concentration were prepared by annealing the crystalline polymers at a higher temperature of 600 K for at least 2 ns, followed by an additional 10 ns equilibration at 400 K.

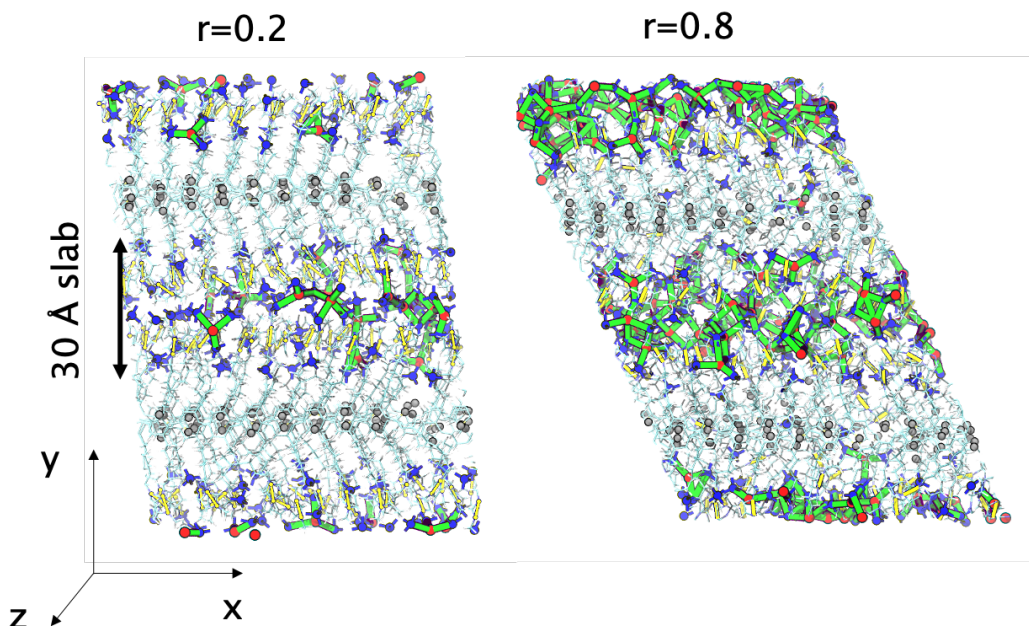


Figure 3.1: MD snapshots for the crystalline polymers at  $r = 0.2$  (left) and  $r = 0.8$  (right). The color code is as follows: red spheres represent Li cations; blue spheres represent  $\text{BF}_4^-$  anions; yellow surfaces represent imidazolium nitrogen atoms; grey spheres represent sulfur atoms of thiophene rings; and green lines connect neighboring Li and  $\text{BF}_4^-$  within 4 Å.

The OPLS force field [79, 80], a non-polarizable and all-atom model, was used to describe the potential energy functions of all molecules. Interactions between atoms were described using both electrostatic and Lennard-Jones (LJ) interactions. The cross terms of LJ interaction were obtained using the geometric mixing rule. Intramolecular interactions were described using harmonic potential energy functions for bonds and angles, and the sum of cosine functions for dihedral and improper angles. Bonding and non-bonding coefficients were obtained using the online generator LibParGen [41]. To incorporate the effects of polarizability for ionic species, all atomic charges were multiplied by a constant scalar (0.7) as previously suggested

in the MD literature [117, 93]. All simulations were conducted using the LAMMPS simulation package [140].

In all cases during both equilibration and production runs, the MD trajectories were integrated using the velocity-Verlet algorithm with a timestep of 1 fs. Both LJ and Coulomb interactions were cut at 12 Å, and particle-particle particle-mesh Ewald summation [72] was used to compute Coulomb interactions beyond the cutoff distance. Periodic boundary conditions (PBC) were applied for both crystalline and amorphous polymers. The Nosé-Hoover thermostat (100 fs relaxation) and the Nosé-Hoover barostat (1000 fs relaxation) were applied in all simulations to control the temperature (300 K or 400 K) and the pressure (1 atm). All transport properties reported here were averaged using simulation trajectories over at least 80 ns after at least 20 ns long equilibration.

### Calculation of ion-transport properties

Charge mean-squared displacement,  $\Sigma(t)$ , is calculated via the Einstein relation [4, 50, 47, 46, 49] as follows:

$$\Sigma(t) = \frac{1}{k_B T \langle V \rangle} = \sum_{i=1}^N \sum_{j=1}^N z_i z_j \langle [r_i(t) - r_i(0)] [r_j(t) - r_j(0)] \delta(|r_i(0) - r_j(0)| - r_{cut}) \rangle, \quad (3.1)$$

where  $N$  is the total number of ions including Li cations,  $\text{BF}_4$  anions, and nitrogen atoms of imidazolium pendants,  $z_i$  (either +1  $e$  or -1  $e$ ) is the charge of  $i^{\text{th}}$  ion,  $\vec{r}_i(t)$  is the position of  $i^{\text{th}}$  ion at time  $t$ ,  $V$  is the volume of a system, and  $\langle \dots \rangle$  represents the ensemble average. For faster computation, we consider only ion pairs within a cut-off distance,  $r_{cut}$  ( $=8$  Å), at an initial time. This cut-off distance is determined by radial distribution of  $\text{BF}_4$  around a Li ion (Fig. 3.7). This  $\Sigma(t)$  is a collective property that takes all correlations into account, whose slope with respect to time is the ionic conductivity. The ion conductivity ( $\sigma_{GK}$ ) were estimated using the slope between two points of  $\Sigma(t)$  at  $t_1 = 10$  ns and  $t_2 = 100$  ns:

$$\sigma_{GK} = \frac{1}{6} \frac{\Sigma(t_2) - \Sigma(t_1)}{t_2 - t_1}, \quad (3.2)$$

where GK represents Green-Kubo formula. Note that in the simulated time window,  $\Sigma(t)$  is not linear with time but sub-diffusive, i.e.,  $\Sigma(t) \propto t^b$  with an exponent  $b \approx 0.98 - 0.9$ , indicating that the ionic correlations do not fully decay on timescales less than 100 ns, regardless of salt concentration. Use of different values of time for  $t_1$  and  $t_2$  did not qualitatively change these findings. When all correlations (off-diagonal

terms) are negligible, it becomes the same as the Nernst-Einstein (NE) equation [47, 46, 49]:

$$\sigma_{NE} = \frac{e^2}{k_B T \langle V \rangle} N_{monomer} \left[ r D_{Li} + (1 + r) D_{BF_4} + D_N \right], \quad (3.3)$$

where  $D$  is ion self-diffusion coefficient (Li,  $BF_4$ , or N),  $N_{monomer}$  is the total number of monomers, and  $r$  is the number ratio of  $LiBF_4$  to the monomers. The ion self-diffusion coefficients ( $D$ ) were estimated using the slope between two points of mean-squared displacement as for  $\sigma_{GK}$ :  $D = \frac{1}{6} \frac{MSD(t_2) - MSD(t_1)}{(t_2 - t_1)}$ . Lithium transference number ( $t_{Li}$ ) is calculated using diffusion coefficients of the ions, without taking other correlations into account except for self-correlations:  $t_{Li} = D_{Li} / (D_{Li} + D_{BF_4})$ . Contact duration,  $H(t)$ , is calculated for a pair of Li and  $BF_4$  as follows:  $H(t) = \langle h(t)h(0) \rangle / \langle h(0)h(0) \rangle$ , where  $h(t) = 1$  if a pair of Li and  $BF_4$  is within  $4 \text{ \AA}$  at time  $t$ , or  $h(t) = 0$ , otherwise, based on the first plateau in the cumulative distribution of  $BF_4$  around a central Li in Fig. 3.7. The average contact duration,  $\tau = \tau_H \left( \frac{e}{A_H} \right)^{1/b_H}$ , was estimated using a fit to a stretched exponential function:  $H(t) \approx A_H \exp[-(t/\tau_H)^{b_H}]$ .

### Percolating behavior of the ionic network

To quantify the percolation transition of the ionic network as a function of salt concentration, we construct a graph whose nodes are Li ions and B atoms of  $BF_4$  ions. Edges between the nodes are defined if the distance between Li and B is less than  $4 \text{ \AA}$ . We use NetworkX (<https://networkx.org>) to find the largest cluster in the graph. We define the largest cluster to percolate the simulation box if the longest distance between two Li ions in the cluster is larger than the simulation box size. In this calculation, all the Li ions in the cluster are in the primitive simulation cell, and the longest distance is calculated without periodic boundary conditions applied. Then, the probability of forming a percolating ionic network,  $P_{perc}$ , is calculated:  $P_{perc} = \langle p \rangle$ , where  $p = 1$  if the largest cluster percolates the simulation box, or 0 otherwise.

## 3.4 Results and Discussion

### P3HT-IM polymers with $BF_4$ counterions

A semicrystalline polythiophene-based conjugated polymer with ionic side chains was developed as a model mixed ion and electron conductor. Polythiophene serves as an ideal model conjugated polymer backbone because it belongs to a well-studied class of semicrystalline conjugated polymers with reasonable mobility and long-

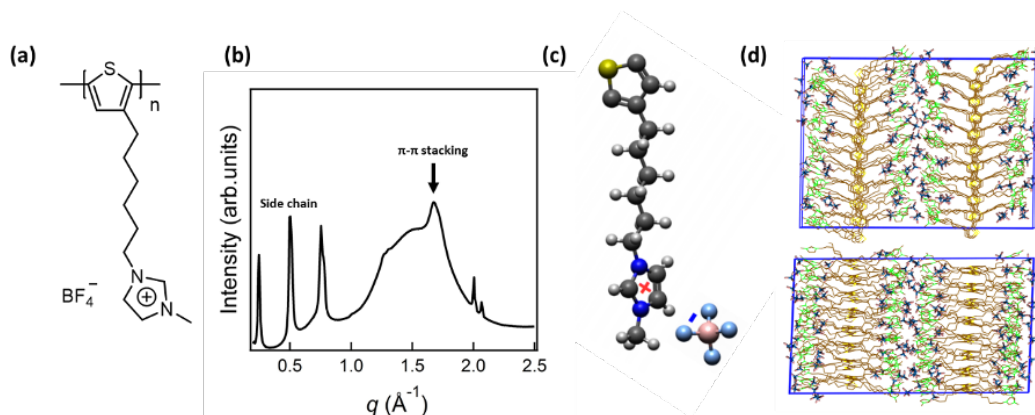


Figure 3.2: Chemical structure and structural characterization of P3HT-IM. (a) Schematic structure of the thiophene-based conjugated polymeric ionic liquid used in this study. (b) Azimuthally integrated GIWAXS patterns for neat P3HT-IM. (c) Illustration of the polymer model used in MD simulations. (d) MD snapshot of the simulation box used for the crystalline polymer.

range order. To promote ion solvation, cationic imidazolium group was tethered to the polythiophene polymers on which diffuse, polarizable charge is expected to foster weak physical associations between ions. Tetrafluoroborate ( $\text{BF}_4^-$ ) was chosen as a model counterion for mixed conduction studies because the intermediate size imparts a low  $T_g$  (20°C) in the amorphous domain of the polymer, while still allowing for a high degree of long-range order in the crystalline domains.

The resulting P3HT-IM polymer is shown in Fig 3.2a. A high degree of semicrystalline order is evident in the grazing incidence wide angle X-ray scattering (GIWAXS) patterns for drop cast films of P3HT-IM shown in Fig. 3.2b. A series of peaks starting with a first order peak at  $q = 0.247 \text{ \AA}^{-1}$  and higher order peaks at integer multiples indicate a lamellar side chain stacking structure, while a peak at  $q = 1.674 \text{ \AA}^{-1}$  corresponds to  $\pi - \pi$  stacking [90, 36].

### Experimental results: Monotonic increase in ionic conductivity of P3HT-IM polymers upon $\text{LiBF}_4$ addition at significant concentrations

The ionic conductivity and electronic conductivity of P3HT-IM can be simultaneously or independently tuned through the addition of salt and oxidative dopants. Here, we confine our interest only to the ionic transport behaviors of the P3HT-IM polymers.

P3HT-IM is capable of solvating and transporting  $\text{LiBF}_4$  over a wide range of salt concentrations. That is supported by the lack of diffraction peaks specific to

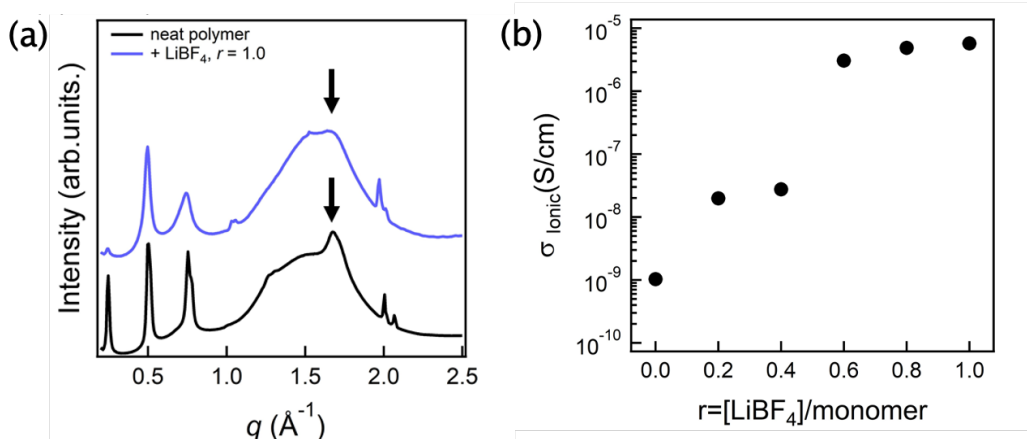


Figure 3.3: Experimental results for the P3HT-IM polymers upon LiBF<sub>4</sub> salt addition. (a) Integrated GIWAXS patterns for neat P3HT-IM and P3HT-IM with added LiBF<sub>4</sub> salt at  $r = 1$ , where  $r$  is the ratio of the moles of salt to the moles of monomer. (b) Ionic conductivity as a function of lithium salt addition at room temperature.

crystalline LiBF<sub>4</sub> in GIWAXS patterns for P3HT-IM with added salt (Fig. 3.3a). Further, the polymer retains some crystalline order after the addition of lithium salt, even though the peak broadening in the GIWAXS suggests that LiBF<sub>4</sub> does affect the crystalline order of the polymer at high concentrations, which could in turn affect the electronic conduction pathways in the polymer. Notably, at this concentration ( $r = 1$ ), the sample is roughly 22% salt by mass.

Ionic conductivity of the polymer with LiBF<sub>4</sub> addition was measured by electrochemical impedance spectroscopy (EIS). Nyquist plot shows a single semicircle with a capacitive tail, which suggests that there are only ionic charge carriers present in the P3HT-IM polymers without electronic dopants at significant LiBF<sub>4</sub> concentrations. Surprisingly, the ionic conductivity of the polymer shows a monotonic increase up to the highest salt concentration of  $r = 1$  (Fig. 3.3c). By contrast, most polymeric ion conductors with ion coordinating groups are incapable of solvating salt at concentrations higher than  $r = 0.5$ , and often show a maximum in conductivity at intermediate salt concentrations (generally  $r = 0.1$  to  $r = 0.2$ ) due to salt aggregation and physical cross-linking [145, 143, 190, 52, 169, 17]. It is also worth noting the stark jump in the conductivity observed at  $r \approx 0.6$ . This suggests that there is a structural/mechanistic change in the system beyond this salt concentration that aids ion transport, the mechanism of which can be investigated in detail via MD simulations.

## MD simulation results: Formation of ionic network as a primary mechanism of ion conduction

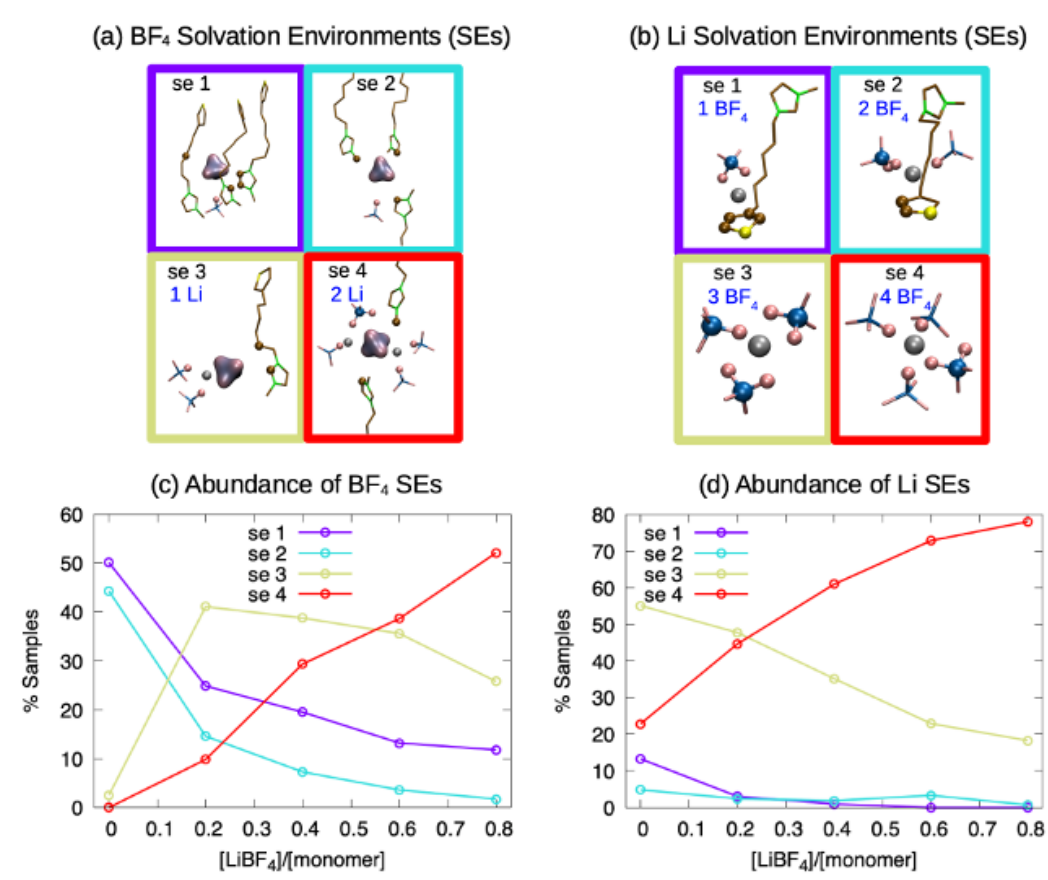


Figure 3.4: MD simulation results for the ion solvation environment [112] in crystalline P3HT-IM polymers at different salt concentrations at 300 K. (a) Snapshots of representative  $\text{BF}_4^-$  solvation environments in P3HT-IM and (b) their abundance as a function of salt concentration. (c) Snapshots of representative  $\text{Li}^+$  solvation environments in P3HT-IM and (d) their abundance as a function of salt concentration.

Molecular dynamics (MD) simulations were performed to provide mechanistic insights on ion solvation and transport in both crystalline and amorphous phases of P3HT-IM. For simulations of the crystalline domains of the polymer, the crystalline structure of the polymer remained stable as a stacked configuration characteristic of most thiophene-based polymers, in which clear  $\pi - \pi$  stacking and lamellar alkyl spacing were observed. This agrees with the structural features observed experimentally via GIWAXS. Addition of salt to the simulation enables a detailed characterization of the solvation environment for both  $\text{Li}^+$  and  $\text{BF}_4^-$  in the polymer (Fig. 3.4). For MD simulations of the crystalline polymer, both  $\text{Li}^+$  and  $\text{BF}_4^-$  ions segregate in the confined lamellar regions formed by the charged side chains

(Fig. 3.1). At low salt concentrations, a fraction of  $\text{Li}^+$  ions in the system is solvated (in part) by thiophene while most ions are coordinated by three  $\text{BF}_4^-$  counterions. At high salt concentrations,  $\text{Li}^+$  ions are almost exclusively coordinated by four  $\text{BF}_4^-$  counterions. A similar analysis for  $\text{BF}_4^-$  reveals that  $\text{BF}_4^-$  is solvated by the imidazolium pendants and  $\text{Li}^+$  ions. As the salt concentration is increased, the imidazolium contributes less to  $\text{BF}_4^-$  solvation, and the excess  $\text{BF}_4^-$  counterions become coordinated by up to two  $\text{Li}^+$  ions in its first solvation shell. Overall, the observed shift in the nature of  $\text{Li}^+$  and  $\text{BF}_4^-$  solvation with salt concentration indicates that the solvation structures are becoming more independent from the polymer backbone, where mobile ions are mainly interacting with other mobile ions of opposite charge.

Ion-solvation structures in P3HT-IM become more interconnected and decouple from polymer chains as the salt concentration is increased. Ion transport in the polymer network is partly dependent on the distance between solvation sites [145, 143, 190]. Accordingly, the density and connectivity of solvation environments in the polymer influences the ion dynamics. The spatial distribution of  $\text{Li}^+$  solvation in MD simulations is illustrated in Fig. 3.5(a-d) for both amorphous and crystalline polymers. At low salt concentrations,  $\text{Li}^+$  solvation sites are dispersed in the polymer matrix and are characterized by localized ion-pairs between  $\text{Li}^+$  and  $\text{BF}_4^-$ . At high salt concentrations, however, the ion solvation sites form transient interconnected domains, being decoupled from polymer chains. Instead of being "featureless" aggregates, the ionic domains organize a spatially extended network, percolating the simulation box (Fig. 3.5e). The formation of this ionic network is promoted by the charged imidazolium sidechains in both crystalline and amorphous domains. In the amorphous phase, pendant imidazolium side chains stabilize a percolated solvation network throughout the amorphous domain. In the crystalline P3HT-IM polymer, these percolating solvation networks are planar and confined to the inter sidechain region (Fig. 3.4), which is delimited by high dielectric sheets formed by the charged imidazolium groups. The segregation of ions in these confined regions is more energetically favorable than a uniform distribution throughout the lattice which would destabilize the  $\pi - \pi$  stacking. This mechanism is supported by GIWAXS experiments which found that  $\pi - \pi$  stacking remains intact upon the addition of salt even at the highest concentration, indicating that the salt is predominantly located in the inter-side-chain stacking region.

The increased ion network interconnectivity at high salt concentrations leads to faster

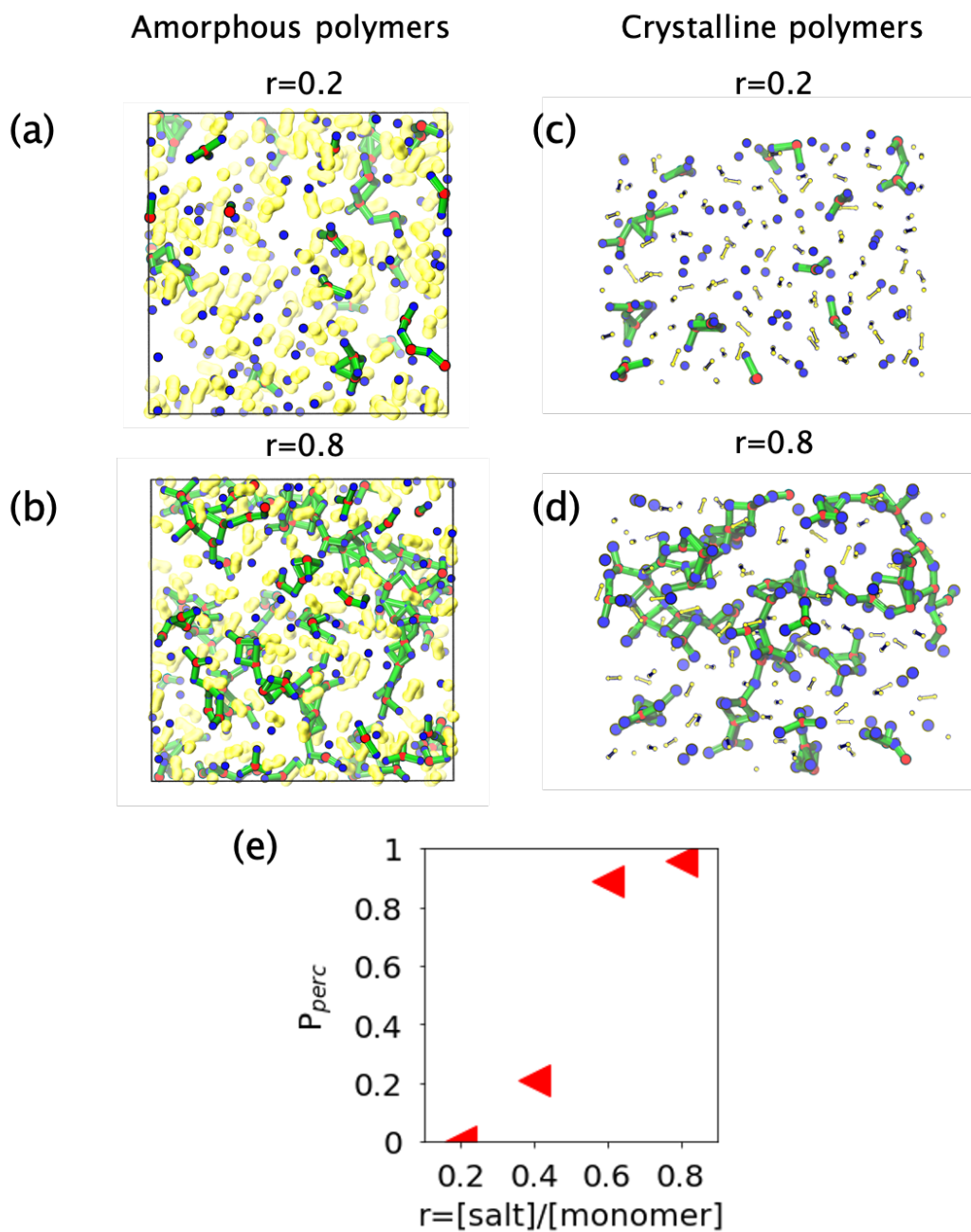


Figure 3.5: Simulation results for ion solvation in the amorphous (a-b) and crystalline (c-d) P3HT-IM polymers at 400 K. (a,c) Dispersed localized ion pairs of  $\text{Li}^+$  and  $\text{BF}_4^-$  at low salt concentration ( $r = 0.2$ ) (b,d) Percolating network of  $\text{Li}^+$  and  $\text{BF}_4^-$  at high salt concentration ( $r = 0.8$ ). (e) Probability,  $P_{perc}$ , that the largest ionic network in the amorphous P3HT-IM polymer percolates the simulation box at several salt concentrations. The color code in (a-d) is as follows: red spheres represent  $\text{Li}^+$ ; blue spheres represent  $\text{BF}_4^-$ ; and yellow surfaces represent imidazolium groups; green lines connect neighboring  $\text{Li}^+$  within 4 Å.

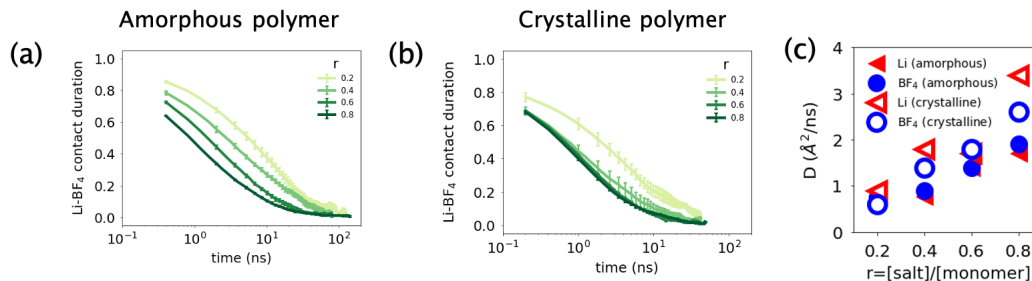


Figure 3.6: Simulation results for ion network and transport in both amorphous and crystalline P3HT-IM polymers at 400 K. Li-BF<sub>4</sub> contact duration in (a) amorphous and (b) crystalline polymers. (c) Calculated diffusion coefficients for Li<sup>+</sup> and BF<sub>4</sub><sup>-</sup> as a function of salt concentration in the amorphous (solid symbols) and crystalline polymer (open symbols).

ion dynamics. Long MD trajectories were used to monitor the dynamics of ions in the polymer and understand how the change in the ion network connectivity affects ion transport. The average contact duration between Li<sup>+</sup> and BF<sub>4</sub><sup>-</sup> ions is plotted in Fig. 3.6(a-b) for the amorphous and crystalline polymers. This reveals that the average contact duration between ions is shorter at higher salt concentrations, which suggests that the formation of a percolated solvation network decreases the time scale of ion-ion interaction. In this system, ion transport can be characterized by a hopping motion between solvation sites via partner exchange in a transient network. The increased proximity and connectivity of the solvation network at high salt concentrations facilitate partner exchange and thereby aid ion hopping dynamics [212, 30, 18, 126]. This supports the monotonic increase in ion conductivity observed in experimental impedance measurements (Fig. 3.3c). The discontinuous change in conductivity observed in the experiment at around  $r = 0.6$  could be understood as a transition into the percolating regime (Fig. 3.5e).

Experimentally measured ion dynamics aligns closely with ion dynamics in MD simulations. To further investigate ion transport, mean square displacements (MSD) for both Li<sup>+</sup> and BF<sub>4</sub><sup>-</sup> (Fig. 3.8) were calculated in the MD simulation to estimate the diffusivity of different ion species over a range of salt concentrations. A jump in the diffusion constants for both ions is observed at intermediate salt concentrations for both the crystalline and amorphous simulations (Fig. 3.6(c)), in agreement with the experimentally measured jump in conductivity shown in Fig. 3.3. Furthermore, the calculated diffusivities of Li<sup>+</sup> and BF<sub>4</sub><sup>-</sup> are similar over the entire range of salt concentrations (Tables 3.1) with a transference number of approximately 0.5. To further corroborate the ion dynamics observed in MD simulations with the exper-

Amorphous polymers							
$r$	$\tau$ (ns)	$D_{Li}$	$D_{BF_4}$	$t_{Li}$	$D_N$	$\sigma_{NE}$	$\sigma_{GK}$
0.8	1.7 (1)	1.7 (1)	1.8 (1)	0.49	0.09 (1)	0.64 (3)	0.39 (1)
0.6	2.7 (2)	1.4 (1)	1.4 (1)	0.5	0.13 (1)	0.35 (2)	0.28 (1)
0.4	5.9 (5)	0.76 (1)	0.76 (1)	0.5	0.09 (1)	0.25 (2)	0.17 (1)
0.2	10 (2)	0.65 (1)	0.74 (1)	0.47	0.07 (1)	0.09 (1)	0.11 (1)
Crystalline polymers							
$r$	$\tau$ (ns)	$D_{Li}$	$D_{BF_4}$	$t_{Li}$	$D_N$	$\sigma_{NE}$	$\sigma_{GK}$
0.8	1.1 (1)	3.4 (1)	2.6 (2)	0.57	0.07 (1)	0.44 (2)	0.30 (1)
0.6	1.2 (1)	1.7 (1)	1.8 (1)	0.49	0.08 (1)	0.24 (1)	0.26 (1)
0.4	1.8 (2)	1.8 (1)	1.4 (1)	0.56	0.03 (1)	0.17 (1)	0.22 (1)
0.2	4 (1)	0.9 (1)	0.6 (1)	0.6	0.03 (1)	0.08 (1)	0.10 (1)

Table 3.1: Computed ion-transport coefficients in the P3HT-IM polymers at various  $r$  ([LiBF<sub>4</sub>]/[monomer]) at 400 K. Diffusion coefficients ( $D$ ) are in unites of  $\text{\AA}^2/\text{ns}$ . Ionic conductivities ( $\sigma$ ) are in unites of S/m. Statistical errors of the final digit are indicated in parentheses.

imental polymer system, pulsed-field-gradient (PFG) NMR was used to measure the self-diffusion coefficients of  $^7\text{Li}$  and  $^{19}\text{F}$  in P3HT-IM upon salt addition at a concentration of  $r = 1$ . The measured self-diffusion coefficients were  $0.0145 \text{ \AA}^2/\text{ns}$  for  $^7\text{Li}$  and  $0.0101 \text{ \AA}^2/\text{ns}$  for  $^{19}\text{F}$  at 353 K. This results in a lithium transference of  $t_{Li} = 0.59$ , which is in close agreement with the transference numbers found in MD simulations. In contrast, polymer electrolytes with ion coordinating groups, such as PEO, PAN, and PVA, generally display transference numbers between 0.1 to 0.337 [169]. This suggests that the ion transport mechanism in P3HT-IM deviates from that of standard ion-conducting polymers and further supports the formation of a percolating ionic network as the primary mechanism for ion transport.

### 3.5 Conclusion

P3HT-IM serves as an effective solvent-free mixed ion and electron conducting model system in which the ionic and electronic charge carrier concentration can be modulated through the addition of salt. The polymer shows evidence of significant  $\pi - \pi$  stacking and side-chain stacking, even after the addition of salt at high concentrations ( $r = 1$ ); this long-range ordering facilitates electron transport. P3HT-IM solvates LiBF<sub>4</sub> salt up to a concentration of  $r = 1$ , as evidenced by the lack of peaks for the crystalline salt in scattering studies. Surprisingly, the polymer displays a monotonic increase in ionic conductivity up to this concentration. MD simulations indicate that this is enabled by the formation of a percolated network of

solvation sites at high salt concentrations, which facilitates ion transport via facile partner exchange. Furthermore, ion diffusivities from both MD simulations and PFG NMR measurement indicate a lithium transference number of approximately 0.5, supporting that the percolated solvation network promotes lithium transport in a way that is unique from many ion-conducting polymers where ion transport is strongly coupled to polymer segmental dynamics. These results suggest that the addition of diffuse ionic-liquid-like groups to a conjugated polymer backbone serves as an effective design approach to facilitate simultaneous lithium-ion conduction and electronic conduction in the absence of solvent, which has significant utility in the field of cathode binders and cathode coatings for solvent-free lithium-ion batteries.

### 3.6 Appendix

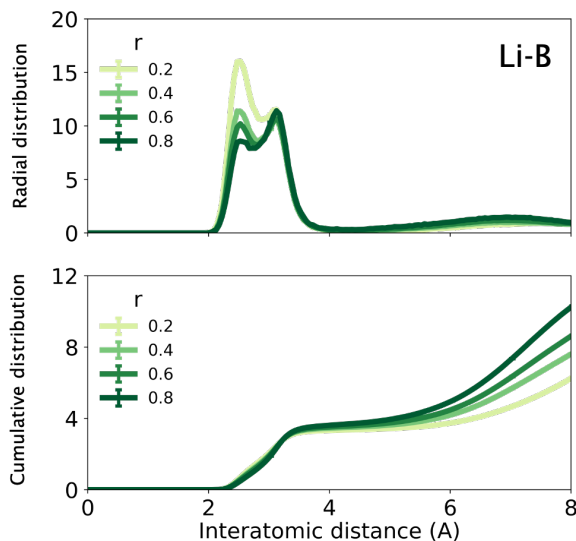


Figure 3.7: Li solvation by  $\text{BF}_4$  in the amorphous polymers as a function of interatomic distance between Li and B.

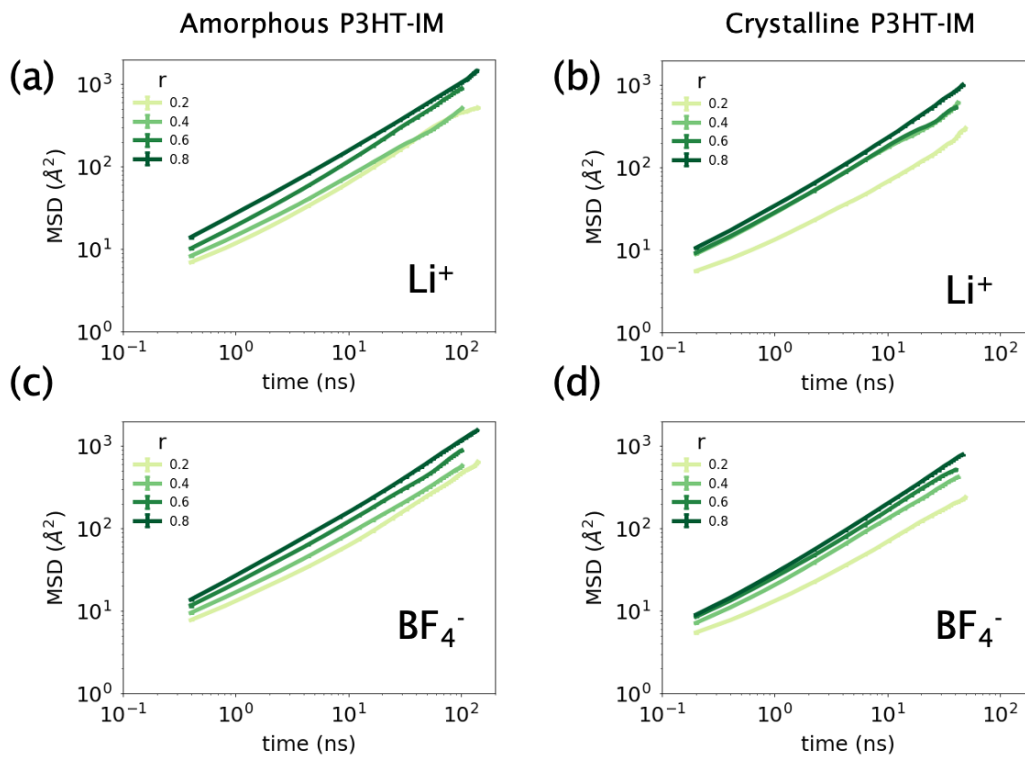


Figure 3.8: Mean-square displacement of ions in the amorphous (left column) and the crystalline (right column) polymers at several salt concentrations.

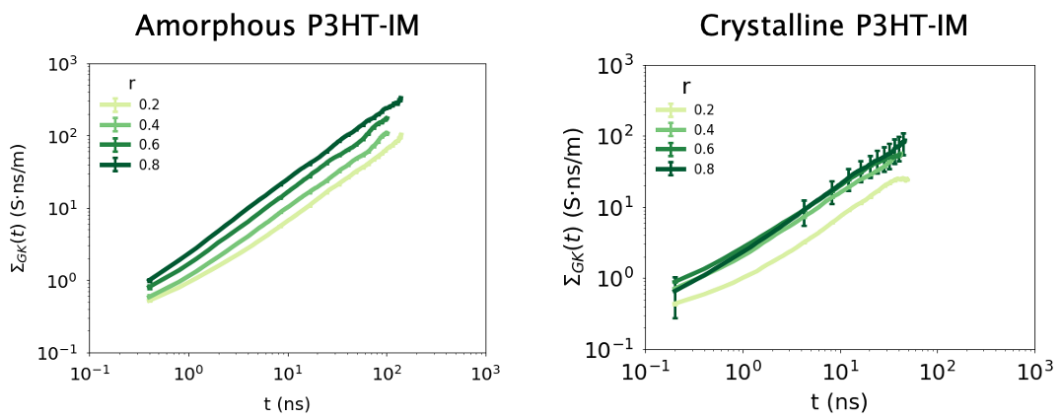


Figure 3.9: Charge mean-squared displacement,  $\Sigma_{GK}(t)$ , in the amorphous (left) and the crystalline (right) polymers.

*Chapter 4***LITHIUM-ION TRANSPORT IN POLYBORANE-BASED  
ELECTROLYTES****4.1 Abstract**

In Chapter 3, we discuss how the formation of a percolating ion network facilitates ion transport decoupled from polymer segmental dynamics. The unique ion conduction mechanism enables monotonically increased ionic conductivity up to exceptionally high lithium salt concentrations.

In this chapter, we discuss an ion transport mechanism in recently developed polyborane-based electrolytes that utilize the formation of a spatially extended ion network to facilitate lithium-ion transport. Herein, as a proof-of-concept, we discuss simulation results of the lithium-ion conduction mechanism in butylated polydiethylboranes (poly-b2EtB) at various salt concentrations. The electrolyte is accessible through the modification of polybutadiene (an abundant polyolefin) by introducing dialkylborane moieties to the backbone through hydroboration. By adding butyllithium or methyllithium into a polyborane, an ionically conductive polymer film is created. The negatively charged boron moiety enables lithium-ion solvation in this solvent-free single-ion conducting polymer electrolyte.

All-atom simulations show that lithium ions in the solvent-free poly-b2EtB are transported mainly by a partner exchange mechanism. With increasing salt concentration, the exchange rate increases to accelerate lithium-ion conduction, even with the increased viscosity. Simulations suggest that the enhanced lithium-ion transport at high salt concentration is associated with the formation of a percolating ion network that allows for frequent partner exchanges, while lithium-ion motion is spatially localized in small ion aggregates at low salt concentrations. Furthermore, an additional increase in lithium-ion conduction is found possible by the addition of an ethereal co-solvent. The added tetrahydrofuran (THF) co-solvent is found to further facilitate lithium-ion conductivity by participating in lithium-ion solvation and reducing the overall viscosity.

## 4.2 Introduction

Solid polymer electrolytes (SPEs) are considered promising for increasing the safety of battery technologies. They exhibit better contact with a metal electrode and better thermodynamic stability than their liquid counterparts. However, their low ion transport has been a central obstacle to practical implementation, despite their better safety and cycling stability [116]. For example, lithium-doped polyethylene oxide (PEO), a canonical SPE, exhibits ionic conductivity between  $10^{-5}$  to  $10^{-8}$  S cm<sup>-1</sup> at ambient temperatures [144, 123], while practical applications require  $> 10^{-3}$  S cm<sup>-1</sup> that PEO could achieve only at elevated temperatures.

Semi-crystalline PEOs show their maximum ion conductivity at a low salt concentration relative to their salt solubility limit due to the increased viscosity with more salts added. The primary drawback is related to the strong lithium-polymer interaction via Lewis-basic oxygen moiety, differently from loosely coordinated anions. With increasing salt concentration, more physical crosslinking between lithium and oxygen moiety elevates the viscosity substantially. Together with ion pairs, the increased viscosity decreases ion conductivity; lithium-ion diffusion is more suppressed than anion diffusion due to the strong interaction with the PEO, leading to a low lithium transference number substantially less than 0.5. Since this issue originates from the Lewis-basic ether oxygen itself, other PEO-based architectures suffer the similarly limited ion conduction [190].

Achieving high lithium conductivity by tailoring the strength of the polymer-ion interaction is still challenging [116]. Lithium ion is freer from polymer segments with a weaker polymer-ion interaction, so lithium diffusion is enhanced. However, at the same time, decreased polymer-ion interaction lowers the dielectric constant of the polymer backbone, so the salt solubility is reduced with less mobile lithium ions. Thus, the final ion conductivity is a delicate balance between two competing effects, which is hard to predict.

Recent computational work [157] suggested to invert ion solvation environment by using a Lewis-acidic boron moiety, as opposed to a Lewis-basic moiety such as ether group. A Lewis-acidic SPE interacts more favorably with anions than lithium cations, increasing lithium mobility relative to that of the anion. Further, salt solubility is not necessarily deteriorated thanks to the favorable polymer-anion interaction. Thus, in principle, the inverted ion solvation environment facilitates lithium-ion transport with weak interaction with the polymer host, yet not compromising ion solubility thanks to the strong interaction between the polymer host and anions.

Another strategy to facilitate ion transport is utilizing salt-concentrated polymer electrolytes such as polycarbonates [180], phenylsulfonate-based single-ion conductor [126], and conjugate polymers with a charged pendant [146] in Chapter 3. The concentrated polymer-based electrolytes often exhibit decoupled ion transport from polymer segmental dynamics [17] that is associated with the self-assembled continuous morphologies of ion aggregates. One instance is a phenylsulfonate-based single-ion conductor (p5PhSA-X) [126]. The ions were found to nanophase separate from the polymer backbone, forming ionic aggregates, owing to the polarity difference between the ionic groups and the hydrocarbon backbone. The morphological features of the ion aggregates, such as stringy, ribbon-like, planar, and isotropic clusters, result in different ion transport mechanisms: percolating aggregates allow for long-range ion diffusion, while isolated aggregates hinder ion diffusion due to the slower reorganization processes such as merging, breaking-up, or diffusion. The morphology is also found specific to mobile ions, thereby leading to ion-specific transport. Therefore, the p5PhSA-X provides continuous morphologies of ion aggregates, leading to a percolating ion network to effectively transport mobile ions. Further, the ion conductivity follows Arrhenius temperature dependence instead of Vogel–Fulcher–Tammann dependence, suggesting that the ion transport is decoupled from polymer segmental relaxation; this is consistent with the mechanism that ions diffuse through the connected pathways in the percolating ion aggregates. This decoupled ion transport presents an opportunity for more mechanically robust polymer-based electrolytes, not compromising ion conductivity.

This chapter presents the ion conduction mechanism in a novel, single-ion conducting, polyborane-based electrolyte. The electrolyte is synthesized by modifying polybutadiene through hydroboration of dialkylborane moieties to its backbone. Then, butyllithium is added to the polyborane. The ion-conducting polymer film exhibits geometry-normalized ion conductivities approaching  $10^{-7} \text{ S cm}^{-1}$  at  $50^\circ\text{C}$ , measured by electrochemical impedance spectroscopy (EIS). EIS-measured conductivity follows Arrhenius temperature dependence, suggesting that the ion conduction is decoupled from segmental relaxation of the polyborane-based electrolytes. Atomic-resolution simulations provide molecular insights into the ion conduction mechanisms in the solvent-free butylated polydiethylboranes (poly-b2EtB). Simulated poly-b2EtBs exhibit enhanced lithium-ion transport, associated with the formation of a percolating ion network with frequent exchange of partner anions at high salt concentrations, which is similar to the mechanism introduced in Chapter 3. It is also found that the added tetrahydrofuran further increases the ion conductivity

via both reduced viscosity and change in the ion solvation environment.

### 4.3 Simulation Model and Method

#### Molecular dynamics simulations

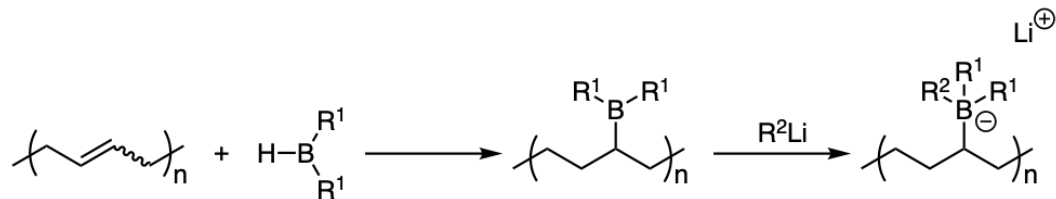


Figure 4.1: Mechanism for synthesis of polyborane-based electrolytes.

All-atom molecular dynamics simulations for polyborane-based polymers with butyllithium (BuLi) salts are carried out. An ether-free single-ion conducting polymer can be synthesized by hydroboration of polybutadiene with a variety of dialkylboranes, followed by the subsequent addition of an organolithium reagent to provide lithium ions (Fig. 4.1). Our simulation model assumes that the butyl reagent reacts with a random boron site quickly, resulting in a random copolymer with both neutral and negatively charged boron moieties. We employ a single linear polymer chain of length 128 units for a butylated polydiethylborane (poly-b2EtB). Hence, the multi-chain effect is excluded. Randomly chosen borane moieties are butylated according to the molar ratio of the butyllithium to the borane moiety. After a short equilibration (1 ns) of the Li-free polymer, the equal amount of lithium ions to butylated borane sites are added in a random position in a simulation box. Thus, charge neutrality is kept in all simulations. Then, another equilibration is run at least for 5 ns.

The OPLS force field [79, 80, 41], a non-polarizable and all-atom model, was used to describe the potential energy functions of all molecules; details are given in Section 3.3. To incorporate the effects of polarizability for ionic species, atomic charges of the butylated borane moiety were multiplied by a constant scalar (0.7) as previously suggested [93, 47]. All simulations were conducted using the LAMMPS simulation package [140].

In all cases during both equilibration and production runs, the MD trajectories were integrated using the velocity-Verlet algorithm with a timestep of 2 fs; rigid-body constraints for all carbon-hydrogen bonds were enforced using the SHAKE algorithm [155] Both LJ and Coulomb interactions were cut at 12 Å, and particle-particle particle-mesh Ewald summation [72] was used to compute Coulomb interactions

beyond the cutoff distance. Periodic boundary conditions (PBC) were applied along all dimensions. The Nosé-Hoover thermostat (100 fs relaxation) and the Nosé-Hoover barostat (1000 fs relaxation) were applied in all simulations to control the temperature (400 K) and the pressure (1 atm). All transport properties reported here were averaged using simulation trajectories over at least 80 ns after at least 20 ns long equilibration.

## 4.4 Results and Discussion

### Experimental results for ion conductivity

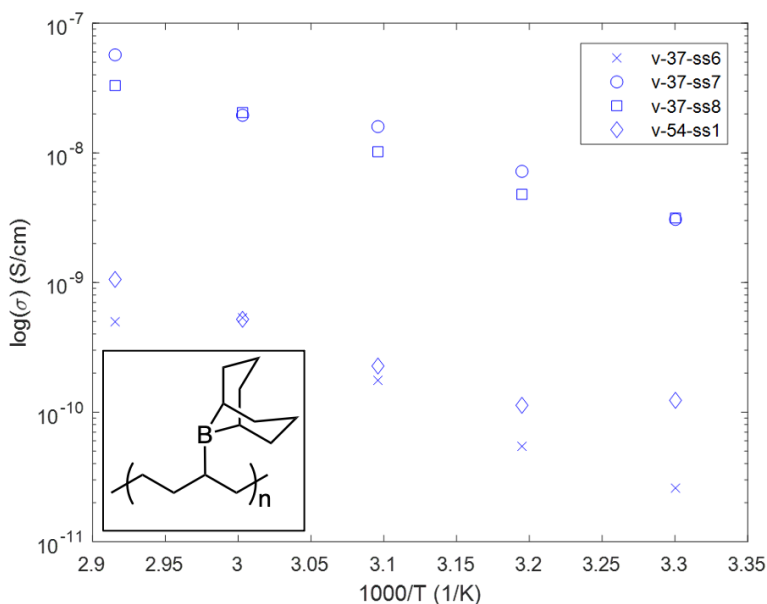


Figure 4.2: EIS-measured ionic conductivity ( $\sigma$ ) of poly-b9BBN at  $R_{salt}=[9BBN]/[BuLi]=8$  at various temperatures. Inset displays chemical details of poly-9BBN before the reaction with BuLi. Experiments were conducted by Fernando Villafuerte.

Fig. 4.1 displays a synthetic scheme of polyborane single-ion conductors (poly-b9BBN), based on the hydroboration of polybutadiene and the commercially available 9-borabicyclo(3.3.1)nonane (9BBN). Note that high levels (>95%) of hydroboration were achieved using linear polybutadiene of low molecular weight (1800 g mol<sup>-1</sup>). Further, the butylation reaction with BuLi was confirmed by NMR. Salt concentration can be controlled by the moles of BuLi, and the poly-b9BBN has more charged borane moieties with an increasing concentration of BuLi.

Fig. 4.2 shows that the polyborane-based electrolytes do conduct lithium ions despite their low ionic conductivity; the temperature dependence of ionic conductivity

Cell	$\sigma_0$ (S/cm)	$E_a$ (kJ/mol)	$R^2$
v-37-ss6	4.6	64.8	0.73
v-37-ss7	3.7	51.7	0.92
v-37-ss8	8.1	55.0	0.99
v-54-ss1	13	66.3	0.99

Table 4.1: Fitting results of ionic conductivity ( $\sigma$ ) in Fig. 4.2 using the Arrhenius relation:  $\sigma(T) = \sigma_0 \exp(-E_a/RT)$ .  $R^2$  is the coefficient of determination.

( $\sigma$ ) of poly-b9BBN measured via electrochemical impedance spectroscopy (EIS) is displayed. The molar ratio ( $R_{salt}$ ) of 9BBN monomers to BuLi salts is 8. It is immediately clear that in the range of temperature, the experimentally measured  $\sigma$  follows Arrhenius dependence on temperature ( $T$ ):  $\sigma(T) = \sigma_0 \exp(-E_a/RT)$ , where  $E_a$  is the activation energy, and  $R$  is the gas constant (Table 4.1). The Arrhenius-type dependence is considered a signature of ion transport decoupled from polymer segmental dynamics [143]. On the other hand, in semicrystalline PEO, lithium diffusion is strongly coupled to structural relaxation of polymer segments, so the conductivity follows the Vogel-Tammann-Fulcher (VFT) equation:  $\sigma(T) = \sigma_0 \exp(-E_a/R(T - T_0))$ , where  $T_0$  is called equilibrium glass transition temperature. The VFT behavior is commonly observed in disordered and glassy materials. Notably, there are two groups of cells with two different  $E_a$ . This suggests that there are some heterogeneities in polymer synthesis due to the fast butylation reaction in particular. More controlled synthesis processes are required for systematic investigations.

### Computational results

Using atomic-resolution simulations, we study lithium transport in bulk, dry butylated polydiethylborane (poly-b2EtB). In reality, crosslinking between two nearby borane sites results in stable diborane structures, significantly increasing the viscosity and hindering ion transport. In simulations, the crosslinking effect is, however, not considered.

Herein, we discuss lithium ion transport via the formation of an ion network, being decoupled from polymer segmental dynamics. Further, we discuss how the decoupled ion transport enables high ion conduction at exceptionally high salt concentrations, as opposed to other Lewis-basic polymer electrolytes such as PEO.

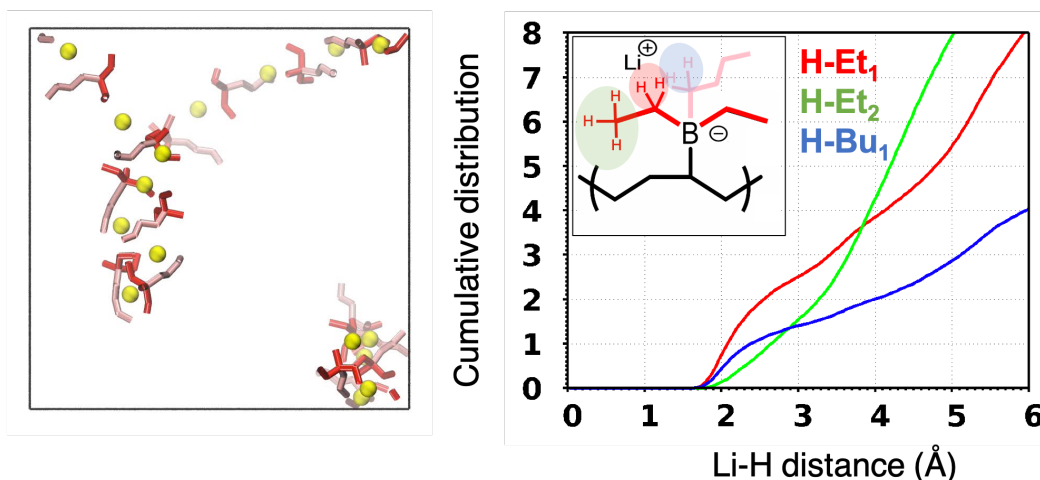


Figure 4.3: Lithium ion solvation in bulk Poly-b2EtB. Left panel: a simulation snapshot at  $R_{salt}=[2EtB]/[BuLi]=8$ . The color code is the following: Yellow spheres represent lithium ions; red sticks represent ethyl side chains for a butylated boron moiety; and pink sticks represent butyl side chains for a butylated boron moiety. Here, all the other atoms of polymer backbone and neutral boron moieties are not drawn for the clarity. Right panel: Cumulative distribution of hydrogens for a lithium ion. Blue line is for hydrogens of the carbon of a butyl side chain next to a butylated boron. Red line is for hydrogens of the carbon of an ethyl side chain next to a butylated boron. Green line is for hydrogens of the end carbon of an ethyl side chain of a butylated boron.

### Lithium ion solvation

Fig. 4.3 displays lithium ion solvation in a butylated polydiethylborane (poly-b2EtB) at  $R_{salt}=[2EtB]/[BuLi]=8$ . It clearly shows that the negatively charged borane moiety is mainly responsible for lithium-ion solvation via attractive electrostatic interaction. The neutral borane moiety or hydrocarbon backbone (absent in Fig. 4.3) are found less interacting with lithium ions. Cumulative distribution of hydrogens in the charged borane moiety shows that four hydrogens on average solvate a lithium-ion within 3 Å. Noticeably, a lithium-ion in poly-b2EtB is shared by two or three charged borane moieties instead of forming a neutral ion pair with single butylated borane.

### Ion transport in poly-b2EtB

Fig. 4.4 displays ion transport in poly-b2EtB. Surprisingly, calculated ionic conductivity monotonically increases with increasing salt concentration up to the ratio=2. The volume-corrected charge mean-square displacement (MSD),  $\Sigma(t)$ , takes all the correlations into account, whose slope with respect to time is the ionic conduc-

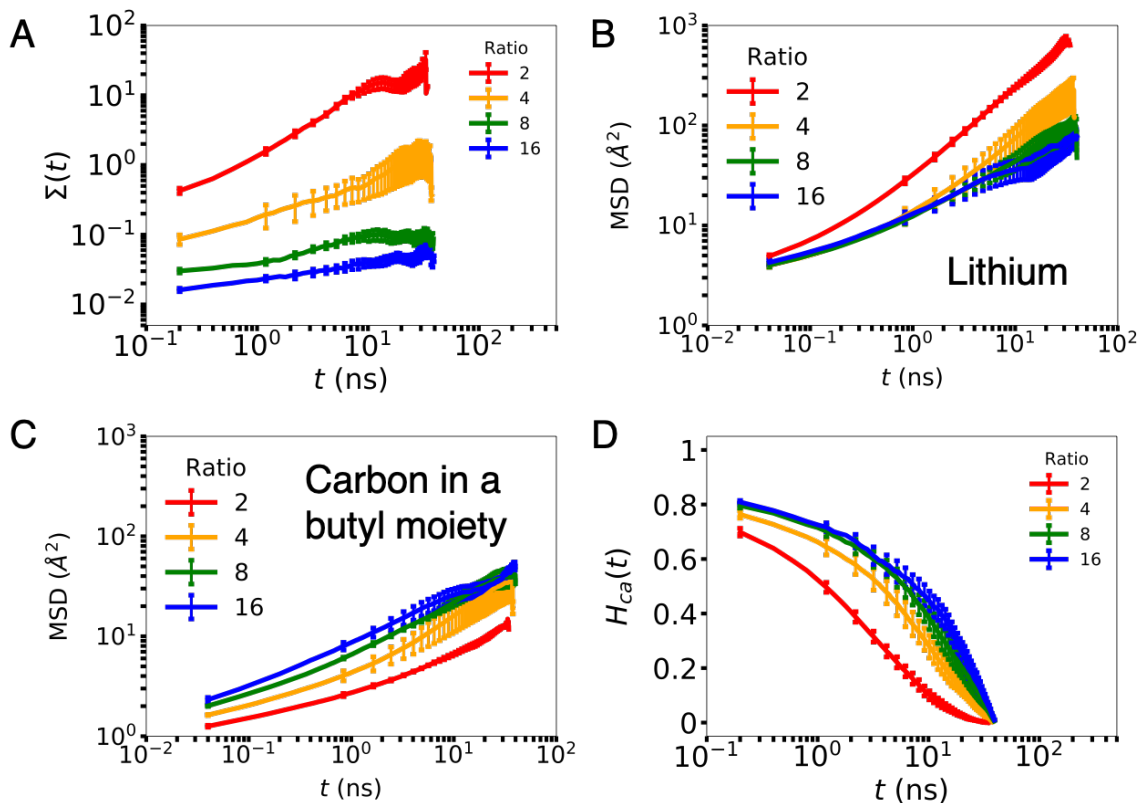


Figure 4.4: Ion transport in Poly-b2EtB. (a) Volume-corrected collective charge mean-square displacement,  $\Sigma(t)$ , as a function of time,  $t$ . The ratio is the molar ratio of 2EtB to BuLi, so the increasing ratio decreases the lithium concentration. (b) Mean-square displacement (MSD) of lithium ion. (c) MSD of carbon in a butyl moiety. (d) Lithium-boron contact duration,  $H_{ca}(t)$ .

tivity. Two factors affect the increased ionic conductivity, including an increasing number of charge carriers and enhanced ion diffusivity that is an intensive quantity. Fig. 4.4B shows that lithium diffusion is faster at higher salt concentrations; it is quite unexpected based on the conventional wisdom on the turnover behavior in ionic conductivity as a function of salt concentration. For example, ionic conductivity in PEO electrolytes initially increases with more salts added. However, after a certain point, it decreases due to the increased viscosity with more physical crosslinking between polymer segments via lithium ions. It turns out that the viscosity of our poly-b2EtB does increase with increasing salt concentration; MSD of carbon atoms in the butyl borane moiety (Fig. 4.4C) is a proxy of the inverse of the viscosity. Thus, the poly-b2EtBs effectively transport lithium ions even at high salt concentrations thanks to (i) more lithium ions and (ii) enhanced lithium diffusivity, despite the increased overall viscosity. Fig. 4.4D supports the decreased lithium-borane

contact duration with increasing salt concentration, which can facilitate lithium-ion transport with more short-lived correlations.

The unexpected ion conductivity trend (Fig. 4.4A) with salt loading can be explained by the partner exchange mechanism in Chapter 3. As is shown in Fig. 4.3, a lithium-ion is solvated by more than one butylated borane moieties, and they form an ionic cluster embedded in a polymer matrix, in which the lithium-ion diffuses by exchanging one of its borane partners. The lithium ion is not likely to diffuse with the same borane solvation shell (i.e., a vehicular mode) since borane diffusion is massively suppressed due to slow polymer segmental dynamics. In this mechanism, the facile partner exchange only requires a local structural relaxation instead of an extensive structural reorganization of a polymer matrix. The partner exchange mechanism further accelerates long-range lithium-ion transport in a large cluster that provides more connectivity. This is discussed below with how the morphology of the ion cluster changes with salt loading.

### **Formation of a percolating ion network**

Fig. 4.6 displays ion clusters at various salt concentrations. At low salt concentrations (e.g.,  $R=16$ ), the ion aggregates form a small cluster localized in space. In a finite ion cluster, a lithium-ion diffuses via partner exchange. However, the cluster itself should diffuse for long-range ion transport by structural reorganization of the polymer matrix. Slow polymer segmental dynamics retards the ion conduction. The effective charge conducted via the cluster diffusion is even quite limited; for instance, a neutral ion cluster composed of two lithium ions and two butylated borane sites transports practically "zero" charge. On the other hand, at high salt concentrations (e.g.,  $R=2$ ), the ion aggregates form a three-dimensional spatially extended network. In the ionic network, lithium ions can travel at both short and long length scale without any significant reorganization of the polymer matrix; only local reorientation of the butylated borane moieties is required to transport lithium ions. After a threshold, an ion network percolates a simulation box, which further facilitates lithium ion transport. This could be related to the notable increase in lithium MSD at  $R=2$  (Fig.4.4B).

The formation of a percolating ion network can explain the increasing ion conductivity with increasing salt concentration (Fig. 4.4). In conventional Lewis-basic polymer electrolytes such as PEO, lithium ion solvation and transport are strongly coupled to polymer segments. Thus, the physical crosslinks between ions and

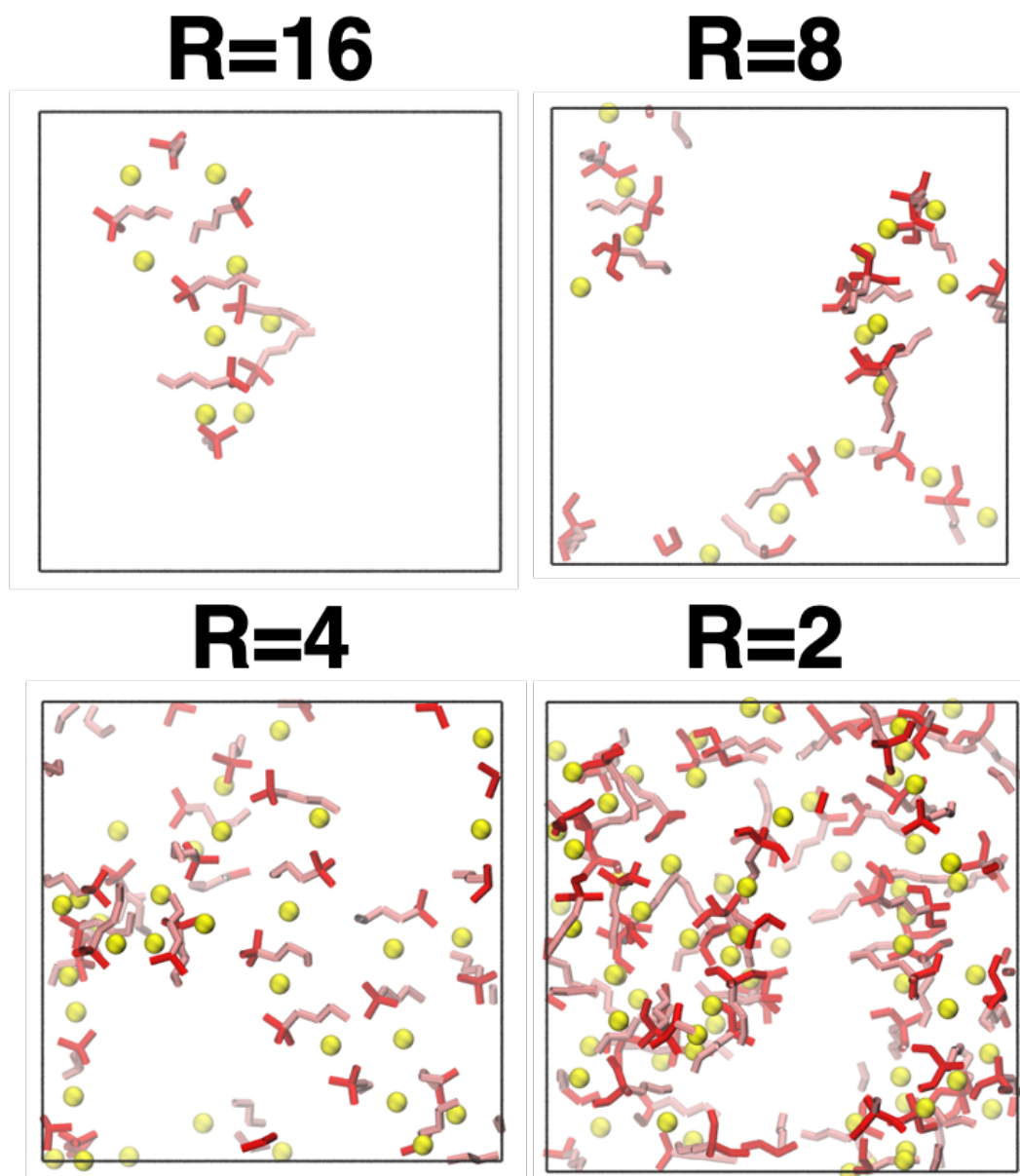


Figure 4.5: Ion aggregates at various salt concentrations, where  $R=[2EtB]/[BuLi]$ . The color code is the same as in Fig. 4.3.

polymer segments significantly increase the viscosity at high salt concentrations. Together with massive ion pairs, the increased viscosity results in substantial suppression in ion conduction. On the other hand, the polyborane-based polymers provide the spatially extended ion network at high salt concentration. The percolating ion network enables ion transport decoupled from polymer segmental relaxation, yet collective relaxation of the ions dominates their transport. The decoupled ion transport in the percolating ion aggregates allows for circumventing the shortcoming of the coupled ion transport, resulting in the enhanced ion conduction at high salt concentrations.

### Addition of ethereal co-solvent for further enhanced ion conductivity

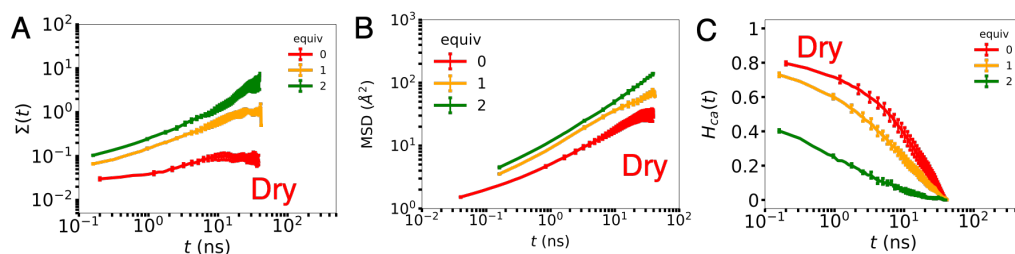


Figure 4.6: Effect of THF co-solvent on ion conductivity of poly-b2EtB at  $R_{salt}=8$  with various equivalent concentration of THF to BuLi. (a) Volume-corrected collective charge mean-square displacement,  $\Sigma(t)$ , as a function of time,  $t$ . The ratio is the molar ratio of 2EtB to BuLi, so the increasing ratio decreases the lithium concentration. (b) Mean-square displacement (MSD) of carbon in a butyl moiety. (c) Lithium-boron contact duration,  $H_{ca}(t)$ .

To further facilitate ion conductivity, molecular co-solvent is often added to dry polymer electrolytes, resulting in gel polymer electrolytes [48]. Here, we mix tetrahydrofuran (THF), one of the ethereal solvents, with dry poly-b2EtB at two different THF concentrations. Fig. 4.6 clearly shows the substantial enhancement in ion conductivity with the addition of THF co-solvent. Low molecular-weight THF co-solvent decreases the solution viscosity (Fig. 4.6B). The reduced viscosity leads to the short-lived cation-anion contact duration (Fig. 4.6C) as well as the enhanced lithium-ion mobility. Further, Lewis-basic oxygen of THF complicates lithium-ion solvation environments, participating in lithium-ion solvation; THF competes with the borane moiety in the polymer. With more THF co-solvents, lithium ions become freer from the borane moiety, facilitating the partner exchange; at high THF concentrations (e.g.  $[\text{THF}]/[\text{BuLi}]=4$ ), ion transport exhibits more character of the

vehicular-type mode. For further optimization of the gel polymer electrolytes, other co-solvents of different chemical moiety, such as benzene or fluorinated benzene moieties, should be investigated at various combinations of  $R_{salt}$  and co-solvent concentration.

#### 4.5 Conclusion

In this work, we study lithium-ion transport mechanisms in novel polyborane-based single-ion conductors. The dry poly-b9BBN film exhibits geometry-normalized ion conductivities approaching  $10^{-7}$  S cm<sup>-1</sup> at 50°C, measured by electrochemical impedance spectroscopy (EIS), implying some heterogeneities in synthesized films. Despite the potential heterogeneities, the Arrhenius temperature dependence suggests that the ion transport is largely decoupled from polymer segmental motion.

Using atomic-resolution simulations, we propose unique ion conduction mechanisms in the solvent-free poly-b2EtB, similar to the one suggested in Chapter 3. The monotonic increase in ionic conductivity is found in simulated poly-b2EtB up to exceptionally high lithium concentrations. The morphological changes of the ion aggregates are clearly shown as a function of lithium concentration: the ion clusters are localized in space in dilute poly-b2EtBs, yet the ion aggregates are interconnected and percolate a simulation box in concentrated poly-b2EtBs. The percolating ion aggregates provide connected pathways for lithium ions to travel without any large-scale reorganization of the polymeric medium, leading to short-lived cation-anion contact duration. In contrast, lithium-ion transport is likely limited by slow structural reorganization of the ion clusters. Therefore, the formation of a percolating ion network facilitates lithium-ion transport via facile anion-partner exchange.

Further, the addition of THF co-solvent also accelerates lithium-ion conductivity via reduced viscosity. However, the gradual change in lithium transport mechanism is observed with more THF added, from partner exchange to vehicular mode, as more THF co-solvents participate in lithium-ion solvation. This co-solvent effect seems to require more systematic investigations, particularly at electrified interfaces for safe battery applications.

## INTERFACIAL ION SOLVATION AND ELECTRON TRANSFER IN SOLID ELECTROLYTE INTERPHASE

### 5.1 Abstract

In this chapter, we investigate electron transfer to lithium ions at the interface between a platinum metal anode and a solid polymer electrolyte, as a chemically and structurally well-defined model for redox processes in the solid electrolyte interphase of battery electrodes. Studied electrolytes include LiTFSI (lithium bis(trifluoromethane)sulfonimide) salts in polyethylene oxide and poly(diethylene oxide-alt-oxymethylene), as well as in the associated liquid electrolytes 1,2-dimethoxyethane and tetraglyme. Atomic-resolution simulations are performed with constant-potential polarizable electrodes to characterize interfacial electron-transfer kinetics, including lithium-ion solvation structures and solvent reorganization effects as a function of applied electrode potential. The linear-response assumptions of the Marcus theory for electron transfer are found to be robust in these systems, yet ion-solvation behavior at the anode interface is strikingly dependent on chain connectivity, solvation environment, and the magnitude of the applied electrode potential, resulting in very different electron-transfer kinetics for lithium electroreduction.

Data and content in this chapter have been published as Ref. [86].

### 5.2 Introduction

Interfacial stability is essential for cycling performance and longevity of rechargeable batteries [175, 197, 122, 182, 178, 105, 53, 59]. For example, lithium-ion battery (LIB) and lithium-metal battery (LMB) interfaces involve various competitive electrochemical reactions, including the electroreduction of non-aqueous electrolytes and salts [197, 122, 137]. These processes result in a structurally and chemically heterogeneous thin film on the electrode surface called the solid electrolyte interphase (SEI)[132, 29, 5, 142, 184, 24, 208, 97], which is a complicated mix of organic, inorganic, and polymeric components. A functionally useful SEI passivates the electrode, conducting ions yet providing electronic insulation to mitigate detrimental electrolyte degradation that leads to battery aging and failure.

Polymeric components in the SEI have been shown to play a role in electrode

passivation, including polyether [10, 88, 217, 31], polyvinylene carbonate [170, 215], polycarbonate [218, 98], and polyolefin species [6]. These systems present diverse environments for ion solvation that may be expected to substantially effect the mechanisms and kinetics of interfacial electron transfer [153, 151, 74, 45, 115, 185, 89, 133, 19, 108]; for example, recent work in molecular liquids has shown that hydrogen bond networks and ion-solvation properties [103, 194, 102, 104] lead to non-trivial interfacial phenomena such as heterogenous charge separation or collective water exchange [104, 85]. However, relatively little is known about ion solvation and electron transfer (ET) in the SEI, which is complicated by the intrinsic heterogeneity and complexity of this material. To address this challenge, we introduce polymer melts as well-defined chemical models for the SEI, enabling mechanistic investigation of ET at the polymer/electrode interface as a proxy for the realistic battery electrode.

In this chapter, molecular dynamics (MD) simulations for atomic-resolution models are performed with constant-potential polarizable electrodes to study factors that govern lithium electroreduction at a polymer/metal interface. Linear ether homopolymer electrolytes are considered as chemically and structurally well-defined models for the SEI, including poly(ethylene oxide) (PEO) and poly(diethylene oxide-alt-oxymethylene), P(2EO-MO). Previous work indicates that polyethers are formed in the SEI via either in-situ or ex-situ polymerization of 1,3-dioxolane (DOL), leading to enhanced cycling stability [10, 88, 217]. Associated liquid ether electrolytes, 1,2-dimethoxyethane (DME) and tetraglyme (G4), are also investigated to explore the degree to which polymerization alters the local monomer interactions with regard to properties that are relevant for electron transfer.

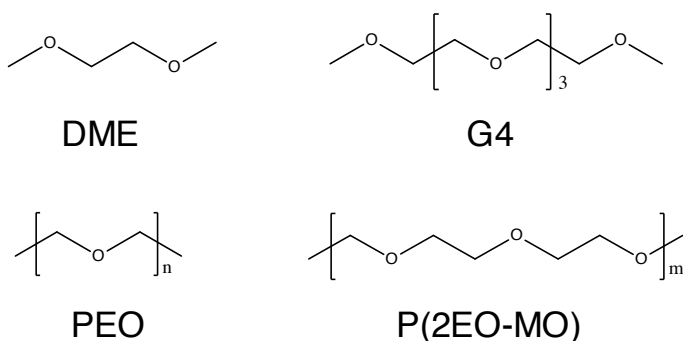


Figure 5.1: Chemical structures of the ethereal molecular electrolytes (DME and G4) and polymer electrolytes (PEO and P(2EO-MO)).

### 5.3 Methods and Calculation Details

We consider a model system that is comprised of two metal electrodes and an electrolyte of LiTFSI salt in either polymer or molecular liquid solvent (Fig. 5.1). The electrodes are modeled using the pristine (111) surface of face-centered cubic (FCC) platinum (Fig. 5.2). Below, we describe the computational details of the interaction potentials, MD simulations, calculated vertical ionization energies, calculated free energy curves associated with an electrochemical ET, and calculated normalized local density of ions and electrolytes. All simulations are conducted using the LAMMPS simulation package [140], and all force field parameters used in this study are provided in Ref. [190].

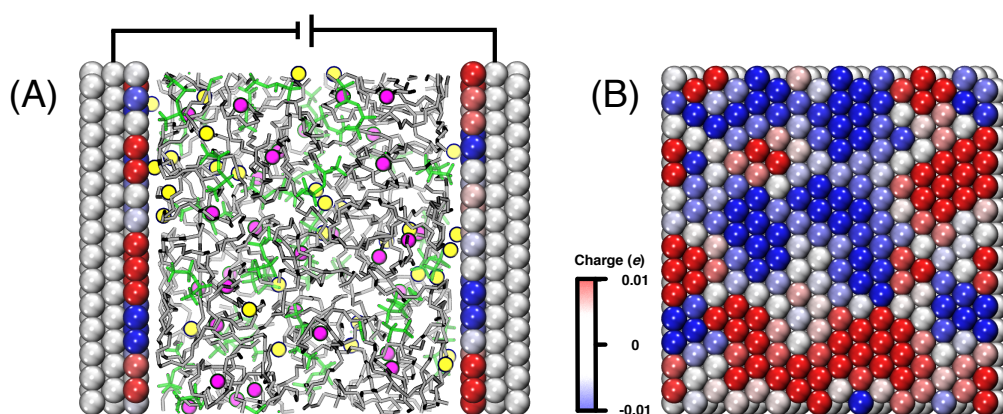


Figure 5.2: Simulation snapshot and electrode-charge polarization. (a) A simulation snapshot including PEO,  $\text{Li}^+$  ions,  $\text{TFSI}^-$  ions,  $\text{Li}^0$  atoms, and model electrodes. The grey strand represents a single PEO chain. Purple spheres represent  $\text{Li}^+$  ions while yellow ones do neutral  $\text{Li}^0$  atoms.  $\text{TFSI}^-$  ions are drawn in green. The two slabs are pristine, polarizable model electrodes held with the bias potential  $\Delta\Psi = 0$  V. Color for the electrode atoms is associated with their induced charges between  $-0.01$  (blue) and  $+0.01$  (red). (b) Electrode-charge polarization on the innermost layer of the anode in (a).

#### Force field details and the constant-potential method

The TraPPE-UA force field [172, 190, 198], a non-polarizable and united-atom model, is used to describe the potential energy functions of the polymers and molecular liquids. The LiTFSI salt is described using the non-polarizable force field of Lopez et al. [107]. Unlike fully polarizable force-field models or ab initio calculations, the model employed here carries fixed point charges for atoms, except for the polarizable electrode atoms. Among all atoms of electrolytes and salts, we employ the standard Lorentz-Berthelot mixing rule for the TraPPE-UA force field,

$\sigma_{ij} = 0.5(\sigma_i + \sigma_j)$  and  $\epsilon_{ij} = \sqrt{\epsilon_i \epsilon_j}$ , where  $\sigma_i$  and  $\epsilon_i$  correspond to the usual LJ parameters for atom  $i$ .

For the platinum electrodes, the constant potential method (CPM) is employed to provide a polarizable description of the electrostatic interactions and to allow for simulation at constant applied potential [167, 148, 58]. This method accounts for the effect of image-charge formation in the electrode in response to charges in the electrolyte (Fig. 5.2). Each electrode atom carries an atom-centered spherical Gaussian charge distribution with fixed width ( $\eta = 1.979 \text{ \AA}^{-1}$ ) and a time-dependent amplitude,  $A_i(t)$  that is determined as a function of the position of the other atomic charges in the system,

$$Q_i(\vec{r}, t) = A_i(t) \left( \frac{\eta^2}{\pi} \right)^{3/2} \exp \left[ -\eta^2 (\vec{r} - \vec{R}_i)^2 \right], \quad (5.1)$$

where  $\vec{R}_i$  is the fixed position of an  $i^{\text{th}}$  electrode atom. We employ the version of the CPM developed in Ref. [188], which employs matrix inversion at each timestep to determine the charge polarization on the electrode atoms. The metal slabs include three layers of atoms, which has been found to provide a sufficiently converged description of the electrode polarization [167, 148]. The cathode layers are held at a positive electrode-potential,  $\Psi^+$  and the anode layers are held at a negative electrode-potential,  $\Psi^- (= -\Psi^+)$ . The bias potential is  $\Delta\Psi = \Psi^+ - \Psi^-$ . Electrode potential in this study is in the unit of volt.

For the non-Coulomb interactions involving the electrode atoms, we fit the platinum force field of Heinz *et al.* [69] to the LJ interaction form, yielding the platinum LJ parameters  $\epsilon = 7.8 \text{ kcal/mol}$  and  $\sigma = 2.534 \text{ \AA}$ . As prescribed by this force field, we employ the geometrical mixing rule for the LJ interactions between the platinum and electrolyte atoms. However, we reduce the LJ interactions between the platinum and electrolyte atoms by half throughout this study, such that  $\epsilon_{ij} = 0.5\sqrt{\epsilon_i \epsilon_j}$  to approximately match the adsorption energy of acetonitrile on platinum [164]. Finally, to avoid rare, unphysical penetration of the lithium ions into the anode layers during the simulations, we employ the additional short-ranged repulsive potential

$$U_w(z) = 4\epsilon_w \left[ \left( \frac{\sigma_w}{z - z_w} \right)^{12} - \left( \frac{\sigma_w}{z - z_w} \right)^6 \right] \text{ if } z < z_c, \quad (5.2)$$

$$= 0 \text{ otherwise,}$$

where  $\epsilon_w = 7.9597 \text{ kcal/mol} = 10RT$  with the gas constant  $R$ ,  $\sigma_w = 2.575 \text{ \AA}$ ,  $z_w = z_c - \sigma_w$ , and  $z_c$  is variable with the solvents, which is the position of the

atoms in the exterior layer of metal atoms on the electrode along the perpendicular component. This steep repulsive potential has no effect on ion solvation.

### MD simulations

For the polymer-electrolyte simulations, we employ a single linear polymer chain of length 1000 and 333 units for PEO and P(2EO-MO), respectively. So, multi-chain effect in the polymers is excluded. For the liquid-electrolyte simulations, 500 DME molecules or 200 G4 ones are employed. Chemical structures of all four solvents are displayed in Fig 5.1. For LiTFSI salt, we keep a ratio of a lithium ion to chemical moieties of each solvent the same such that  $[\text{EO}]:[\text{Li}^+]=15:1$ , where  $[\text{EO}]$ , and  $[\text{Li}^+]$  are the number density of ether oxygen for the electrolytes, and  $\text{Li}^+$  ions, respectively.

In all cases during both equilibration and production runs, the MD trajectories are integrated using the velocity-Verlet methods with a timestep of 1 fs. Both LJ and Coulomb interactions are cut at 14 Å, and particle-particle particle-mesh Ewald summation is used to compute Coulomb interactions beyond the cutoff distance. Periodic boundary conditions (PBCs) are applied along  $xy$  directions only, unless otherwise noted. Moreover, to prevent the long-range contribution of Coulomb interaction along  $z$  direction, the vacuum region of the equal size to the simulation cell is introduced on both sides along the transverse direction [204]. The Nosé-Hoover thermostat (100 fs relaxation) and the Nosé-Hoover barostat (1000 fs relaxation) along  $xy$  directions are applied in all simulations to control the temperature (400 K) and the pressure (1 atm), unless otherwise noted.

Equilibration of both polymer and molecular electrolytes involves four steps. The first step follows a protocol of Ref. [190] which involves steepest descent energy minimization, Langevin dynamics at elevated temperature, and annealing process. This step takes at least 10 ns with PBCs and the barostat along all three directions. Secondly, electrode atoms are introduced at both ends of the simulation cell along  $z$  direction without any overlaps. Lateral dimensions of the cell are slightly modified to meet the lattice periodicity of 111 surface of FCC electrodes. Then, LiTFSI salt is randomly placed in the simulation cell without overlaps with electrode atoms. Steepest descent energy minimization is employed with frozen electrode atoms in space to avoid unduly high forces due to the newly added salt atoms. Thirdly,  $z$  position of the electrode atoms is adjusted in order to remove the undesirable pressure effect across the cell. Each of the electrodes moves as a rigid body according to

the forces including the constant force to meet the desired pressure (1 atm) along z direction, and average force from electrolytes. This step takes at least 10 ns. After being equilibrated, the transverse box length fluctuates with time following a Gaussian distribution. Electrode atoms are fixed in space in accordance to the mean of the Gaussian distribution. Lastly, neutral lithium atoms are added into the simulation cell at random places without overlaps with the electrode atoms. After steepest descent energy minimization, systems are equilibrated with the CPM turned on at each electrode potential during at least 5 ns for molecular-electrolyte or 10 ns for polymer-electrolyte systems. All average quantities and their standard error reported in this work are calculated using at least three independent initial configurations, using block averaging with 20 ns long blocks.

### Vertical ionization energy calculations

For the characterization of electrochemical ET, the vertical ionization energy ( $\Delta E$ ) is computed to provide a reaction coordinate for an electrochemical ET reaction between a lithium species and an anode [73]. For the half-reaction associated with the oxidation of  $\text{Li}^0$ ,  $\Delta E = \delta E^{\text{anode}} + I + \delta qW$ , where  $\delta E^{\text{anode}}$  is the difference in total potential energy,  $\delta q$  is the amount of transferred charge during the half-reaction under a frozen solvent configuration,  $I$  is ionization energy of lithium, and  $W$  is work function of a metal electrode. Similarly, for the half-reaction associated with the reduction of  $\text{Li}^+$ ,  $\Delta E = -\delta E^{\text{anode}} + I + \delta qW$ . The term  $\delta E^{\text{anode}}$  depends on the distance of lithium species from the anode, whereas  $I + \delta qW$  does not. The term,  $I + \delta qW$  is a constant with respect to the lithium position and electrode potential whose value ensures a criterion that free energy curves associated with the ET cross each other at  $\Delta E = 0$  is satisfied [149].

To calculate  $\delta E^{\text{anode}}$  in the presence of the constant-potential electrodes, the approach of Ref. [149] is employed for a given configuration sampled every 0.1 ns. Two terms contribute to  $\delta E^{\text{anode}}$ :  $\delta E^{\text{anode}} = \delta E + \delta E^{\text{elec}}$ , where  $\delta E$  is the difference in total potential energy upon an ET and  $\delta E^{\text{elec}}$  is a correction term. The correction term should be added due to the fact that both electrodes participate in the ET reaction in our simulations on the contrary to the actual experimental situation where only one of them is involved. For a single lithium species, its identity is swapped under a frozen solvent configuration:  $\text{Li}^0 \rightarrow \text{Li}^+$  for oxidation or  $\text{Li}^+ \rightarrow \text{Li}^0$  for reduction. The identity swap for the lithium species is performed by turning on (off) Coulomb interaction with all other atoms for the oxidation (the reduction) with the same LJ interaction parameters, so the difference in total potential energy

should be the same with the difference in total Coulomb energy. Further, the effect of electrode-charge polarization should be included, whose response is treated adiabatically. After the electrode-charge polarization is recalculated along with the lithium identity swap, the difference in total electrode-charge,  $\Delta Q$  should equal to the amount of the charge transferred during the ET so that  $\Delta Q = \delta q = +1e$  for reduction and  $\Delta Q = \delta q = -1e$  for oxidation, where  $Q = \sum_i A_i(t)$  with the index  $i$  running for all atoms of both electrodes.

Finally, the correction term ( $\delta E^{\text{elec}}$ ) is calculated, considering electric work to transfer all the charges to the anode instead of both electrodes:  $\delta E^{\text{elec}} = (\delta q^- + \delta q^+) \Psi^- - (\delta q^- \Psi^- + \delta q^+ \Psi^+)$  with the constraint of total transferred charge conservation ( $\delta q^- + \delta q^+ = \delta q$ ). Here,  $\delta q^-$  is the charge transferred to the anode at  $\Psi^-$ , and  $\delta q^+$  is the charge transferred to the cathode at  $\Psi^+$ . With no bias potential ( $\Psi^- = \Psi^+$ ),  $\delta E^{\text{elec}} = 0$ . In a slit-like geometry, there is the well-known linear relation between the amount of charges transferred to each of the electrodes and the location of Li redox-species in a simulation cell [210, 149]. For  $\text{Li}^+$  reduction, such linear relations should be  $\delta q^- = -e(L_z^{-1}z - 0.5)$  and  $\delta q^+ = e(L_z^{-1}z + 0.5)$ , where  $z$  is the  $z$  position of the  $\text{Li}^+$  ion, and  $L_z$  is the length of the simulation box along  $z$  axis, determined by a distance between atoms in the electrolyte-exposed layer of each electrode. Then,  $\delta E^{\text{elec}} = -e(L_z^{-1}z + 0.5)\Delta\Psi$ , where  $\Delta\Psi$  is a bias potential. To obtain such linear relations for the transferred charges, the vacuum region of double size to the simulation cell along  $z$  direction is required when the electrode-charge polarization is recalculated.

### Free energy curves for an electrochemical ET

The free energy curves,  $F(\Delta E)$  associated with an electrochemical ET are calculated using the following equations in Ref. [149]:

$$F_o(\Delta E) = -k_B T \ln P_o(\Delta E) + \bar{F}_o, \quad (5.3)$$

$$F_r(\Delta E) = -k_B T \ln P_r(\Delta E) + \bar{F}_r, \quad (5.4)$$

where subindices,  $o$  and  $r$ , stand for  $\text{Li}^+$  and  $\text{Li}^0$ , respectively. The minimum of  $F_o(\Delta E)$  is set to be zero ( $\bar{F}_o = 0$ ), so the relative vertical shift of the free energy curves is determined by  $\bar{F}_r$ . Both reorganization energy ( $\lambda$ ) and thermodynamic driving force ( $\Delta F$ ) are calculated using the linear-response assumptions:

$$\lambda = \frac{\langle \Delta E \rangle_r - \langle \Delta E \rangle_o}{2} \quad \Delta F = \frac{\langle \Delta E \rangle_r + \langle \Delta E \rangle_o}{2}. \quad (5.5)$$

Then, the curvature of the parabolic free energies is  $1/2\lambda$  regardless of redox species according to the linear response theory. In order to overcome the limited sampling window in our equilibrium simulations, non-equilibrium points are added according to Zwanzig relation [149, 13]:

$$F_o(\Delta E) - F_r(\Delta E) = \Delta E, \quad (5.6)$$

which linearly relates two free energies to each other.

### Local density calculations

The normalized local density,  $\rho_n(d)$ , of atoms as a function of distance from the anode,  $d$ , is calculated for an atom of  $i$ -species electrolyte:

$$\rho_n(d) = \frac{\rho_i(d)}{\rho_i} = \frac{\langle \sum_{j=1}^{N_i} \delta(d - z_j^i + z_w) \rangle / L_x L_y}{N_i / L_x L_y L_z}, \quad (5.7)$$

where  $\langle \cdot \cdot \cdot \rangle$  represents the ensemble average,  $z_j^i$  is  $z$  position of  $j^{th}$  atom of  $i$ -species ( $j = 1, 2, \dots, N_i$ ),  $N_i$  is the total number of atoms of  $i$ -species electrolyte,  $z_w$  is  $z$  position of atoms in an electrolyte-exposed layer of the anode, and  $L_k$  is the length of the simulation box along each direction,  $k$  for  $k \in \{x, y, z\}$ .  $L_z$  is determined by a distance between atoms in the electrolyte-exposed layer of each electrode.

## 5.4 Results and Discussion

Recent experimental studies have reported that polyethers including PEO and P(2EO-MO) are found to be effective in electrode passivation, enhancing cycling stability, which results from in-situ polymerization via ring-opening reactions of 1,2-dioxolane (DOL) [10, 88, 217, 31]. In-situ polymerization enables to overcome poor contact issue that happens when the polymers are prepared ex-situ. Despite their similar chemical composition, they exhibit different lithium-ion solvation motifs which influence the resulting ion transport [219].

### Lithium-ion solvation at bulk

We begin by considering the lithium-ion solvation in the PEO and P(2EO-MO) bulk polymers. Fig. 5.3 reveals markedly different lithium-ion solvation structures for the bulk polymers. Ether oxygen atoms of PEO and P(2EO-MO) are traced as a function of time,  $t$ , which forms the first solvation shell of a lithium-ion whose distance from the lithium-ion is less than  $2.7 \text{ \AA}$  (the first minimum of radial distribution function between them). The oxygen atoms are numbered sequentially from the beginning of each polymer strand. As was shown previously [190, 191], Fig. 5.3A exhibits

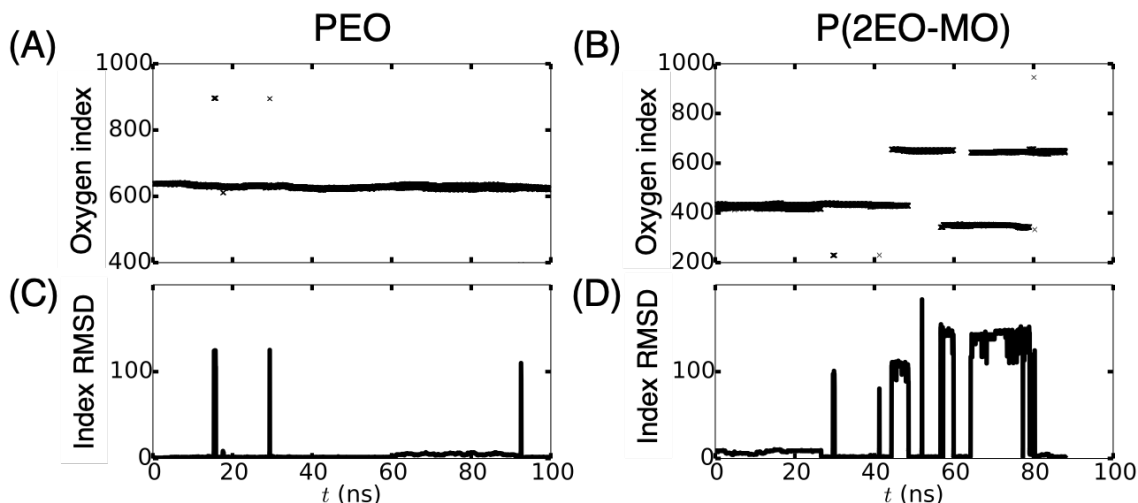


Figure 5.3: Lithium-ion coordination environment at infinite dilution. Index of oxygens of (a) bulk PEO and (b) bulk P(2EO-MO) that forms the first solvation shell of a representative lithium-ion. Root-mean-square-deviation of the indices (i.e., index RMSD) of the oxygens of (c) PEO and (d) P(2EO-MO). PEO exhibits primarily intra-segmental solvation of the lithium ion, whereas P(2EO-MO) exhibits greater inter-segmental character.

a strap-like structure for PEO that is consistent with lithium-ion solvation by the oxygen atoms along a single continuous segment of the PEO chain. In contrast, Fig. 5.3B indicates that in bulk P(2EO-MO), the lithium-ions are solvated by two distant segments along the backbone of the polymer, consistent with a two-chain motif for lithium-ion solvation that has previously been noted for other polyesters [190, 191]. As opposed to the one-chain motif of PEO, the reason for the two-chain motif of P(2EO-MO) is a single methylene unit that separates two oxygen atoms, which is not consistent with lithium-ion solvation [219]. For the  $i^{\text{th}}$  lithium-ion,  $\mathbb{S}_i$  is the set of the oxygen atoms that comprise the first solvation shell of the ion in a given configuration snapshot, with a total of  $N_O$  elements in the set; the first solvation shell is defined as atoms that fall within the distance associated with the first minimum in the oxygen- $\text{Li}^+$  radial distribution function. For single-chain solvation, it is expected that these oxygen-atom would be closely clumped along the backbone of the polymer, exhibiting little spread in the corresponding values of the oxygen indices; in contrast, for multi-chain solvation, it is expected that the oxygen-atom indices would exhibit a greater spread. As a measure of this distinct behavior, we thus consider the root-mean-square-deviation (RMSD) of the indices for the oxygen

	PEO	P(2EO-MO)	G4	DME <sup>a</sup>
one-chain	0.90 (1)	0.63 (2)	0.33 (1)	0.03 (1)
two-chain	0.10 (1)	0.37 (2)	0.67 (1)	0.60 (4)

Table 5.1: Fraction of lithium-ion solvation motifs in bulk electrolytes at finite concentration. Statistical errors of the final digit are indicated in parentheses. <sup>a</sup>The remaining fraction is associated with multi-chain solvation more than two.

atoms that solvate a lithium-ion as a function of time,

$$\text{RMSD} = \sqrt{\frac{1}{N_o} \sum_{j \in \mathbb{S}_i} \left( O_j - \frac{1}{N_o} \sum_{j \in \mathbb{S}_i} O_j \right)^2}, \quad (5.8)$$

where  $O_j$  is an index of  $j^{\text{th}}$  oxygen that forms the first solvation shell of the  $i^{\text{th}}$  lithium-ion. The lithium-ion solvation is considered to exhibit the one-chain solvation motif if this RMSD is less than 5, and a two-chain motif otherwise. Figs. 5.3C and D display the RMSD of the indices for the oxygen that solvate a lithium-ion as a function of time,  $t$ , which discriminates between the lithium-ion solvation motifs of a polymer. Table 5.1 displays the fraction of each lithium-ion solvation motif, quantified via RMSD. About 90% of lithium ions are solvated by a single segment in PEO, as opposed to 63% in P(2EO-MO) which exhibits both intra- and inter-segmental solvation motifs.

Additional insight into these lithium-ion solvation structures is provided in Fig. 5.4 that most of the lithium-ions in bulk polymers are free from ion-pairing, and solvated solely by the polymer electrolytes. The cumulative number,  $c(r)$  of neighbor oxygen atoms around a lithium-ion is calculated as a function of the interatomic distance,  $r$  between the ion and the oxygen atom. The first solvation shell of the lithium-ion includes 5 or 6 ether oxygen atoms of PEO that is the only chemical moiety that interacts preferentially with lithium ions [190, 191]. According to  $c(r)$ , despite the differences in lithium-ion solvation motif and ether oxygen density, both two polymers provide a similar number of ether oxygens in the first solvation shell for a lithium-ion, which outcompetes TFSI oxygen. The second peak of the radial distribution function,  $g(r)$  for P(2EO-MO), not present for PEO, supports that not all three ether oxygens in its monomer unit participate in chelating the lithium-ion, but one ether oxygen atom is excluded in lithium-ion solvation.

Fig. 5.4 further shows that the molecular solvents DME and G4 interact locally with a lithium-ion in a similar way of their associated polymers. The lithium-ion solvation structure is almost the same between PEO and G4. As opposed to

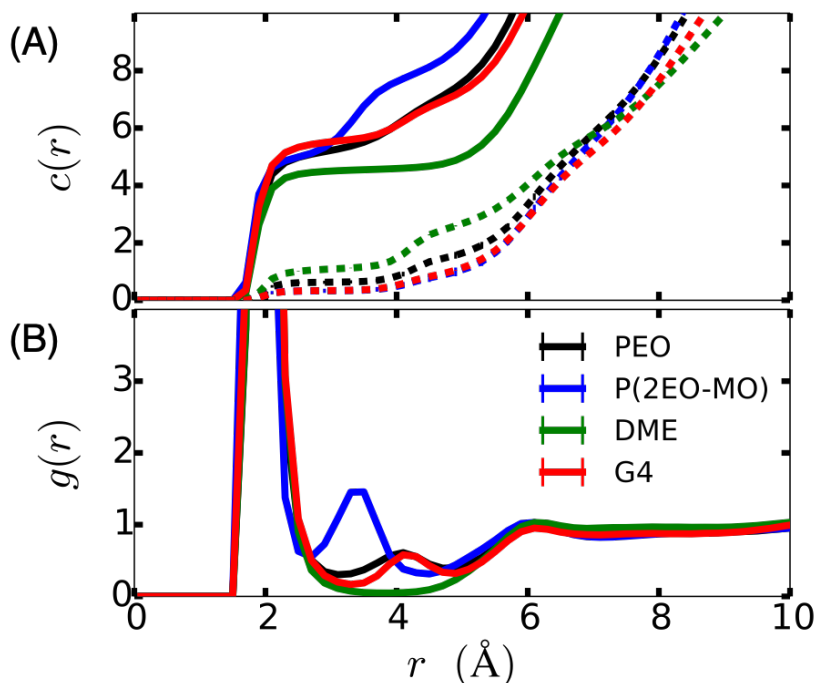


Figure 5.4: Cumulative (a) and radial (b)  $\text{Li}^+$ -oxygen distribution functions for the bulk electrolytes. Solid lines represent oxygen atoms of the electrolyte, and dotted lines represent oxygen atoms of  $\text{TFSI}^-$  anion in each electrolyte.

the one-chain solvation of PEO, two-third of lithium-ions are solvated by two G4 molecules with the remaining ones by a single G4 molecule (Table 5.1). No single DME molecule by nature can fully solvate a lithium-ion, which instead requires at least two DME molecules. The ether oxygen in both DME and G4 outcompetes TFSI oxygen for lithium-ion solvation as it does in both polymers. Taken together, these findings suggest that observed differences between the polymers and their associated molecular solvents are primarily due to the polymer connectivity and resulting solvation motifs.

### Ion solvation at the anode interface

Fig. 6.2 plots the normalized density of  $\text{Li}^+$  ion,  $\text{TFSI}^-$  ion, and electrolyte ether oxygens for each of the considered electrolytes. It is seen that with finite bias potentials,  $\Delta\Psi > 0$  V, the EDL forms in all cases, evidenced by the preferential interaction of  $\text{Li}^+$  ions over  $\text{TFSI}^-$  ions with the anode.

Fig. 5.6 illustrates that the  $\text{Li}^+$  solvation at the interface (i.e., the closest peak to the anode in each case from Fig. 6.2) is different than in the bulk. As discussed in Table 5.1, the bulk solvation exhibits a range of one-chain versus two- or higher-

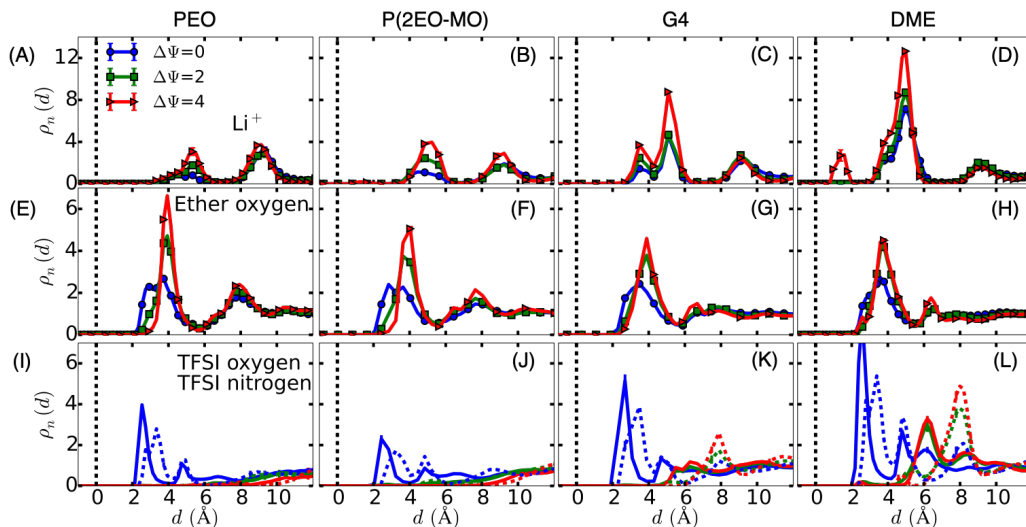


Figure 5.5: The normalized local density (Eq. 5.7) of the ions and electrolytes as a function of distance,  $d$  from the anode at various bias potentials,  $\Delta\Psi$ . The columns of panels correspond to the various considered electrolytes. Row (a-d) presents the distribution for the  $\text{Li}^+$  ions; Row (e-h) presents the distribution for ether oxygen of the electrolyte; Row (i-l) presents the distribution for TFSI $^-$  ions. In panels (i-l), solid lines represent oxygen atoms of TFSI $^-$  anion, and dotted lines represent a nitrogen atom of TFSI $^-$  anion. In all panels, the black vertical line indicates the location of the electrolyte-exposed layer of the anode.

chain solvation environments, depending on the electrolyte. For PEO, the interfacial  $\text{Li}^+$  solvation remains dominated by one-chain solvation, and for DME, it remains dominated by two-chain and higher solvation structures. However, for P(2EO-MO), the fraction of one-chain solvation decreases, and for G4, the fraction of one-chain solvation significantly increases in the vicinity of the anode. The results in Fig. 5.6 are presented for the case of zero bias potential, although the same conclusions hold at non-zero values (Fig. 5.10).

Several additional features in  $\text{Li}^+$  ion solvation are worth noting in Fig. 6.2. Firstly, efficient solvation via the electrolytes leads to a layer of solvent separation between the anode and the  $\text{Li}^+$ , such that the closest peak to the anode is typically at  $d > 2$  Å. However, for DME at the highest bias potential, this solvent-separation layer partially breaks down, allowing for direct contact between the  $\text{Li}^+$  ions and the anode, suggesting a greater propensity to form an inner-Helmholtz layer in this electrolyte. This effect is consistent with the fact that DME only allows for two-chain (or multiple-chain) solvation of the  $\text{Li}^+$  ions (Table 5.1), thereby providing less efficient solvation in the confined environment at the interface. Also, we note that

the interfacial  $\text{Li}^+$  solvation peak for G4 is split into two sub-peaks, with the closest one dominated by one-chain solvation and with the more distant one dominated by two-chain solvation (Fig. 5.10).

Finally, with regard to the  $\text{TFSI}^-$  anion solvation, Fig. 6.2 shows a notable difference between the polymers and molecular liquids. At zero bias, all of the electrolytes show significant peaks near the anode associated with formation of the EDL, and at finite bias potential, these peaks are shifted outward in all cases. For the polymer electrolytes, the anode peak largely flattens to unstructured, bulk-like behavior, whereas for the molecular electrolytes, the anion solvation peak remains sharp and highly structured. Such pronounced differences in the anion solvation at finite potentials may suggest that the polymer electrolytes provide an additional barrier for physical access of anions to the anode interface, thereby retarding the detrimental breakdown of anions [183, 173, 42, 187, 201].

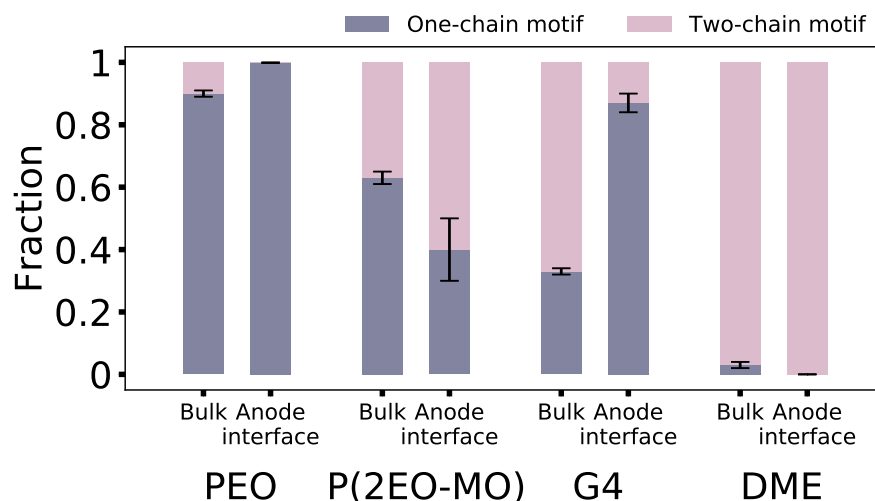


Figure 5.6: Fraction of  $\text{Li}^+$  ion solvation motifs, in bulk and at the anode interface with zero bias.

### Electrode-charge polarization and solvent fluctuations

Just as the presence of electrode influences the solvation structure of the interfacial ions, the ions influence the charge polarization of the electrode. In fact, electrode charge polarization is strongly sensitive to rare fluctuations in the solvent structure [164, 85].

Fig. 5.7 displays the distribution of induced charge per atom of the anode, where  $P(q) = \langle \delta(q - A_j(t)) \rangle$  with the index  $j$  running for all atoms of the anode. For

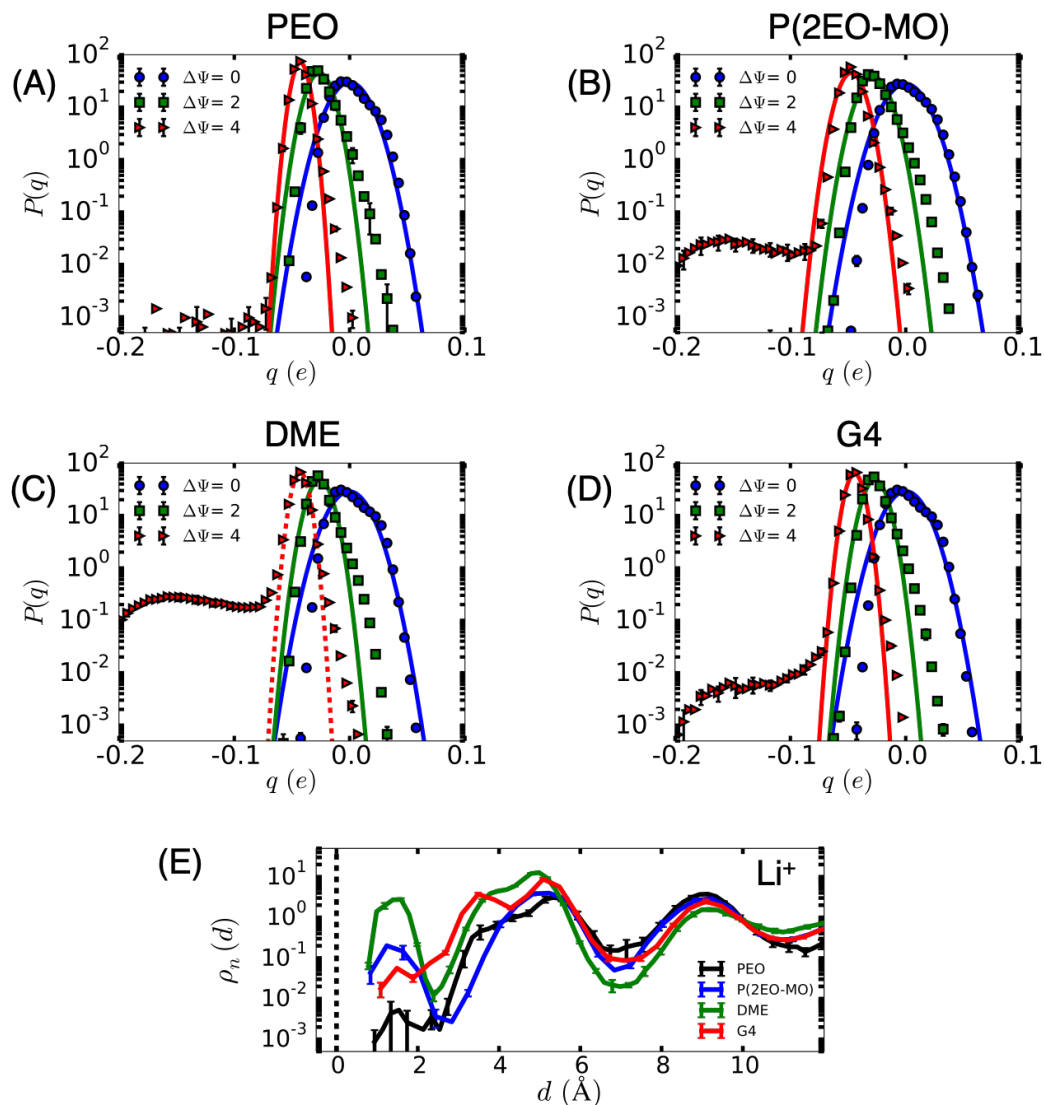


Figure 5.7: Distribution of induced charge per atom of the anode, for the various electrolytes and bias potentials. (a) PEO. (b) P(2EO-MO). (c) DME. (d) G4. Solid lines represent Gaussian fits. (E) Normalized local density of  $\text{Li}^+$  ions on a log-linear scale at  $\Delta\Psi = 4$  V.

small and zero biasing potentials, the distributions are strongly Gaussian, indicating weak correlations in the interfacial solvent fluctuations. However, at the highest bias potential, all four electrolytes exhibit a non-Gaussian tail at negative charges associated with unexpectedly large charge-polarization fluctuations. This tail is largest for DME, which as seen in Fig. 6.2 to support a significant population of  $\text{Li}^+$  ions in direct contact with the anode interface. It is striking, however, that the effect also appears in the other electrolytes for which such direct lithium-anode contact were not seen in Fig. 6.2. Nonetheless, by investigating the ion-distribution plots from Fig. 6.2 on a log scale (Fig. 5.7E), it is seen that rare ion-solvation fluctuations do indeed occur for the PEO, P(2EO-MO), and G4 electrolytes, which give rise to this strongly non-Gaussian interfacial behavior. As expected, PEO, which exhibits efficient single-chain solvation of the  $\text{Li}^+$  ions, best preserves solvent separation between  $\text{Li}^+$  and the electrode and exhibits the smallest degree of non-Gaussian behavior in Fig. 5.7.

### **Outer-sphere ET at the anode interface**

Beyond anion-mediated decomposition, the solvation structure for ions at the electrode interface have significant implications for the redox chemistry and reaction rates that will occur. In the current section, we consider this point from the perspective of the reduction  $\text{Li}^+$  ions via interfacial electron transfer.

In this section, we confine our attention to electrolytes and solvation structures for which the  $\text{Li}^+$  is solvent-separated from the anode. Specifically, we consider outer-sphere ET for  $\text{Li}^+$  ions at a solvent-separated distance of  $2 \text{ \AA} < d < 6 \text{ \AA}$  from the metal anode surface, for which non-adiabatic ET kinetics is applicable. Since the ET rate decays exponentially with the distance from the interface, these  $\text{Li}^+$  ions are expected to be electrochemically reduced at the fastest rate, except for inner-sphere  $\text{Li}^+$  ions that adsorb directly on the anode that requires adiabatic ET kinetics.

Fig. 5.8 confirms that outer-sphere interfacial electrochemical ET in PEO is well described using the assumption of Gaussian fluctuations for local solvent electric field, as is consistent with the observations in Fig. 5.7. The left column in Fig. 5.8 shows that the energy-gap distribution  $P(\Delta E)$  for both  $\text{Li}^+$  and  $\text{Li}^0$  at the PEO/anode interface are Gaussian in nature and similar in width subject to the available simulation sampling. This conclusion is independent of the strength of the bias potential. The right column in Fig. 5.8 further illustrates this point, with the free-energy surfaces in the energy-gap coordinate exhibiting parabolic form; in panels D-F, the solid lines

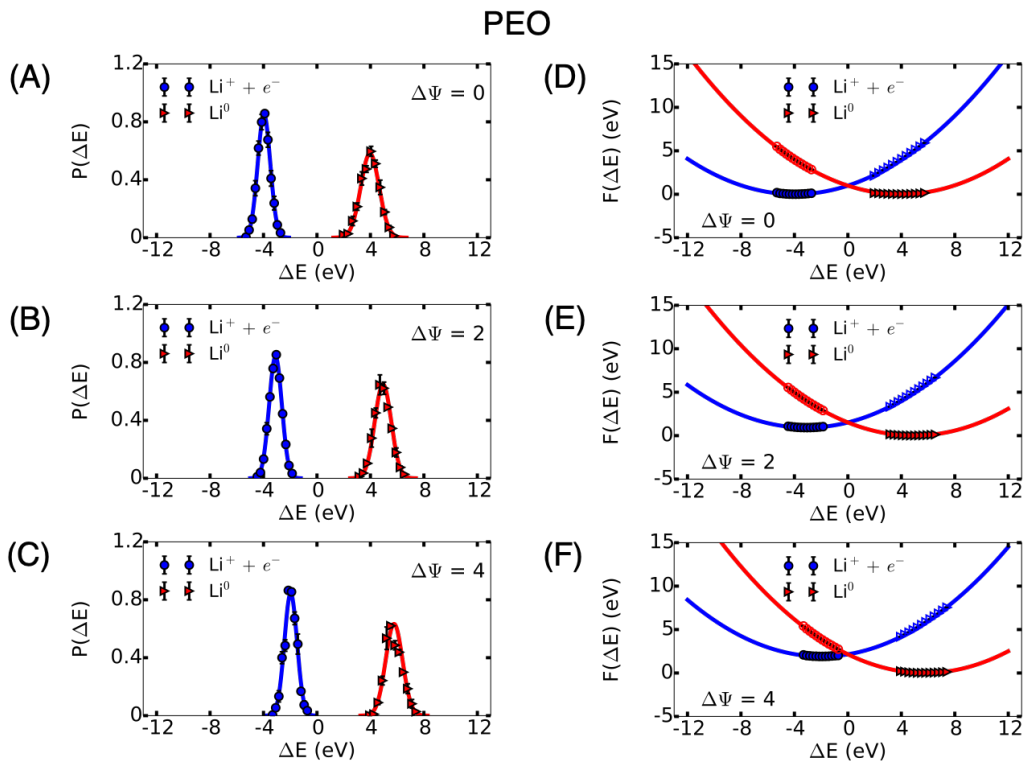


Figure 5.8: Lithium electroreduction in PEO at the anode interface. (a-c) Probability distributions  $P(\Delta E)$  of the vertical energy gap  $\Delta E$ , and (d-f) their associated free energy curves for both the  $\text{Li}^+$  and  $\text{Li}^0$  in PEO. Results are shown for various bias potentials. Solid lines in (d-f) are parabolic curves using linear-response assumptions in Eq. 5.5.

correspond to the assumption of Gaussian fluctuations (Eq. 5.5) and are in excellent agreement with the simulation datapoints. These observations validate the use of linear-response theory for the description of the outer-sphere interfacial ET in these systems. Similar results are found for the outer-sphere ET reactions in the other electrolytes considered.

## 5.5 Conclusions

Interfacial stability has been one of the major bottlenecks in the development of next-generation rechargeable batteries [175, 197, 122, 182, 178, 105, 53, 59]. Functional SEIs passivate an electrode by regulating lithium electrodeposition and by preventing detrimental decomposition reactions of electrolytes. Here, we perform atomic-resolution simulations with constant-potential polarizable electrodes to characterize interfacial electron-transfer kinetics, including lithium-ion solvation structures and solvent reorganization effects as a function of applied electrode po-

tential. Linear ether homopolymers are studied as a chemically and structurally well-defined proxy for polymeric SEIs, including PEO and P(2EO-MO), along with the ethereal molecular solvents G4 and DME.

Simulations show that all considered electrolytes except for DME provide a solvent-separation layer for  $\text{Li}^+$  ions at the anode interface, with both one-chain and two-chain solvation environments. Efficient passivation may facilitate homogeneous lithium electroreduction [178, 105]. Rare fluctuations in solvent structure strongly affect electrode-charge polarization such that direct lithium-anode contact gives rise to a tail of electrode-charge polarization. However, at the highest bias potential, DME allows for direct contact between the  $\text{Li}^+$  ions and the anode with greater propensity. Further, the substantial difference between the polymers and molecular solvents is found in solvation of the interfacial  $\text{TFSI}^-$  anions; the polymer electrolytes largely expel  $\text{TFSI}^-$  anions from the anode interface, which could delay further detrimental anion breakdown [197]. Finally, the assumptions of Gaussian solvent fluctuations for outer-sphere ET for  $\text{Li}^+$  ions are found to be robust in these systems, although both transient and metastable direct-contact pairs between the anode and the  $\text{Li}^+$  ions may be expected to dominate the ET kinetics through an inner-sphere mechanism. The robustness of these observations across the range of polymer and molecule electrolytes here may generalize to other interfacial environments [108, 94, 97].

## 5.6 Appendix

### Mean electric potential

Mean electric potential,  $\Phi(z)$  is calculated, solving the Poisson equation numerically across the simulation cell [149, 60]:

$$\frac{d^2\Phi(z)}{dz^2} = -\frac{\rho(z)}{\epsilon_0}, \quad (5.9)$$

where  $\rho(z)$  is the mean charge density averaged over a xy plane, and  $\epsilon_0$  is the vacuum permittivity. In all considered electrolytes,  $\Phi(z)$  oscillates at the electrode interface due to the electrical double layer. After the screening from the interfacial ions,  $\Phi(z)$  reaches the plateau.

### Spatially-resolved lithium-ion solvation motif at the anode interface

#### Outer-sphere ET at the anode interface

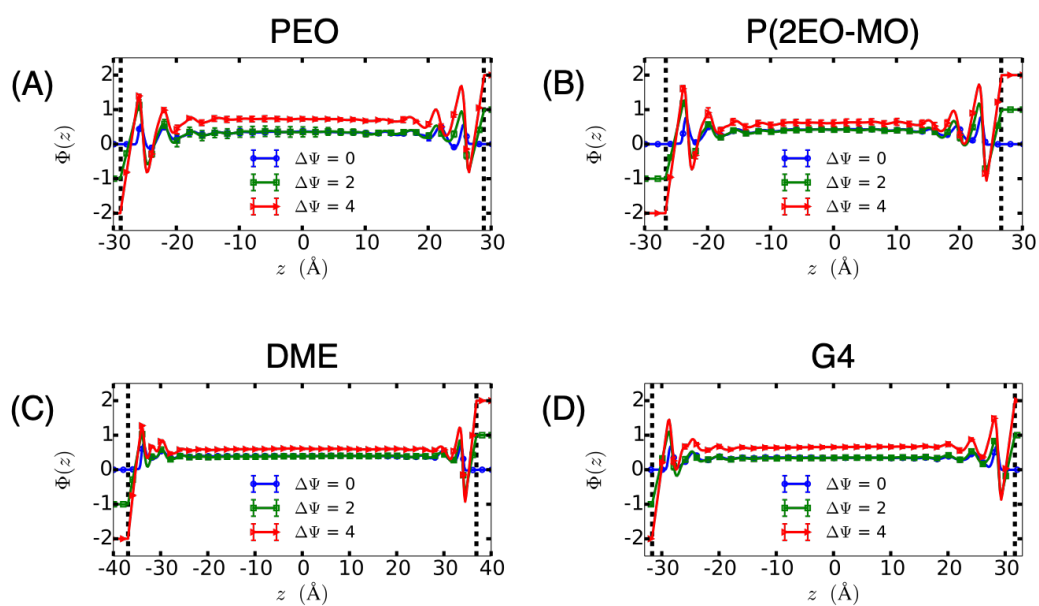


Figure 5.9: Mean electric potential across the simulation cell for the various electrolytes and bias potentials. In all panels, the black vertical line indicates the location of the electrolyte-exposed layer of the anode.

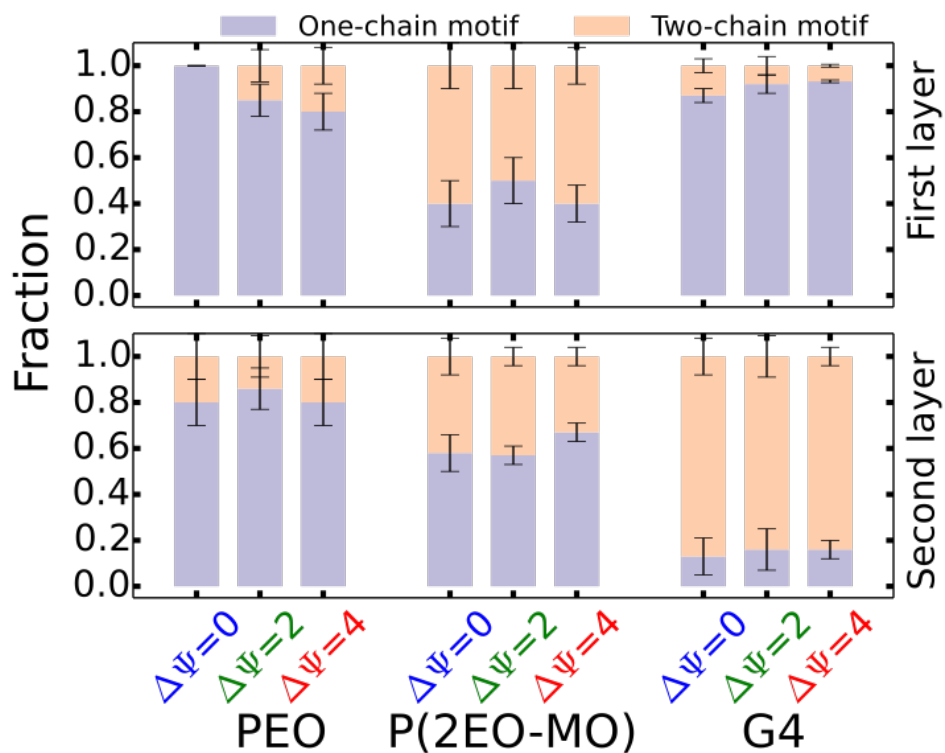


Figure 5.10: Spatially-resolved lithium-ion solvation motif at the anode interface. A top panel is for the first layer of interfacial lithium-ions, and a bottom panel is for the second layer of interfacial lithium-ions. For PEO and P(2EO-MO), the first layer is a region of  $d \in (2, 7)$ , and the second layer is a region of  $d \in [7, 11)$ . For G4, the first layer is a region of  $d \in (2, 4.5)$ , and the second layer is a region of  $d \in [4.5, 7)$ . The distance ( $d$ ) is from the anode in unit of  $\text{\AA}$ .

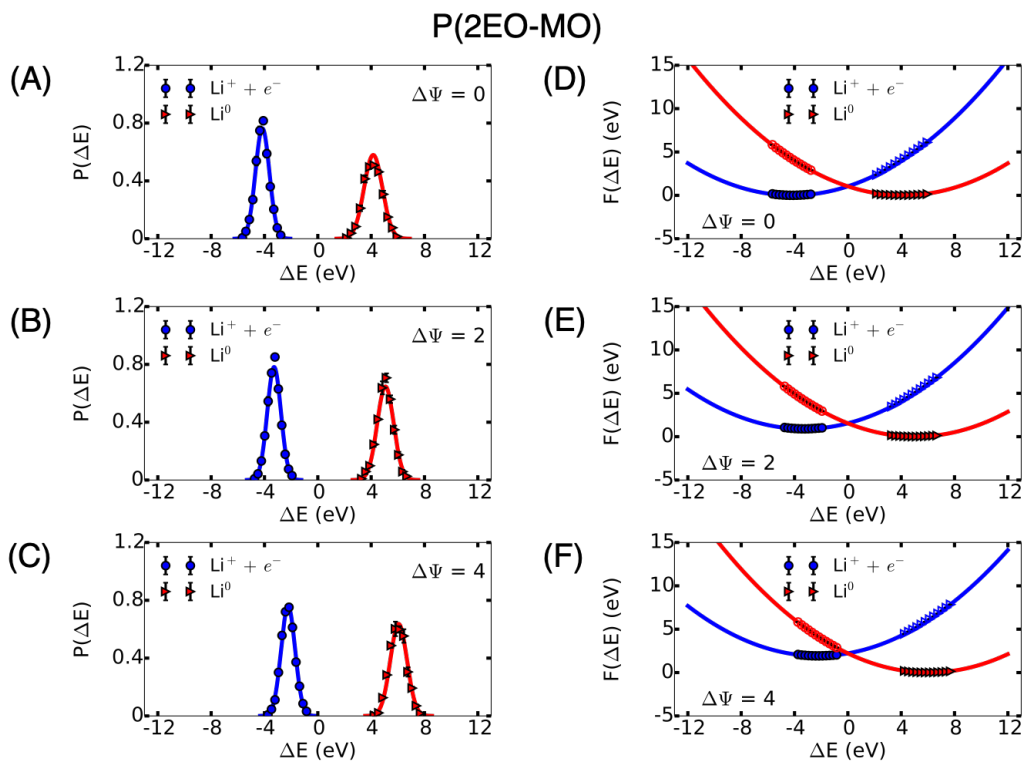


Figure 5.11: Lithium electroreduction in P(2EO-MO) at the anode interface. (a-c) Probability distributions  $P(\Delta E)$  of the vertical energy gap  $\Delta E$ , and (d-f) their associated free energy curves for both the  $\text{Li}^+$  and  $\text{Li}^0$  in P(2EO-MO). Results are shown for various bias potentials. Solid lines in (d-f) are parabolic curves using linear-response assumptions in Eq. 5.5.

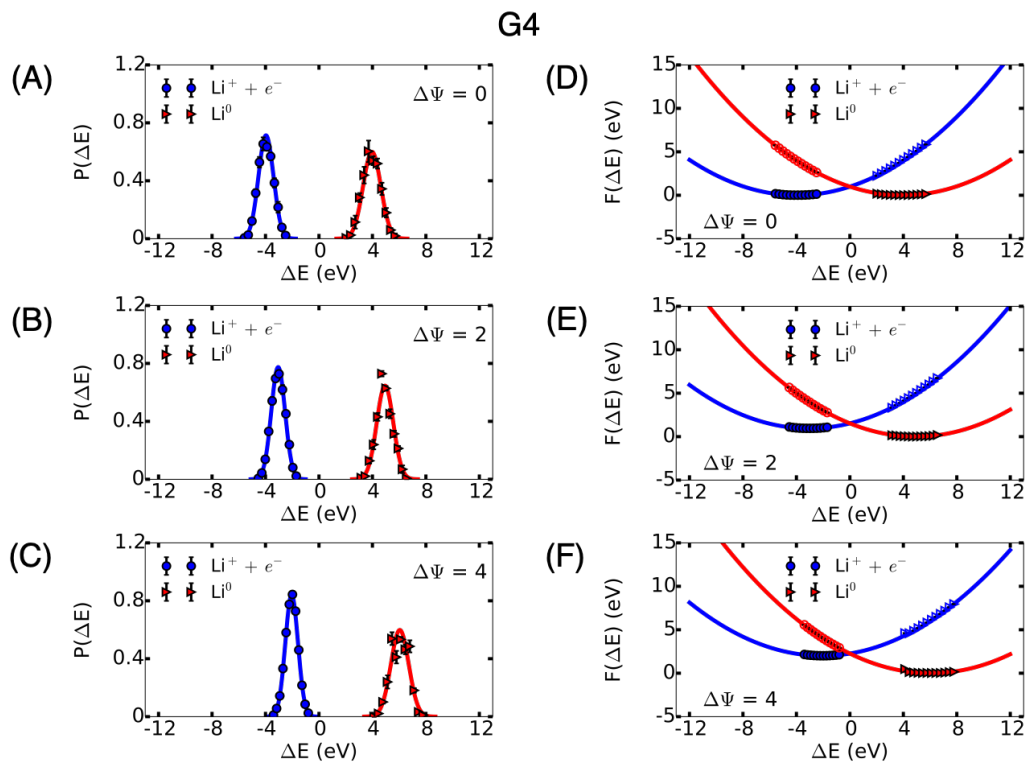


Figure 5.12: Lithium electroreduction in G4 at the anode interface. (a-c) Probability distributions  $P(\Delta E)$  of the vertical energy gap  $\Delta E$ , and (d-f) their associated free energy curves for both the  $\text{Li}^+$  and  $\text{Li}^0$  in G4. Results are shown for various bias potentials. Solid lines in (d-f) are parabolic curves using linear-response assumptions in Eq. 5.5.

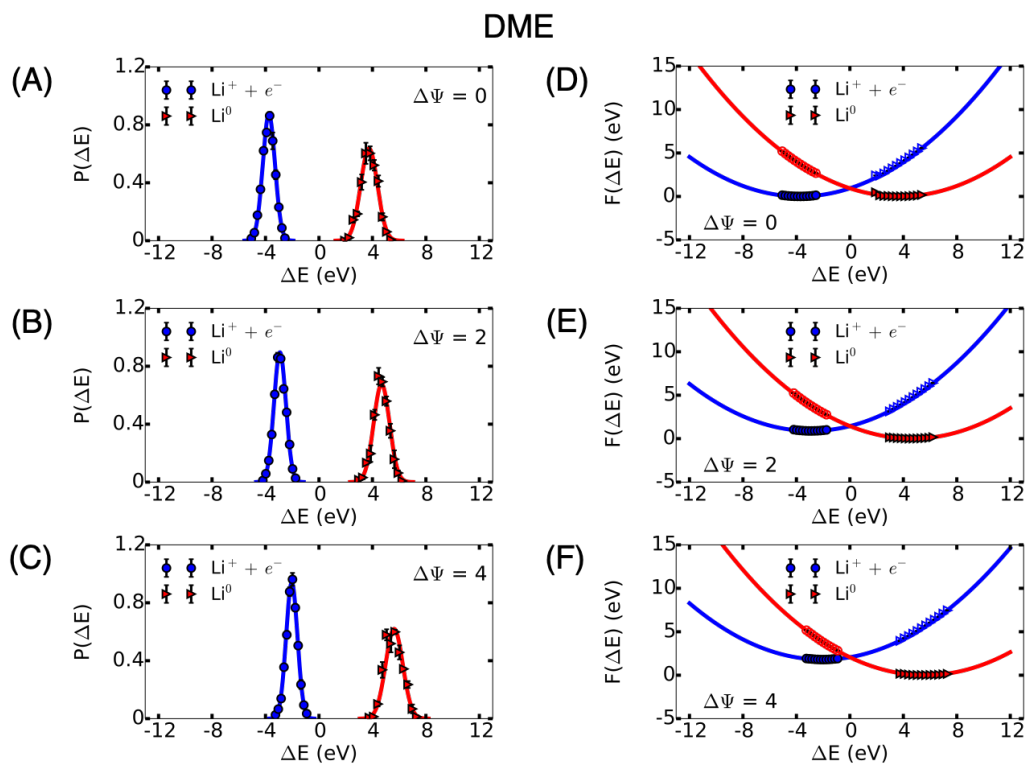


Figure 5.13: Lithium electroreduction in DME at the anode interface. (a-c) Probability distributions  $P(\Delta E)$  of the vertical energy gap  $\Delta E$ , and (d-f) their associated free energy curves for both the  $\text{Li}^+$  and  $\text{Li}^0$  in DME. Results are shown for various bias potentials. Solid lines in (d-f) are parabolic curves using linear-response assumptions in Eq. 5.5.

## DESIGN RULES FOR PASSIVATING SELF-ASSEMBLED MONOLAYERS TO A METAL ELECTRODE FROM FLUORIDE-ION SOLVATION STRUCTURE AND DYNAMICS

### **6.1 Abstract**

This chapter discusses design principles for self-assembled monolayers (SAMs) to passivate a metal electrode. A functionally useful solid electrolyte interphase (SEI) mitigates detrimental electrolyte degradation and promotes homogeneous electrodeposition, so it passivates the electrode, stabilizing the interface and providing an additional kinetic barrier to extend the electrochemical window. Herein, as an artificial SEI, a SAM layer functionalizes a metal electrode by adding sacrificial additives for a safe and long-lasting fluoride-ion rechargeable battery.

Using all-atom simulations, we investigate fluoride-ion solvation structure and dynamics to provide the recipe for the SAM molecules, including great film formation ability, high fluoride-ion solubility, poor solvent penetration, and fast (de-)fluorination. The fluoride-ion SAM solvation structure suggests that a functional SAM molecule needs to exhibit both fluorinated and ether moieties in order to enable efficient  $F^-$  shuttle between the bulk electrolyte and a metal electrode. A structure-dynamics relationship in fluoride-ion SAM solvation is found to reveal a prominent role of the free-energy barrier found in  $F^-$  SAM solvation structure. The presence of a sizable free-energy barrier at a SAM/electrolyte boundary suggests further tailoring of the end group of a SAM layer to facilitate the  $F^-$  transfer across the boundary.

Data and content in this chapter have been published as part of the Patent [199]. The author participated in conducting simulations, discussing the simulation results, and preparing the simulation part of the Patent.

### **6.2 Introduction**

Interfacial stability is essential to enhance cycling performance and longevity of energy storage materials, which is crucial for large-scale energy grid systems and electrical vehicles [175, 197, 122, 54, 182, 178, 105, 53, 59]. As is well known, lithium metal anode is one of strong candidates for next-generation advanced battery

materials thanks to the highest theoretical capacity ( $3,860 \text{ mA h g}^{-1}$  and  $2,061 \text{ mA h cm}^{-1}$ ) and the lowest electrochemical potential ( $-3.04 \text{ V vs. SHE}$ ) [175, 8, 182, 29, 178, 105]. However, its practical applications have been delayed due to the limited interfacial stability of lithium metal, including dendritic lithium deposition, due to its high reactivity, raising serious safety issues that lead to battery failure.

At electrochemical interfaces, typical liquid electrolytes (e.g. a mixture of cyclic and linear carbonates) immediately and spontaneously degrade via various competitive electrochemical reactions [197, 122, 137], resulting in the in situ formation of a structurally and chemically heterogeneous thin film called a solid electrolyte interphase (SEI) [132, 29, 5, 142, 184, 24]. A functionally useful SEI passivates the electrode, conducting ions yet providing electronic insulation, by mitigating detrimental electrolyte degradation that leads to battery capacity loss, aging, and failure. The composition and structure of the SEI do depend on the choice of solvent chemistry, and sacrificial additives [162]. For instance, fluoroethylene carbonate (FEC) was found successful in enhancing SEI stability at battery cycling by enriching the SEI with inorganic lithium fluoride (LiF) component [162, 68].

The other way to introduce a passivating SEI to suppress the lithium dendrites is ex situ fabrication [63, 83, 68, 207]. One of the advantages of the artificial SEI is the ability to control its composition and structure in a systematic way [177]. For example, Li-C composite microparticles, coated with a self-assembled monolayer (SAM), exhibit high specific capacity and high Coulombic efficiency [83]. The SAM film of octadecylphosphonic acid (OPA) was coated on a lithium electrode due to the reactive phosphonic acid group. Further, the saturated hydrocarbon chain drives the densely packed SAM layer that blocks moisture in air or trace amounts of water in solvents. The slurry-coated Li anode was also found to retain 82.5% capacity after 250 cycles at 1C when paired with a commercial  $\text{LiFePO}_4$  cathode.

Another successful implementation of an artificial SEI is hard-shell protection for a metal cathode that enables reversible room-temperature fluoride-ion shuttle, paired with liquid ether solvents [38]. Fluoride-ion battery (FIB) is one of advanced high-energy-density batteries, which enables multivalent fluoride conversion reactions in addition to the electronegativity and low mass of fluorine for higher energy density than lithium-ion one [7, 62, 38, 200]. However, the fluoride-ion battery operates only at elevated temperatures. Related challenges for the fluoride-ion shuttle in liquid electrolytes include (i) low solubility of metal fluoride electrolyte salts and (ii) low chemical stability due to formation of  $\text{HF}_2^-$  ( $0.7 \text{ V}$ ) or irreversible  $\text{F}^-$  complexation.

A recent study reported room-temperature fluoride-ion shuttle that ethereal liquid solvents readily transport fluoride ions of dry tetraalkylammonium fluoride salts, including bis(2,2,2-trifluoroethyl) ether (BTFE) and glyme [38]. Alpha-hydrogens in the ether solvents are responsible for solvating fluoride ions, maintaining high chemical stability against hydrogen abstraction reactions.

A novel cathode, consisting of a copper core and a lanthanum trifluoride shell, enables the room-temperature cycling, paired with the liquid ether solvents. An artificial hard-shell SEI provides high electrochemical stability by mitigating challenges associated with cathode metal dissolution. The hard-shell protection permits a reversible fluoride ion shuttle that is related to the conversion of Cu to CuF<sub>2</sub>. Nevertheless, anode stabilization is required for safe operation at complete cycles.

This chapter presents simulation-aided design recipes for SAMs to passivate a metal anode for fluoride-ion batteries. The primary goal is to provide molecular insights into fluoride-ion solvation structure and dynamics at the functional SAM-decorated metal interface. A functional SAM layer should primarily satisfy the following: (i) high film formation ability, (ii) high fluoride-ion solubility, (iii) poor solvent penetration, and (iv) fast (de-)fluorination. Herein, inspired by the ether solvents found to enable room temperature fluoride-ion shuttle, four different chemical structures of the SAM molecule are investigated, combining carbon monofluoride (CF<sub>x</sub>) and ether moieties [38].

We conduct all-atom simulations with polarizable metal electrodes coated with a SAM layer to investigate fluoride-ion solvation structure and dynamics. Four SAM layers are studied; they have a different spacer part of different chemistry, yet the same ethyl anchor and end group. The fluoride-ion SAM solvation structure suggests that a functional SAM molecule needs to exhibit both fluorinated and ether moieties in order to enable facile F<sup>-</sup> shuttle between the bulk electrolyte and a metal electrode. Thanks to the polarizable metal electrode included in our model, the kinetics of fluoride-ion SAM solvation are estimated using non-equilibrium simulation trajectories with a reversed bias potential. The fluoride-ion SAM solvation dynamics is found consistent with the associated structure. In particular, a sizable free-energy barrier for F<sup>-</sup> penetration at a SAM/electrolyte boundary is found for all SAM molecules studied, suggesting that optimizing the end group of the SAM molecule could facilitate the F<sup>-</sup> transfer across the SAM/electrolyte boundary.

Simulations also propose a scenario for the previous experiment to successfully protect the Ce or Ca anode surface with FOTS (1H,1H,2H,2H-Perfluorooctyl-

SAM <sup>a</sup>	Spacer feature	Fluorinated?	$\alpha$ -CH <sub>2</sub> moiety?
E-(CH <sub>2</sub> ) <sub>2</sub> -(CF <sub>2</sub> CH <sub>2</sub> OCH <sub>2</sub> CF <sub>2</sub> ) <sub>2</sub> F	BTFE-like	Yes	Yes
E-(CH <sub>2</sub> ) <sub>2</sub> -(CF <sub>2</sub> CH <sub>2</sub> ) <sub>3</sub> -CF <sub>3</sub>	PVDF-like	Yes	No <sup>b</sup>
E-(CH <sub>2</sub> ) <sub>2</sub> -(CH <sub>2</sub> OCH <sub>2</sub> ) <sub>3</sub> -CF <sub>3</sub>	Glyme-like	No	Yes
E-(CH <sub>2</sub> ) <sub>2</sub> -(CF <sub>2</sub> ) <sub>7</sub> -CF <sub>3</sub>	FOTS-like	Yes	No

Table 6.1: Four SAM molecules considered in this study. <sup>a</sup>E represents an electrode surface. <sup>b</sup> CH<sub>2</sub> moiety is present next to CF<sub>2</sub> without an oxygen atom.

trichlorosilane) additives, confirmed by cyclic voltammetry and electrochemical impedance spectroscopy studies [38]. Results for a FOTS-like SAM layer suggest that the passivation is enabled mainly by steric repulsion with unfavorable interactions of the FOTS-like SAM with the BTFE electrolyte and the ions.

### 6.3 Methods and Calculation Details

We consider a model system that is comprised of two metal electrodes and an electrolyte of Np<sub>2</sub>F salt in BTFE solvent (Fig. 6.1). The electrodes are modeled using the pristine (111) surface of face-centered cubic (FCC) platinum as in Chapter 5. Below, we describe the computational details of the SAM molecules, the interaction potentials, MD simulations, calculated local density of ions, and electrolytes.

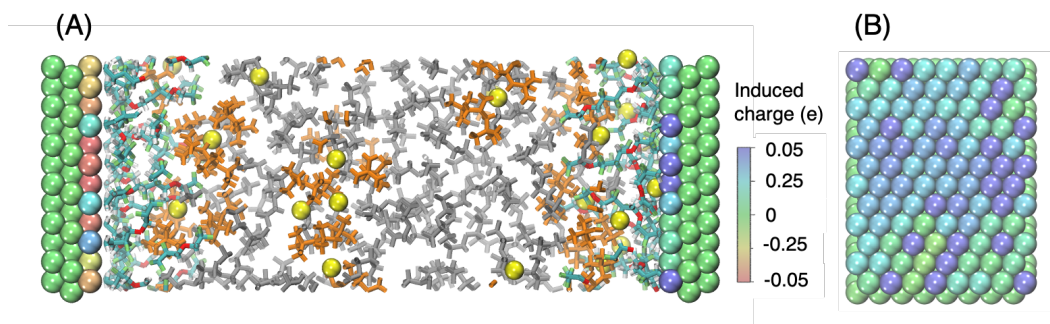


Figure 6.1: Simulation snapshot and electrode-charge polarization. (a) A simulation snapshot including a BTFE-like SAM layer, Np<sub>2</sub>F salt, BTFE solvent, and model electrodes. Yellow spheres represent F<sup>-</sup> ions and Np<sub>2</sub><sup>+</sup> ions are drawn in orange. BTFE solvents are drawn in grey. Two slabs are pristine, polarizable model electrodes (purple spheres for the anode and pink ones for the cathode) held with a bias potential  $\Delta\Psi = 4$  V. Color for electrode atoms is associated with their induced charges between  $-0.05$  e (red) and  $+0.05$  e (blue). (b) Electrode-charge polarization on the innermost layer of the anode in (a).

### SAM molecules

Four different SAM molecules were considered, depending on fluorination and/or  $\alpha$ -CH<sub>2</sub> moieties (Table 6.1). Both considerations were identified to have to do with fluoride-ion solvation in the previous study [38]. Further, the FOTS additive was shown to form a SEI on the Ce or Ca anode surface; cyclic voltammetry and electrochemical impedance spectroscopy studies showed that the SEI confirmed by XPS analysis delays further side reactions of electrolytes. Note that all the SAMs considered here have a (CH<sub>2</sub>)<sub>2</sub> linker at one end anchored to the electrode, considered to be inert. Surface coverage was fixed at 2.5 nm<sup>-2</sup> of the SAM layer ( $\sigma_{SAM}$ ), unless otherwise noted. At  $\sigma_{SAM} = 2.5 \text{ nm}^{-2}$ , the majority of the SAM molecules stand up against the electrode, so the SAM layers are dense enough to prevent electrolyte penetration via steric repulsion.

### Force field details and MD simulations

Molecular dynamics simulations were performed using a polarizable model for metal electrodes. The electrode atoms are fixed in the face-centered cubic structure with a lattice parameter of 0.392 nm and a (111) termination at the interface. The orthorhombic simulation cell is oriented such that the z coordinate is perpendicular to the electrode surface, and the simulation cell is periodically replicated only in the x and y coordinates. Moreover, to prevent the long-range contribution of Coulomb interaction along z direction, the vacuum region of the equal size to the simulation cell is introduced on both sides along the transverse direction [204]. In all simulations, each electrode is described using three layers of atoms, with each layer containing 96 atoms (for a total of 576 electrode atoms). The cathode layers are held at a negative electrode-potential,  $\Psi^-$  and the anode layers are held at a positive electrode-potential,  $\Psi^+ (= -\Psi^-)$ . The bias potential is  $\Delta\Psi = \Psi^+ - \Psi^-$ . Electrode potential in this study is in the unit of volt.

Self-assembled monolayer (SAM) molecules were anchored on top of each electrode. The anchor was enforced by a harmonic bond between an electrode atom in the inner-most layer and a carbon atom in (CH<sub>2</sub>)<sub>2</sub> linker in the polymer. An angle potential was additionally introduced for the carbon atom with its hydrogen and the electrode atom, to keep its local geometry of sp<sup>3</sup> character. Given  $\sigma_{SAM}$ , SAM molecules were tethered to randomly chosen electrode atoms. Partial charges of SAM molecules were calculated averaging charge distributions of configurations sampled in condensed-phase MD simulations [157, 37]. Initial partial charges (OPLS) of SAM molecules were obtained from the LigParGen website [41]. Quan-

tum chemistry calculations were done using the entos software package [113]. The B3LYP-D3/ma-def2-TZVP level of theory was used in electronic structure calculations for each configuration.

$\text{Np}_2\text{F}$  (N,N,N-dimethyl-N,N-dineopentylammonium fluoride) salt was introduced in the simulation cell with BTFE electrolyte, which was identified to be able to solvate the bare  $\text{F}^-$  anion. Mole fraction of  $\text{Np}_2\text{F}$  salt to the BTFE electrolyte was chosen to be 0.2, representing a typical operational concentration ( $\sim 1.2\text{M}$ ).

Interactions between atoms in the electrode and other electrolytes and salts were described using both electrostatic and Lennard-Jones (LJ) interactions. The charges of the metallic atoms of the constant-potential electrodes were allowed to fluctuate in response to charges of other components in the simulation cell, described in terms of a sum of atom-centered spherical Gaussian functions. Details are given in Section 5.3. We employed the version of the CPM developed in Ref. [188], which employs matrix inversion at each timestep to determine the charge polarization on the electrode atoms. LJ parameters for electrode atoms were described by Heinz group force field [69].

The OPLS-AA force field [79, 80, 41], a non-polarizable and all-atom model, was used for electrolytes, salts, and SAM molecules. The cross terms were obtained using the geometric mixing rule. The LJ interactions and the real-space part of the Coulomb interactions were truncated at 1.4 nm; the long-range contribution of Coulomb interaction was treated by the particle-particle particle-mesh method [72]. Intramolecular interactions for electrolytes, salts, and SAM molecules were described by harmonic bond and angle potentials, and OPLS dihedral angle potential. Both LJ and Coulomb interactions were reduced by half for 1-4 particles. During equilibration, the position of the electrodes along the  $z$  coordinate was adjusted so that the pressure of the confined simulation cell was 1 atm. In this stage, all the charges of electrode atoms were fixed to zero. After the equilibration, the electrode atoms were fixed in space, and their charges were allowed to fluctuate in time.

The classical molecular dynamics equations of motion were evolved using the velocity Verlet integrator with a timestep of 2 fs; rigid-body constraints for a bond between carbon and hydrogen atoms in all considered molecules were enforced using the SHAKE algorithm [155]. The simulations were performed at a temperature of 400 K, enforced via the The Nosé-Hoover thermostat with a damping timescale of 100 timesteps, and at a pressure of 1 atm along only  $xy$  directions, enforced via the Nosé-Hoover barostat with a damping timescale of 1000 fs relaxation. All

simulations were performed using the LAMMPS software package [140]. All the quantities reported here were averaged using simulation trajectories over more than 10 ns after equilibration at least during 5 ns.

### Calculations of local density and the associated potential of mean force

The local density,  $\rho(d)$  of atoms as a function of distance from an electrode,  $d$  is calculated for an atom of  $i$ -species electrolyte [50]:

$$\rho(d) = \frac{1}{L_x L_y} \left\langle \sum_{j=1}^{N_i} \delta(d - z_j^i + z_w) \right\rangle, \quad (6.1)$$

where  $\langle \dots \rangle$  represents the ensemble average,  $z_j^i$  is  $z$  position of  $j^{\text{th}}$  atom of  $i$ -species ( $j = 1, 2, \dots, N_i$ ),  $z_w$  is  $z$  position of atoms in an electrolyte-exposed layer of the electrode, and  $L_k$  is the length of the simulation box along each direction,  $k$  for  $k \in \{x, y, z\}$ .

The cumulative average,  $\rho_{ca}(d)$  of the local density in a region of  $[0, d]$  is defined as below:

$$\rho_{ca}(d) = \frac{1}{d} \int_0^d \rho(x) dx, \quad (6.2)$$

where  $x$  is the distance from the electrode. SAM ion-density is then defined using  $\rho_{ca}(d)$ :

$$\rho_{\text{SAM}} = \rho_{ca}(l_{\text{SAM}}) = \frac{1}{l_{\text{SAM}}} \int_0^{l_{\text{SAM}}} \rho(x) dx, \quad (6.3)$$

where  $l_{\text{SAM}}$  is the length of a SAM region on top of the electrode. Here,  $l_{\text{SAM}} = 1.2$  nm is used for all the SAM molecules according to the average position of the end group ( $\text{CF}_3$ ). Then, the average distance of the atom from the electrode is defined:

$$d_{\text{SAM}} = \frac{1}{\rho_{\text{SAM}}} \frac{1}{l_{\text{SAM}}} \int_0^{l_{\text{SAM}}} x \rho(x) dx. \quad (6.4)$$

Finally, potential of mean force,  $W(d)$ , associated with the local density is calculated:

$$W(d) = -k_B T \ln \left[ \frac{\rho(d)}{\rho_b} \right], \quad (6.5)$$

where  $k_B$  is Boltzmann constant,  $T$  is the temperature, and  $\rho_b$  is its bulk density  $\rho_b = \frac{1}{2l_b} \int_{-l_b}^{l_b} \rho(x) dx$  with  $l_b = 1$  nm.

### Calculation of the relaxation time of SAM intercalation and de-intercalation

The rate of fluorination and de-fluorination is measured by the relaxation time of the SAM local density. For a given equilibrium snapshot, the electrode polarization is

reversed. Then, the relaxation time toward a new equilibrium is measured:

$$\bar{\rho}_{\text{SAM}}(t) = (\bar{\rho}_{\text{SAM}}(0) - \rho_{\text{ne}}) \exp[-t/\tau_{\rho}] + \rho_{\text{ne}}, \quad (6.6)$$

where  $\bar{\rho}_{\text{SAM}}(t)$  is a transient ion SAM-density at time  $t$ ,  $\rho_{\text{ne}}$  is the ion SAM-density at a new equilibrium, and  $\tau_{\rho}$  is the relaxation time of ion SAM-density. Another kinetic measure is the time-dependent charge-polarization of a metal electrode:

$$\bar{Q}(t) = (\bar{Q}(0) - Q_{\text{ne}}) \exp[-t/\tau_Q] + Q_{\text{ne}}, \quad (6.7)$$

where  $\bar{Q}(t)$  is total electrode charge at time,  $t$ ,  $Q_{\text{ne}}$  is new equilibrium value of  $Q(t)$ , and  $\tau_Q$  is its relaxation time.

## 6.4 Results and Discussion

### Statistics of SAM ion-solvation

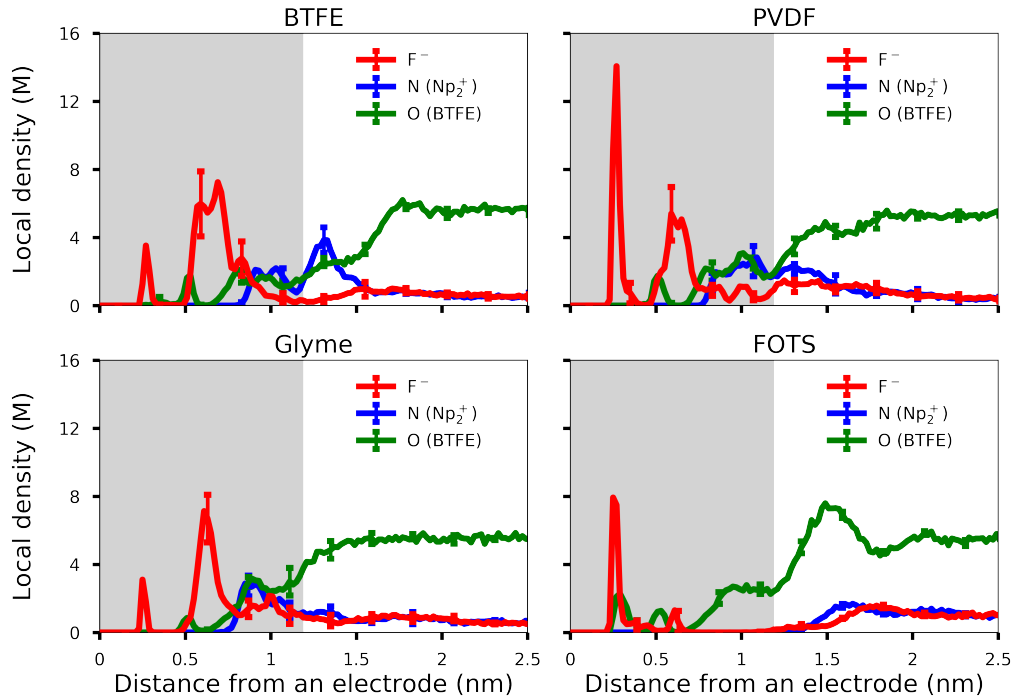


Figure 6.2: Local density of electrolyte atoms as a function of the distance from an anode with bias potential ( $\Delta\Psi = 4$  V) for various SAM layers. In each panel, the grey box indicates the 1.2 nm thick SAM region.

We begin by considering the fluoride-ion solvation inside the SAM region with a finite bias potential relevant to the experimental conditions. Fig. 6.2 illustrates the penetration of  $\text{F}^-$  across a SAM/electrolyte interface with a bias potential ( $\Delta\Psi = 4$  V). Grey boxes represent a 1.2 nm thin SAM region. Since a charging process is studied,

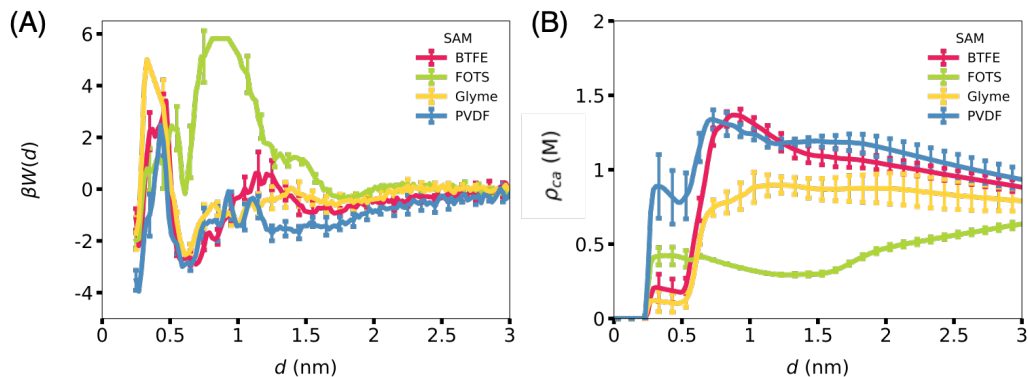


Figure 6.3: Fluoride-ion SAM density with bias potential ( $\Delta\Psi = 4$  V) for various SAM layers. (a) Potential of mean force ( $\beta W(d)$ ) associated with fluoride-ion SAM density, where  $\beta = 1/k_B T$ . (b) Cumulative average ( $\rho_{ca}$ ) of  $F^-$  density as a function of the distance ( $d$ ) from the anode surface.

all the SAM-decorated anode surfaces are positively charged, so they preferentially interact with  $F^-$  over  $Np_2^+$ . Bulky  $Np_2^+$  resides only at the SAM/electrolyte interface, being repelled from the anode surface. The SAM layers, except for a FOTS-like one, are found to allow for appreciable  $F^-$  penetration, all of which provide both solvation states for  $F^-$ , including inner-solvation ( $d < 0.5$  nm) and outer-solvation state ( $0.5 \text{ nm} < d < 1$  nm). Two states of  $F^-$  SAM solvation are also clearly shown in the associated potential of mean force ( $W(d)$ ), separated by a sizable barrier (Fig. 6.3A). In the inner-solvation state,  $F^-$  ions interact with the ethyl anchor and the electrode while interacting with the SAM spacer region in the outer-solvation state.

A FOTS-like SAM layer, on the other hand, exhibits significant suppression of the outer-solvation of  $F^-$  with an appreciable amount of inner-solvated  $F^-$ . Instead, there is a significant broad barrier in  $\beta W(d)$  that separates the inner-solvation state and bulk BTFE electrolytes (Fig. 6.3A). Another notable difference at the FOTS-decorated anode interface is the BTFE electrolyte local density, including the populated density at the BTFE/FOTS interface (Fig. 6.2). Both features indicate that the FOTS-like SAM layer has unfavorable interactions with the ions and BTFE electrolytes. Thus, simulations suggest that the successful passivation of FOTS additives in the experiments could be driven by steric repulsion of the BTFE electrolytes while allowing for the  $F^-$  penetration mainly via electrostatic attraction.

Fig. 6.4B shows the cumulative average ( $\rho_{ca}$ ) of  $F^-$  molar density from the anode

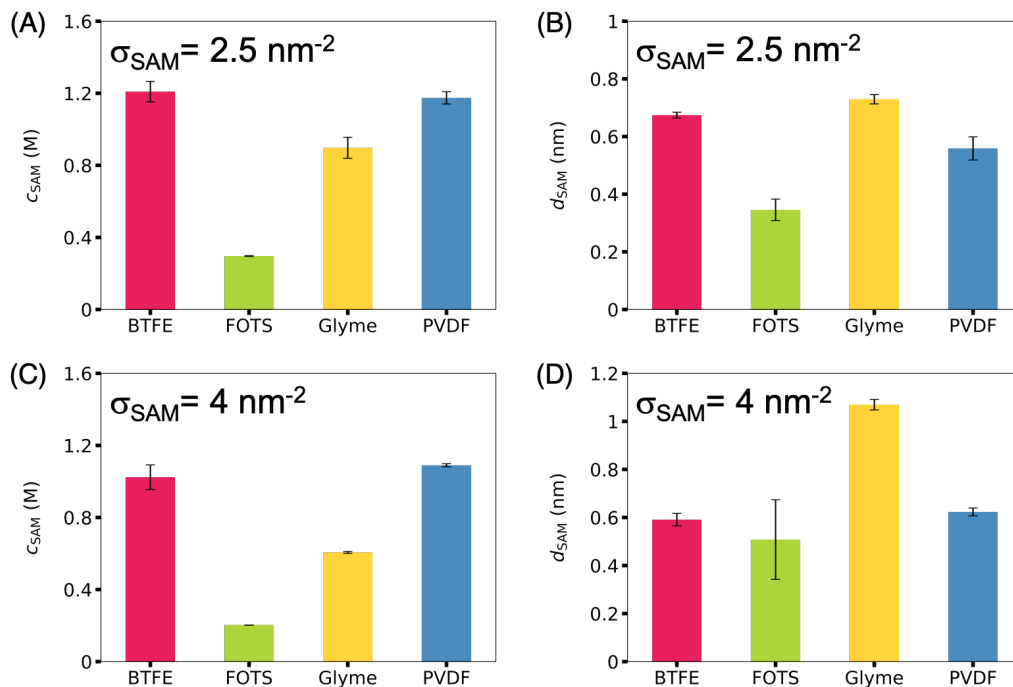


Figure 6.4: Statistics of F<sup>-</sup> SAM density on the anode with bias potential ( $\Delta\Psi = 4 \text{ V}$ ) for various SAM layers at two different coverage densities ( $\sigma_{SAM}$ ). (a,c) Cumulative average of F<sup>-</sup> density as a function of the distance,  $d$ , from the anode surface. (b,d) The average distance of F<sup>-</sup> from the anode.

surface that summarizes the observations in Fig. 6.2 and ranks order SAM layers regarding F<sup>-</sup> SAM penetration. It is immediately apparent that F<sup>-</sup> anions penetration is dependent on SAM chemistry. A nonzero value of  $\rho_{ca}$  less than 0.5 nm indicates the inner-solvation of F<sup>-</sup>. The BTFE-like SAM layer shows a rapid increase in  $\rho_{ca}$  in the region ( $0.5 < d < 1 \text{ nm}$ ) that corresponds to the outer-solvation of F<sup>-</sup>, where  $d$  is the distance from the anode interface. In contrast, the FOTS-like SAM layer shows a long plateau of  $\rho_{ca}$  in the region, manifesting the suppressed outer solvation of F<sup>-</sup>.

Fig. 6.4 also quantifies F<sup>-</sup> SAM penetration as well as how deeply F<sup>-</sup> anions penetrate to the anode surface at two different SAM coverage densities ( $\sigma_{SAM}$ ). The SAM region considered here is 1.2 nm thin from the anode for all SAMs. Based on the F<sup>-</sup> anions penetration statistics, BTFE-like and PVDF-like moieties are almost equally efficient as an artificial SEI; on average, F<sup>-</sup> anions reside inside the SAM  $\sim 0.6\text{-}0.7 \text{ nm}$  away from the anode, and their SAM concentration is  $\sim 1.2 \text{ mol L}^{-1}$  (Fig. 6.4A-B and Table 6.2). A PVDF-like layer is the easiest for F<sup>-</sup> to access an

F <sup>-</sup> anion	BTFE-like	FOTS-like	Glyme-like	PVDF-like
$\Psi = 2$ V	0.97 (7)	0.28 (5)	0.86 (4)	1.1 (1)
$\Psi = -2$ V	0.38 (3)	0.01 (1)	0.31 (2)	0.50 (3)
Np <sub>2</sub> <sup>+</sup> cation	BTFE-like	FOTS-like	Glyme-like	PVDF-like
$\Psi = 2$ V	0.61 (3)	0.02 (1)	0.46 (4)	0.70 (3)
$\Psi = -2$ V	0.77 (4)	0.06 (1)	0.68 (4)	0.91 (4)
Excess charge	BTFE-like	FOTS-like	Glyme-like	PVDF-like
$\Psi = 2$ V	-0.36 (8)	-0.26 (5)	-0.20 (4)	-0.31 (3)
$\Psi = -2$ V	+0.39 (5)	+0.05 (1)	+0.37 (5)	+0.41 (5)

Table 6.2: Ion SAM molar density at various bias potentials ( $\Psi$ ). Excess charge molar density is the difference between ion molar density with the charge considered. Statistical errors of the final digit are indicated in parentheses.

inner-solvation state, while a BTFE-like layer hosts F<sup>-</sup> the most in an outer-solvation state. The F<sup>-</sup> solvation behaviors in more densely packed SAM layers ( $\sigma_{sam} = 4$  nm<sup>-2</sup>) are more or less the same, with less F<sup>-</sup> SAM concentration (Fig. 6.4C-D). Further, Table 6.2 clearly shows that the application of an attractive or repulsive potential either enhances or retards this solvation (i.e., polarization can assist in F<sup>-</sup> transfer through the SAM). Therefore, both fluorinated and  $\alpha$ -CH<sub>2</sub> moieties in the SAM molecules need to be present in the SAM molecules in order to enable efficient F<sup>-</sup> shuttle between the bulk electrolyte and a metal electrode. The conclusion here is insensitive to the choice of the size of a SAM region. Note that Fig. 6.5 shows no dramatic effect of the bias potential on the F<sup>-</sup> SAM penetration in two effective BTFE-like and PVDF-like SAM layers.

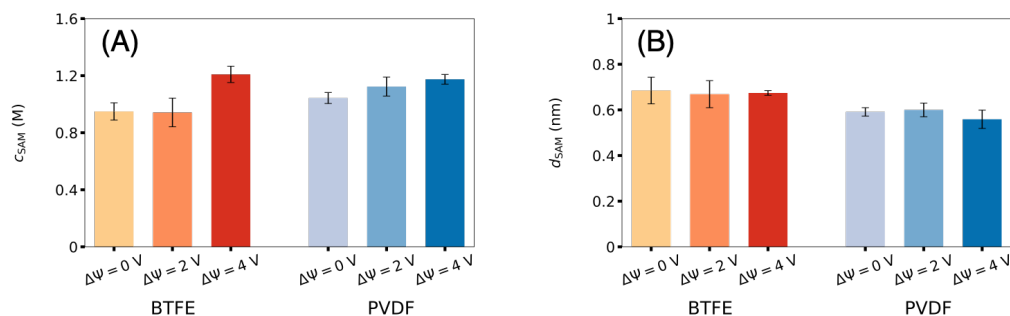


Figure 6.5: Statistics of F<sup>-</sup> SAM intercalation on the anode for BTFE-like and PVDF-like SAM layers with various bias potentials,  $\Delta\Psi$ . (a) Average F<sup>-</sup> SAM density. (b) The average distance of F<sup>-</sup> from the anode.

### Kinetics of F<sup>-</sup> SAM intercalation and de-intercalation

All cases in Fig. 6.3A show a dip in the local density of F<sup>-</sup> at a SAM/electrolyte interface ( $\sim 1.5$  nm from the anode), which indicates a barrier for F<sup>-</sup> penetration. The deeper this dip, the greater the penetration barrier. This barrier has direct relevance to the kinetics of F<sup>-</sup> SAM penetration, as discussed below.

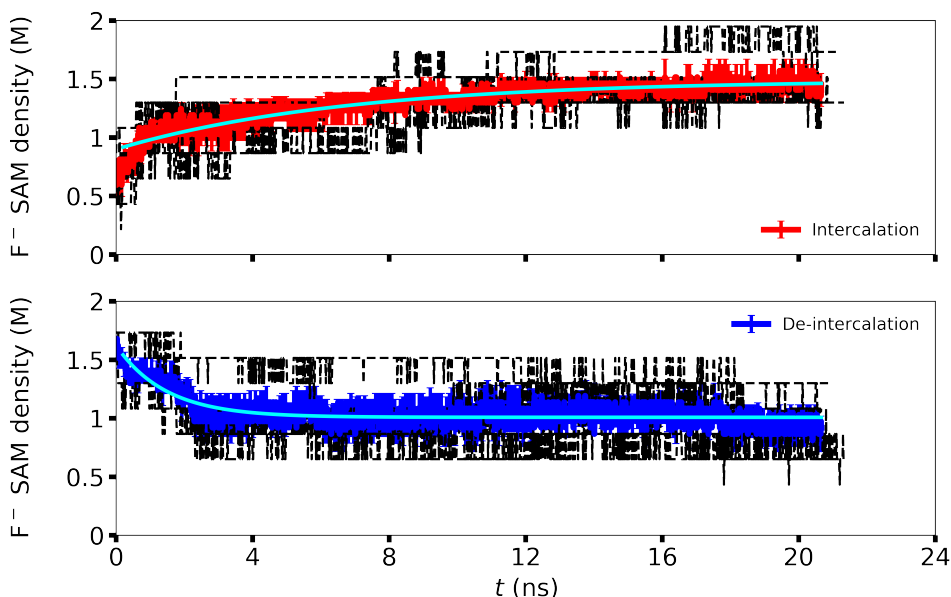


Figure 6.6: F<sup>-</sup> density in a BTFE-like SAM layer as a function of time ( $t$ ) after bias potential is reversed (from  $\Delta\Psi = 4$  V to  $\Delta\Psi = -4$  V). Top panel: SAM intercalation. Bottom panel: SAM de-intercalation. In both panels, black dotted lines represent the results from different initial configurations, and colored lines are the averaged density over the initial configurations. Cyan lines are the fit using the Eq. 6.6.

To investigate the rate of (de-)fluorination, we conduct non-equilibrium simulations, reversing the bias potential; a positively charged anode becomes more positively charged, and a negatively charged cathode becomes more negatively charged under the reversed bias potential. After a certain amount of time, both electrodes relax into a new equilibrium. For sufficient statistics of the kinetics of F<sup>-</sup> SAM (de-)intercalation, at least four different non-equilibrium trajectories are averaged starting from different initial configurations sampled from equilibrium simulations and at least five ns apart from each other.

Fig. 6.6 displays F<sup>-</sup> SAM molar density during the SAM (de-)intercalation on each metal electrode. For all SAMs, each of their regions is 1.2 nm thin from each

electrode as in other static data. All time-dependent  $F^-$  SAM densities starting from different initial configurations follows an exponential relaxation in both processes (Eq. 6.6). Thanks to our polarizable metal electrodes, we can also trace the time-dependent charge polarization on each electrode (Fig. 6.8 in Appendix). One advantage of measuring the electrode polarization kinetics is that there is no arbitrary parameter such as the size of a SAM region. Fig. 6.8 clearly shows more rapid initial change in  $\bar{Q}(t)$  ( $< 1$  ns) during both processes than the initial change in  $F^-$  SAM density (Fig. 6.6). This seems to imply that  $\bar{Q}(t)$  is more responsible for the change in the density of inner-solvated  $F^-$  ions than in that of outer-solvated  $F^-$  ions, yet it is likely the opposite for the change in  $F^-$  SAM density. Thus, we suggest that the relaxation time of each measure for the kinetics of  $F^-$  SAM (de-)intercalation provides dynamical behaviors of  $F^-$  SAM solvation in each state.

To rank order the SAM molecules in regard to the kinetics of  $F^-$  SAM (de-)intercalation, the relaxation times of  $F^-$  SAM (de-)intercalation obtained using Eqs. 6.6 and 6.7 are shown in Figs. 6.7 and 6.8. Note that the initial rapid change ( $< 0.2$  ns) of  $\bar{Q}(t)$  is not included in its fitting process. It is immediately clear that both measures show that the de-intercalation is faster than the intercalation for all SAM molecules considered here. Nevertheless, the trends in the rate across different SAMs are the same for both processes. This asymmetric kinetic behavior suggests that one needs to take care of  $F^-$  transport more in charging than in discharging.

FOTS-like SAMs exhibit exceptionally slow relaxation time of  $\bar{Q}(t)$  (Fig. 6.8), which is consistent with the absence of the outer-sphere  $F^-$  solvation state in FOTS-like SAMs (Fig. 6.3);  $F^-$  ions should be transferred between the inner-solvation state in FOTS-like SAMs and its bulk solvation state ( $d > 1.5$  nm) across a considerably high free-energy barrier. The relatively short (de-)intercalation time seems relevant to transient crossing events across the arbitrary SAM/electrolyte boundary at  $d = 1.2$  nm. This suggests that a SAM-specific boundary should be considered for fair comparisons.

Exceptionally fast kinetics of Glyme-like SAMs also reveals the shortcoming of the arbitrary SAM/electrolyte boundary. Glyme-like SAMs exhibit a relatively flat region of  $W(d)$  around  $d \approx 1.2$  nm (Fig. 6.3), smoothing the barrier crossing events. That is alleviated in the relaxation time of  $\bar{Q}(t)$  (Fig. 6.8), supporting that the surprisingly fast kinetics is an artifact of the choice of a SAM region. However, Glyme-like SAMs even show the fastest kinetics of  $\bar{Q}(t)$  among the SAMs considered here. It seems consistent with  $W(d)$  for  $F^-$  ions that reveals that the less

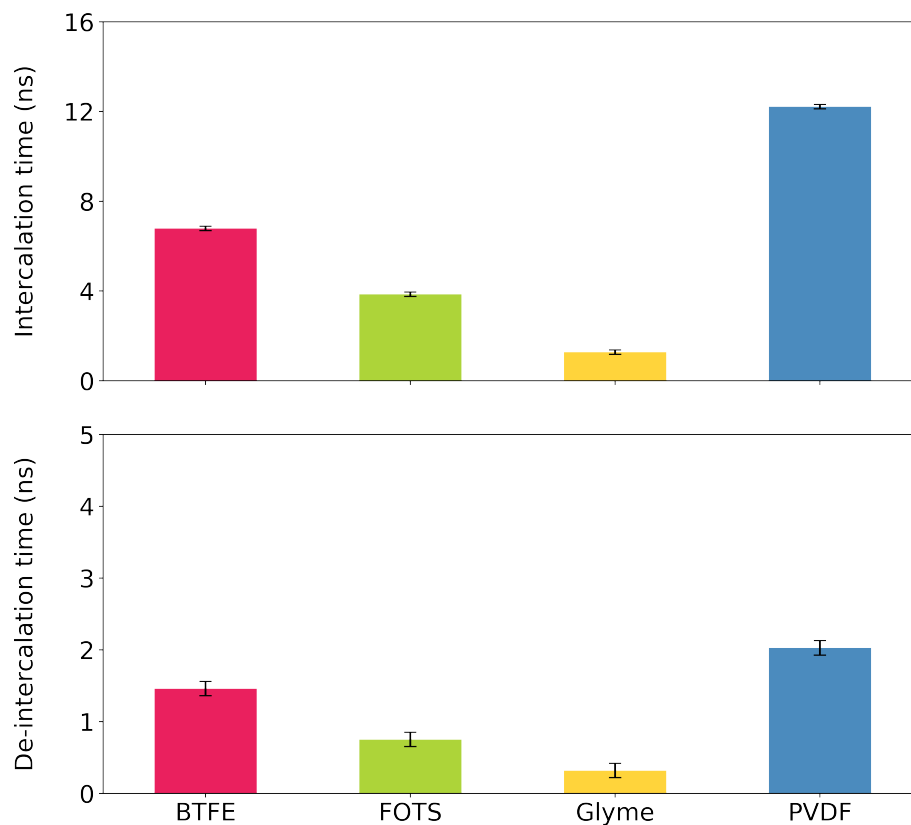


Figure 6.7: Average time (Eq. 6.6) of  $F^-$  SAM intercalation (top) and de-intercalation (bottom) in various SAM layers.

stable inner-solvation state than the outer-solvation state.

Interestingly, PVDF-like SAMs, the best SAM regarding the statistics of  $F^-$  SAM solvation, exhibit a relatively slow (de-)intercalation time (Fig. 6.8), which is consistent with the presence of a metastable state shown in  $W(d)$  at  $d \approx 1.5$  nm (Fig. 6.3) at the SAM/electrolyte boundary. In this case,  $F^-$  ions should visit the metastable state during the intercalation, slowing down the associated kinetics. Moreover, PVDF-like SAMs are the most stable inner-solvation state for  $F^-$  ions among the SAMs considered here, which delays the de-intercalation process.

Similarly, BTFE-like SAMs exhibit a metastable state shown in  $W(d)$  at  $d > 1.5$  nm (Fig. 6.3). However, the mismatch of the location of its metastable state and the

arbitrary SAM/electrolyte boundary leads to relatively facilitated kinetics instead of PVDF-like SAMs.

## 6.5 Summary and Conclusions

In this chapter, we employ all-atom simulations to study  $F^-$  SAM solvation structure and dynamics at the metal electrode. The potential of mean force associated with  $F^-$  SAM solvation clearly shows that  $F^-$  SAM solvation structure that includes the inner- and outer-solvation states inside the SAM and the metastable state at the SAM/electrolyte boundary. The statistics of  $F^-$  SAM solvation suggests that both fluorinated and  $\alpha$ - $CH_2$  moieties are necessary for functional SAM molecules; it is found that a PVDF-like SAM is the most effective, while a FOTS-like SAM is the least effective. A BTFE-like SAM is found similarly efficient to a PVDF-like SAM. The passivation shown in previous experiments [38] is suggested due to the steric repulsion with unfavorable interactions with the BTFE electrolyte as well as the ions.

The dynamics of  $F^-$  shuttle inside and across the SAMs is investigated using non-equilibrium simulations with a reversing bias potential. The dynamics of  $F^-$  SAM solvation is found consistent with its structure in the potential of mean force, suggesting the structure-dynamics relationship in  $F^-$  SAM solvation. A PVDF-like SAM, the best one regarding the static properties, is found not to be the most effective one for  $F^-$  shuttle across the SAM/electrolyte boundary. Relative slow (de-)intercalation of a PVDF-like SAM, responsible for dynamics of outer-solvated  $F^-$  ions, is partly related to the presence of the metastable state of  $F^-$  solvation at the boundary. Kinetics of electrode-charge polarization of a PVDF-like SAM, responsible for dynamics of inner-solvated  $F^-$  ions, is similar to that of a BTFE-like SAM. The results suggest that SAM molecules could be further optimized by changing the end group, which faces toward the SAM/electrolyte boundary, to facilitate  $F^-$  shuttle across the SAM.

We note that some artifacts of an arbitrary SAM/electrolyte boundary are found in the kinetics of  $F^-$  SAM (de-)intercalation; the comparisons for the SAM molecules appear unfair without considering the  $F^-$  SAM solvation structure, so a SAM-specific boundary needs to be considered for fair comparisons.

In the future, the following is worth investigating: (i) whether the response of the electrode-charge polarization is linear or not, and (ii) the structure-dynamics-function relationship via solvation site distribution. In Chapter 5, we found the robustness of the linear-response assumptions for the interfacial lithium electrore-

duction, despite the non-Gaussian behavior of electrode-charge polarization using equilibrium simulations. In this chapter, however, we found a connection between the electrode-charge polarization and the  $F^-$  inner-solvation state in their kinetic response to a reversed bias potential in non-equilibrium simulations. We could further explore some connections between equilibrium fluctuation of electrode-charge polarization and non-equilibrium relaxation [50] to test the robustness of the assumptions of linear-response theory at a SAM/metal interface.

Moreover, for the purpose of fast high-throughput screening, we could further abstract the atomistic SAM models into few key descriptors. One of the successful descriptors is ion-solvation site density, and its connectivity [190]; a higher density of interconnected ion-solvation sites in polymer electrolytes leads to facile ion hopping between the sites, thus predicting higher ion conductivity. For the SAM layers, we can make similar approaches. Fig. 6.9 displays an example of fluoride-ion solvation sites found in a BTFE-like SAMs. We could explore the connections between the structural information of the SAM solvation sites and their dynamic behaviors as we find here a preliminary structure-dynamics relationship in  $F^-$  SAM solvation.

## 6.6 Appendix

### Solvation site distribution on a metal-SAM interface

Fig. 6.9 represents a snapshot of the spatial locations within the SAM at which a fluoride ion could be favorably solvated or bound. The fluoride-ion solvation site distribution is determined at each configuration of the SAM using a distance-based criterion. The solvation sites are pruned to avoid redundancies and steric clashes with other atoms in the SAM. The protocol used is: (i) Sites are initially prepared on a rectangular grid (146520 sites). (ii) Sites are collected if they have at least four nearby hydrogen atoms of SAM molecules within 3 Å. (ii) Two sites are considered the same if they share at least the same closest four hydrogen atoms. The position of a representative site for a set of the site of having the same closest four hydrogen atoms is the centroid of the sites. (iii) The site has to have no significant overlap with all other atoms of SAM molecules and of an electrode (interatomic distance is less than 2 Å). (iv) The last step consolidates the sites if (a) they share at least the same two hydrogen atoms, and (b) their intersite distance is less than 1 Å. The position of the final consolidated site is the centroid of the sites that is being consolidated.

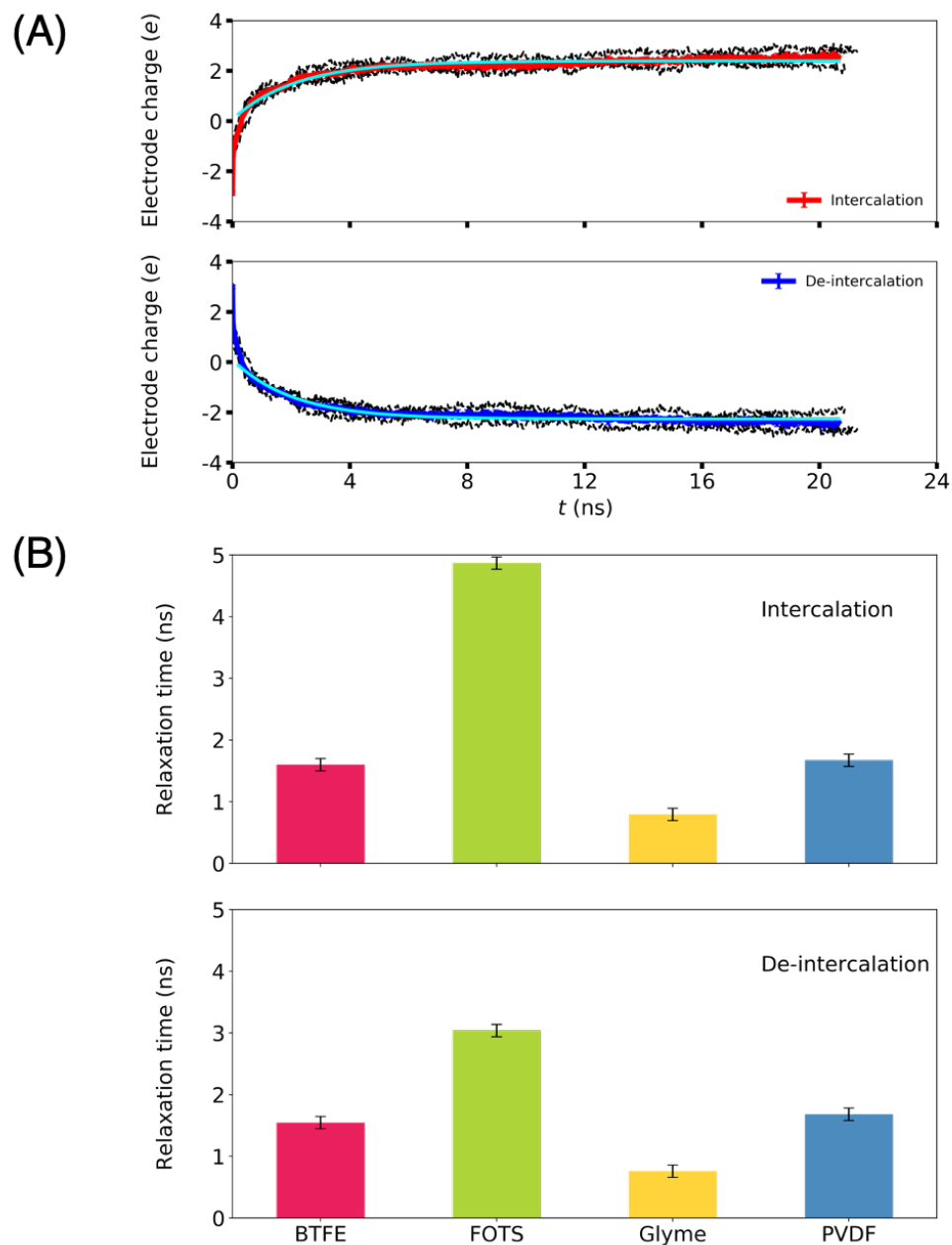


Figure 6.8: Kinetics of the electrode polarization during  $F^-$  SAM (de-)intercalation. (a) Time-dependent charge polarization of each electrode during  $F^-$  SAM (de-)intercalation in Fig. 6.6. (b) Relaxation time (Eq. 6.7) of the electrode polarization for  $F^-$  SAM intercalation (top) and de-intercalation (bottom) in various SAM layers.

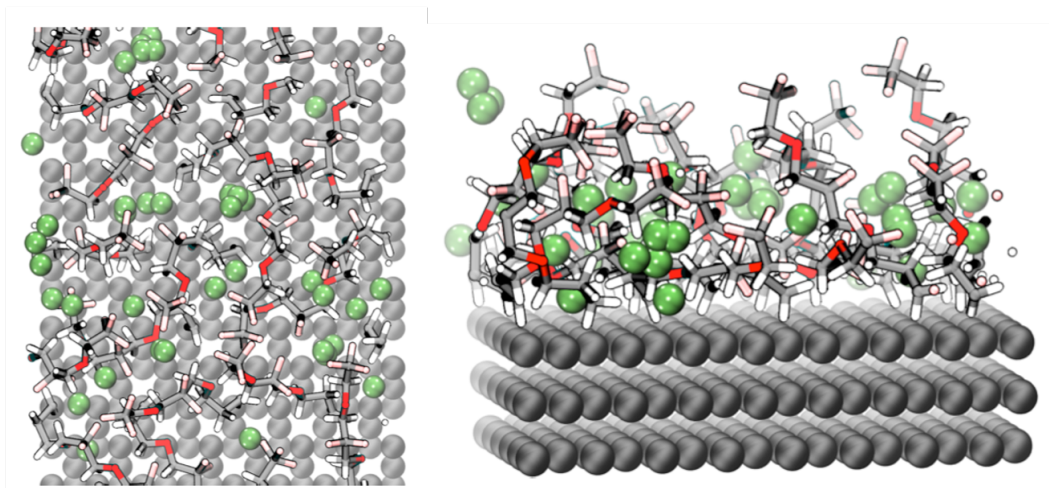


Figure 6.9: Fluoride-ion solvation sites in a BTFE-like SAM layer on a metal electrode.

### Mixture effect on fluoride-ion transport

Data and content in this section have been published as Ref. [37]. The author participated in conducting simulations, discussing the results of ion solvation and transport in mixtures, and preparing a draft.

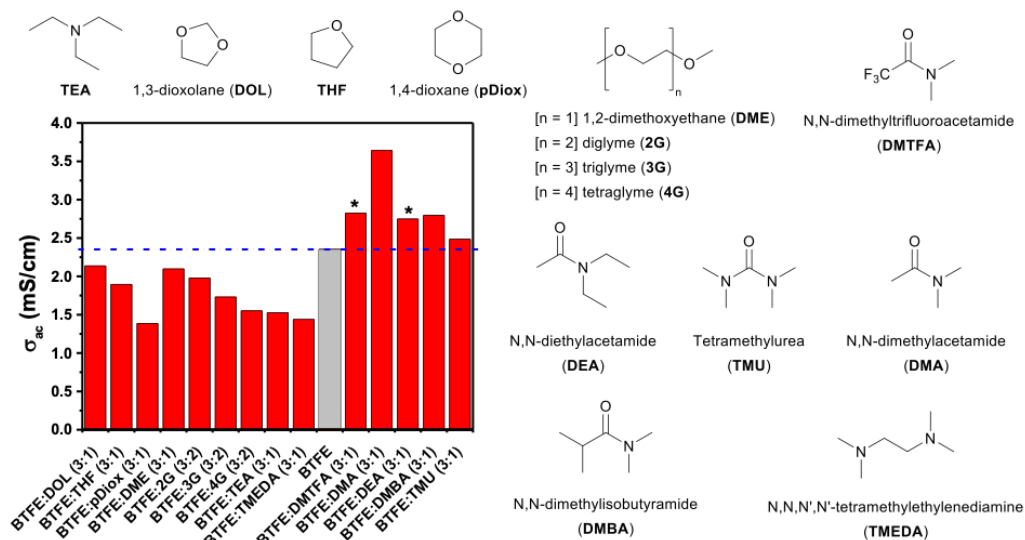


Figure 6.10: Experimental results for ionic conductivity of  $\text{Np}_1\text{F}$  (0.75 M) in BTFE:co-solvent mixtures. Asterisks indicate that a color change was observed during the experiment, suggesting reaction of  $\text{F}^-$  with the co-solvent.

In this Appendix, we discuss the  $\text{F}^-$  conductivity in co-solvent mixtures with  $\text{Np}_1\text{F}$ /BTFE [37]. Experiments (Fig. 6.10) show all the ethers and amines stud-

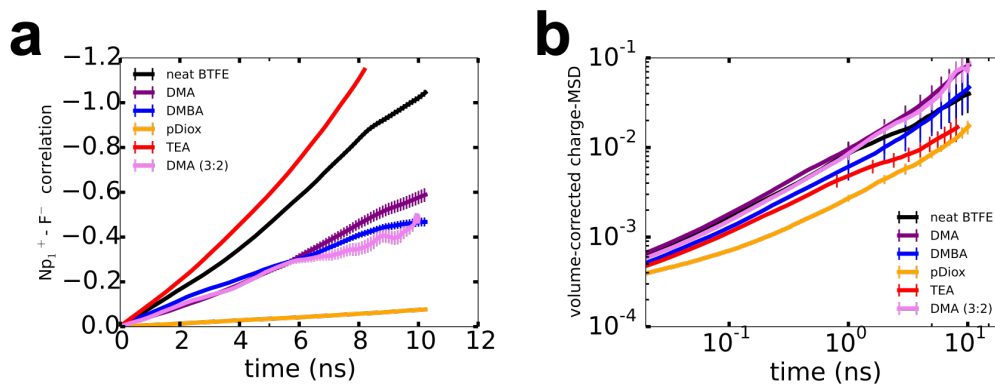


Figure 6.11: Ion transport in BTFE:co-solvent mixtures. (a) Correlation in displacement between  $Np_1^+$  and  $F^-$ ,  $z_i z_j \langle [r_i(t) - r_i(0)][r_j(t) - r_j(0)] \rangle / V$ , where  $i$  indicates  $Np_1^+$ ,  $j$  indicates  $F^-$ , and  $V$  is the volume of simulation box. (b) Volume-corrected charge MSD on a log-log scale, the slope of which indicates calculated ion conductivity.

Electrolyte <sup>e</sup>	$D_F$	$D_{Np}$	$D_{BTFE}$	$D_{Cosol}$	$\alpha^a$	$X^b$	$Y^c$	$Z^d$
Pure BTFE	11 (1)	13 (2)	63 (3)	-	0.0022 (9)	2.64 (8)	-	2.45 (8)
BTFE:DMA	9 (2)	9 (3)	44 (3)	51 (4)	0.082 (5)	2.17 (5)	0.50 (2)	2.53 (6)
BTFE:DMBA	10 (2)	11 (2)	50 (3)	49 (7)	0.02 (3)	2.4 (2)	0.18 (2)	2.3 (2)
BTFE:TEA	12 (2)	13 (3)	63 (6)	85 (7)	0.002 (3)	1.93 (5)	0.026 (7)	3.13 (7)

<sup>a</sup>Degree of ion dissociation, determined from computational calculations. <sup>b</sup>Number of BTFE molecules in the  $F^-$  solvation sheath. <sup>c</sup>Number of co-solvent molecules in the  $F^-$  solvation sheath. <sup>d</sup>Number of  $Np_1^+$  ions in the  $F^-$  solvation sheath. <sup>e</sup>The molar ratio of BTFE to co-solvent in the mixture is 3.

Table 6.3: Diffusion constants ( $\text{\AA}^2/\text{ns}$ ), ion dissociation, and  $F^-$  solvation sheath composition,  $(BTFE)_X-(\text{co-solvent})_Y-(Np_1^+)_Z$ , in 0.75 M  $Np_1F$  electrolytes determined from all-atom simulations. Statistical errors of the final digit are indicated in parentheses.

ied here universally-decreased ionic conductivity compared to that of pure BTFE. In contrast, amides served to increase the measured values. In certain cases (DMTFA and DEA),  $\tilde{F}^-$  was found to react with the co-solvent during the experiment, although DMA, DMBA, and TMU-containing mixtures were chemically stable and exhibited improved ionic conductivity.

Computational investigation (See Calculation Method below) into ion–ion and ion–solvent interactions was carried out for selected 0.75 M  $\text{Np}_1\text{F}$  BTFE:co-solvent electrolyte mixtures. Analysis of the simulation results provides insight into the diffusive dynamics and  $\tilde{F}^-$  solvation environment of the mixtures (Table 6.3).

The experimentally-observed trends (Fig. 6.10) in conductivity likely emerge from a competition between the effects of changing viscosity and changing ion-pairing via the co-solvent. In the calculations, although extensive ion-pairing is predicted to occur, the viscosity effect is found to be dominant for determining trends in conductivity; some disagreement between the calculated and experimental trends in conductivity suggests that accurately balancing the effects of viscosity and ion-pairing in the simulations requires the use of potential energy functions that are more accurate than the simple point-charge potentials employed here [44, 157, 49].

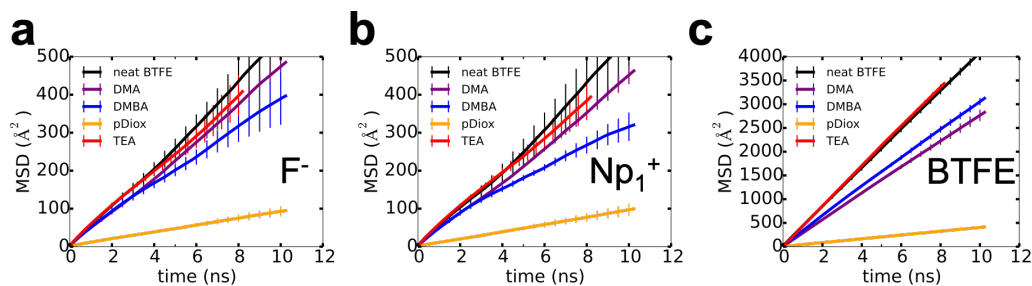


Figure 6.12: Mean-square displacement of (a)  $\text{F}^-$ , (b)  $\text{Np}_1^+$ , and (c) BTFE in a mixture with a co-solvent or neat BTFE solution.

We begin with an analysis of fluoride-ion solvation sheath, composed of BTFE molecules, co-solvent molecules, and  $\text{Np}_1^+$  ions. Table 6.3 reports the composition of the fluoride-ion solvation sheath in terms of the number of BTFE molecules ( $X$ ), co-solvent molecules ( $Y$ ), and  $\text{Np}_1^+$  ions ( $Z$ ) surrounding one fluoride ion in a 0.75 M  $\text{Np}_1\text{F}$ /BTFE:co-solvent (3:1) electrolyte mixture. Molecules or ions are counted as part of the solvation sheath if they provide at least two hydrogens within  $3 \text{ \AA}$  of a single fluoride ion, according to the first peak of radial distribution functions. The fraction of fluoride ions without  $\text{Np}_1^+$  ions in the solvation sheath to fluoride ions

with  $\text{Np}_1^+$  ions in the solvation sheath is also reported in Table 6.3. This fraction is representative of the degree of ion dissociation,  $\alpha$ . Results show that all co-solvent molecules barely participate in solvation of  $\text{F}^-$ , as reflected by experimental observations; that is, the pure co-solvents are not able to dissolve the  $\text{Np}_1\text{F}$  salt in the absence of BTFE. Similar numbers of  $\text{Np}_1^+$  ions and BTFE molecules in the  $\text{F}^-$  solvation sheath indicate that all of these mixtures exhibit substantial ion-pairing and aggregation, consistent with prior results from diffusion-ordered NMR spectroscopy [38]. Our simulation results further show that “good” amide co-solvents participate more in the solvation sheath than TEA (a representative “poor” co-solvent), but still remain the minority solvent molecule. Despite this, DMA and DMBA co-solvents improve ion dissociation by an order of magnitude compared to 100% BTFE electrolyte. Fig. 6.11a presents the correlation in dynamics of  $\text{Np}_1^+$  and  $\text{F}^-$  diffusion. Results support the role of ion pairing on the decreased conductivity of the mixture, as indicated by the strong correlation in the counterion diffusion. Except p-Diox co-solvent, addition of a co-solvent leads to the enhanced correlation in ion diffusion, with the mixture involving TEA co-solvent exhibiting the strongest effect. In BTFE:TEA, ions are mostly present in the form of ion pairs or ion aggregates with a negligible number of free ions ( $\alpha = 0.002$ ). Hence, we hypothesize that DMA and DMBA partition between  $\text{Np}_1^+$  cations and  $\text{F}^-$  anions, creating better ionic separation, reducing ion-pairing and facilitating improved ionic conductivity.

We now explore the effect of solution viscosity on the mixture conductivities. Mean-squared displacement (MSD) was calculated as a function of time for  $\text{F}^-$  anions,  $\text{Np}_1^+$  cations, and BTFE molecules (Fig. 6.12), and used to obtain the diffusion coefficient. We used the inverse of the calculated BTFE diffusion coefficient as measure of viscosity of the mixture, via the Stokes-Einstein relation [67]. For most of the mixtures investigated, the BTFE diffusion coefficient varies in a similar manner to the individual ions; the diffusion coefficient of BTFE decreases when there is co-solvent present in the electrolyte solution, suggesting that the electrolyte solutions become more viscous in the presence of a co-solvent (Fig. 6.12c). The exception is for the TEA-containing mixture, which exhibits particularly high ion pairing ( $Z = 3.13$ ). Fig. 6.11b shows that the simulated conductivities of all mixtures are suppressed by the presence of a co-solvent. The trends in simulation-calculated conductivities more closely reflect those of the solution viscosity than either the single-ion diffusion coefficients or the degree of ion-pairing, suggesting that this is the dominant effect in the calculations. Thus, we conclude that the experimentally-observed trends reflect a delicate balance between the factors of co-solvent-induced

changes in viscosity and ion pairing.

**Calculation Method.** All-atom molecular dynamics simulations were performed to provide an understanding of the mixture effect on conductivity, with co-solvents including DMA, DMBA, pDiox, and TEA. Following the experiments,  $\text{Np}_1\text{F}$  salt concentration is fixed at 0.75 M, and the volume ratio of BTFE solvent to co-solvent is 3:1 for all simulated mixtures.

The OPLS force field [79, 80, 41] was used to describe the potential energy functions of all molecules including BTFE, co-solvents, and  $\text{Np}_1\text{F}$  salt. Details of the OPLS force field are given in Section 6.3. All simulations were conducted using the LAMMPS simulation package [140].

In all cases during both equilibration and production runs, the MD trajectories were integrated using the velocity-Verlet methods with a timestep of 1 fs. Both LJ and Coulomb interactions were cut at 14 Å, and particle-particle particle-mesh Ewald summation [72] was used to compute Coulomb interactions beyond the cutoff distance. Periodic boundary conditions were applied along all directions. The Nosé-Hoover thermostat (100 fs relaxation) and the Nosé-Hoover barostat (1000 fs relaxation) were applied in all simulations to control the temperature (300 K) and the pressure (1 atm). All the quantities reported here were averaged using simulation trajectories over 10 ns after equilibration at least during 5 ns.

Volume-corrected charge mean-squared displacement,  $\text{vc-cMSD}(t)$ , is calculated via the Einstein relation [50, 67] as follows:

$$\text{vc-cMSD}(t) = \frac{1}{V} \sum_{i=1}^N \sum_{j=1}^N z_i z_j [r_i(t) - r_i(0)][r_j(t) - r_j(0)], \quad (6.8)$$

where  $N$  is the total number of ions,  $z_i$  is charge of  $i^{\text{th}}$  ion,  $\vec{r}_i(t)$  is the position of  $i^{\text{th}}$  ion at time  $t$ ,  $V$  is the volume of a mixture, and  $\langle \dots \rangle$  represents the ensemble average. This  $\text{vc-cMSD}$  is a collective property that takes all correlations into account, whose slope with respect to time is the conductivity. When all correlations (off-diagonal terms) are negligible, it becomes the same as the Nernst-Einstein equation.

The ion self-diffusion constants ( $D$ ) were estimated using the slope between two points of mean-squared displacement (MSD) at  $t_1 = 0.1$  ns and  $t_2 = 0.2$  ns:

$$D = \frac{1}{6} \frac{\text{MSD}(t_2) - \text{MSD}(t_1)}{t_2 - t_1}. \quad (6.9)$$

Note that in the simulated time window (nanosecond scale), MSD is not linear with time but subdiffusive, i.e.,  $\text{MSD} \sim t^b$  with an exponent  $b \approx 0.8$ , which means that  $D$

is time dependent at a subdiffusive regime. Use of larger values of time for  $t_1$  and  $t_2$  did not qualitatively change these findings.

PART II. ENERGY TRANSDUCTION OF WATER KINETIC  
ENERGY TO ELECTRICITY USING METAL NANOLAYERS

## GENERATING ELECTRICITY USING METAL NANOLAYERS FROM A FLOW OF ALTERNATING SALINITY GRADIENTS

### 7.1 Abstract

In this chapter, we discuss kinetic:electrical energy transduction using metal nanolayers formed in a single step from earth-abundant elements. The metal nanolayers are found to induce electrical current with a linear flow of salinity gradients in addition to flowing aqueous droplets across the nanolayers or with an oscillatory flow of a constant salinity. Other so-called “hydrovoltaic” transducers, such as graphene and silicon-based semiconducting devices that convert energy from water flow to electricity, suggested that the energy conversion mechanism of the (pseudo)capacitive current primarily relies on ion adsorption and desorption at water-solid interfaces, requiring the boundaries of electrical double layers at such interfaces.

As efficient as other hydrovoltaic transducers, our heterostructured metal nanolayers suggest additional design rules, including electron transfer within their thermal oxide nano-overlayer terminating the metal and a proper nanoconfinement for electron transfer within the metal below. Herein, we present simulation approaches to rationalize the design rules by providing molecular understanding, constructing connections between microscopic variables to device-level observables.

Data and content in this chapter have been published as Ref. [15]. The author participated in conducting simulations, discussing the results, and preparing a draft.

### 7.2 Introduction

Current approaches of so-called "hydrovoltaic" technologies for kinetic/gravitational energy to electrical energy conversion have used conducting or semiconducting layered materials in contact with moving aqueous droplets or brushes [213]. The successful approaches, based on carbon nanotubes [55], graphene [205, 174, 176, 202], oxides [95, 78], and dielectric-semiconductor architectures [128, 130], are promising as they show efficiencies of around 30 percent. However, they pose challenges regarding fabrication and scaling. Metal nanolayers are found to convert water kinetic energy to electrical power, fabricated by physical vapor deposition of an inexpensive metal (Fe, Ni, Al, Cr) onto solid or flexible substrates (glass, plastics,

polymers). 10 nm to 30 nm thin nanolayers of iron or nickel produce several tens of mV and several  $\mu\text{A cm}^{-2}$  at aqueous flow velocities of just a few  $\text{cm s}^{-1}$ , which is as efficient as other hydrovoltaic materials prepared using multistep fabrication. The nanolayers also generate electrical power in various modes of operation with moving liquids, including sliding liquid droplets, oscillatory moving liquids, and salinity gradients in a flowing liquid.

The metal nanolayers exhibit a layered structure where an oxide nano-overlayer, which forms spontaneously when the iron nanolayer is exposed to air, covers a metal underneath. For example, for iron nanolayers grazing incidence angle X-Ray diffraction experiments indicate the presence of crystalline zero-valent iron with low index faces exposed, but no crystallinity of the iron oxide overlayer [14]. The exposure of iron nanolayers in ambient air results in  $\sim 3$  nm thin oxidized iron nano-overlayer [43, 14], which remains stable over prolonged periods. Raman and XPS spectroscopy of the iron nanolayers indicate that the oxide nano-overlayer is composed of some Fe (III),  $\text{Fe}_3\text{O}_4$ , and other forms of iron oxide [43]. Further, the oxide overlayer possesses the nm-scale spatial variation that leads to the dendritic interface of the heterostructure.

The nanostructural features of metal nanolayers are directly related to the energy conversion mechanism and efficiency. The surface of an oxide overlayer provides sites for ion adsorption and desorption, whose state, such as surface potential, depends on a variety of factors such as solution pH, salt concentration, temperature, and point of zero charge of the oxide [109]. As most oxides are negatively charged in ambient conditions, one may expect the preferential adsorption of cations over anions in the solution, i.e., an electrical double layer (EDL) forms at the aqueous oxide interface. In this case, the interfacial cations electrostatically attract electrons in the metal below, as in field-effect transistors [128, 130]. We expect that this charge induction is possible since only a few nanometers thick thermal oxide enables the electrostatic potential to polarize the metal below after penetrating the oxide overlayer. The induced electrons at the heterostructure interface are transferred from one EDL boundary to the other via the potential difference generated by water motion, which is the essence of the energy conversion mechanism. Interestingly, in addition to the passivation of the metal below, we find a prominent role of the thermal oxide nano-overlayer, whose redox activity strongly affects the energy conversion performance. Experiments suggest a possible role for intra-oxide electron transfer for Fe and Ni nanolayers, as their thermal oxides contain multiple metal oxidation

states. In contrast, controls using Al or Cr nanolayers, which self-terminate with oxides that are redox inactive under the experimental conditions, exhibit dramatically diminished performance.

A metal underlayer should transfer the induced electrons by ion adsorption and desorption, enabling electrical power generation. As discussed above, there are nanoscale structural heterogeneities at the heterostructure interface [14], which could result in heterogeneities of the electrostatic potentials and thereby charge distributions in the metal below. Such heterogeneities complicate the electron transfer process and energy conversion mechanism as well. More interestingly, the energy conversion is strongly sensitive to the thickness of the metal underlayer, exhibiting an optimal thickness similar to the electron mean free path.

This chapter presents simulation approaches to rationalize the experimentally observed features in hydrovoltaic energy conversion using metal nanolayers in contact with a flow of alternating salinity gradients. We utilize molecular simulations to connect microscopic variables (e.g., spatially-varying fluctuation of induced electrons) to device-level output (e.g., the electrical current generated), so finally to propose functional energy conversion mechanisms. Further, we discuss other factors for energy conversion efficiency and scalability by using simple models.

### **7.3 Simulation Method**

Molecular dynamics simulations are performed using a polarizable model for the conductive regions of the iron nanolayer. The atoms in the nanolayer are fixed in the face-centered cubic structure with a lattice parameter of 0.392 nm and a (111) termination at the interface. The orthorhombic simulation cell is oriented such that the z coordinate is perpendicular to the nanolayer surface, and the x coordinate coincides with the direction of the gate motion, and the simulation cell is periodically replicated only in the x and y coordinates. In all simulations, the length of the simulation cell in the x and y coordinates is 4.979 nm and 4.791 nm, respectively, such that the nanolayer is described using seven layers of atoms, with each layer containing 360 atoms (for a total of 2520 nanolayer atoms). Atoms in the nanolayer are modeled as being either oxide-like (i.e., non-polarizable) or metallic (i.e., perfectly conductive). In all simulations, the top layer of atoms in the nanolayer is assumed to be oxide-like, and the arrangement of oxide-like atoms below the nanolayer surface is varied to model the subsurface heterostructure, as described.

Interactions between atoms in the nanolayer and other atoms in the simulation cell are described using both electrostatic and Lennard-Jones (LJ) interactions. Oxide-like atoms in the nanolayer are uncharged, while the charges of the metallic atoms of the nanolayer are allowed to fluctuate in response to charges in the solution. The metallic portion of the nanolayer is modeled as one of two fixed-potential electrodes with zero potential bias, with the fluctuating charge distribution in the metallic portion of the nanolayer described in terms of a sum of atom-centered spherical Gaussian functions,

$$Q_i(r, t) = A_i(t) \left( \frac{\eta^2}{\pi} \right)^{3/2} \exp(-\eta^2 (r - R_i)^2) \quad (7.1)$$

of width  $\eta=19.79 \text{ nm}^{-1}$  and amplitude  $A_i(t)$  that is determined using an extended Lagrangian method [167, 148]. Although all calculations involving the iron nanolayer focus on a single solid/liquid interface, the fixed-potential electrode simulation model requires that two electrodes be included in the simulation cell; the second polarizable electrode was simply placed a large distance from the interface of interest, separated by  $\sim 10 \text{ nm}$  of vacuum in the  $z$  coordinate. All simulations are performed using the LAMMPS software package [140].

For liquid/nanolayer interfaces, simulations of aqueous solutions in contact with the nanolayer were performed using SPC/E water [12] and NaCl ions [168]. LJ parameters for the  $\text{Na}^+$ ,  $\text{Cl}^-$ , and nanolayer atoms are provided in Table 7.1. The cross terms are obtained using Lorentz-Berthelot mixing rule. The LJ interactions and the real-space part of the Coulomb interactions are truncated at  $0.98 \text{ nm}$ ; the long-range contribution of Coulomb interaction is treated by the particle-particle particle-mesh method [72].

	$\sigma$ (nm)	$\epsilon$ (kcal/mol)
$\text{Na}^+$	0.235	0.13
$\text{Cl}^-$	0.44	0.1
O (SPC/E water)	0.3166	0.1554
Nanolayer atom [69]	0.2534	0.078

Table 7.1: Lennard-Jones parameters for water, ions, and nanolayer atom.

To enforce the regions of alternating salinity in the solution (Fig. 7.2), semipermeable boundaries are introduced to interact only with the NaCl ions; the boundaries are positioned at  $x = 1.25 \text{ nm}$  and  $x = -1.25 \text{ nm}$  in the simulation cell, and they interact only with the salt ions via a truncated LJ potential with  $\epsilon=10 \text{ kcal/mol}$  and

$\sigma = \text{cutoff} = 0.1$  nm. Simulations of the solution/nanolayer were initialized with a slab of water/ions in contact with the nanolayer; after a short period of equilibration, the outermost layer (furthest from the nanolayer) was frozen in space to provide a fixed, amorphous boundary between the solution region and the vacuum of the remaining simulation cell. Finally, the distance between this fixed layer of water molecules and the position of the nanolayer was adjusted so that the pressure of the confined solution was 1 atm, and it was confirmed that the osmotic pressure introduced by the semipermeable boundaries did not significantly alter the density of water in the ionized vs. deionized solution regions. The final thickness of water along the confinement is  $\sim 3$  nm.

The classical molecular dynamics equations of motion were evolved using the velocity Verlet integrator with a timestep of 2 fs; rigid-body constraints for the water molecules were enforced using the SHAKE algorithm [155]. The simulations were performed at a temperature of 298.15 K, enforced via the Nose-Hoover thermostat with a damping timescale of 100 timesteps.

#### **7.4 Design Rules Found in Experiments**

Metal nanolayers of different metals were tested for energy conversion with a flow of alternating salinity, including Fe:FeOx nanolayers having 5, 10, 20, and 50 nm thickness, which differ in their transparency (Fig. 7.1a), as well as 5 and 20 nm thin Al:AlOx and 10 nm Cr:CrOx, V:VOx, and Ni:NiOx nanolayers. All the nanolayers were deposited onto  $3 \times 1$  in<sup>2</sup> as well as  $3 \times 9$  in<sup>2</sup> glass microscope slides. Details of the fabrication method and experimental setup are given in Ref. [15]. Fig. 7.1b clearly shows that a 10 nm thin Fe:FeOx nanolayer in the small cell induces currents of  $\sim 0.2$  A, as well as voltages in the mV range, when flowing water of alternating salinity (flowing deionized water at pH 5.8 for 20 sec, followed by a 20-sec flow of 1 M NaCl held at pH 7) at  $20 \text{ mL min}^{-1}$  across the nanolayer. The preferential adsorption of Na<sup>+</sup> rationalizes the positive current at the aqueous interface of the Fe:FeOx nanolayer, which is consistent with second harmonic generation measurements [43, 125] of the iron nanolayer that indicates a negative interfacial charge density of  $-0.007(3) \text{ C m}^{-2}$  at pH 7. Notably, the current exhibits the peak-like shape, as opposed to a constant current generated from a moving water droplet using graphene devices [205, 202], which is discussed using computation in a later section.

A series of experiments were carried out to gain a mechanistic understanding of

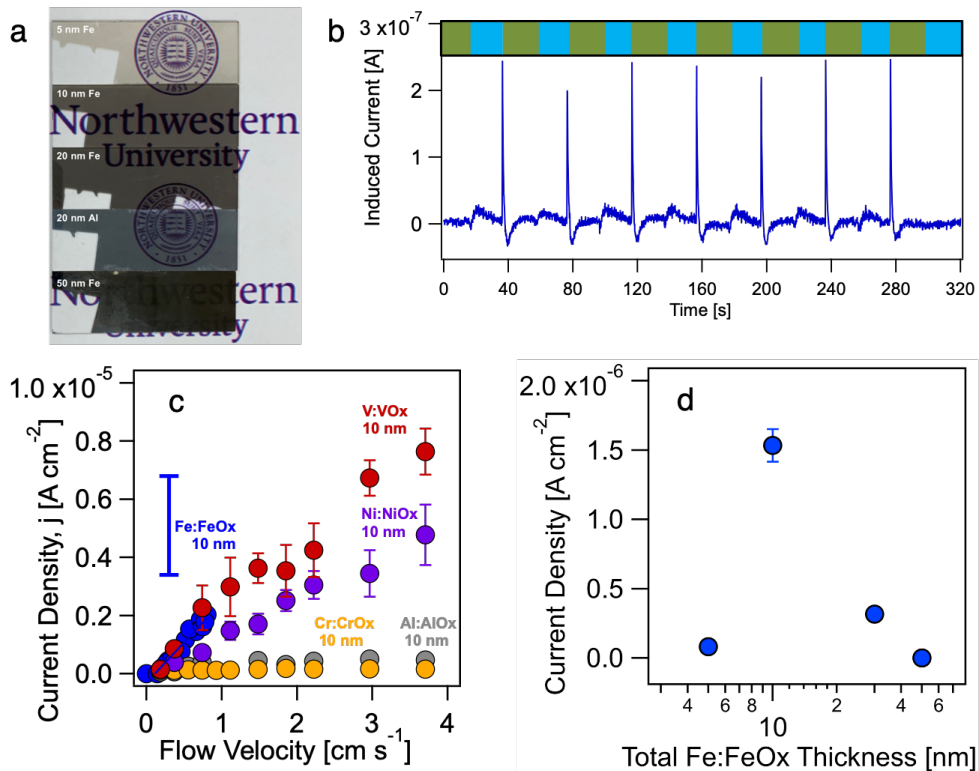


Figure 7.1: Experimental results of energy conversion using metal nanolayers with a flow of alternating salinity. (a) Photographs of iron and aluminum nanolayers with indicated thicknesses on microscope glass slides over the Northwestern University seal. (b) Current induced in a 10 nm Fe:FeOx nanolayer ( $3 \times 1 \text{ in}^2$ ) when flowing deionized (DI) water at pH 5.8 for 20 sec (blue segment), followed by 20 sec flow of 1 M NaCl held at pH 7 (green segment), and six subsequent replicates, all at a constant flow rate of  $20 \text{ mL min}^{-1}$ . (c) Average current densities measured as a function of aqueous flow velocity using 10 nm thin nanolayers of Fe:FeOx (blue-filled circles), Ni:NiOx (purple-filled circles), V:VOx (red-filled circles), Al:AlOx (grey-filled circles), and Cr:CrOx (orange-filled circles) while alternating deionized water (pH=5.8) and 0.6 M NaCl solution (pH~7) segments every 20 sec, and current density obtained for  $30 \mu\text{L}$  drops falling with a  $0.1$  to  $0.2 \text{ cm}^2$  contact area onto a 10 nm thick Fe:FeOx nanolayer deposited onto a  $1 \times 3 \text{ in}^2$  glass substrate while alternating the drop salinity between deionized water and 0.6 M at a drop rate of  $2 \text{ mL min}^{-1}$  and an incident angle of  $160^\circ$  (vertical blue bar). Error bars on point estimates shown are for 1 standard deviation from 7 or 8 replicate measurements per flow rate. (d) Current density recorded for Fe:FeOx nanolayers varying in total thickness obtained with a flow velocity of  $0.74 \text{ cm s}^{-1}$  while alternating deionized water and 0.6 M NaCl solution segments every 20 sec.

the current generation. Fig. 7.1c clearly shows two groups of the metal nanolayers as follows. In one group, Fe:FeOx, Ni:NiOx, and V:VOx nanolayers of 10 nm

thickness produce currents that increase linearly with increasing flow rate at a rate of  $\sim 1$  to  $\sim 3 \mu\text{A cm}^{-2}$  per  $\text{cm s}^{-1}$  increase in flow rate. The produced currents are also comparable to what has been reported previously [205, 128]. In the other group, 10 nm thin metal nanolayers prepared from Cr and Al produce considerably less current than 10 nm thin nanolayers prepared from Fe, Ni, or V at comparable flow conditions. The observation rationalizes these results that the iron, vanadium, and nickel nanolayers are terminated by thermal oxides that contain Fe(II) and Fe(III), V(IV) and V(V), and Ni(II) and Ni(III), respectively, whereas the aluminum and chromium metal nanolayers are terminated by thermal oxides that only contain metal in the +3 oxidation state. This effect of redox-activity of the oxide-overlayer provides evidence that intra-oxide electron transfer [203] between  $\text{M}^{m+}$  and  $\text{M}^{n+}$  contributes to the current generation to a larger extent than would be expected from induced electrons transferred in a metal underlayer.

Further, Fig. 7.1d shows that a 10 nm thin Fe:FeOx structure produces the highest currents when compared to thinner (5 nm) or thicker (30 nm and 50 nm) layers, clearly suggesting that the effect of the nanolayer's thickness on the electricity generation. The thickness effect is expected to be originated from the metal underlayer since the thickness of the thermal oxide overlayer is more or less the same with a varying total thickness of a nanolayer. The volcano-type thickness effect suggests that film thickness on the order of the mean free path of the electron [51] enhances current generation, offering a nanoconfinement for the electron current flow in a metal underlayer. The conclusion is based on the observation that a Fe:FeOx nanolayer without a metal underlayer produces negligible current.

In summary, experiments suggest the following design rules for the nanofilms: (i) there is an optimal thickness for the nanofilms, comparable to electron mean-free path, and (ii) the metal oxide needs to be redox-active, containing several metal-oxidation states. We provide the rationales for the experimentally observed mechanistic insights by using molecular simulations and modeling.

## 7.5 Computational Results and Discussion

### Charge induction and effect of subsurface dendrite

We begin by discussing the charge induction mechanism of the metal nanolayers using a model nanolayer with a columnar subsurface dendrite (Fig. 7.6).

To probe the charge fluctuations in the metal:metal oxide (M:MOx) nanolayer in the presence of moving ions, calculations were performed using an all-atom molecular

dynamics model for the solvent, ions, and a M:MO<sub>x</sub> nanolayer, including charge-polarization of the nanolayer and image-charge interactions between the nanolayer and the solution. The M:MO<sub>x</sub> nanolayer is modeled after the APT reconstruction of the Fe:FeO<sub>x</sub> nanolayer (Fig. 7.2) as a polarizable metal conductor (Fig. 7.2b, grey) with a non-polarizable oxide heterostructure (pink). The subsurface metal/oxide heterostructure is modeled in a simple columnar geometry with a range of values for the width,  $d$ . For a given width of the oxide heterostructure ( $d = 1.3$  nm), Fig. 7.2c illustrates the distribution of induced charge in the nanolayer for several positions of a sodium cation. Substantial polarization of the metal for ion positions away from the nonpolarizable heterostructure is reduced when the cation is positioned above the heterostructure (Fig. 7.2c and Fig. 7.6 in Appendix). This position-dependence of the induced charge manifests in the Coulomb interaction between the ion and the nanolayer (Fig. 7.2d), leading to a heterostructure-dependent interaction potential between the M:MO<sub>x</sub> nanolayer and the ion, with a potential energy barrier appearing in the region of the nonpolarizable heterostructure.

To examine these nanolayer polarization effects in the presence of a solution with alternating salinity, Fig. 7.2e shows a snapshot of all-atom MD simulations, with vertical lines indicating semipermeable boundaries for the solvated ions and with the instantaneous induced charge fluctuations on the electrode shown in red-blue scale. Fig. 7.2f shows the time-averaged (black) charge induced charge distribution for the shown simulation cell, as well as 0.5 ns block-averages of the distribution (other colors). Two features are immediately clear: (i) the induced charge distributions in the metal/oxide nanolayer undergo dramatic fluctuations with changes of the ion and water configuration, which reflect changes in the transient electrostatic interactions between the nanolayer and the solvated ions, and (ii) these induced charges are massively damped out in the vicinity of the nonpolarizable heterostructure, i.e. the oxide nano-overlayer. Fig. 7.2g shows that the effect of the heterostructure on the average induced charge is much smaller than its effect on the fluctuations.

The simulations in Fig. 7.2f-g reveal that the nonpolarizable heterostructure model of the metal oxide nano-overlayer creates spatial variation in the local induced charge fluctuations in the metal nanolayer below. This variation is proportional to the local interfacial capacitance [100, 101]. Given that this interfacial capacitance has been proposed as the primary quantity that connects droplet motion to induced current in the low-bandgap semi-conducting structures studied earlier [128], the simulations provide a direct connection between the morphology of the oxide heterostructure

and the gate-induced current presented here. However, the mechanism for electrical current generation in the all-inorganic devices described here involves the additional steps of intra-oxide electron transfer as well as electron transfer between the oxide nano-overlayer and the metal nanolayer below via a surpassable Schottky barrier.

### **Current generation mechanisms and corresponding equivalent circuit**

In this section, we discuss the details of the current-generating mechanisms and an associated equivalent circuit. The linear increase in the current output with the flow rate suggested that a dynamic charging-discharging mechanism, proposed in previous devices made of low-dimensional materials [205, 128], applies to our metal nanolayers. The mechanism primarily relies on ion adsorption and desorption at an electrical double layer (EDL) boundary along with an aqueous flow.

Consider an ionic water droplet of width  $W$  and length  $L$  on top of the energy transducer; the current is generated once the droplet is moving, while there is no current generation without the movement of the water droplet. At the interface, an EDL builds up with the preferential ion adsorption (for example,  $\text{Na}^+$  preferentially adsorbs on an aqueous graphene interface over  $\text{Cl}^-$ ). The adsorbed ions electrostatically attract electrons in the energy transducer to the interface. In this model, a parallel-plate capacitor is considered, whose length is determined by the length ( $L$ ) of the droplet; one of its plates is charged by the interfacial ions, and the electrons charge the other plate. Two material-dependent parameters characterize the capacitor: the potential drop ( $\psi_0$ ) and the areal capacitance ( $C_0$ ). In this example, the EDL boundaries are an air-water interface at which the capacitor is terminated. The EDL boundaries are the only region where the ions adsorb and desorb along with the moving droplet; the front capacitor is charged with the newly adsorbed ions, while the rear capacitor is discharged with the newly desorbed ions. Then, the equal amount of the electrons to the ions accumulate and dissipate with the ion adsorption and desorption, which flow in the energy transducer from the rear to the front capacitor. Note that in this case, the capacitance changes in the charge-discharge processes depend only on the physical dimension of the capacitors, not on the material-dependent parameters. Thus, the amount of the generated (pseudo)capacitive current ( $I_i$ ) is as follows:

$$I_i = -\frac{dQ_F}{dt} = -\psi_0 \frac{dC_F}{dt} = -\psi_0 C_0 \frac{d(L \cdot W)}{dt} = -\psi_0 C_0 W \frac{dL}{dt} = -\psi_0 C_0 W v_{\text{flow}}, \quad (7.2)$$

where  $Q_F$  is the amount of electrons newly accumulated at the front capacitor, and  $C_F$  the capacitance of the front capacitor. The first equality is the definition of

the current and the second equality is the definition of the capacitance. Here, the negative sign represents that the current flow the opposite direction to the electrons. Thus, this simple model, a dynamic capacitor model, predicts the linear dependence of the  $I$  on the flow velocity ( $v_{\text{flow}}$ ) as in our experiments.

The flow of alternating salinity gradients on our metal nanolayers also forms two EDL boundaries at both salinity boundaries (Fig. 7.3A). Thus, the amount of the generated current depends on the difference in the capacitance of high and low salinity regions:

$$I_i = -\left[\psi_{0,H}C_{0,H} - \psi_{0,L}C_{0,L}\right]Wv_{\text{flow}}, \quad (7.3)$$

where subscripts ( $H$  and  $L$ ) represent the high and low salinity region, respectively. We note that  $I_i$  estimated by Eq. 7.2 or Eq. 7.3 is solely determined by ion dynamics along with the water motion; that is why we put subscript  $i$ . Further,  $I_i$  is the maximum current that we can generate in this energy conversion. On the other hand, the short-circuit current ( $I_{SC}$ ) with zero external current connected to the transducer depends not only on  $I_i$  but also on the physical dimension of the size of salinity blob (or the droplet) and of the energy transducer.

The mechanism we discussed above is summarized in the equivalent circuit (Fig. 7.3B). The flow of salinity gradient charges and discharges the capacitors at both ends at the same rate. The charge-discharge processes effectively transfer the interfacial ions and electrons via the ionic solution and the metal nanolayer, respectively, from the rear to the front capacitor, generating the (pseudo)capacitive current. The resistance of the ionic water and the nanolayer is  $R_W$  and  $R_N$ . Again, the direction of the current is opposite to that of electrons (the dotted arrow in Fig. 7.3B). According to the equivalent circuit, the open-circuit voltage with infinite external resistance is:

$$V_{OC} = R_N I_i = R_N \left[\psi_{0,H}C_{0,H} - \psi_{0,L}C_{0,L}\right]Wv_{\text{flow}}. \quad (7.4)$$

Here, it is assumed that  $R_N = R_{N,H} + R_{N,L}$ , so  $R_N$  is the resistance of the metal nanolayer.

### Two competing scenarios to the design rules for the metal nanolayers

In this section, we propose two competing functional scenarios to rationalize the design rules found in section 7.4: (i) pseudo-2D & redox-activity model, and (ii) "sweet spot" resistance model. We note that we need more control experiments to tell which scenario works better in the energy conversion using metal nanolayers.

The first design rule requires a proper confinement effect on electron transport or charge induction process. The pseudo two-dimension of our metal nanolayers decreases backpropagation with less scattering than bulk nanolayers. Thus, the electron transport in the (pseudo)two-dimensional nanolayers is likely more directional, i.e., less resistant [51]. Nevertheless, too strong confinement significantly increases the surface contribution of the electron scattering, leaving only a few nm thin metal underlayer to conduct electrons in response to the ion adsorption and desorption. In the case of 5 nm thin nanolayers, the conducting metal underlayer is only 1-2 nm according to the atom probe tomography (APT) [43]. That explains the turnover behavior in the generated  $I_{SC}$  or  $V_{OC}$  as a function of the nanolayer thickness. Further, carbon composite materials [129] were reported that only a limited range of resistance is in the Ohm regime that is assumed in the capacitor model (Eq. 7.4). The second design rule suggests that the redox activity of the oxide overlayer substantially enhances the capacitance. That comes from the contribution of mobile charges in the oxide in addition to the dielectric contribution [120, 96]. Therefore, we suggest a scenario, called a pseudo-2D & redox-activity model, combining both effects.

The second model only considers the resistance of the metal nanolayers that depends on both their thickness and redox activity; electrical resistance needs to be neither too high nor too low. It was found that bulk metal [205, 95] cannot generate electricity from water kinetic energy. That is because bulk metal exhibits too low electrical resistance; the potential difference across the bulk metal is decreased with decreasing resistance (Eq. 7.4). Further, redox activity plays a role in determining the resistance. In particular, our metal nanolayers exhibit a dendritic subsurface structure that significantly affects the electrical resistance; redox-active oxides with intra-oxide electron transfer [203, 121] are less resistant than redox inactive ones.

### **Other factors that determine energy conversion efficiency**

This section discusses other factors for the energy conversion efficiency of the metal nanolayers with the flow of salinity gradients, including frequency of salinity alternation and turbulent mixing.

### **Scalability in energy conversion with tunable frequency of salinity alternation**

To simplify the discussion, consider a droplet of an ionic solution, whose length is  $l$  and width is  $W = 1$  inch, on top of the metal nanolayer of same width  $L$  but different

length  $L = 3$  inch (Fig. 7.4A). The oxide overlayer is negatively charged, and its binding site density ( $\Gamma = 4 - 20 \text{ nm}^{-2}$ ) depends on pK, pH, and salt concentration [109]. The negatively charged oxide interface allows for the preferential adsorption of cations (e.g.,  $\text{Na}^+$ ). A hypothetical maximum ion adsorption density is  $\Delta Q_{ion}^{max} = e\Gamma_{ion}^{max} = e\Gamma$  and its minimum is  $\Delta Q_{ion}^{min} = e\Gamma_{ion}^{min} = 0$ . We note that this estimation does not consider electrostatic and steric repulsion between interfacial ions. Then, according to the Eq. 7.2, the maximum current generated by ion dynamics in the droplet with the velocity ( $v_d$ ) is  $I_i^{max} = W \cdot \Delta Q_{ion}^{max} \cdot v_d$ , which implies that the current generated is linearly proportional to  $\Gamma$ , one of the material parameters of the oxide overlayer. Then, the maximum electrical outputs are as follows:

$$I_{SC}^{max} = \frac{l}{L} \cdot I_i^{max} = \frac{l}{L} W \cdot \Delta Q_{ion}^{max} \cdot v_d, \quad (7.5)$$

and

$$V_{OC}^{max} = R_N \cdot I_{SC}^{max} = l \cdot R_s \cdot \Delta Q_{ion}^{max} \cdot v_d, \quad (7.6)$$

where  $R_N$  and  $R_s$  is the resistance and the square resistance of the nanolayer, respectively.

Firstly, consider the case of multiple droplets of the same size (Fig. 7.4A). Multiple droplets increase the total volume of the droplet so the contact area. The increased number of pairs of the EDL boundaries along the flow direction linearly increases both the  $I_i$  and the  $I_{SC}$  with the number of the droplets ( $n$ ):

$$I_{SC}^{max} = \frac{nl}{L} \cdot I_i^{max} = \frac{l}{L} W \cdot \Delta Q_{ion}^{max} \cdot v_d. \quad (7.7)$$

On the other hand, when a large droplet is broken into several multiple droplets (Fig. 7.4B), there is no increase in the total volume of the droplet in contact with the nanolayer. The increased number of pairs of the EDL boundaries again increases the  $I_i$ , yet  $I_{SC}$  does not increase due to the same contact area, i.e., the same  $nl$  that is related to the resistance. This suggests that the alternating salinity gradients should, in principle, generate the same amount of current regardless of the frequency of the gradients as long as the contact area is the same. The energy conversion efficiency depends on how large the high salinity regions cover the surface; the highest current is expected to be obtained when the region of high salinity blobs cover almost the entire film area, regardless of the number of the blobs

### **Turbulent mixing, peak-like current, and salinity boundary dynamics**

To understand the peak-like shape of the current output, we estimate the time-dependent current output with salinity boundary dynamics. Fig. 7.5 displays the

effect of salinity boundary sharpness on the shape of current output. We consider a one-dimensional model nanolayer whose width is 100 (from  $x_i=0$  to  $x_f=100$ ). Once a salinity boundary is located on top of the nanolayer, the charge is induced and its distribution,  $-\delta Q(x, t)$ , is estimated using the dynamic capacitor model (Eq. 7.2):

$$-\delta Q(x, t) = -\frac{1}{2} \tanh[k(t)(x - v \cdot t)] + \frac{1}{2}, \quad (7.8)$$

where  $k(t)$  defines the sharpness of the salinity boundary at time  $t$ ,  $v$  is the flow velocity. The initial time,  $t = 0$ , is when the flow starts to wet the nanolayer at  $x = 0$ . Turbulent mixing decreases the salinity gradient around its boundary so the time dependence of  $k(t)$  is defined using an exponential function:  $k(t) = k_0 \exp(-t/\tau_k)$  with the relaxation time,  $\tau_k$ . Then, the time-dependent current output,  $I(t)$ , is calculated:

$$I(t) = \int_{x_i}^{x_f} dx \left[ \frac{d}{dx} \delta Q(x, t) \right]. \quad (7.9)$$

In case of a constant salinity gradient ( $k(t) = k_0$ ), the current output return to its form (Eq. 7.2):  $I(t) = -[\delta Q(x_f, t) - \delta Q(x_i, t)] \cdot v$ . When the salinity boundary dynamics is on the same time scale as the flow dynamics, the result is the peak-like current as in the experiment. Thus, turbulent mixing hinders the constant current generation instead of producing a peak-like current, smearing the salinity boundary out.

## 7.6 Conclusion

In this chapter, we present simulation approaches to rationalize the design rules observed in experiments for energy conversion using metal nanolayers in contact with a flow of alternating salinity gradients. The oxide dendrites electrostatically repel the ions from the aqueous oxide interface, suppressing the charge polarization of the metal below. By showing that the fluctuation of induced electrons in a metal is spatially varying due to the presence of the dendrites, we show the dendritic heterostructure affect the energy conversion efficiency.

To account for the design rules, we propose two functional mechanisms of the energy conversion: pseudo-2D & redox-activity model and "sweet-spot" resistance model, both of which seem to explain the experimental observations. Further systematic investigations are needed to discriminate the mechanisms, such as controls for dendritic subsurface. One may compare the performance of metal nanolayers, one of which exhibits thermal oxide overlayer, yet the other of which exhibits ALD-coated oxide overlayer that has an (atomically) flat interface. Suppose they showed

the only minor difference in the energy conversion efficiency. In that case, one could exclude the "sweet-spot" resistance model since the hypothesis heavily relies on the tunability of resistance depending on the dendrites' redox activity.

Finally, the peak-like shape of the current output is discussed regarding the dynamics of the salinity boundary from turbulent mixing observed in experiments. When the time scales of the salinity boundary dynamics and the flow rate are similar, the time series of current output becomes peak-like. However, on the other hand, it is a constant plateau when the flow dynamics is much faster than the salinity boundary dynamics, i.e., almost static.

## **7.7 Appendix**

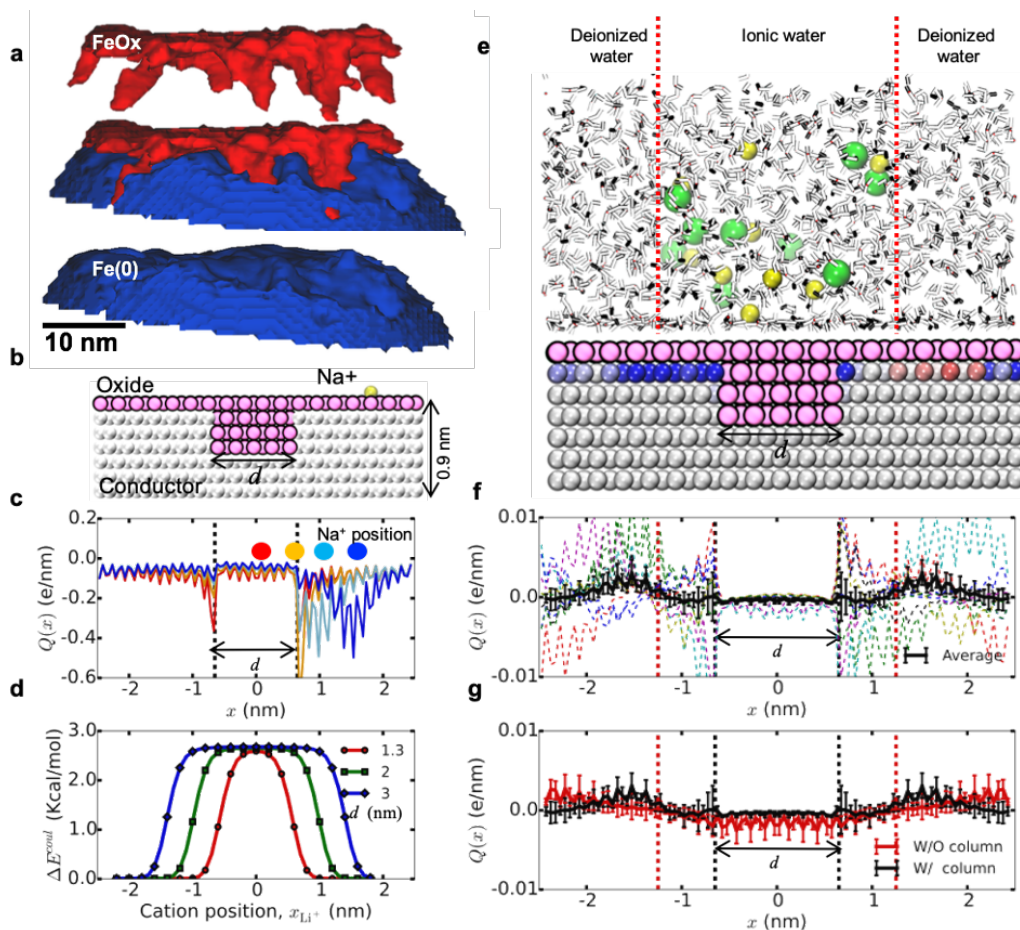


Figure 7.2: Model of charge mobility in nanoconfined, insulator-terminated metal conductor. (a) Atom probe tomography reconstruction of the heterostructured Fe:FeOx nanolayer (Center). Iron oxide and iron metal shown separately on top (red) and bottom (blue), respectively. (b) All-atom representation of the heterostructured nanolayer, including the metal conductor (gray) and a nonpolarizable oxide overlayer and with columnar subsurface heterostructure (pink); a single-probe Na<sup>+</sup> cation is shown at a distance of 1.6 Å from the nanolayer. (c) Induced charge distribution,  $Q(x)$ , by the Na<sup>+</sup> cation at 4 different lateral positions relative to the position of the nonpolarizable heterostructure as in Fig. 7.6. (d) Ion–nanolayer Coulomb interaction as a function of function of lateral ion position, for various widths,  $d$ , of the nonpolarizable heterostructure;  $\Delta E_{coul}$  is the difference in the ion–nanolayer Coulomb interaction for the nanolayer systems with and without the subsurface heterostructure. (e) MD simulation snapshot for alternating regions of ionized (0.43 M NaCl) water/DI water in contact with the nanolayer with columnar heterostructure ( $d = 1.3$  nm). The nanolayer is shown as in (b), but with the instantaneous charge polarization of metal conductor atoms also indicated (range =  $[-0.005 e$  (blue),  $+0.005 e$  (red)]). Vertical dotted lines indicate semipermeable boundaries for the ions to preserve the salinity boundaries. (f) For the simulation cell shown in (e), the time-averaged induced charge distribution,  $Q(x)$  (black), as well as the 0.5-ns block averages of the same quantity. (g) Comparison of the time-averaged induced charge distribution for the system with (black) and without (red) nonpolarizable heterostructure.

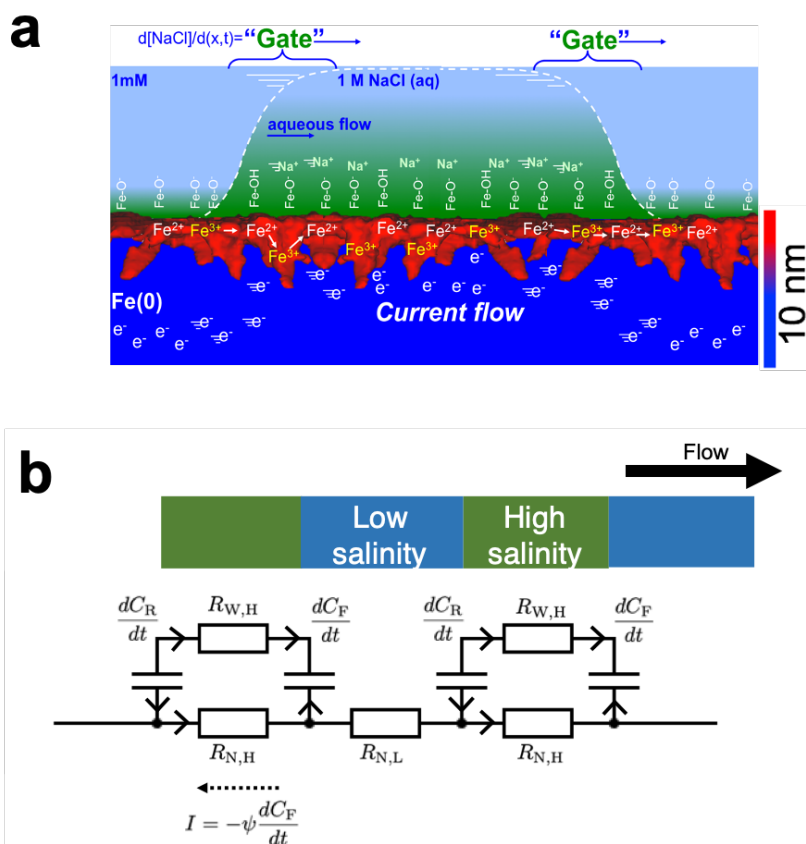


Figure 7.3: Illustration of energy conversion mechanism (a) and its equivalent circuit (b). See the text for details.

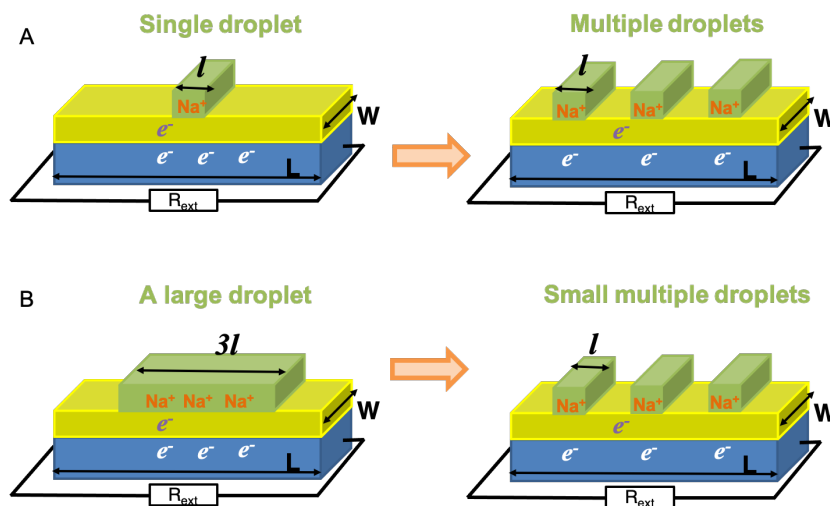


Figure 7.4: Scalability of energy conversion using metal nanolayers (a) with multiple droplets of same size, and (b) with breaking a large droplet into smaller ones.

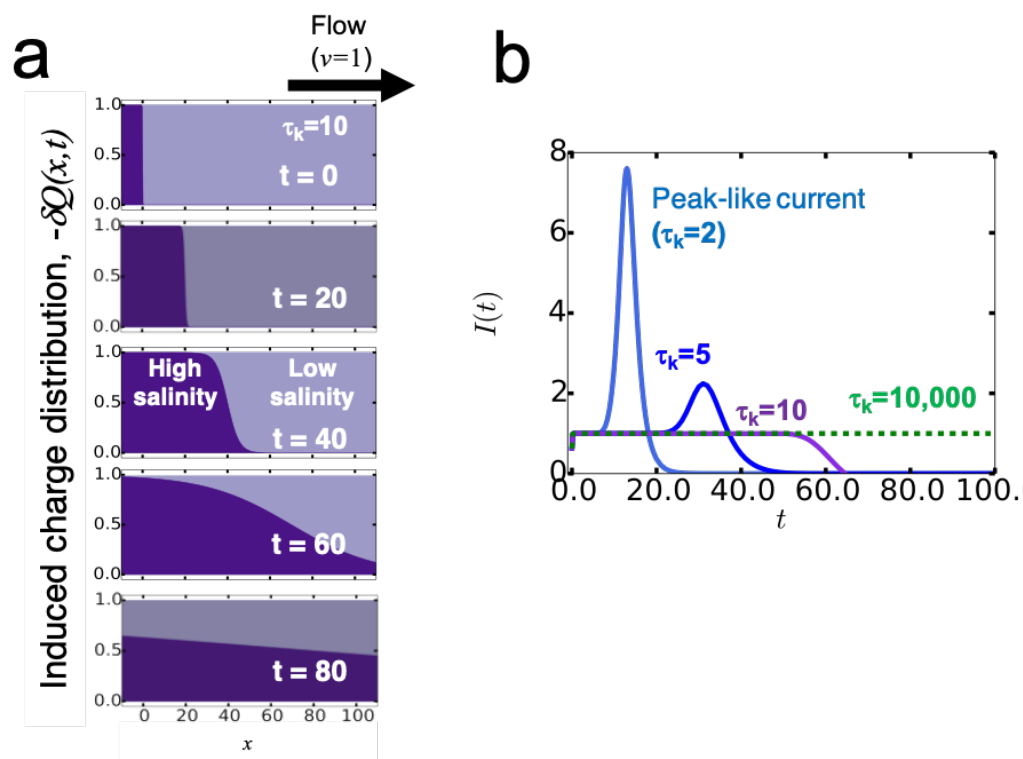


Figure 7.5: Salinity boundary dynamics. (a) Induced charge distribution ( $-\delta Q(x, t)$ ) as a function of time ( $t$ ) after a water flow starts to cover a model nanolayer from  $x = 0$ . (b) Calculated time-dependent current output,  $I(t)$  with various relaxation times ( $\tau_k$ ) of the salinity gradient dynamics. Here,  $k_0 = 10$ .

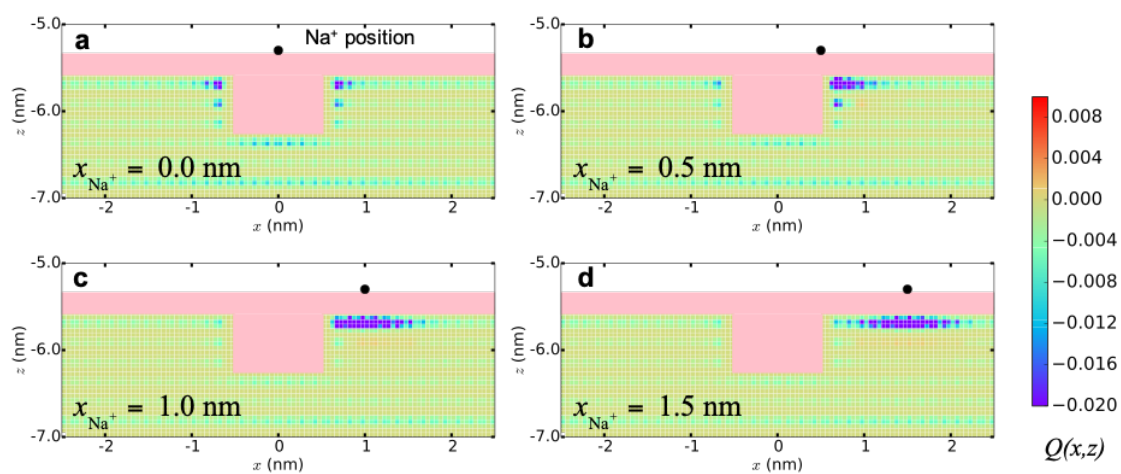


Figure 7.6: For various positions of a single monocation, the distribution of induced charge in the metallic portion of the nanolayer,  $Q(x, z)$ , integrated over the  $y$ -coordinate of the simulation cell. Nonpolarizable oxide atoms are indicated in pink. The position of the monocation is indicated with the black circle, illustrating various displacements with respect to the position of the subsurface heterostructure.

## ENERGY CONVERSION USING METAL NANOLAYERS IN A WAVE TANK

### 8.1 Abstract

In this chapter, we present mechanisms of electricity generation using metal nanolayers, operating in a 210-liter wavetank filled with ocean water mimic. The energy conversion is enabled by ion adsorption and desorption at a moving air-water boundary along with wave action, which subsequently induces electrons in the metal. With a wetted area of  $2.5 \times 6.4 \text{ cm}^2$  and average wave velocity of  $5 \text{ cm s}^{-1}$ , a 10 nm Ni nanolayer on a glass substrate can produce current of up to  $1.5 \mu\text{A}$  and voltage of up to 0.15 mV, generating instantaneous electric power density of  $140 \text{ nW m}^{-2}$ .

Using both experiment and computation, we explore how a metal nanolayer's current and voltage scale with the film's thickness and its footprint based on predictions from the waving potential model. Additional factors including metal element and substrate are also investigated to optimize the energy conversion efficiency. With their scalable nature and ease of making, these metal nanolayers are appealing cost-effective alternatives for real-life applications in the open ocean to harvest wave energy.

Data and content in this chapter are taken from a draft for publication [195]. The author participated in conducting computation, designing experiments, discussing the results, and preparing a draft.

### 8.2 Introduction

Ocean waves constitute a considerable reservoir of ambient mechanical energy that is increasingly sought after for the production of renewable energy. As an alternative to ocean-based turbines located on or near the shore, hydrovoltaic technology is being pursued as a means for harnessing wave energy in the remote ocean [189, 213]. For example, Guo and coworkers have found that a graphene film can produce a few millivolts when vertically inserted into and pulled out from ionic solutions at a few  $\text{cm s}^{-1}$  velocities [206]. This phenomenon was explained through a waving potential across the graphene film that varies as the electrical double layer (EDL) at the liquid:solid boundary varies with wave action [205, 206]. Building on this

finding, similar performance has been reported for materials such as ZnO [95], doped graphene oxide [211], MoS<sub>2</sub> [3], and Si wafers [128, 130, 141] in a variety of operating modalities. With no moving parts, this emerging family of hydrovoltaics has the potential to develop into an alternative to ocean-based turbines for low-power applications in terms of scalability and maintenance cost [213].

In our previous study, we demonstrated c.a. 10 nm thin metal nanolayers composed of Fe, V, and Ni transduce electricity in a flow cell from alternating salinity gradients [15]. The metal nanolayers were fabricated in a single-step by physical vapor deposition (PVD) onto a glass substrate. The nanolayers were composed of a metal underlayer and an oxide overlayer that formed spontaneously in ambient air. Both components were involved in the energy transduction [43, 14]. The native oxide overlayer sets up a negative surface potential that attracts Na<sup>+</sup> over Cl<sup>-</sup> at pH 5.8 or 8. The amount of electricity generated substantially depended on the redox-activity of the oxide overlayer. Metal nanolayers containing redox-active metal centers (Fe, V, and Ni) generated almost an order of magnitude higher electricity than ones that contained redox-inactive metal centers (Al, Cr), implying a possible role for intra-oxide electron transfer and polaron mobility [203, 121]. The metal underlayer allowed for charge carrier transport along with the flow. The salinity boundary in the flow worked as a moving EDL boundary to create a potential gradient to produce electricity. Depending on the choice of metal, the nanolayers produced 0.2  $\mu$ A and  $\sim$ 0.1 mV with a flow velocity of 2-4 cm s<sup>-1</sup> [15].

In this chapter, we present the performance of our metal nanolayers in a wave tank to test their applicability for harvesting ocean wave energy. The practical applications will have to rely on an energy conversion processes that is scalable with the dimension of the materials at their optimal efficiency. Moreover, the nanolayers should be stable in the ocean environment, where corrosion and delamination are a concern, and the substrates should be marine-grade. To address these additional points, we test our devices with a scaling of up to four-fold in the x- and y-dimensions inside a 210-liter wavetank half-filled with Instant Ocean water operating with a wave generator at  $\sim$ 0.5 Hz. We also examine different metals and two substrates for further optimization. Using both experiment and model computation, we discuss electricity generation mechanisms at an air:water interface in the wavetank operation, and provide a guiding principles for scaling up operations of metal nanolayer hydrovoltaics.

### 8.3 Calculation Methods

#### Wavefront dynamics modeling and energy conversion performance based on the waving potential model

We modeled the wavefront dynamics using a flattened sinusoidal function,  $F(t)$ , as a function of time,  $t$ , given by:

$$F(t) = A \sqrt{\frac{1 + b^2}{1 + b^2 \cos^2(\Omega t + \varphi)}} \cos(\Omega t + \varphi) + F_0, \quad (8.1)$$

where  $A$  is the wave amplitude,  $\Omega$  is the frequency of the wave,  $\varphi$  is a phase parameter, and  $b$  is the flattening parameter. According to our experimental setup,  $\Omega = 2\pi/1.6$  Hz,  $A = 0.5(F_h + F_l) = 3.81$  cm, and  $F_0 = 0.5(F_h - F_l) = 1.27$  cm, where  $F_h$  and  $F_l$  are the highest and the lowest location of the wavefront along a nanolayer surface. All positions in this model are relative to the resting water level. The flattening parameter ( $b$ ) was introduced to control the idling and soaking stages and to match the modeled wavefront to the one observed in the laboratory by video footage. With  $b = 0$ ,  $F(t)$  returns to a cosine function. In this work,  $b = 2$  was chosen to match the electrical outputs in our experiments, resulting in the height vs. time profile shown in Fig. 8.1b. There are four different stages of model-wave action, each of which is color-coded: red for the wetting stage, white for the soaking stage, blue for the de-wetting stage, and yellow for the idling stage.

The velocity of the wavefront,  $F'(t)$ , is then given by:

$$F'(t) = -A\Omega \sqrt{\frac{1 + b^2}{1 + b^2 \cos^2(\Omega t + \varphi)}} \left[ \frac{\sin(\Omega t + \varphi)}{1 + b^2 \cos^2(\Omega t + \varphi)} \right]. \quad (8.2)$$

The sign in Eq. 8.2 is positive for the wetting event and negative for the de-wetting event. According to  $F(t)$  and the film location with respect to the resting water level, the time-dependent height of the wetted region,  $H_{wet}(t)$ , is given by:

$$H_{wet}(t) = \begin{cases} F(t), & \text{if } L_l < F(t) < L_h \\ 0, & \text{otherwise.} \end{cases} \quad (8.3)$$

Here, the top ( $L_h$ ) and bottom ( $L_l$ ) positions for a given 5.8 cm tall nanolayer are 4.8 cm and -1.0 cm.

Time-dependent electrical outputs of current and voltage were then estimated by

using the waving potential model [205, 128]:

$$I_{out}(t) = \begin{cases} I_{water}, & \text{if } F(t) > L_h \\ I_{ion}(t) \cdot \frac{0.5 \cdot R_{sq} \cdot H_{wet}(t)/W_f}{R_{sq} \cdot [H_f - 0.5 \cdot H_{wet}(t)]/W_f + R_{ext}} + I_o(t), & \text{if } L_l < F(t) < L_h \\ I_{air}, & \text{if } F(t) < L_l \end{cases}, \quad (8.4)$$

and

$$V_{out}(t) = \begin{cases} V_{water}, & \text{if } F(t) > L_h \\ R_{sq} \cdot I_{ion}(t) \cdot \frac{0.5 \cdot R_{sq} \cdot H_{wet}(t)/W_f}{R_{sq} \cdot [H_f - 0.5 \cdot H_{wet}(t)]/W_f + R_{ext}} + V_o(t), & \text{if } L_l < F(t) < L_h \\ V_{air}, & \text{if } F(t) < L_l. \end{cases} \quad (8.5)$$

Here,  $I_{ion}(t) = s_D \cdot Q_{net} \cdot F'(t) \cdot W_f$ , where  $Q_{net}$  ( $= 1.5 \text{ me/nm}^2$ ) is the number of charges per area we assume to be transferred during one wave cycle,  $R_{sq}$  ( $= 43 \text{ } \Omega/\text{sq}$ ) is the experimentally determined square resistance of the nanolayer under investigation,  $H_f$  is its height ( $H_f = L_h - L_l = 5.8 \text{ cm}$ ), and  $W_f$  is its width (2.5 cm). The parameter  $s_D$ , either +1 or -1, determines the direction of generated current or the polarity of the voltage according to either the picoammeter's or multimeter's lead configuration in the experiments (Fig. 8.1). Here,  $s_D = -1$ . As in the experiments, the electrical outputs are stationary in both soaking (constant  $I_{water}$  and  $V_{water}$ ) and idling (constant  $I_{air}$  and  $V_{air}$ ) stages when a given nanolayer is either fully submerged or fully in air. Offset values in both wetting or de-wetting stages,  $I_o(t)$  and  $V_o(t)$ , are estimated assuming both of them scale linearly with the resting values in idling and soaking stages during wave action:

$$I_o(t) = \frac{H_{wet}(t)}{H_f} \cdot (I_{water} - I_{air}) + I_{air} \quad (8.6)$$

and

$$V_o(t) = \frac{H_{wet}(t)}{H_f} \cdot (V_{water} - V_{air}) + V_{air}. \quad (8.7)$$

Finally, the open-circuit voltage,  $V_{oc}(t)$ , with infinite external resistance, and the short-circuit current,  $I_{sc}(t)$ , with the zero external resistance, are given by:

$$V_{oc}(t) = \begin{cases} V_{oc,water}, & \text{if } F(t) > L_h \\ s_D \cdot 0.5 \cdot R_{sq} \cdot Q_{net} \cdot F'(t) \cdot H_{wet}(t) + V_o(t), & \text{if } L_l < F(t) < L_h \\ V_{oc,air}, & \text{if } F(t) < L_l \end{cases} \quad (8.8)$$

and

$$I_{sc}(t) = \begin{cases} I_{sc,water}, & \text{if } F(t) > L_h \\ s_D \cdot W_f \cdot Q_{net} \cdot F'(t) \cdot \frac{0.5 \cdot H_{wet}(t)}{H - 0.5 \cdot H_{wet}(t)} + I_o(t), & \text{if } L_l < F(t) < L_h \\ I_{sc,air}, & \text{if } F(t) < L_l. \end{cases} \quad (8.9)$$

### Thomas-Fermi model for a metal underlayer exposed to external electric fields

The two-dimensional Poisson equation was numerically solved for a Thomas-Fermi model for a metal underlayer using the Newton-Raphson iteration method [22, 60]:

$$\nabla^2 \Psi(x, y) = \kappa_{TF}^2 \Psi(x, y), \quad \text{for } 0 \leq x \leq L \text{ and } 0 \leq y \leq H, \quad (8.10)$$

where  $\Psi(x, y)$  is the two-dimensional electrostatic potential,  $L$  ( $= 6$  nm) and  $H$  ( $= 15$  nm) are the length and the height of the model metal, respectively. The wave action works along y-axis and is perpendicular to x-axis. A Thomas-Fermi metal is characterized by the inverse of the screening length,  $\kappa_{TF}^{-1}$  [82, 158]. We chose  $\kappa_{TF} = 0.2 \text{ nm}^{-1}$ , which is a typical value for metals. For simplicity sake, the oxide overlayer is not included in the calculation; the air-metal interface is at  $x = 0$ .

In this simplified model, an electric field was introduced to represent the preferential ion adsorption at the nanolayer's surface. The strength of the external electric field is different for different regions either in equilibrium or out of equilibrium. At equilibrium, zero electric field was introduced to represent no preferential ion adsorption based on our discussion in the main text. On the other hand, we introduce a non-zero electric field ( $E_{ext}$ ) whose direction follows the preferential ion adsorption at the interface for transient non-equilibrium right after a wetting event. The non-zero electric field ( $E_{ext} = -\frac{Q_{ion}}{\epsilon_0}$ ) is applied only to the 3 nm long upper region of the metal (one fifth of its height), and the rest of the metal is under zero electric field. Here,  $Q_{ion}$  represents the surface charge per area from the ion adsorption, and  $\epsilon_0$  is the vacuum permittivity ( $8.854 \times 10^{-12} \text{ F m}^{-1}$ ). We choose  $Q_{ion}$  to be either  $+10 \text{ mC m}^{-2}$  or  $-10 \text{ mC m}^{-2}$ . The two external electric fields determine the boundary conditions at  $x = 0$  for the Poisson equation, together with the fact that the model metal is grounded at  $x = L$  (dry end of the model film). Along the y axis, the periodic boundary condition is enforced, whose effect on the result is negligible due to the fact that the electric potential decays quite fast inside the model metal on the scale of the metal's height (15 nm). The two-dimensional space was discretized with rectangular finite elements whose size is 0.05 nm along the x-axis and of 0.2 nm along the y-axis.

## 8.4 Results and Discussion

### Waving potential at a water:air:oxide triple junction

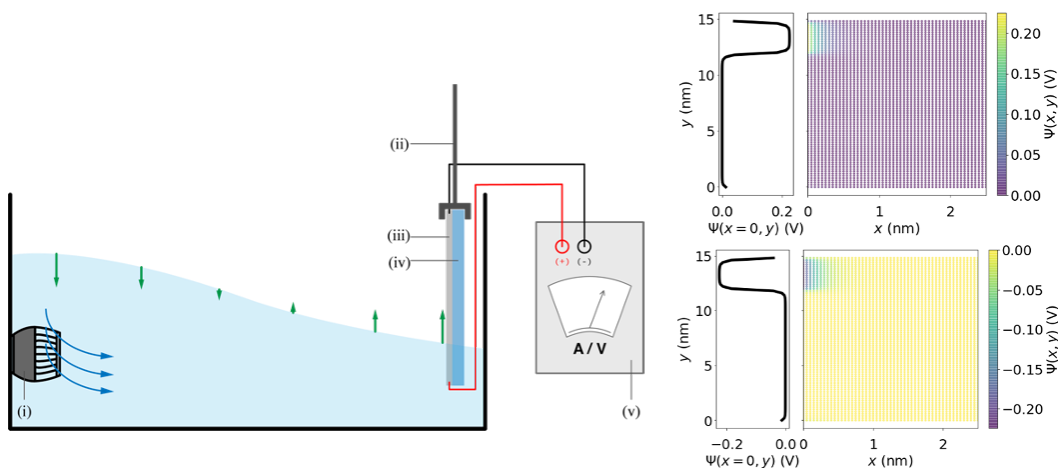


Figure 8.1: Schematic illustration of our experimental setup (left panel), including (i) water pump, (ii) column post to hold samples, metal nanolayer, (iii) deposited on its substrate (iv), and (v) picoammeter/Multimeter for electrical measurements. Green arrows indicate the direction of wave motion. Figure not drawn to scale. Right panel: calculated two-dimensional electrostatic potential inside a metal underlayer,  $\Psi(x, y)$  (Eq. 8.10), with the preferential adsorption of (top)  $\text{Na}^+$  ions ( $Q_{ion} = +10 \text{ mC m}^{-2}$ ), and (bottom)  $\text{Cl}^-$  ions ( $Q_{ion} = -10 \text{ mC m}^{-2}$ ).

We test the performance of our metal nanolayers in a wave tank (Fig. 8.1). Just like in the liquid flow cell [15], operation of the nanolayers at a water:air interface should involve ion adsorption and desorption in the electrical double layer above the oxide:water interface terminating the metal nanolayers. The sign and magnitude are influenced by the point of zero charge (PZC) of the oxide overlayer and pH of the saltwater. Based on pH (8.6) of the saltwater and PZC (8-9) of nickel oxides [87], the Gouy-Chapman potential at the water:oxide interface is a few mV for Ni nanolayers. This potential is much smaller than estimates from theory of the electrostatic potential at the air-water interface, which is close to or on the order of 1 V [84, 11, 26]. The substantial difference in the surface potentials momentarily facilitates ion adsorption in the newly wetted part of the surface as the wave ascends, creating a transient non-equilibrium state. Just like what has been termed a "waving potential in graphene" [206], a potential gradient should be established vertically across the water:air:oxide triple junction, with a polarity that is determined by the ions that preferentially adsorb (Fig. 8.1). During wave action, the resulting transient potential should be higher in the newly wetted area than in the already submerged area of the device. When the circuit is closed, the current flows from higher to lower

potential, along the transient potential gradient, and in the opposite direction to the wave action (Fig. 8.2c).

### **Current, voltage, and wave dynamics**

Fig. 8.2a shows typical electrical outputs produced by a 10 nm thin Ni nanolayer in response to wave action. The nanolayer is found to perform well for at least 72 hours, producing current and voltage. When our devices were connected in series to an external load of 100  $\Omega$  in the wavetank, in-phase current (c.a. 0.6  $\mu\text{A}$ ) and voltage (c.a. 0.06 mV) were produced. The frequency of current or voltage peaks is consistent with that of a wave event at approximately 0.5 Hz. Each of the current and voltage showed a peak at the end of the wetting stage when the exposed area of the film was fully wetted. The wetting stage during a wave event is the main driver for the energy conversion observed from the Ni nanolayers operating in our Instant Ocean wavetank.

According to the waving potential model [206], similar peak-like currents and voltages are expected during de-wetting (Fig. 8.2b). However, the experiments showed no significant electrical outputs during this stage (Fig. 8.2a). We attribute this result to the hydrophilicity of the metal nanolayers, which differs from hydrophobic graphene or Si-based devices [206, 128, 130]. The hydrophilic surfaces may slow the rate of ion desorption, resulting in much smaller or even no electrical output during de-wetting. Recently, we showed that the asymmetric response of ions in Stern layer at the aqueous silica interfaces to the salinity exchange; the de-wetting of  $\text{Na}^+$  ions are much slower than the wetting [111]. This interpretation is consistent with reports of ZnO-based devices that generate much lower voltage when pulled out of the water than when pushed into the water due to their hydrophilic surface [95]. Addition of a filter threshold to only allow for current and voltage output during the wetting stage results in reasonable agreement between the observed and modeled current and voltage outputs.

Two additional stages are present in a wave action: a soaking stage when the film is fully submerged and an idling stage when it is not in contact with water (Fig. 8.2a). Freeze-frame video footage analysis shows that the soaking and the idling stages correspond to the shoulder next to and the plateau before the peaks in the wetting stage, respectively. As expected, current and voltage remain stationary during these two stages when there is no moving air-water boundary on the metal nanolayer.

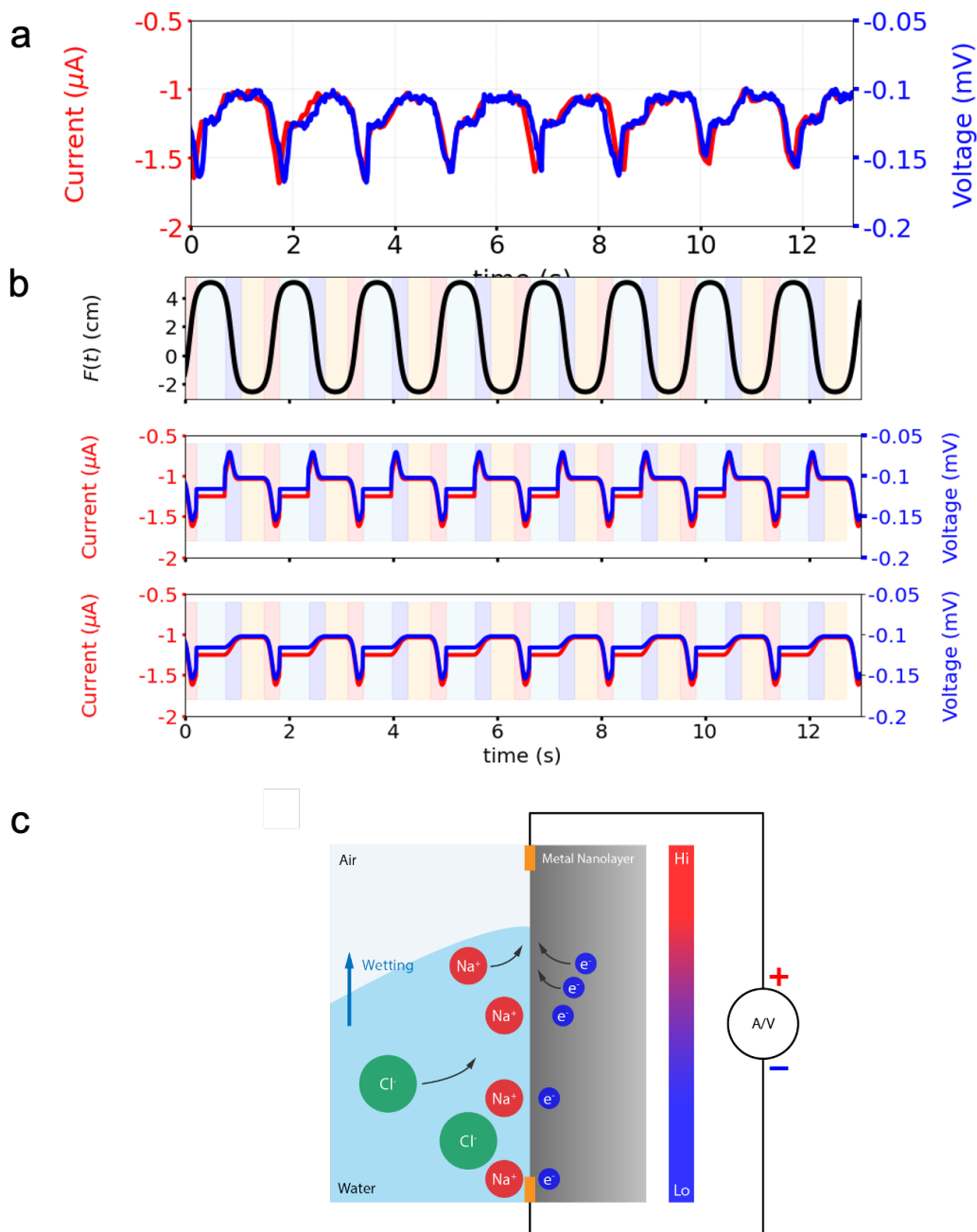


Figure 8.2: Electrical outputs in experiment and in computation. (a) Electrical outputs via a 10 nm Ni nanolayer on glass connected in series to a  $100\ \Omega$  external resistor in our Instant Ocean wavetank. The wet area is  $2.5 \times 6.4\ \text{cm}^2$ . (b) Calculated electrical outputs (Eq. 8.4- 8.5) for a 10 nm Ni nanolayer connected in series to a  $100\ \Omega$  external resistor using a model wave,  $F(t)$  (Eq. 8.1 with  $b = 2$ ). The same wet area is used as in (a). (c) Microscopic depiction of waving potential during the wetting stage of a wave event. The colorbar represents the potential gradient along a model metal nanolayer.

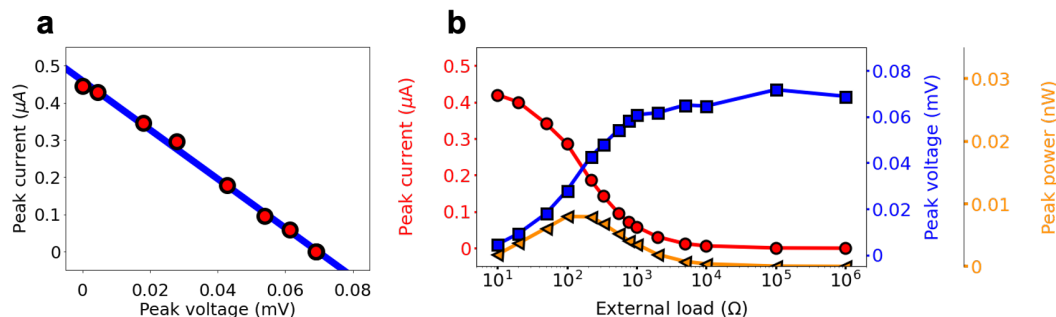


Figure 8.3: Ohmic contact in 10 nm thick Ni nanolayers with a wetted area of  $2.5 \times 6.4 \text{ cm}^2$ . (a) Linear relationship between peak current and peak voltage with variable external resistors. (b) Peak current, peak voltage, and peak power generated with variable external resistors.

### Power Curves

Fig. 8.3 displays peak values of open-circuit voltage (OCV) and short-circuit current (SCC) collected during the wetting stages from 10 nm thin Ni nanolayers connected to an external load of various resistances. The peak value is the difference between the baseline in air and the minimum of each electrical output for each wave event (Fig. 8.8 in Appendix). The linear relationship between the peak OCV and SCC confirms Ohmic contact in the Ni nanolayers (Fig. 8.3a), as has been reported for other energy transducers made of a Si wafer [128]. The slope in Fig. 8.3a reveals the 10 nm thick Ni nanolayer's resistance is  $130 \Omega$ , which is consistent with the one measured in the dry state. The resistance is substantially lower than for previously reported materials, including graphene, doped graphene films, Si wafers, and 50 nm thick ZnO films [95]. Fig. 8.3b further supports Ohmic contact in the Ni nanolayers, showing a maximum peak power density of  $60 \text{ nW m}^{-2}$  when connected to an external load of  $100 \Omega$  resistance, where peak power is the product of peak current and peak voltage.

The amount of charge transferred ( $Q_{\text{net}}$ ) in the wetting stage is an important indicator to estimate the performance of the metal nanolayers. It is estimated via the waving potential model [205, 128] based on the assumption that the devices have Ohmic contact:

$$V_{oc, peak} = V_{oc, air} - \min [0.5 \cdot H_{wet}(t) \cdot R_{sq} \cdot Q_{net} \cdot F'(t)]. \quad (8.11)$$

Here,  $R_{sq}$  is square resistance of the nanolayer ( $43 \Omega/\text{sq}$ ),  $V_{oc, air}$  is the baseline value of the OCV in air (idling stage), and  $V_{oc, peak}$  is the peak value of the OCV. We applied the model wavefront velocity,  $F'(t)$  (Eq. 8.2), and the wetted

height,  $H_{\text{wet}}(t)$  (Eq. 8.3) to Eq. 8.11 and obtained  $Q_{\text{net}}$  to be  $0.24 \text{ mC m}^{-2}$  ( $\approx 1.5 \text{ me nm}^{-2}$ ). According to the mechanism discussed above, the magnitude of the potential gradient across the nanolayer (Fig. 8.2c), which can be represented by the difference in the electric field strength of the regions at equilibrium and transient non-equilibrium (Fig. 8.1c), dominates in determining  $Q_{\text{net}}$ . In our case of no preferential ion-adsorption in equilibrium for the Ni nanolayers ( $\text{pH} \approx \text{PZC}$ ), the electric field strength in a transient non-equilibrium state dominates in determining  $Q_{\text{net}}$ . The anion screening in solutions of seawater concentration can also further decrease the magnitude of the transient electric field. This effect was discussed in a previous study of doped graphene films in contact with 0.6 M NaCl solutions, where  $Q_{\text{net}}$  ( $1 \text{ mC m}^{-2}$ ) contributed only about 4% of the graphene oxide's surface charge. The authors attributed the low  $Q_{\text{net}}$  to the substantial screening from anions in the narrow interfacial region (Debye length is shorter than 1 nm at 0.6 M NaCl) [211]. We conclude that the power generation mechanism is dominated by the air:water potential difference.

### Nanolayer thickness

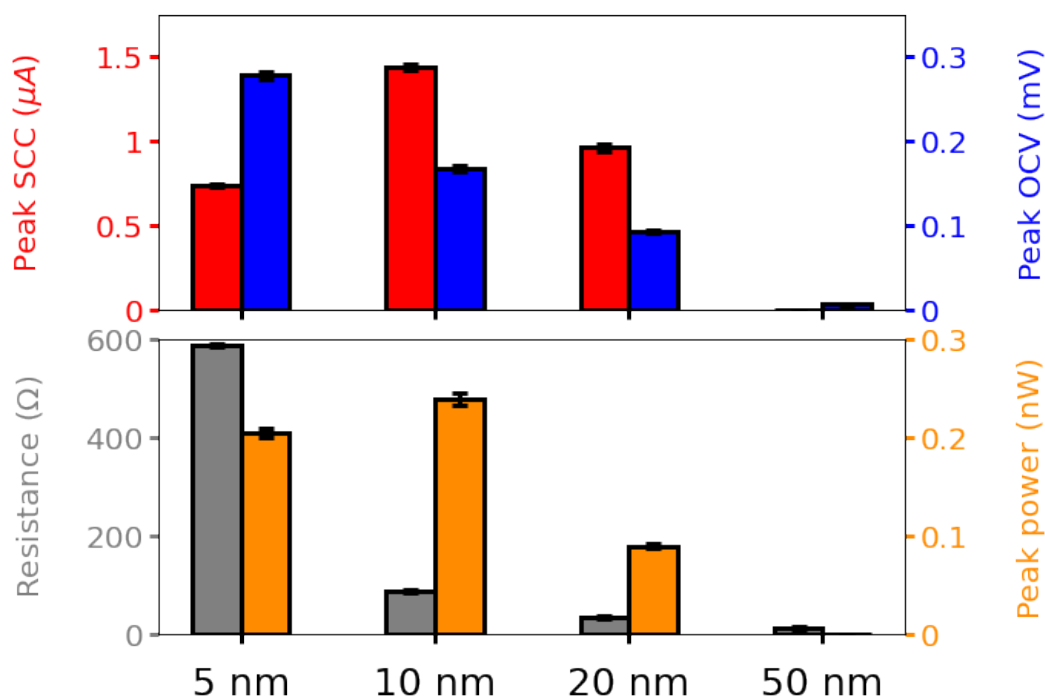


Figure 8.4: Energy conversion via Ni nanolayers of various thicknesses with a wet area of  $2.5 \times 6.4 \text{ cm}^2$ .

Our previous liquid flow cell experiments suggested that the thickness of the metal

nanolayers is crucial to the amount of generated current and voltage outputs [15]. A similar trend applies to the metal nanolayers in the wavetank. Fig. 8.4 shows that the resistance strongly depends on nanolayer thickness. Thickness, in turn, is inversely related to the square resistance of the nanolayers (Eq. 8.5), so it is expected that the peak OCV should increase as the nanolayer becomes thinner. Fig. 8.4 shows that this expectation is indeed met by the experimental data. Moreover, this result is consistent with multi-layered carbon devices, which also show an increase in generated voltage when they approach few-carbon layers (single-, bi-, or tri-layers of graphene) [205].

Fig. 8.4 shows that the peak power generated by the Ni nanolayers is at the maximum when their thickness is 10 nm. Previous XPS results confirmed that the thickness of the oxide overlayer is around 3-4 nm and is independent relative to the overall film thickness [14]. Thick metal nanolayers greater than 50 nm generate negligible electrical outputs, similar to a macroscopically thick Cu metal sheet [205]. We attribute this outcome to the increased conductivity in the thicker nanolayers, which inhibits the formation of a potential gradient across the moving air-water boundary and screens the external electric field from adsorbed ions within the range of a few angstroms.

The 5 nm thin nanolayers show little electrical power as well. Given the thickness of their oxide nano-overlayers, the metal underlayer is only 1-2 nm thick [14], making these structures significantly more resistant than the 10 or 20 nm ones, as shown in the figure. Given these considerations, we do not expect even thinner nanolayers to produce any more power than the 5 nm thin nanolayers. Thus, the appropriate extent of nanoconfinement enables efficient energy conversion by tuning the film resistance to support decent currents and potentially enhancing the directionality of electron transfer.

The turnover in peak SCC (Fig. 8.4) is consistent with our previous liquid flow cell experiments [15] for which Fe nanolayers generated the highest peak SCC at ~10 nm thickness. However, the peak OCV recorded in the wavetank monotonically increases with decreasing nanolayer thickness up to 5 nm, which is attributable to the increase in the metal nanolayer's square resistance. The 5 nm thin Ni nanolayer has a substantially higher resistance ( $> 0.5\text{k}\Omega$ ) to compensate for the decreased peak SCC, causing it to produce the high peak OCV. This difference in the OCV dependence on nanolayer thickness for the wavetank vs. the flow cell experiments supports the importance of the electrostatic potential at the air:water interface, which

is absent in the liquid flow cell.

## Scalability

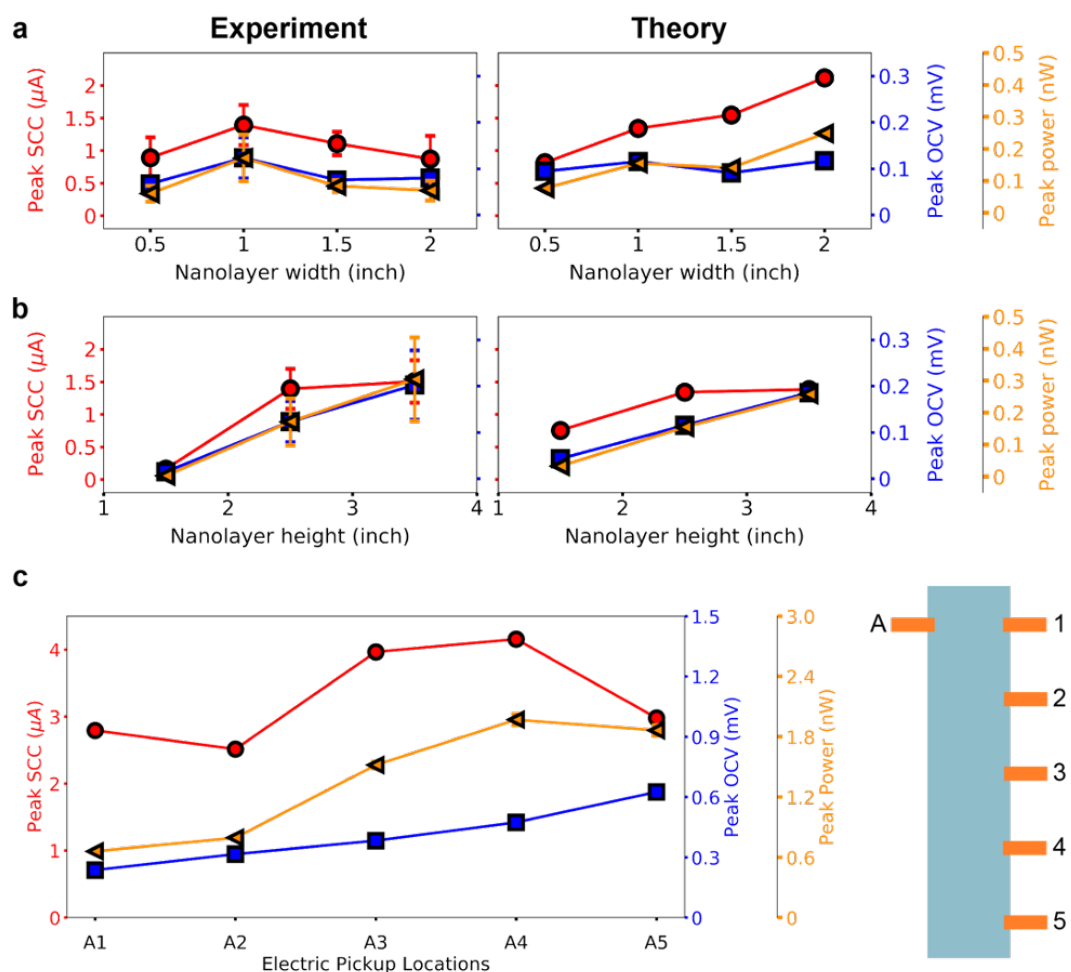


Figure 8.5: Energy conversion via 10 nm thick Ni nanolayers of various sizes in experiment (left column) and in theory (right column). (a) The width of the nanolayers is fixed at 6.4 cm. (b) The height of the nanolayers is fixed at 2.5 cm. (c) Scalability depending on the location of electric pickups.

For large-scale applications, the energy conversion needs to be scalable with device size. Fig. 8.5 shows electrical outputs during energy conversion using Ni nanolayers of various sizes at the optimal thickness (10 nm nickel on glass). Each pair of OCV and SCC peak values in Fig. 8.5 are averaged from measurements on three different nanolayers of the same size prepared in the same batch of PVD (Fig. 8.9). The Ni nanolayers were fixed at the top in the same position. Note that the square

resistances of Ni nanolayers prepared in the same batch are almost the same (data is not included).

Fig. 8.5 indicates the experimentally determined energy conversion scales with height, as predicted by the waving-potential model with a constant wave velocity, but not with width of metal nanolayers, at least within the uncertainty of our point estimates. Contrary to the experimental outcome, the electrical outputs would be expected to be additive with the increasing width according to the waving-potential model (Fig. 8.5b), since the width is perpendicular to the wave action.

Fig. 8.5c shows another experiment we performed on a single nanolayer for which we varied the distance between the current collectors at the top and at bottom. When the distance between two current collectors is increased, the average distance for the electrons to travel increases, and consequently, the flow of electrons is subject to higher resistance. With the increased resistance, higher peak OCV is obtained (see Eq. 8.8). Non-uniform deposition on the wide substrate ( $2 \times 9 \text{ in}^2$ ) leads to the spatially variable square resistance, as  $R_{sq}$  is higher in the thinner parts of the film on the edges (data is not included). The overall output power is found to increase with distance. These outcomes provide another design parameter for improving the energy transduction process with no additional cost and effort.

Yet, we caution that despite our best efforts to keep the fabrication process consistent, the current and voltage point estimates vary within a factor of two for the triplicate samples tested separately under identical conditions. The data in Fig. 8.5 indicate that this factor is similar to the expected change in SCC and OCV with nanolayer width and height predicted from the waving potential model. We therefore conclude that larger nanolayer areas, for which the current and voltage differences are expected to be larger, need to be explored.

### **Choice of metal and substrate**

Nanolayers made of different metals are expected to exhibit different  $Q_{\text{net}}$  as well as  $R_{sq}$  (Eq. 8.5). Fig. 8.6 displays energy conversion results for various elements at constant thickness (10 nm) and wetted area ( $2.5 \times 6.4 \text{ cm}^2$ ). Of the four metals tested, iron produced the highest peak power whereas nickel produced the lowest. Peak SCCs of iron and nickel (redox-active oxide) nanolayers are higher than those of chromium and titanium (redox-inactive oxide), which is consistent with our previous study [15]. Nickel showed the smallest OCV, which we attribute to its resistance, which is the lowest in the series of elements we investigated. Depending on the metal,

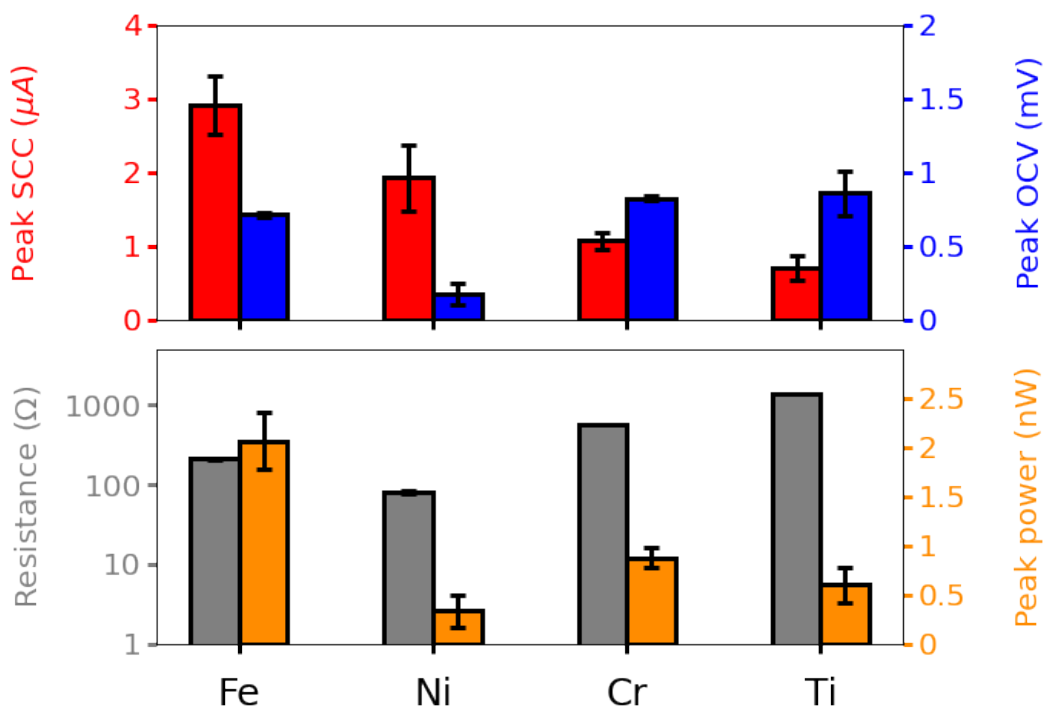


Figure 8.6: Energy conversion via 10 nm thick nanolayers of various metal elements with a wet area of  $2.5 \times 6.4 \text{ cm}^2$ .

the film resistance varies more than an order of magnitude. The comparatively low resistance of the nickel nanolayers results in the lowest peak power among the metal nanolayers we considered. Thus, the results suggest that metal nanolayers having a high resistance (enabling high peak OCV) exhibit increased energy conversion as long as they are electronically conducting. We note that all the nanolayers of the various metal elements have oxide overlayers of similar thicknesses (3-4 nm) [14].

Lastly, the substrate was also varied as it is another component of our device that may affect performance and durability. Plastic substrates would be preferred for large-scale applications due to their low cost, weight, and mechanical properties relative to glass. The two substrates tested in this study were glass and polyethylene terephthalate (PET); the latter chosen for its widespread use in marine applications [114]. Given the flexible nature of the PET slides, we worked with (1 mm thickness), the nanolayer:PET devices were affixed to a rigid glass support to avoid possible contributions from flexoelectric effects stemming from PET [163]. In contrast to single-layered materials like graphene and  $\text{MoS}_2$  [206, 3], we only found minor differences in the magnitude of power generated from 10 nm Ni nanolayers deposited on glass vs. PET after 1 hour in the wavetank (Fig. 8.7). We attribute this outcome

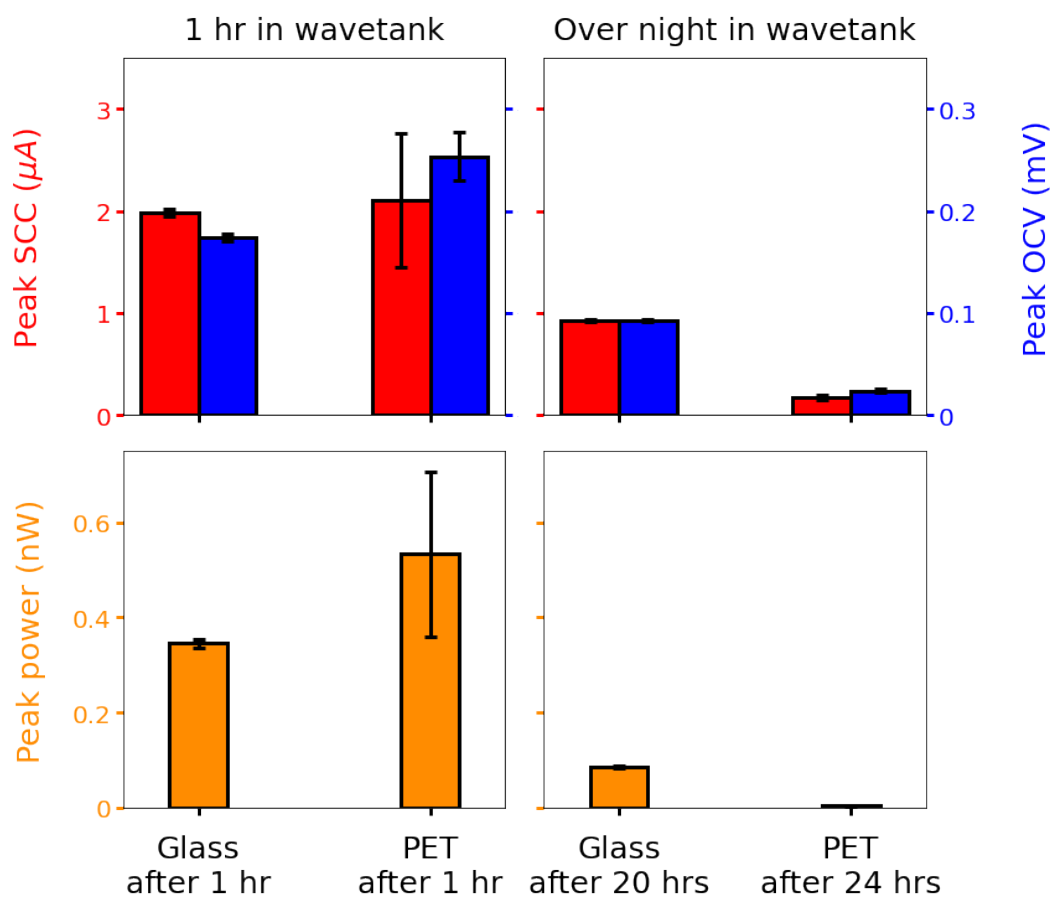


Figure 8.7: Energy conversion via 10 nm thick Ni nanolayers on various substrates with a wet area of  $2.5 \times 6.4 \text{ cm}^2$ .

to screening of the electric field by the metal underlayer so that it does not reach the substrate, and vice versa. Unlike the nickel nanolayers on glass, the nanolayers on PET produced negligible power after 24 hours in the tank. This result was surprising as we noted little to no visual deterioration on any of the nanolayers on either substrate after 24 hours in the wavetank. This outcome indicates that while the nanolayers are resistant to delamination or corrosion in the tank, more research is needed to understand why the nanolayer performance on the PET substrates is so different when compared to that on glass.

## 8.5 Conclusion

Metal nanolayers have been recently found to be potentially cost-effective yet efficient material to transduce kinetic energy of a water flow to electricity. The ease of fabrication aids scalability. We have investigated the energy conversion mechanisms and scalability using the metal nanolayers in our 210-liter wavetank filled with a

seawater mimic for practical large-scale applications. Ni nanolayers were the main focus due to their resistance to corrosion and delamination in the harsh environment of the wavetank in order to perform for at least several weeks.

In summary, with a wetted area of  $2.5 \times 6.4 \text{ cm}^2$  and average wave velocity of  $5 \text{ cm s}^{-1}$ , Ni nanolayers transduced electrical outputs up to  $1.5 \mu\text{A}$  and  $0.15 \text{ mV}$ . The performance was the best at its thickness of  $10 \text{ nm}$ , and negligible electrical outputs were obtained for films thicker than  $50 \text{ nm}$ . At its optimal thickness, Ni nanolayers generated the peak-like current and voltage outputs, each of which was scalable with the thickness of each metal nanolayer dimension. The scalability with the nanolayers' width remains in question due to the limited accessibility to the nanolayers' surface in this study.

When fully wetted,  $10 \text{ nm}$  thin Ni nanolayers generate peak-like current (c.a.  $1.5 \mu\text{A}$ ) and voltage (c.a.  $0.2 \text{ mV}$ ) from a single,  $0.5 \text{ Hz}$  wave event. The electrical outputs were generated due to a waving potential created across the moving air:water boundary. Both peak values of generated current and voltage are found to be scalable with the metal nanolayer dimensions, which is promising for large-scale applications.

## 8.6 Appendix

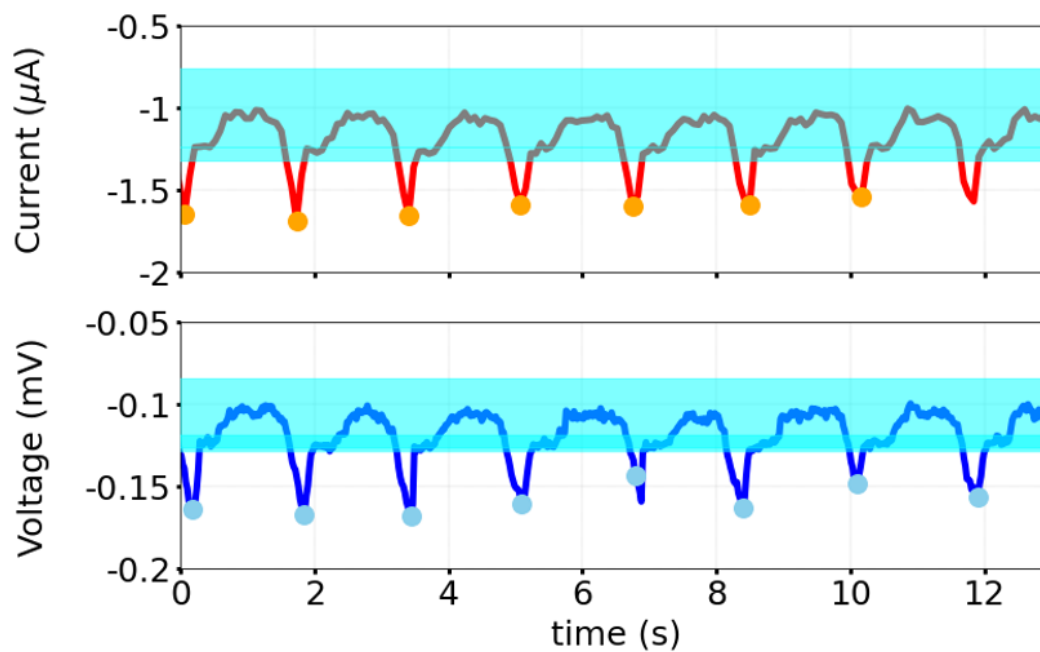


Figure 8.8: Current (top) and voltage (bottom) recorded during wave action for 10nm thin nickel nanolayers on glass. Circles represent peaks picked from the time series. The cyan region is a buffer zone to exclude small irregularities in periodic signals and ensure the peaks are appropriately included. The peak finding method employed here infrequently misses peaks and rarely finds slightly false peaks for both current and voltage. However, we have sampled enough peaks for statistical analysis on both of the electrical outputs.

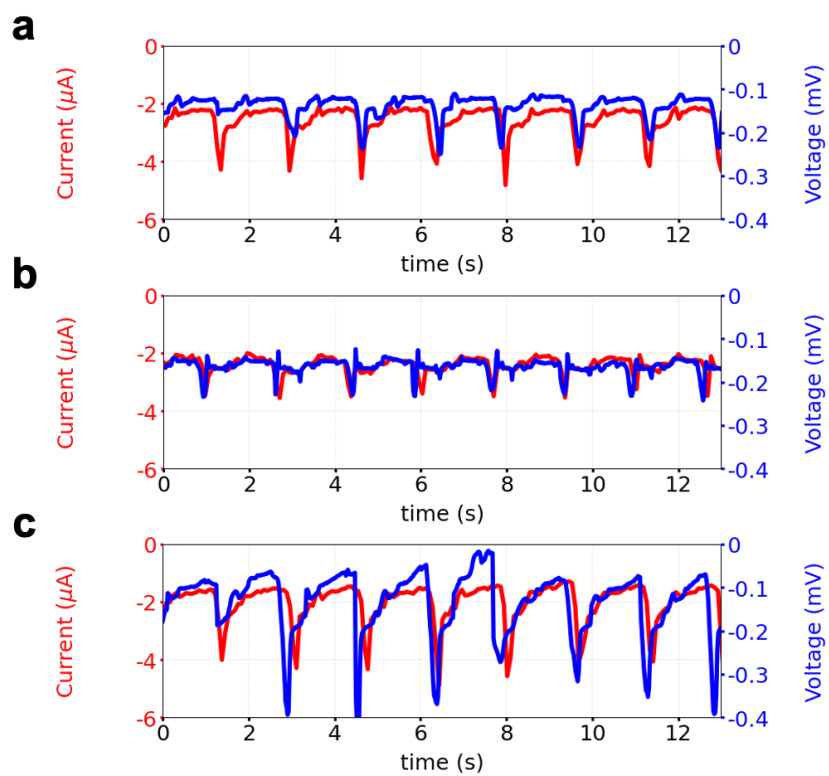


Figure 8.9: Triplicate electrical outputs of 10 nm Ni nanolayers in our Instant Ocean wavetank deposited via PVD in the same batch on glass substrate. The wet area is  $2.5 \times 6.4 \text{ cm}^{-2}$ .

## COUPLED AND DECOUPLED DYNAMICS OF STERN AND DIFFUSE LAYERS AT AQUEOUS OXIDE INTERFACES

### 9.1 Abstract

To advance materials design for "hydrovoltaic" energy transducers in Chapters 7 and 8, fundamental understandings of how water molecules and ions respond to external stimuli at electrified interfaces are required. In this chapter, we utilize atomistic simulations to provide molecular insights of the atomic structures at aqueous silica interface that are responsible for the non-linear responses to an abrupt salinity transition of ionic solutions while maintaining the bulk solution pH.

Heterodyne-detected second harmonic generation (HD-SHG) measurements, which provide disentangled electrical double layer (EDL) information, show that the dynamics in the Stern and diffuse layers are decoupled from one another under some conditions (e.g. from 0.1 M to 10  $\mu$ M), while they change in lockstep under others (e.g. from 0.1 M to 1 mM) as the ionic strength in the aqueous bulk solution varies. Our atomistic simulations suggest a prominent role of contact ion pairs in the Stern layer that specifically interact with the oxide surface, responsible for their decoupled kinetics of the EDL layers upon bulk salinity transitions.

Data and content in this chapter have been published as Ref. [111]. The author participated in conducting simulations, discussing the results of both experiments and simulations, and preparing a draft.

### 9.2 Introduction

A long-standing goal in the field of aqueous interfaces is to advance a microscopic understanding of the electrical double layer (EDL) [91, 21, 209, 57]. EDL descriptions remain largely confined to Bragg-Williams (mean field) approximations [40, 71], such as Gouy-Chapman theory and its variants such as constant capacitance, Gouy-Chapman-Stern or 'triple layer' model [28]. While these models are powerful through their ease of use and applicability, their derivation required "strong idealization and simplification," as stated by Stern when he first reported his model [171]. Since then, determination of structure and electrostatics in the Stern and Diffuse layers, the two basic components of the most established and commonly used EDL

model [109, 57], have been sought by many through experimental [127, 23, 35, 39, 92, 150] and computational [28, 135, 134] investigations of aqueous interfaces.

Experimental evidence of dynamic exchange of ions between these two EDL regions is now just beginning to emerge [92, 16]. Challenges to characterize kinetic responses of the EDL, which cannot be addressed using static mean-field models, are related to the rates of physical and chemical processes in the Stern and diffuse layers, such as whether the responses of the EDL layers to varying conditions in bulk equilibrium phase are coupled to one another, and under what conditions processes in these two regions occur synchronously or asynchronously. A related question concerns the molecular origin of hysteresis [56, 106, 39], in which a surface may stay in a charged state that is incommensurate with what is expected from bulk equilibrium thermodynamics.

Measurements of amplitude ( $E_{sig}$ ) and phase ( $\varphi_{sig}$ ) of non-resonant second harmonic generation (SHG) signals from aqueous interfaces provide the second-order nonlinear susceptibility of the interface,  $\chi^{(2)}$ , and the total surface potential,  $\Phi(0)_{tot}$  [165, 193, 61, 125, 150, 27, 118, 35].  $\chi^{(2)}$  is a fundamental structural property of matter in noncentrosymmetric environments, while  $\Phi(0)_{tot}$  contains the Coulomb, dipole, quadrupole, and other contributions at the interface. Using a proper model, disentangled information of the EDL layers is obtained [125, 16, 110]: on one hand, the  $\chi^{(3)}\Phi(0)_{tot}$  product is understood to report on changes in the diffuse layer as experiments [193, 33] and computations [81] show that  $\chi^{(3)}$  for water is invariant with ionic strength, pH, surface composition. On the other hand, values of  $\chi^{(2)}$  report directly on molecular structure in the Stern layer; as the most abundant species at an aqueous interface is water,  $\chi^{(2)}$  depends on the dipolar alignment of water molecules, at least to leading order. Thanks to heterodyne-detected SHG (HD-SHG) that provides point estimates for both  $\chi^{(2)}$  and the  $\chi^{(3)}\Phi(0)_{tot}$  product, one can now start to think about separating processes in the Stern and diffuse layers.

In this chapter, we utilize atomistic molecular dynamics simulations to provide molecular understandings on HD-SHG measurements of how interfacial EDL structure and total potential vary as we transition an aqueous solution over fused silica between various concentrations of NaCl at constant bulk solution pH. Experiments evidently show that the dynamics in the Stern and Diffuse layers are decoupled from one another under some conditions (e.g. large salinity change), while they are strongly coupled under other conditions (e.g. small salinity change) that are readily identified. Atomistic insights from simulations are used to identify molecular

arrangements of interfacial species that recapitulate the experimentally determined values of  $\chi^{(2)}$ . Simulation results suggest that contact ion pairs between sodium ions and surface silanol groups are responsible for the decoupled kinetics of EDL layers, since the desodiation process is slow [92] due to the specific interaction in contact ion pairs and takes place along the structural reorganization of the surface silanol groups.

### 9.3 Simulation Method and Calculation of SHG Responses

#### MD simulation and model

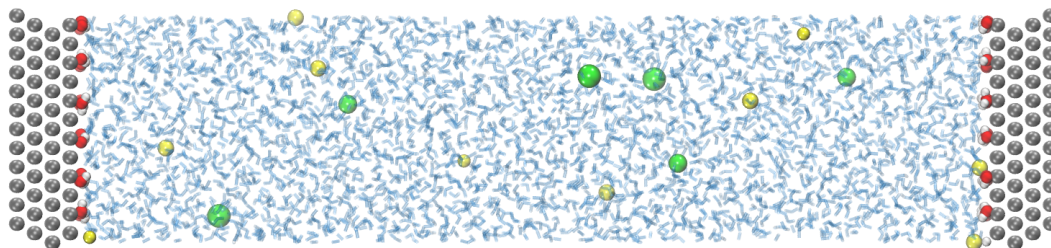


Figure 9.1: A simulation snapshot with 0.1 M NaCl with  $\sigma_0 = -0.04 \text{ C m}^{-2}$ . The inert layers are grey spheres, on top of which are hydroxyl groups (red and white spheres). Water molecules are in blue. Yellow and green spheres are  $\text{Na}^+$  and  $\text{Cl}^-$  ions, respectively.

Molecular dynamics simulations (Fig. 9.1) of aqueous solutions in contact with silica surfaces were performed using SPC/E water [12], NaCl ions [168], and model slit-like silica [76, 15]. The model slit-like silica is composed of two substrates symmetrically placed in a simulation cell with respect to a plane of  $z = 0$ , each of which is composed of a hydrophobic substrate (four layers of neutral atoms) [15] and terminal silanol groups [76]. The simulation cell is periodically replicated only in the  $x$  and  $y$  coordinates, in each of which the length of the simulation cell is 2.77 nm and 2.88 nm, respectively. To provide the hydrophilic nature of the silica surface, 30 terminal silanol groups (OH) are uniformly placed on top of the (111) terminal interface of each hydrophobic substrate. The surface density of the silanol groups is  $3.76 \text{ nm}^{-2}$ , comparable to the value of a simulated amorphous silica surface [28]. The OH bond is modeled as a rigid rotor (bond length of 0.143 nm) around the Si-O axis with the fixed Si-O-H angle ( $109.47^\circ$ ), where a Si atom is the one to which the oxygen atom of the is attached in the terminal hydrophobic substrate. At our simple model silica surface, there are water molecules that both donate and accept a hydrogen bond to and from the terminal silanol group as at other amorphous or

crystalline silica surfaces [136, 28]. The surface charge density of the silica surface is controlled by the number of deprotonated hydroxyl groups, ranging from  $0 \text{ C m}^{-2}$  (zero deprotonated silanol groups) to  $-0.08 \text{ C m}^{-2}$  (4 deprotonated silanol groups,  $\text{Si-O}^-$ ).

A total of 3,000 SPC/E water molecules are randomly inserted between two silica surfaces. To reduce an artificially high pressure along the confinement, the  $z$  position of the silica substrates is adjusted, satisfying the ambient pressure (1 atm) along  $z$  axis. The final distance between oxygen atoms of the silanol groups along  $z$  axis is 11.54 nm. After another short equilibration, NaCl ions are randomly placed between the surfaces according to their concentration (either 0.1 or 1 M). Interactions between all atoms are described by Coulomb and Lennard-Jones (LJ) potentials without polarization. For cases of a charged silica interface with no contact ion pairs ( $\text{SiO} \cdots \text{Na}^+$  with no salt, semipermeable boundaries are introduced to interact only with  $\text{Na}^+$  ions, which is described by the truncated LJ potential.

**Inert silica substrate.** Atoms in the inert substrate are fixed in the face-centered cubic structure with a lattice parameter of 0.392 nm and a (111) termination at the interface [15]. The orthorhombic simulation cell is oriented such that the  $z$  coordinate is perpendicular to the silica surface, and the simulation cell is periodically replicated only in the  $x$  and  $y$  coordinates. In all simulations, the length of the simulation cell in the  $x$  and  $y$  coordinates is 2.77 nm and 2.88 nm, respectively, such that each of the silica inert substrates is described using four layers of inert atoms, with each inert layer containing 120 atoms (for a total of 960 inert atoms).

**Semipermeable boundaries for interfacial  $\text{Na}^+$  ions.** For cases of a charged silica interface with no direct contact ion pairs, semipermeable boundaries are introduced to interact only with  $\text{Na}^+$  ions. The boundaries are located at  $z = \pm 5.5$  nm in case of solvent-separated ion pairs or at  $z = \pm 5.175$  nm in case of no ion pairs. The purely repulsive boundaries for  $\text{Na}^+$  ions are described by the truncated LJ with an  $\epsilon = 7.9597 \text{ kcal/mol}$ , a  $\sigma = 0.235 \text{ nm}$ , and a  $r_{\text{cutoff}} = 0.235 \text{ nm}$ .

**Shortcomings of our simple model.** Here, we list the shortcomings of our simplified model in MD simulations. (i) The interface probed in our experiments is unlikely to be entirely void of adsorbed ions at the lowest ionic strength examined here ( $10 \mu\text{M}$ ), which is modeled using 0 M [salt] in our simulations. (ii) Our idealized model neglects many aspects of the experiment, such as acid-base chemistry of the amphoteric SiOH groups, electronic structure, surface reconstructions, dissolved carbonate, protons, hydroxide ions, etc. (iii) Our simple MD model is built upon

a fixed lattice of inert atoms with a fictitious mass, whereas the experiment employs fused amorphous silica. (iv) SPC/E water used in our model is not polarizable.

	$\sigma$ (nm)	$\epsilon$ (kcal/mol)	q (e)
NaCl ions [168]			
Na <sup>+</sup>	0.235	0.13	+1
Cl <sup>-</sup>	0.44	0.1	-1
SPC/E water [12]			
O	0.3166	0.1554	-0.8476
Model silica substrate			
Inert neutral atom [69]	0.2534	7.8	0
Protonated hydroxyl group (Si-OH) [76]			
Si	0.2534	7.8	0.265
O	0.3166	0.1554	-0.7
H	0	0	0.435
Deprotonated hydroxyl group (Si-O <sup>-</sup> ) [76]			
Si	0.2534	7.8	-0.9825
O	0.3166	0.1554	-0.0175

Table 9.1: Lennard-Jones parameters and atomic charge of water, ions, and model silica atoms.

All MD simulations were performed using the LAMMPS software package [140]. In all cases during both equilibration and production runs, the MD trajectories were integrated using the velocity-Verlet methods with a timestep of 1.5 fs. Rigid-body constraints for the water molecules and the terminal silanol groups were enforced using the SHAKE [155]. The Nosé-Hoover thermostat (100 fs relaxation) and the Nosé-Hoover barostat (1000 fs relaxation) along xy directions were applied in all simulations to control the temperature (298.15 K) and the lateral pressure (1 atm). The long-range contribution of Coulomb interaction is treated by particle-particle particle-mesh method [72]. To prevent the long-range contribution of the Coulomb interaction along the z direction, the vacuum region of the equal size to the simulation cell was introduced on both sides along the z direction [166, 28, 204]. All the quantities reported here were averaged using simulation trajectories of 2-4 independent initial configurations over 30 ns after equilibration at least during 10 ns.

### Calculation of total electric potential

We calculated total mean electric potential,  $\Phi_{tot}(z)$ , integrating Poisson equation as follows [166, 28, 204]:

$$\Phi_{tot}(z) = \frac{1}{\epsilon_0} \int_{L_b}^z dz' (z' - z) \rho_{q,s}(z'), \quad (9.1)$$

where  $\epsilon_0$  is vacuum permittivity, and  $L_b = -L_z/2$ , where  $\Phi_{tot}(L_b) = 0$ . To enhance sampling statistics, the symmetrized mean local charge density ( $\rho_{q,s}(z) = 0.5 [\rho_q(z) + \rho_q(-z)]$ ) is used, where  $\rho_q(z)$  is mean local charge density, calculated for all species including water molecules, NaCl ions, Si-OH, and Si-O<sup>-</sup> groups:

$$\rho_q(z; \Delta z) = \frac{1}{L_x L_y \Delta z} \int_{-\frac{L_x}{2}}^{\frac{L_x}{2}} \int_{-\frac{L_y}{2}}^{\frac{L_y}{2}} \int_z^{z+\Delta z} \sum_i q_i \delta(z - z_i) dx dy dz, \quad (9.2)$$

where  $i$  is a running index for species,  $L_x$  and  $L_y$  are simulation box size along x and y coordinates, respectively,  $\Delta z$  (0.02 nm) is the grid size along the z axis, and  $q_i$  and  $z_i$  are charge and z-position of the  $i^{th}$  atom, respectively. The water contribution,  $\Phi_{wat}(z)$ , to the potential is calculated with the assumption of linear polarization [166, 166]:

$$\Phi_{wat}(z) = \frac{-1}{\epsilon_0 (\epsilon_{wat} - 1)} \int_{L_b}^z dz' (z' - z) \rho_{q,s}^{wat}(z'), \quad (9.3)$$

where  $\epsilon_{wat}$  (=70.7) [147] is relative dielectric permittivity of SPC/E water, and  $\rho_{q,s}^{wat}(z)$  the symmetrized mean local charge density of water molecules.

### Calculation of total second-order susceptibilities including water and terminal SiOH contributions

We calculated two contributions of total susceptibility ( $\chi_{tot}^{(2)}$ ): one from water molecules ( $\chi_{wat}^{(2)}$ ), and the other from Si-OH groups ( $\chi_{SiOH}^{(2)}$ ). Both susceptibilities are in units of  $10^{-22} \text{ m}^2 \text{ V}^{-1}$ . First, macroscopic susceptibility tensor elements,  $\chi_{wat}^{(2)}$  in the polarization of zxx (z for out, and x for in) are calculated using the first hyperpolarizability,  $\beta$ , and the Euler rotation matrix, R, relating the space-fixed frame (with subscripts, xyz) to the molecule-fixed frame (with subscripts, abc), following Chen and Singer [28]. Water molecule is placed in the zx plane with the z axis as a bisector. Microscopic Kleinman symmetry (permutation symmetry) is also applied:  $\beta_{abc} = \beta_{bac} = \beta_{bca} = \beta_{cab} = \beta_{cba}$ .

$$\begin{aligned} \chi_{zxx}^{(2)}(z) = \frac{1}{\epsilon_0} \frac{\rho_{wat}(z)}{4} l^{2\omega} (l^\omega)^2 & \left[ (-\beta_{caa} - \beta_{cbb} + 2\beta_{ccc}) \langle -\cos(z) \rangle \right. \\ & \left. + (3\beta_{caa} + 3\beta_{cbb} - 2\beta_{ccc}) \langle -\cos 3\theta(z) \rangle \right], \end{aligned} \quad (9.4)$$

where  $l^\omega$  is the local field correction factor at frequency  $\omega$ , and  $\rho_{wat}(z)$  is local number density of water molecule. The angle  $\theta(z)$  is calculated between the  $z$  axis and a dipole vector of water molecule at  $z = z$ . The factor of -1 in front of cosine functions is included since the surface normal vector points from the aqueous region to the silica region. The values of the first hyperpolarizability are taken from Jansen et al. [77] as in Singer et al. [28]. The susceptibility of water contribution is calculated as follows, integrating over the interfacial region along  $z$  axis and normalized by the local field correction factor.

$$\chi_{wat}^{(2)} = \frac{1}{2} \frac{1}{l^{2\omega} (l^\omega)^2} \int_{z_s}^{z_b} dz \chi_{zxx}^{(2)}(z), \quad (9.5)$$

where  $z_b$  represents the boundary between a SHG-active region and the bulk (a SHG-inactive region), and  $z_s$  represents the boundary between ionic water and the silica surface. Here,  $z_b=0$  nm and  $z_s = -5.77$  nm, where oxygens of the silanol sites are placed.

Second, the contribution of SiOH to the susceptibility,  $\chi_{SiOH}^{(2)}$ , in the same polarization is calculated following the same procedure for the  $\chi_{wat}^{(2)}$ . To calculate  $\beta$ , we perform SiOH placed in the  $zx$  plane. The OH bond is aligned along the  $c$  axis, and the  $b$  axis is orthogonal to the  $ca$  plane and parallel to the  $y$  axis. The first hyperpolarizabilities in the non-resonant (NR) condition for the OH oscillator are calculated using the following relation [118, 119, 66]:

$$\beta_{abc}^{NR} = \frac{1}{2} \beta_{abc}^{static} = \frac{1}{2} |\beta_{abc}^R(\omega \rightarrow 0)| \approx 5.3 \times 10^{-22} \times \frac{d\alpha_{ab}^{(1)}}{dr_{OH}} \frac{d\mu_c}{dr_{OH}} (\text{\AA}^2 \text{m}^2 \text{V}), \quad (9.6)$$

where  $\beta_{abc}^R$  is the first hyperpolarizability in the resonant condition, and  $\beta_{abc}^{static}$  is its magnitude at the static limit. The harmonic-oscillator approximation is applied to calculate  $\beta_{abc}^R$  as follows:

$$\beta_{abc}^R(\omega) \approx \frac{1}{2m_{OH}\omega_{OH}} \frac{d\alpha_{ab}^{(1)}}{dr_{OH}} \frac{d\mu_c}{dr_{OH}} \frac{1}{(\omega_{OH} - \omega + i\Gamma_{OH})}, \quad (9.7)$$

where  $m_{OH}$  is the reduced mass of the OH oscillator,  $\omega_{OH}$  is the frequency of the oscillator,  $\alpha_{ab}^{(1)}$  is  $ab$  element of the linear polarizability tensor,  $\mu_c$  is  $c$  element of the dipole moment vector, and  $\Gamma_{OH}$  is the dissipation from the environment. In this work,  $\omega_{OH} = 3,000 \text{ cm}^{-1}$ , and  $\Gamma_{OH} = (0.5 \text{ ps})^{-1}$  [192]. Both derivatives of the linear polarizabilities and the dipole moment are obtained from Backus et al. [32] and Gageot et al. [134]. Then,  $\chi_{SiOH}^{(2)}$  as a function of the fixed tilt angle ( $\theta_0$ ) is

given as follows:

$$\begin{aligned} \chi_{\text{SiOH}}^{(2)}(\theta_0) = \rho_{\text{SiOH}} \cos^2(\phi) & \left[ (-\beta_{aca} - \beta_{aac} - \beta_{aaa} + \beta_{ccc})(-\cos \theta_0) \right. \\ & + \left( \beta_{aca} + \beta_{aac} + \beta_{aaa} - \beta_{ccc} + \left( \frac{1}{\langle \cos^2 \phi \rangle} - 1 \right) \beta_{cbb} \right) (-\cos^3 \theta_0) \quad (9.8) \\ & \left. + (\beta_{cac} + \beta_{cca} - \beta_{abb})(\sin \theta_0 - \sin^3 \theta_0) - \beta_{acc} \sin^3 \theta_0 \right], \end{aligned}$$

where  $\rho_{\text{SiOH}}$  is the number density of the hydroxyl groups at the silica surface. The azimuthal angle is found uniform so  $\langle \cos^2 \phi \rangle = \langle \sin^2 \phi \rangle = 0.5$ . The tilt angle is considered fixed at  $\theta_0$ . As for  $\chi_{\text{wat}}^{(2)}$ , the factor of -1 in front of cosine functions is included since the surface normal vector points from the aqueous region to the silica region, and the local field correction is not included.

#### Variation of $\chi_{\text{SiOH}}^{(2)}$ with Si-OH

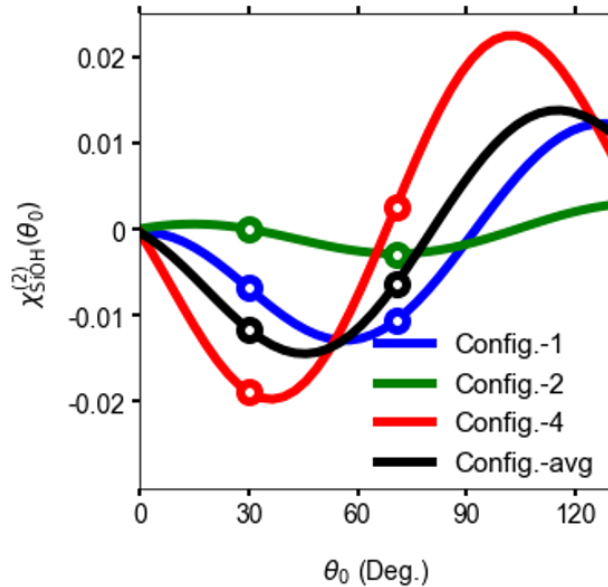


Figure 9.2: Second-order nonlinear susceptibility of a single SiOH group,  $\chi_{\text{SiOH}}^{(2)}$ , as a function of the tilt angle,  $\theta_0$ .

The four different sets of hyperpolarizabilities of an OH oscillator are considered in Fig. 9.2, borrowed from Cyran et al. [32]. The tilt angle ( $\theta_0$ ) is the angle of the OH bond relative to the surface normal vector that is antiparallel to the associated Si-O bond. Each configuration exhibits distinct interaction between the OH bond in the silicic acid and water molecules. Configuration 1 is for an Si-bound OH oscillator that donates the hydrogen bond, while configuration 2 is for the H-bond accepting

OH oscillator. In configuration 4, one Si-bound OH oscillator interacts with two water molecules, both donating and accepting an H-bond from water molecules. The average over each configuration was calculated using the relative population (0.59 for config.-1, 0.01 for config.-2, and 0.4 for config.-4), according to Cyran et al. [32]. In the main text (Table 9.1), SiOH contributions are calculated using config.-4, which is the most relevant to conditions of model silica surface.

## 9.4 Results and Discussion

### Heterodyne-detected SHG measurements on abrupt salinity transitions at fused silica:water interfaces

Fig. 9.3A-B shows SHG measurements on two salinity transitions (first quickly lowered, kept there for some time, and then quickly raised) from the same initial [salt] to two different target [salt], and their return to the original [salt] at constant bulk pH = 5.8. At our flow rate of 5 mL min<sup>-1</sup> and the total cell volume of 2 mL, the ionic strength drop occurs with a half-time of 50 to 60 sec, as evidenced by the green dotted line that tracks the solution conductivity in the flow cell. Note that in each condition, two point estimates of  $\chi^{(2)}$  and  $\Phi(0)_{tot}$  are obtained from the experimentally determined SHG signal and SHG phase; details of the SHG data processing are given in Ref. [110, 111].

For the first five minutes, the 0.1 M to 10  $\mu$ M jump (large salinity change) results in a continuous change in the surface potential to increasingly negative values, as one may expect. In contrast,  $\chi^{(2)}$  first rises, reaches a maximum at ca. 3 minutes, and then decreases to a constant value at longer times. This time scale is comparable to what was recently reported from time-resolved X-ray reflectivity measurements of ion exchange between the inner and outer Helmholtz plane over aqueous mica interfaces [92]. The discontinuity in the  $\chi^{(2)}$  and  $\Phi(0)_{tot}$  values that occurs at ca. 7 minutes is due to the fast, in-line conductivity meter reaching its sensitivity limit at that time. Off-line measurements of the 10  $\mu$ M eluent shows that the conductivity at that point should arrive at approximately 2  $\mu$ S cm<sup>-1</sup> in the flow cell. The return jump is quick, with the changes in the  $\chi^{(2)}$  and  $\Phi(0)_{tot}$  values not resolvable using our existing time resolution of 12 seconds. Hysteresis is not observed.

The 0.1 M to 1 mM jump (low salinity change) shows the expected decrease in surface potential along with a monotonic increase in  $\chi^{(2)}$  until ca. double its starting value. The return jump results in quick return to the starting values, just like in the initial jump. Finally, the 1 mM to 10  $\mu$ M jump results in the expected

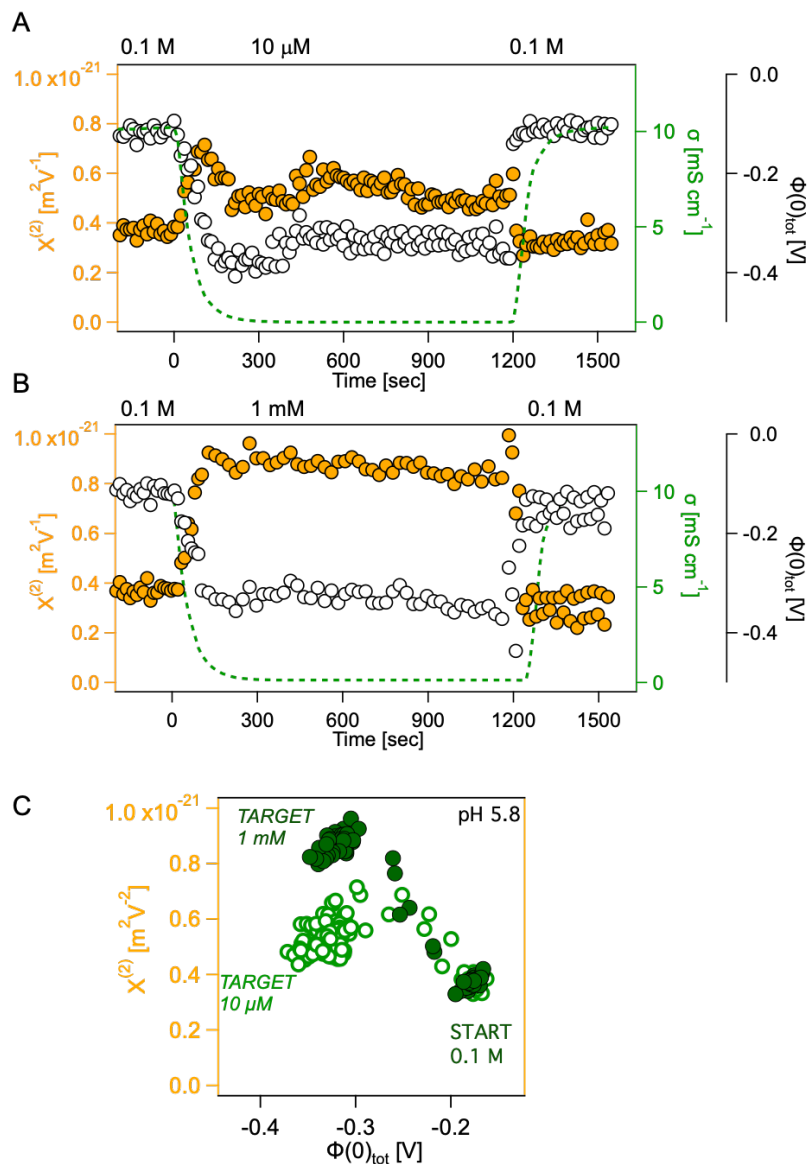


Figure 9.3: Heterodyne-detected SHG measurements on abrupt salinity transitions. (a-b) Point estimates of  $\chi^{(2)}$  (orange) and  $\Phi(0)_{tot}$  (blue) obtained from the experimentally determined SHG signal and SHG phase for ionic strength conditions indicated. (c) Correlation plot of  $\chi^{(2)}$  and  $\Phi(0)_{tot}$  for 0.1 M to 10  $\mu$ M jump (light green) and 0.1 M to 1 mM NaCl (dark green). Portion shown is for forward (high to low [salt]) jumps only, the results for the return jumps are omitted.

change in surface potential to more negative values, while  $\chi^{(2)}$  undergoes a brief small increase followed by a slightly smaller value than what is observed at the start. The return jumps for these experiments show again no hysteresis.

Fig. 9.3C displays a  $\chi^{(2)} : \Phi(0)_{tot}$  correlation plot. It is immediately clear that  $\chi^{(2)}$

and  $\Phi(0)_{tot}$  are linearly correlated for the entirety of the 0.1 M to 1 mM jump, while the data for the 0.1 M to 10  $\mu$ M target condition shows considerable curvature in the correlation plot. As the current consensus in the field is that  $\chi^{(2)}$  and  $\Phi(0)_{tot}$  report on structure and dynamics in the Stern and diffuse layers, respectively, we conclude that the two do not necessarily act in concert, depending on the path by which one changes the ionic strength.

The experimental results raise the question in regards to the connection between the interfacial EDL structure and the interfacial potential. Moreover, under what conditions do the interfacial potential and interfacial structure change in lockstep, and when do they not?

### **MD simulation results at aqueous silica interfaces**

We carry out classical MD simulations of aqueous silica interfaces to explore what structures might recapitulate, at least qualitatively, the different  $\chi^{(2)}$  and  $\Phi(0)_{tot}$  point estimates obtained from the HD-SHG experiments, addressing the questions in the previous section. We follow the approach by Chen and Singer for computing non-resonant  $\chi^{(2)}$  estimates from interfacial water molecules,  $\chi_{water}^{(2)}$ , and now include contributions of the terminal silanol groups,  $\chi_{SiOH}^{(2)}$ . While the experiments report the total  $\chi^{(2)}$  and  $\Phi(0)_{tot}$ , the computational approach disentangles the contributions from the silanol groups and the water molecules.

### **Ion-oxide interaction: Contact ion pairs vs. solvent-separated ion pairs**

The jumps from high to low ionic strength should involve  $\text{Na}^+$  ion desorption [136]. We therefore constructed several plausible interfacial models having a varying proportion of  $\text{SiOH}:\text{SiO}^-:\text{Na}^+:\text{H}_2\text{O}:\text{NaCl}$  (Fig. 9.4A). To simulate surfaces in contact with 0.1 M salt, we placed water containing 0.1 M NaCl in contact with a silica surface having  $\text{SiO}^-$  groups to which  $\text{Na}^+$  cations are coordinated as a direct contact ion pair (CIP). The 1 mM experiment is not feasible to simulate in general, so we employed instead an ion-free aqueous phase in contact with the same number of CIPs we modeled in the 0.1 M case. This model choice is motivated by the notion that the Debye length at 1 mM is around 10 nm [9], resulting in a considerable number of ions at the interface. We also contrasted contact with solvent-separated ion pairs (SSIPs). Finally, we simulated the 10  $\mu$ M experiments using an ion-free aqueous phase in contact with the same negatively charged silica surface we modeled in the 0.1 M case that is, however, void of interfacial  $\text{Na}^+$  cations (no ion pairs, "NIP;")

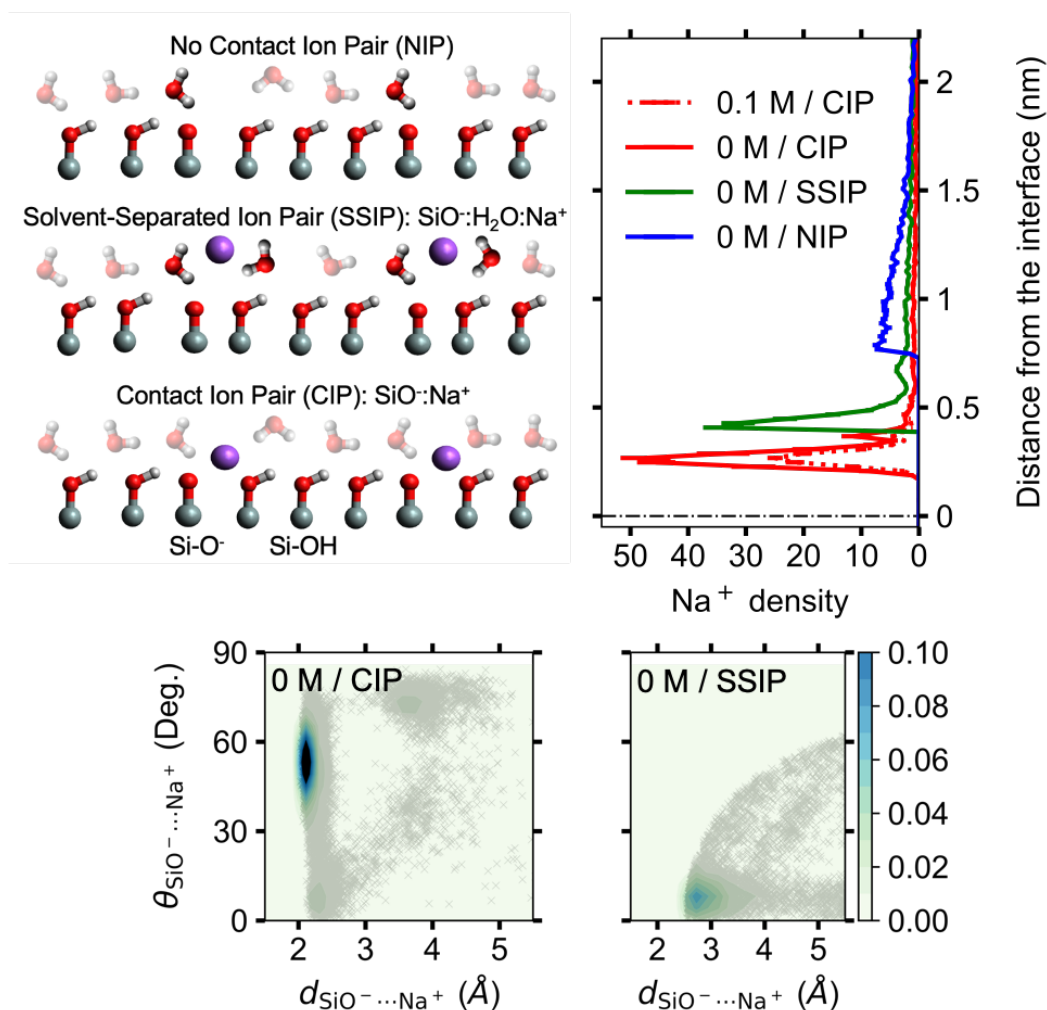


Figure 9.4: Atomistic simulation model and interfacial ion distribution. (Top left) Atomistic models used in our analysis. (Top right) Calculated distributions of Na<sup>+</sup> ion at the silica surface for the four situations examined. (Bottom) Angle:distance probability density plots at zero NaCl concentration for the contact ion (left) and solvent-separated (right) ion pairs. See text for details.

charge neutrality is provided by Na<sup>+</sup> ions confined deep inside the aqueous phase). In the cases of the solvent-separated and no-ion pairs, semipermeable boundaries (see Section 9.3) are included to prevent Na<sup>+</sup> ions from reaching the interface.

To further describe the CIP and SSIP cases, we present Fig. 9.4B-D, which show the Na<sup>+</sup> ion density and the SiO<sup>-</sup> ··· Na<sup>+</sup> distance probability densities as a function of SiO<sup>-</sup> ··· Na<sup>+</sup> distance from the surface, respectively. The results follow the expected trends, with the solvent-separated pair distance being further apart than that of the direct contact pairs. In addition to the SiO<sup>-</sup> ··· Na<sup>+</sup> distance differences,

the angle:distance correlation plots for the  $\text{SiO}^- \cdots \text{Na}^+$  ion pairs indicate a most probable  $\text{SiO}^- \cdots \text{Na}^+$  angle of  $45^\circ$  to  $70^\circ$  for the CIPs, while the SSIPs show most probable  $\text{SiO}^- \cdots \text{Na}^+$  angles around  $10^\circ$ .

### Computed second-order non-linear susceptibility and orientational ordering of interfacial water molecules

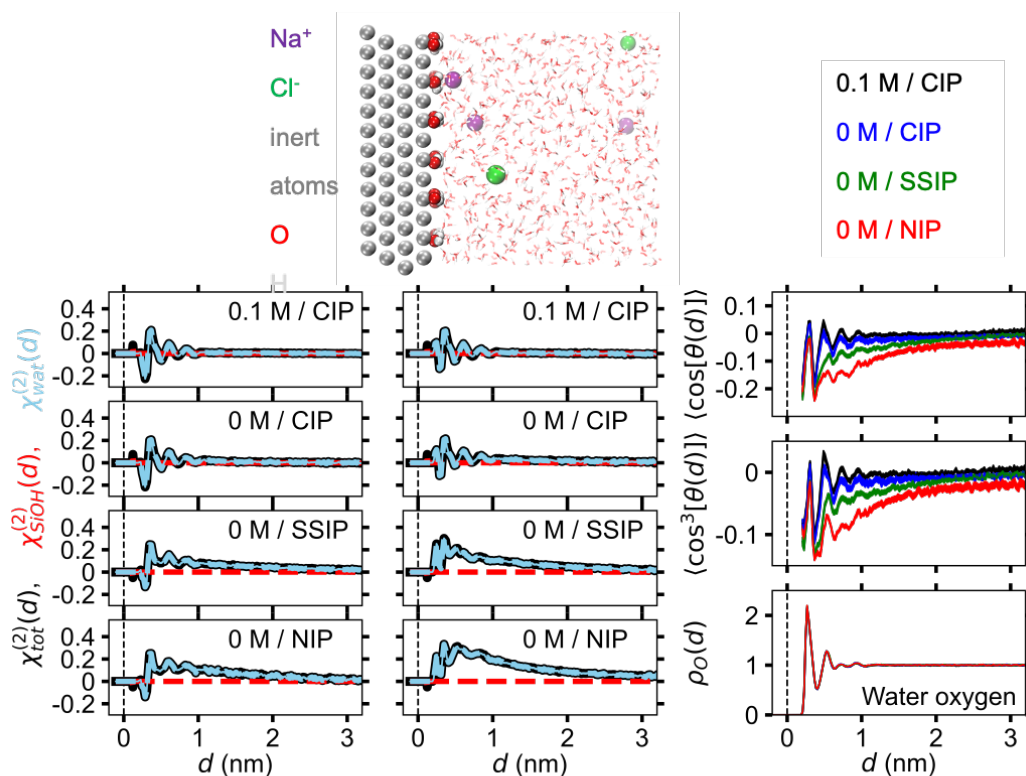


Figure 9.5: Second-order nonlinear susceptibility estimates computed for the various models and scenarios examined as a function of distance from the interface (Left and Center). First and third moments of the water orientation angle and water oxygen density as a function of distance from the interface (Right) for the various models and scenarios examined.

We then computed  $\chi_{water}^{(2)}$ ,  $\chi_{SiOH}^{(2)}$  and  $\chi_{tot}^{(2)}$  as well as  $\Phi(0)_{water}$  and  $\Phi(0)_{tot}$  for all four cases (0.1 M/CIP, 0 M/CIP, 0 M/SSIP, and 0 M/NIP) and for each of the three surface charge densities (Table 9.2; to connect to the s-in/p-out polarization combination used in the experiments, we computed the zxx tensor element). In all three 0 M cases, the local water density remains the same. Contributors to  $\chi_{tot}^{(2)}$ , such as the  $\text{Na}^+$ ,  $\text{Cl}^-$ , and  $\text{SiO}^-$  groups, are neglected. We instead limit our calculations to

the contributions of the much more abundant SiOH groups and the water molecules, i.e.,  $\chi_{tot}^{(2)} = \chi_{SiOH}^{(2)} + \chi_{water}^{(2)}$ .

The calculated  $\chi_{water}^{(2)}$  values (Table 9.2, Figs. 9.4- 9.5) increase upon removal of the  $\text{Na}^+$  ions from the surface  $\text{SiO}^-$  groups due to the decreased screening of the DC field from the surface  $\text{SiO}^-$  groups. On the silica side, however, desodiation accompanies a reorientation of the adjacent SiOH groups towards a more upright configuration, as recent electronic structure calculations coupled to MD of the  $\alpha$ -quartz:water interface by Pfeiffer-Laplaud and Gaignot report [136]. We therefore computed  $\chi_{SiOH}^{(2)}$  using molecular hyperpolarizabilities,  $\beta$ , obtained with their density functional theory approach [32], for their silica:water cluster as a function of the SiO–H tilt angle relative to the surface normal. We note that the calculation of  $\chi_{water}^{(2)}$  from our MD runs does not include any effects of reorientation of interfacial SiOH groups due to desodiation. The computed  $\chi_{SiOH}^{(2)}$  value (Table 9.2) is indeed decreased relative to  $\chi_{water}^{(2)}$  when the interface is void of ions. The maximum  $\chi_{total}^{(2)}$  value calculated from the atomistic simulations corresponds to a state in which the interface is void of ions in the model.

Using our simulation box, which is shown in Fig. 9.5 for the medium charge density we studied ( $-0.04 \text{ C m}^{-2}$ ), we also computed the  $\chi_{water}^{(2)}$  and  $\chi_{tot}^{(2)} = \chi_{SiOH}^{(2)} + \chi_{water}^{(2)}$  values (in unites of  $10^{-22} \text{ m}^2 \text{ V}^{-1}$ ) as a function of distance,  $z$ , up to 3 nm from the interface, for the two low charge densities we considered (Fig. 9.5). Consistent with the entries in Table 9.2, we find that the resulting  $\chi_{SiOH}^{(2)}$  for both CIP cases is positive, while that for the SSIP and NIP cases is negative, irrespective of surface charge density ( $\sigma_0$ ). Relative to the  $\text{Na}^+$ -saturated case (0.1 M/CIP), the main differences in  $\chi_{tot}^{(2)}$  occur for the bare,  $\text{Na}^+$ -free system (0 M/NIP), and the SSIP model (0 M/SSIP). Additional differences occur in the innermost water layer, where distance-dependent variations in the water tilt angles for low vs high charge density results in one additional undulation of the second-order nonlinear susceptibility values. Fig. 9.5 also shows that as the interface becomes void of  $\text{Na}^+$  ions,  $\chi_{tot}^{(2)}$  increases. This increase is consistent with more pronounced net alignment of water molecules as fewer and fewer ions are present at the interface, as demonstrated by the  $z$ -dependence of the first moment,  $\cos(\theta)$ , of the angle distribution. Fig. 9.5 also shows that the skewness of the distribution (reported by the third moment), is close to zero at 2 nm distance and beyond. Despite the distinct water orientation distributions, the local water density ( $\rho_O(d)$ ) remains the same in all three 0 M cases (Fig. 9.5). Taken together, the results indicate that the net alignment of the

water molecules does not extend far into the bulk phase, even when the interface is void of any ions. We can then propose that the diffuse layer contribution to the SHG process, again reported by the  $\chi^{(3)}\Phi(0)_{tot}$  product, is likely due to the polarization of water molecules in the diffuse layer as opposed to their alignment.

$\sigma_0 = -0.02 \text{ C m}^{-2}$				
	0.1 M / CIP	0 M / CIP	0 M / SSIP	0 M / NIP
$\Phi(0)_{tot}$ [V]	-0.52	-0.52	-0.58	-0.59
$\Phi(0)_{wat}$ [V]	-0.016	-0.020	-0.056	-0.061
$\chi_{wat}^{(2)}$ [ $10^{-22} \text{ m}^2\text{V}^{-1}$ ]	0.015	0.037	0.183	0.24
$\chi_{SiOH}^{(2)}$ [ $10^{-22} \text{ m}^2\text{V}^{-1}$ ]	0.075	0.075	-0.05	-0.05
$\chi_{tot}^{(2)}$ [ $10^{-22} \text{ m}^2\text{V}^{-1}$ ]	0.09	0.112	0.133	0.19
$\sigma_0 = -0.04 \text{ C m}^{-2}$				
	0.1 M / CIP	0 M / CIP	0 M / SSIP	0 M / NIP
$\Phi(0)_{tot}$ [V]	-0.57	-0.58	-0.67	-0.72
$\Phi(0)_{wat}$ [V]	-0.017	-0.032	-0.072	-0.12
$\chi_{wat}^{(2)}$ [ $10^{-22} \text{ m}^2\text{V}^{-1}$ ]	0.021	0.08	0.25	0.41
$\chi_{SiOH}^{(2)}$ [ $10^{-22} \text{ m}^2\text{V}^{-1}$ ]	0.073	0.073	-0.19	-0.19
$\chi_{tot}^{(2)}$ [ $10^{-22} \text{ m}^2\text{V}^{-1}$ ]	0.094	0.153	0.06	0.22
$\sigma_0 = -0.08 \text{ C m}^{-2}$				
	0.1 M / CIP	0 M / CIP	0 M / SSIP	0 M / NIP
$\Phi(0)_{tot}$ [V]	-0.66	-0.68	-0.82	-0.92
$\Phi(0)_{wat}$ [V]	-0.022	-0.037	-0.095	-0.18
$\chi_{wat}^{(2)}$ [ $10^{-22} \text{ m}^2\text{V}^{-1}$ ]	0.04	0.1	0.34	-0.92
$\chi_{SiOH}^{(2)}$ [ $10^{-22} \text{ m}^2\text{V}^{-1}$ ]	0.068	0.068	-0.45	-0.45
$\chi_{tot}^{(2)}$ [ $10^{-22} \text{ m}^2\text{V}^{-1}$ ]	0.108	0.168	-0.11	0.22

Table 9.2: Electric potentials and second-order susceptibilities at various surface-charge densities ( $\sigma_0$ ) and NaCl concentrations (0.1 M or 0 M). Three different conditions for interfacial  $\text{Na}^+$  ions are investigated: CIP represents contact pairs of  $\text{SiO}^- \cdots \text{Na}^+$ , SSIP represents solvent-separated contact pairs of  $\text{SiO}^-$  and  $\text{Na}^+$ , NIP represents the case of no interfacial  $\text{Na}^+$ .

Table 9.2 shows that while the computational estimates qualitatively recapitulate the results obtained from the experiments, they are about 10 times smaller in  $\chi_{tot}^{(2)}$  when compared to the experiment, depending on surface charge density ( $\sigma_0$ ). Likewise, the total computed surface potential does not change by as much as it does in the experiment, even though it follows the expected trend (lower potential at higher salt concentration, or at lower  $\sigma_0$ ). We attribute this mismatch to the lack of an electronic structure calculation in our all-classical MD trajectories, the simplifying

assumptions in our largely rigid silica model, possible contributions to  $\chi_{tot}^{(2)}$ , from  $\text{Na}^+$ ,  $\text{Cl}^-$ , and  $\text{SiO}^-$ , and the use of a cubic crystalline bulk of inert atoms as opposed to amorphous bulk silica. Yet, the electrostatic potentials due to only the water molecules listed in Table 9.2 are comparable to those reported by Chen and Singer [28], and span the range of the experimentally derived point estimates of  $\Phi(0)_{tot}$ . Moreover, we find qualitative agreement between the experimental and molecular dynamics results regarding  $\chi_{tot}^{(2)}$ , as discussed next.

### Molecular insights from calculated SHG responses to the decoupled kinetics of Stern and diffuse layers

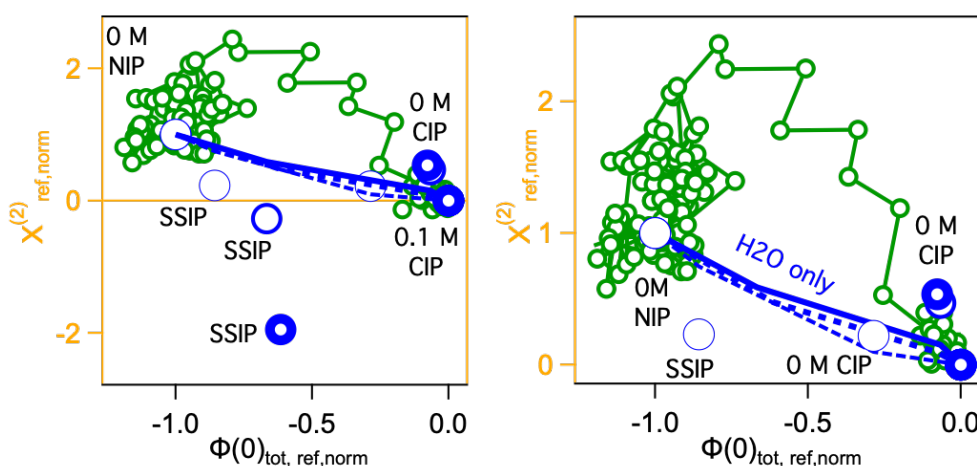


Figure 9.6: Comparison between experiment and simulation. (Left)  $\chi_{tot}^{(2)} : \Phi(0)_{tot}$  correlation plot after normalization and referencing overlaying the experimental (green circles) and model-computed (blue circles) results. (Right) Same data but showing only the positively signed portion on the ordinate. Thicker the blue circles indicate higher charge density in the model ( $-0.02$ ,  $-0.04$ , and  $-0.08 \text{ C m}^{-2}$ ). Blue lines show the  $\chi_{water}^{(2)}$  results only. See text for details.

For the 0.1 M to 10  $\mu\text{M}$  jump, we referenced the experimental and computational point estimates of  $\chi_{tot}^{(2)}$  and  $\Phi(0)_{tot}$  to their smallest value in a given experiment, and then normalized them to their maximum value. Our referencing and normalization approach sets the  $\chi_{tot}^{(2)}$  and  $\Phi(0)_{tot}$  point estimates at the initial (0.1 M salt) and final (10  $\mu\text{M}$  water) to 0 and 1, respectively. Fig. 9.6A shows that the approach is useful for identifying atomistic model scenarios that do or do not recapitulate the experimental  $\chi_{tot}^{(2)}$  and  $\Phi(0)_{tot}$  point estimates. Specifically, we find that the SSIPs do not reproduce the experimental trends, whereas the CIPs at zero salt do, especially for the intermediate and high surface charge densities. Zooming in on

the  $(\chi_{tot, ref\ norm}^{(2)}, \Phi(0)_{tot, ref\ norm})$  pairs matching the experiment (Fig. 9.6B), we find that including  $\chi_{SiOH}^{(2)}$  into the calculation of  $\chi_{tot}^{(2)}$ , along with  $\chi_{water}^{(2)}$ , better matches the experiments than just  $\chi_{water}^{(2)}$  alone (unlike it was the case for  $\Phi(0)_{tot}$  vs  $\Phi(0)_{water}$ ). The results are consistent with an initial condition in which the surface contains a number of CIPs at high [salt], then transitions to the same, or a slightly smaller, number of CIPs as the ionic strength drops (modeled by setting the salt concentration to zero in the atomistic model), and finally arrives at no more CIPs as the final condition of 10  $\mu\text{M}$  [salt]. CIPs are evidently more important contributors than SSIPs to explain the experimental observations.

In summary, a drop in the ionic strength, as considered in our present high-to-low ionic strength jumps, expands the diffuse layer and increases the interfacial potential towards more negative values as fewer and fewer mobile ions are present in the diffuse layer to screen surface charges. The structure of the Stern layer should change as specifically bound sodium ions (CIPs in our analysis) leave the surface to be replaced by protons, both of which are processes that may either coincide with the diffuse layer expansion ("lockstep response") or lag it ("not in lockstep"). Since high  $\chi_{tot}^{(2)}$  values in our MD model indicate surface sites void of  $\text{Na}^+$  ions, we posit that the nonlinearities in the  $\chi_{tot}^{(2)}:\Phi(0)_{tot}$  correlation plots shown in Figs. 9.3 and 9.6 suggest that desodiation and surface protonation begin before the diffuse layer has fully expanded, as opposed to the other way around, when jumping from 0.1 M to 10  $\mu\text{M}$ . These results are likely to be influenced by how strongly the ions in the inner Helmholtz plane are bound, indicating that they should be subject to ion specific effects, like those characterized by the Hofmeister series [64].

## 9.5 Conclusion

We utilize atomistic MD simulations to provide molecular insights on the structure and dynamics of EDL layers at an aqueous silica interface, recapitulating the results of heterodyne-detected SHG measurements.

In experiments, we transition an aqueous solution over fused silica substrate from high (0.1 M) to low (10  $\mu\text{M}$ ) salt concentration and back while maintaining the bulk solution pH at 5.8. Interestingly, the kinetics of the SHG responses (the second-order nonlinear susceptibility,  $\chi_{tot}^{(2)}$ , which encodes structural information about the Stern layer, and the interfacial potential,  $\Phi(0)_{tot}$ , which encodes information about the diffuse layer) is found to depend on how big the change in ionic strength is. Along with ionic strength jumps between 1 mM and 0.1M, we provide concrete

evidence that the dynamics in the Stern and Diffuse layers are decoupled from one another under some conditions we surveyed (large change in ionic strength), while they are strongly coupled under others (smaller change in ionic strength).

Atomistic simulations suggest a prominent role of CIPs, as opposed to SSIPs in the Stern layer, in determining whether the SHG responses in EDL layers are coupled or decoupled. We propose a scenario that the slow desodiation of CIPs from the silica surface accompanies the structural reorganization of the terminal silanol groups, which is supported by MD simulation results that the experimentally measured  $\chi^{(2)}$  is likely to include both contributions of surface silanols and interfacial water molecules.

Despite several shortcomings in our simulation model (Section 9.3), we are excited to lay out a path for connecting the structural and electrostatic information from the experiments to atomic structure. Likewise, the results presented here may serve for further analysis of existing atomistic models of aqueous silica interfaces, as  $\chi_{tot}^{(2)}$  and  $\Phi(0)_{tot}$  are straight-forward to obtain from already completed calculations. Taken together, our combined computational and experimental approach opens a door to quantifying interfacial structure and electrostatics at charged, buried aqueous interfaces in real time.

## 9.6 Appendix

### Contributions of bulk oxide defects and surface roughness to SHG phase and angle measurement

Data and content in this section have been published as Ref. [110]. The author participated in conducting computations, discussing the computation results, and preparing a draft.

Recently, we proposed the existence of a nonlinear susceptibility term that is associated with a  $90^\circ$  phase shift to recapitulate experimental data in non-resonant second harmonic generation phase and amplitude measurements [110]. To do so, we needed to show minor contributions of (i) bulk oxide defects and (ii) oxide surface roughness, both of which are supported by computations as is explained below.

Fused silica contains impurities, for which we considered using one-dimensional finite element calculations (0.01 nm steps, see computational methods below) of a solid having a relative permittivity of 3.8 [99], and 100 ppb charged impurities [2] with vacuum on one side and a 0.1 M aqueous salt solution on the other side. The surface charge density is set to  $-0.015 \text{ C m}^{-2}$ , and the relative permittivity of the 0.1

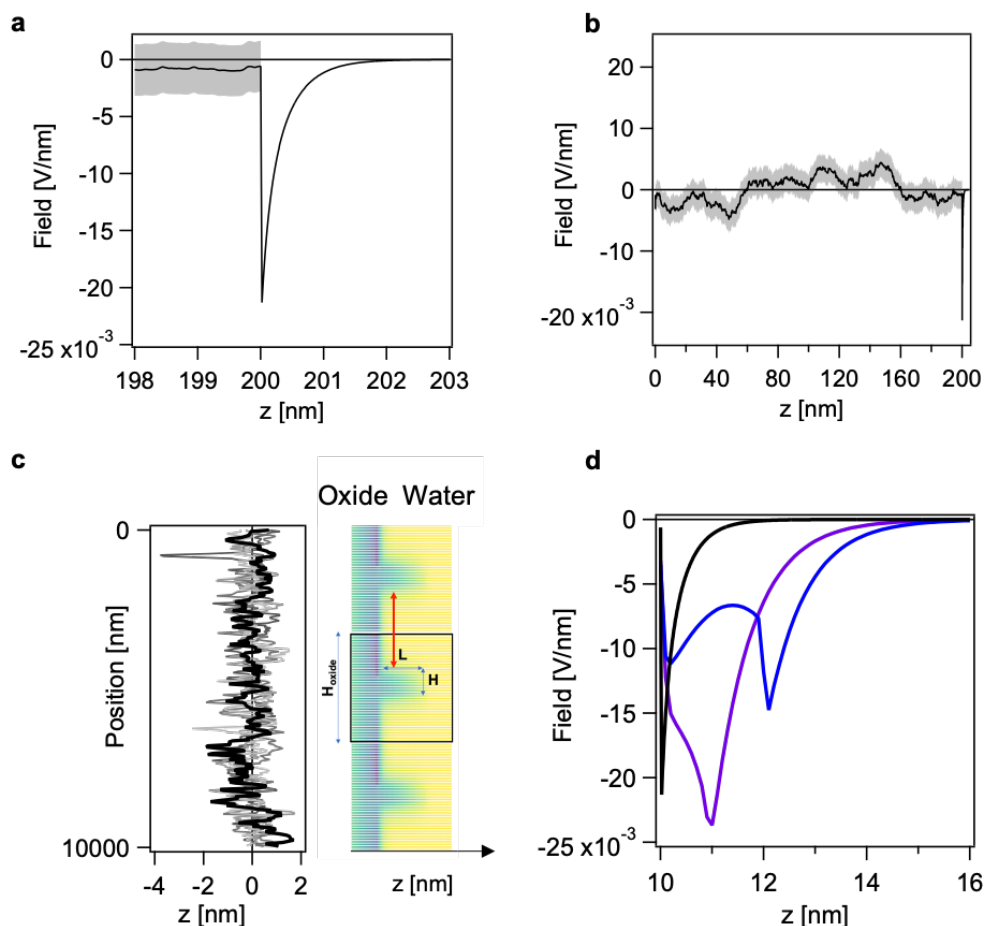


Figure 9.7: Calculated electric field for model silica:water interfaces. (a, b) Electrostatic field across the fused silica:water interface from finite element calculations. The silica contains 100 ppm of charged impurities and the aqueous phase is at 0.1 M [NaCl]. The relative permittivity in the aqueous phase is 78. (c, d) Height vs. position profiles from several atomic force microscopy lines scans across the flat side of our fused silica hemispheres, primitive cell used for finite element calculations shown in black box nested in between its periodic images, and electrostatic field across an atomically smooth (black line) and rough (purple line for  $L=H=1$  nm features, blue line for  $L=H=2$  nm features) fused silica:water interface. Horizontal dashed line depicts the E-field value used for the 1-nm wide rough region. The relative permittivity of the aqueous phase is 78. The surface charge density is  $-0.015 \text{ C m}^{-2}$ .

M salt solution is taken to be 78 [9]. Averaged over 200 nm of solid, and  $10^6$  random impurity realizations, the model shows that the electric field is  $-100 \text{ kV m}^{-1} \pm 2 \text{ MV m}^{-1}$ , i.e. statistically indistinguishable from zero (Fig. 9.7A-B). Nevertheless, using the point estimate of  $-100 \text{ kV m}^{-1}$  between  $z=0$  nm, the laser focus position, to  $z=-b=-0.0127$  m, the hemisphere's edge, we obtain  $\chi_{dc, \text{SiO}_2}^{(2)} = 8 \times 10^{-25} \times e^{-145i} \text{ m}^2 \text{ V}^{-2}$ ,

which is again much smaller than the  $\chi_{water}^{(3)}$  contribution. Note that we can also integrate  $E_{DC}(z)$  obtained from the finite element calculations over 200 nm, 2 x the coherence length in our experiments, which yields -0.013 V, three times larger than the result obtained using the field point estimate of  $-100 \text{ kV m}^{-1}$ , arriving at the same conclusion. Our two analyses indicate that the bulk silica contribution is not enough to explain the pH-dependent SHG phase observed at short Debye lengths (0.5 M [NaCl]), at least within the electric dipole approximation.

We also considered the impact on the third-order contribution due to the finite roughness of the surface of the fused silica hemispheres. Atomic force microscopy shows the surface to have a root-mean-square roughness of 0.4 nm, with +/- 1 nm variation in surface height (Fig. 9.7C). We therefore assigned the aqueous:solid interface a width,  $\varpi$ , of 1 nm, as opposed to being atomically flat. We treat this 1 nm wide region with a third-order susceptibility taken to be the geometric mean of  $\chi_{water}^{(3)}$  and  $\chi_{SiO_2}^{(3)}$ , i.e.  $\chi_{\varpi}^{(3)} = 6 \times 10^{-22} \text{ m}^2 \text{ V}^{-2}$ . The second-order dc-contribution is then

$$\chi_{dc,\varpi}^{(2)} = \chi_{\varpi}^{(3)} \int_{\varpi=-1nm}^0 E_{DC}(z) e^{i\Delta k_z z} dz, \quad (9.9)$$

where  $E_{DC}(z)$  can be approximated, again guided by finite element calculations (Fig. 9.7D), to be constant at  $E_{DC}(z) = -\frac{\Phi(0)}{1 \times 10^{-9}} \text{ V m}^{-1}$  over the 1-nm wide rough interfacial region. The second-order dc contribution to the second order nonlinear susceptibility then becomes  $\chi_{dc,\varpi}^{(2)} = -\Phi(0) \times \frac{6 \times 10^{-22} \text{ m}^2 \text{ V}^{-2}}{1 \times 10^{-9} \text{ m}} \int_{\varpi=-1nm}^0 E_{DC}(z) e^{i\Delta k_z z} dz = -\Phi(0) \times 6 \times 10^{-22} \times e^{-0.3i} \text{ m}^2 \text{ V}^{-1}$ , having, again, an imaginary part that is insufficient to explain the observed pH-dependent SHG phase shift at high ionic strength.

### Finite-element calculation methods

The one-dimensional Poisson equation was numerically solved for an oxide in contact with ionic water of  $0.1 \text{ mol L}^{-1}$  NaCl using the Newton-Raphson iteration method [22, 60].

$$\frac{d^2\Psi(x)}{dx^2} = \begin{cases} -\frac{e[\delta(x_p) - \delta(x_n)]}{\epsilon_{ox}\epsilon_0}, & \text{if } x \leq L_{ox} \\ -\frac{e\rho_b}{\epsilon_w\epsilon_0} [e^{-e\beta\Psi} + e^{e\beta\Psi}], & \text{if } L_{ox} < x < L \end{cases} \quad (9.10)$$

Here,  $\Psi(x)$  is the one-dimensional electrostatic potential, and  $L$  (= 220 nm) is the total length of the system, including a 200 nm thick oxide and a 20 nm thick water region. The water-oxide interface is located at  $x = L_{ox} = 200 \text{ nm}$ . The vacuum permittivity is  $\epsilon_0 = 8.854 \times 10^{-12} \text{ F m}^{-1}$ , the relative dielectric permittivities are  $\epsilon_{ox} = 4$  for the oxide and  $\epsilon_w = 78$  for the ionic water,  $e$  is the elementary charge, and  $\beta = k_B T^{-1}$

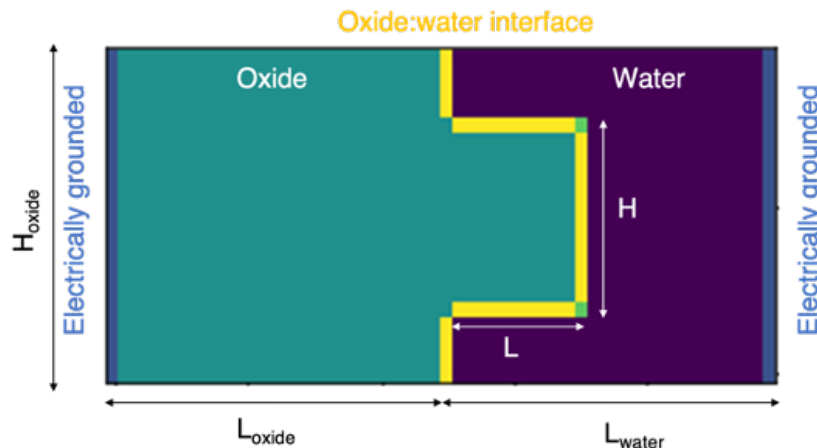


Figure 9.8: Finite element calculation model for a corrugated oxide:water interface. The rough oxide:water interface is modeled using a nanoscale dendrite of height ( $H$ ) and length ( $L$ ), represented by the yellow region. Bright green elements are the dendrite corners where the oxide:water boundary is along both the  $x$ - and  $y$ -axes.

with  $T$  being the temperature (300 K) and  $k_B$  being the Boltzmann constant. The bulk ion density in the ionic water is  $\rho_b = 0.1 \text{ mol L}^{-1}$  with monovalent cations and anions whose thermal motion is incorporated using the Boltzmann factor. The oxide is modeled to include a pair of positively and negatively charged point defects that decrease the electric field inside the oxide. A positively charged defect ( $x = x_p$ ) is randomly placed inside the oxide region, followed by a random insertion of a negatively charged defect ( $x = x_n$ ) according to a Poisson distribution having an average of 100 nm, so the distance between the defects is 100 nm on average to recapitulate the 100 ppm defect density in commercially available silica.

Three boundary conditions are applied in our model using the fact that the oxide surface in contact with water is lightly charged and both the oxide and water boundaries are electrically grounded. We employ (i) the Dirichlet condition with  $\Psi(x = 0) = 0$  at the oxide end, (ii) the Dirichlet condition with  $\Psi(x = L) = 0$  at the water end, and (iii) the Neumann condition at the aqueous oxide interface ( $x = L_{ox}$ ) as follows:

$$\epsilon_{ox} \left. \frac{d\Psi(x)}{dx} \right|_{x=L_{ox}} - \epsilon_w \left. \frac{d\Psi(x)}{dx} \right|_{x=L_{ox}} = \frac{Q_s}{\epsilon_0}, \quad (9.11)$$

where  $Q_s$  ( $= -0.015 \text{ C m}^{-2}$ ) is the oxide surface charge density. The differential equation is solved by discretizing the space with finite elements whose size is 0.01 nm along the  $x$ -axis. Note that 0.01 nm is short enough to properly recapitulate the Debye screening length (0.39 nm at  $1 \text{ mol L}^{-1}$  NaCl) in the water region. The

iteration is terminated once  $L_2$ -norm of the solution is less than  $10^{-6}$ . The electric potential and the associated electric field is averaged over  $10^6$  realizations with the random insertion of the defects inside the oxide.

The two-dimensional linearized Poisson-Boltzmann equation was numerically solved for rough oxide:water interfaces (Fig. 9.8), modeled by a small dendrite of height ( $H$ ) and length ( $L$ ):

$$\left(\frac{d^2}{dx^2} + \frac{d^2}{dy^2}\right)\Psi(x, y) = \begin{cases} 0, & \text{in the oxide region} \\ \kappa^2\Psi(x, y), & \text{in the water region,} \end{cases} \quad (9.12)$$

where  $\kappa (= \sqrt{\frac{2e^2\beta\rho_b}{\epsilon_w\epsilon_0}})$  is the inverse of Debye screening length and  $\Psi(x, y)$  is the two-dimensional electrostatic potential. Here, the length of each region is fixed with a 10 nm thick oxide and a 20 nm thick water region. The height of the oxide region varies according to the height of the dendrite:  $H_{oxide} = 2H$ . Other parameters are kept the same as in the one-dimensional model above. Boundary conditions are applied as in the one-dimensional model. We employ (i) the Dirichlet condition with  $\Psi(x, y) = 0$  at both oxide and water ends (blue line in Fig. 9.8), and (ii) the Neumann condition at the corrugated aqueous oxide interface,  $\partial$ , (yellow line in Fig. 9.8) as follows:

$$\epsilon_{ox} \left(\frac{d}{dx} + \frac{d}{dy}\right)\Psi_{ox}(x, y) \Big|_{\partial} \cdot \hat{n} - \epsilon_w \left(\frac{d}{dx} + \frac{d}{dy}\right)\Psi_w(x, y) \Big|_{\partial} \cdot \hat{n} = \frac{Q_s}{\epsilon_0}. \quad (9.13)$$

Here,  $\hat{n}$  is the unit normal vector pointing the water region from the oxide region. The differential equation is solved by discretizing the space with finite elements whose size is 0.1 nm along both x- and y-axes. Note that 0.1 nm is still short enough to properly recapitulate the Debye screening length (0.39 nm at  $0.1 \text{ mol L}^{-1}$  NaCl) in the water region. The linear equation is solved using Jacobi and Gauss-Seidel methods with successive over-relaxation [60]. The relaxation method is terminated once  $L_2$ -norm of the solution is less than  $10^{-12}$ .

## BIBLIOGRAPHY

- [1] URL: <https://www.energy.gov/eere/articles/energy-department-awards-more-20-million-wave-and-tidal-energy-projects>.
- [2] URL: <https://www.corning.com/media/worldwide/csm/documents/5bf092438c5546dfa9b08e423348317b.pdf>.
- [3] Adha Sukma Aji et al. “High output voltage generation of over 5 V from liquid motion on single-layer MoS<sub>2</sub>.” In: *Nano Energy* 68 (2020), p. 104370.
- [4] Michael P. Allen and Dominic J. Tildesley. *Computer Simulation of Liquids*. 1989.
- [5] Seong Jin An et al. “The state of understanding of the lithium–ion–battery graphite solid electrolyte interphase (SEI) and its relationship to formation cycling”. In: *Carbon* 105 (2016), pp. 52–76.
- [6] Yongling An et al. “Lithium metal protection enabled by in-situ olefin polymerization for high-performance secondary lithium sulfur batteries.” In: *Journal of Power Sources* 363 (Sept. 2017), pp. 193–198.
- [7] M. Anji Reddy and M. Fichtner. “Batteries based on fluoride shuttle.” In: *Journal of Materials Chemistry* 21.43 (2011), pp. 17059–17062.
- [8] Michael Armand and Jean-Marie Tarascon. “Building better batteries.” In: *Nature* 451.7179 (Feb. 2008), pp. 652–657.
- [9] Peter Atkins and Julio De Paula. *Atkins’ Physical Chemistry*. OUP Oxford, 2014.
- [10] Doron Aurbach, Orit Youngman, and Pnina Dan. “The electrochemical behavior of 1,3-dioxolane-LiClO<sub>4</sub> solutions-II. Contaminated solutions.” In: *Electrochimica Acta* 35.3 (1990), pp. 639–655.
- [11] Marcel D. Baer et al. “Electrochemical surface potential due to classical point charge models drives anion adsorption to the air–water interface.” In: *The Journal of Physical Chemistry Letters* 3.11 (2012), pp. 1565–1570.
- [12] H. J. C. Berendsen, J. R. Grigera, and T. P. Straatsma. “The missing term in effective pair potentials.” In: *The Journal of Physical Chemistry* 91.24 (1987), pp. 6269–6271.
- [13] J. Blumberger and M. Sprik. “Redox free energies from vertical energy gaps: Ab initio molecular dynamics implementation.” In: *Lecture Notes Physics* 704 (2006), pp. 481–506.
- [14] Mavis D. Boamah, Dieter Isheim, and Franz M. Geiger. “Dendritic oxide growth in zerovalent iron nanofilms revealed by atom probe tomography.” In: *The Journal of Physical Chemistry C* 122.49 (2018), pp. 28225–28232.

- [15] Mavis D. Boamah et al. “Energy conversion via metal nanolayers.” In: *Proceedings of the National Academy of Sciences* 116.33 (2019), pp. 16210–16215. DOI: 10.1073/pnas.1906601116.
- [16] Mavis D. Boamah et al. “Specifics about specific ion adsorption from heterodyne-detected second harmonic generation.” In: *The Journal of Physical Chemistry B* 123.27 (2019), pp. 5848–5856.
- [17] Vera Bocharova and Alexei P. Sokolov. “Perspectives for polymer electrolytes: A view from fundamentals of ionic conductivity.” In: *Macromolecules* 53.11 (2020), pp. 4141–4157.
- [18] Jonathan A. Bollinger, Mark J. Stevens, and Amalie L. Frischknecht. “Quantifying single-ion transport in percolated ionic aggregates of polymer melts.” In: *ACS Macro Letters* 9.4 (2020), pp. 583–587.
- [19] Oleg Borodin et al. “Competitive lithium solvation of linear and cyclic carbonates from quantum chemistry.” In: *Physical Chemistry Chemical Physics* 18.1 (Jan. 2016), pp. 164–175.
- [20] Oleg Borodin et al. “Uncharted waters: super-concentrated electrolytes.” In: *Joule* 4.1 (2020), pp. 69–100.
- [21] Gordon E. Brown. “How minerals react with water.” In: *Science* 294.5540 (2001), pp. 67–69.
- [22] Matthew A. Brown, Guilherme Volpe Bossa, and Sylvio May. “Emergence of a Stern layer from the incorporation of hydration interactions into the Gouy–Chapman model of the electrical double layer.” In: *Langmuir* 31.42 (2015), pp. 11477–11483.
- [23] Matthew A. Brown et al. “Determination of surface potential and electrical double-layer structure at the aqueous electrolyte-nanoparticle interface.” In: *Physical Review X* 6.1 (2016), p. 011007.
- [24] Heinz Bültner et al. “Spatiotemporal changes of the solid electrolyte interphase in lithium-ion batteries detected by scanning electrochemical microscopy.” In: *Angewandte Chemie International Edition* 53.39 (2014), pp. 10531–10535.
- [25] David Xi Cao et al. “The importance of sulfonate to the self-doping mechanism of the water-soluble conjugated polyelectrolyte PCPDTBT-SO<sub>3</sub>K.” In: *Materials Chemistry Frontiers* 4.12 (2020), pp. 3556–3566.
- [26] Joseph R. Cendagorta and Toshiko Ichiye. “The surface potential of the water–vapor interface from classical simulations.” In: *The Journal of Physical Chemistry B* 119.29 (2015), pp. 9114–9122.
- [27] HanByul Chang et al. “Direct measurement of charge reversal on lipid bilayers using heterodyne-detected second harmonic generation spectroscopy.” In: *The Journal of Physical Chemistry B* 124.4 (2020), pp. 641–649.

- [28] Si-Han Chen and Sherwin J. Singer. “Molecular dynamics study of the electric double layer and nonlinear spectroscopy at the amorphous silica–water interface.” In: *The Journal of Physical Chemistry B* 123.29 (2019), pp. 6364–6384.
- [29] Xin-Bing Cheng et al. “A review of solid electrolyte interphases on lithium metal anode.” In: *Advanced Science* 3 (2016), p. 1500213.
- [30] Yizi Cheng et al. “Design rules for highly conductive polymeric ionic liquids from molecular dynamics simulations.” In: *Macromolecules* 51.17 (2018), pp. 6630–6644.
- [31] Snehashis Choudhury et al. “Stabilizing polymer electrolytes in high-voltage lithium batteries.” In: *Nature Communications* 10.1 (2019), p. 3091.
- [32] Jenée D. Cyran et al. “Molecular hydrophobicity at a macroscopically hydrophilic surface.” In: *Proceedings of the National Academy of Sciences* 116.5 (2019), pp. 1520–1525.
- [33] Laetitia Dalstein, Kuo-Yang Chiang, and Yu-Chieh Wen. “Direct quantification of water surface charge by phase-sensitive second harmonic spectroscopy.” In: *The Journal of Physical Chemistry Letters* 10.17 (2019), pp. 5200–5205.
- [34] Scott P. O. Danielsen et al. “Mixed conductive soft solids by electrostatically driven network formation of a conjugated polyelectrolyte.” In: *Chemistry of Materials* 30.4 (2018), pp. 1417–1426.
- [35] Akemi M. Darlington et al. “Separating the pH-dependent behavior of water in the Stern and diffuse layers with varying salt concentration.” In: *The Journal of Physical Chemistry C* 121.37 (2017), pp. 20229–20241.
- [36] Pratyusha Das et al. “Dihexyl-substituted poly(3,4-propylenedioxythiophene) as a dual ionic and electronic conductive cathode binder for lithium-ion batteries.” In: *Chemistry of Materials* 32.21 (2020), pp. 9176–9189.
- [37] Victoria K. Davis et al. “Fluoride-ion solvation in non-aqueous electrolyte solutions.” In: *Materials Chemistry Frontiers* 3.12 (2019), pp. 2721–2727. DOI: 10.1039/C9QM00512A.
- [38] Victoria K. Davis et al. “Room-temperature cycling of metal fluoride electrodes: Liquid electrolytes for high-energy fluoride ion cells.” In: *Science* 362.6419 (2018), pp. 1144–1148.
- [39] Emma L. DeWalt-Kerian et al. “pH-dependent inversion of Hofmeister trends in the water structure of the electrical double layer.” In: *The Journal Of Physical Chemistry Letters* 8.13 (2017), pp. 2855–2861.
- [40] Ken A. Dill, Sarina Bromberg, and Dirk Stigter. *Molecular Driving Forces: Statistical Thermodynamics in Biology, Chemistry, Physics, and Nanoscience*. Garland Science, 2010.

- [41] Leela S. Dodda et al. “LigParGen web server: an automatic OPLS-AA parameter generator for organic ligands.” In: *Nucleic Acids Research* 45.W1 (2017), W331–W336.
- [42] Xiulin Fan et al. “Highly fluorinated interphases enable high-voltage Li-metal batteries.” In: *Chem* 4.1 (2018), pp. 174–185.
- [43] Danielle Faurie-Wisniewski and Franz M Geiger. “Synthesis and characterization of chemically pure nanometer-thin zero-valent iron films and their surfaces.” In: *The Journal of Physical Chemistry C* 118.40 (2014), pp. 23256–23263.
- [44] Christopher J. Fennell et al. “Ion pairing in molecular simulations of aqueous alkali halide solutions.” In: *The Journal of Physical Chemistry B* 113.19 (2009), pp. 6782–6791.
- [45] Todd R. Ferguson and Martin Z. Bazant. “Nonequilibrium thermodynamics of porous electrodes.” In: *Journal of The Electrochemical Society* 159.12 (2012), A1967–A1985.
- [46] Kara D. Fong et al. “Ion correlations and their impact on transport in polymer-based electrolytes.” In: *Macromolecules* 54.6 (2021), pp. 2575–2591.
- [47] Kara D. Fong et al. “Onsager transport coefficients and transference numbers in polyelectrolyte solutions and polymerized ionic liquids.” In: *Macromolecules* 53.21 (2020), pp. 9503–9512.
- [48] Hunter O. Ford et al. “Enhanced  $\text{Li}^+$  conduction within single-ion conducting polymer gel electrolytes via reduced cation–polymer interaction.” In: *ACS Materials Letters* 2.3 (2020), pp. 272–279.
- [49] Arthur France-Lanord and Jeffrey C. Grossman. “Correlations from ion pairing and the Nernst-Einstein equation.” In: *Physical Review Letters* 122.13 (2019), p. 136001.
- [50] Daan Frenkel and Berend Smit. *Understanding Molecular Simulation: From Algorithms to Applications*. Vol. 2. Academic Press, Inc., 1996.
- [51] Daniel Gall. “Electron mean free path in elemental metals.” In: *Journal of Applied Physics* 119.8 (2016), p. 085101.
- [52] Venkat Ganesan. “Ion transport in polymeric ionic liquids: recent developments and open questions.” In: *Molecular Systems Design & Engineering* 4.2 (2019), pp. 280–293.
- [53] Magali Gauthier et al. “Electrode-electrolyte interface in Li-ion batteries: current understanding and new insights.” In: *The Journal of Physical Chemistry Letters* 6.22 (Nov. 2015), pp. 4653–4672.

- [54] Magali Gauthier et al. “Electrode–electrolyte interface in Li–ion batteries: Current understanding and new insights”. In: *The Journal of Physical Chemistry Letters* 6.22 (2015), pp. 4653–4672.
- [55] Shankar Ghosh, A.-K. Sood, and N. Kumar. “Carbon nanotube flow sensors.” In: *Science* 299.5609 (2003), pp. 1042–1044.
- [56] Julianne M. Gibbs-Davis et al. “Jammed acid-base reactions at interfaces.” In: *Journal of the American Chemical Society* 130.46 (2008), pp. 15444–15447.
- [57] Brian Giera et al. “Electric double-layer structure in primitive model electrolytes: Comparing molecular dynamics with local-density approximations.” In: *Langmuir* 31.11 (2015), pp. 3553–3562.
- [58] Todd R. Gingrich and Mark Wilson. “On the Ewald summation of Gaussian charges for the simulation of metallic surfaces.” In: *Chemical Physics Letters* 500.1-3 (2010), pp. 178–183.
- [59] Livia Giordano et al. “Chemical reactivity descriptor for the oxide-electrolyte interface in Li–ion batteries.” In: *The Journal of Physical Chemistry Letters* 8.16 (2017), pp. 3881–3887.
- [60] Nicholas J. Giordano. *Computational Physics*. Prentice Hall, 1997.
- [61] Grazia Gonella et al. “Second harmonic and sum-frequency generation from aqueous interfaces is modulated by interference.” In: *The Journal of Physical Chemistry C* 120.17 (2016), pp. 9165–9173.
- [62] Antonin Grenier et al. “Electrochemical reactions in fluoride-ion batteries: mechanistic insights from pair distribution function analysis.” In: *Journal of Materials Chemistry A* 5 (July 2017), pp. 15700–15705.
- [63] Antonin Grenier et al. “Solid fluoride electrolytes and their composite with carbon: issues and challenges for rechargeable solid state fluoride-ion batteries.” In: *The Journal of Physical Chemistry C* 121.45 (2017), pp. 24962–24970.
- [64] Marc C. Gurau et al. “On the mechanism of the Hofmeister effect.” In: *Journal of the American Chemical Society* 126.34 (2004), pp. 10522–10523.
- [65] Lisa M. Hall, Mark J. Stevens, and Amalie L. Frischknecht. “Effect of polymer architecture and ionic aggregation on the scattering peak in model ionomers.” In: *Physical Review Letters* 106.12 (2011), p. 127801.
- [66] Shaun A. Hall, Ashley D. Hickey, and Dennis K. Hore. “Structure of phenylalanine adsorbed on polystyrene from nonlinear vibrational spectroscopy measurements and electronic structure calculations.” In: *The Journal of Physical Chemistry C* 114.21 (2010), pp. 9748–9757.
- [67] Jean-Pierre Hansen and Ian Randal McDonald. *Theory of Simple Liquids: With Applications to Soft Matter*. Academic Press, 2013.

- [68] Mingfu He et al. “The intrinsic behavior of lithium fluoride in solid electrolyte interphases on lithium.” In: *Proceedings of the National Academy of Sciences* 117.1 (2020), pp. 73–79.
- [69] Hendrik Heinz et al. “Accurate simulation of surfaces and interfaces of face-centered cubic metals using 12–6 and 9–6 Lennard-Jones potentials.” In: *The Journal of Physical Chemistry C* 112.44 (2008), pp. 17281–17290.
- [70] Frank H. J. van der Heyden, Derek Stein, and Cees Dekker. “Streaming currents in a single nanofluidic channel.” In: *Physical Review Letters* 95.11 (2005), p. 116104.
- [71] Terrell L. Hill. *An Introduction To Statistical Thermodynamics*. Courier Corporation, 1986.
- [72] Roger W. Hockney and James W. Eastwood. *Computer simulation using particles*. crc Press, 2021.
- [73] Jenn K. Hwang and Arieh Warshel. “Microscopic examination of free-energy relationships for electron transfer in polar solvents.” In: *Journal of the American Chemical Society* 109 (1987), pp. 715–720.
- [74] Matthew T. Irwin et al. “Lithium salt-induced microstructure and ordering in diblock copolymer/homopolymer blends.” In: *Macromolecules* 49.13 (2016), pp. 4839–4849.
- [75] Mark Z. Jacobson et al. “100% clean and renewable wind, water, and sunlight (WWS) all-sector energy roadmaps for the 50 United States.” In: *Energy & Environmental Science* 8.7 (2015), pp. 2093–2117.
- [76] Jiří Janeček and Roland R. Netz. “Interfacial water at hydrophobic and hydrophilic surfaces: Depletion versus adsorption.” In: *Langmuir* 23.16 (2007), pp. 8417–8429.
- [77] Lasse Jensen, Piet T.-H. Van Duijnen, and Jaap G. Snijders. “A discrete solvent reaction field model for calculating frequency-dependent hyperpolarizabilities of molecules in solution.” In: *The Journal of Chemical Physics* 119.24 (2003), pp. 12998–13006.
- [78] Hudong Jin et al. “Cu<sub>x</sub>O nanowires based flexible ionovoltaic device for droplet-flow-induced electrical energy generation.” In: *ACS Applied Energy Materials* 3.2 (2019), pp. 1253–1259.
- [79] William L. Jorgensen, David S. Maxwell, and Julian Tirado-Rives. “Development and testing of the OPLS all-atom force field on conformational energetics and properties of organic liquids.” In: *Journal of the American Chemical Society* 118.45 (1996), pp. 11225–11236.
- [80] William L. Jorgensen and Julian Tirado-Rives. “Potential energy functions for atomic-level simulations of water and organic and biomolecular systems.” In: *Proceedings of the National Academy of Sciences* 102.19 (2005), pp. 6665–6670.

- [81] Tatsuya Joutsuka et al. “Effects of third-order susceptibility in sum frequency generation spectra: A molecular dynamics study in liquid water.” In: *Physical Chemistry Chemical Physics* 20.5 (2018), pp. 3040–3053.
- [82] V. Kaiser et al. “Electrostatic interactions between ions near Thomas–Fermi substrates and the surface energy of ionic crystals at imperfect metals.” In: *Faraday Discussions* 199 (2017), pp. 129–158.
- [83] Tuo Kang et al. “Self-assembled monolayer enables slurry-coating of Li anode.” In: *ACS Central Science* 5.3 (2019), pp. 468–476.
- [84] Shawn M. Kathmann et al. “Understanding the surface potential of water.” In: *The Journal of Physical Chemistry B* 115.15 (2011), pp. 4369–4377.
- [85] John A. Kattirtzi, David T. Limmer, and Adam P. Willard. “Microscopic dynamics of charge separation at the aqueous electrochemical interface.” In: *Proceedings of the National Academy of Sciences* 114.51 (Dec. 2017), pp. 13374–13379.
- [86] Jeongmin Kim, Brett M. Savoie, and Thomas F. Miller III. “Interfacial electron transfer and ion solvation in the solid electrolyte interphase.” In: *The Journal of Physical Chemistry C* 125.8 (2021), pp. 4614–4622. DOI: 10.1021/acs.jpcc.0c11194.
- [87] Marek Kosmulski. “The pH dependent surface charging and points of zero charge. VI. Update.” In: *Journal Of Colloid And Interface Science* 426 (2014), pp. 209–212.
- [88] Andrea La Monaca et al. “1,3-dioxolane: A strategy to improve electrode interfaces in lithium ion and lithium-sulfur batteries.” In: *ChemElectroChem* 5.9 (2018), pp. 1272–1278.
- [89] E. Laborda et al. “Asymmetric Marcus-Hush theory for voltammetry.” In: *Chemical Society Reviews* 42 (2013), pp. 4894–4950.
- [90] Chun-Han Lai et al. “Application of poly(3-hexylthiophene-2, 5-diyl) as a protective coating for high rate cathode materials.” In: *Chemistry of Materials* 30.8 (2018), pp. 2589–2599.
- [91] D. Langmuir, P. Hall, and J. Drever. *Aqueous Environmental Chemistry*. 1997.
- [92] Sang Soo Lee et al. “Real-time observation of cation exchange kinetics and dynamics at the muscovite-water interface.” In: *Nature Communications* 8.1 (2017), pp. 1–9.
- [93] Igor Leontyev and Alexei Stuchebrukhov. “Accounting for electronic polarization in non-polarizable force fields.” In: *Physical Chemistry Chemical Physics* 13.7 (2011), pp. 2613–2626.

- [94] Bin Li, Ying Wang, and Shubin Yang. “A material perspective of rechargeable metallic lithium anodes.” In: *Advanced Energy Materials* 8.13 (2018), p. 1702296.
- [95] Xuemei Li et al. “Hydroelectric generator from transparent flexible zinc oxide nanofilms.” In: *Nano Energy* 32 (2017), pp. 125–129.
- [96] Yiyang Li and William C. Chueh. “Electrochemical and chemical insertion for energy transformation and switching.” In: *Annual Review of Materials Research* 48 (2018), pp. 137–165.
- [97] Yunsong Li and Yue Qi. “Energy landscape of the charge transfer reaction at the complex Li/SEI/electrolyte interface.” In: *Energy & Environmental Science* 12.4 (2019), pp. 1286–1295.
- [98] Yuzhang Li et al. “Atomic structure of sensitive battery materials and Interfaces revealed by cryo-electron microscopy.” In: *Science* 358.6362 (2017), pp. 506–510.
- [99] David R. Lide et al. *CRC Handbook of Chemistry and Physics*. 2005.
- [100] David T Limmer et al. “Charge fluctuations in nanoscale capacitors.” In: *Physical Review Letters* 111.10 (2013), p. 106102.
- [101] David T. Limmer. “Interfacial ordering and accompanying divergent capacitance at ionic liquid-metal interfaces.” In: *Physical Review Letters* 115.25 (2015), p. 256102.
- [102] David T. Limmer and Adam P. Willard. “Nanoscale heterogeneity at the aqueous electrolyte-electrode.” In: *Chemical Physics Letters* 620 (2015), pp. 144–150.
- [103] David T. Limmer et al. “Hydration of metal surfaces can be dynamically heterogeneous and hydrophobic.” In: *Proceedings of the National Academy of Sciences* 110.11 (2013), pp. 4200–4205.
- [104] David T. Limmer et al. “Water exchange at a hydrated platinum electrode is rare and collective.” In: *The Journal of Physical Chemistry C* 119.42 (2015), pp. 24016–24024.
- [105] Dingchang Lin, Yayuan Liu, and Yi Cui. “Reviving the lithium metal anode for high-energy batteries.” In: *Nature Nanotechnology* 12.3 (Mar. 2017), pp. 194–206.
- [106] Dan Lis et al. “Liquid flow along a solid surface reversibly alters interfacial chemistry.” In: *Science* 344.6188 (2014), pp. 1138–1142.
- [107] José N. Canongia Lopes and Agílio A. H. Pádua. “Molecular force field for ionic liquids composed of triflate or bistriflylimide anions.” In: *The Journal of Physical Chemistry B* 108.43 (2004), pp. 16893–16898.

- [108] Jeffrey Lopez et al. “Effects of polymer coatings on electrodeposited lithium metal.” In: *Journal of the American Chemical Society* 140.37 (2018), pp. 11735–11744.
- [109] Johannes Lyklema. *Fundamentals Of Interface And Colloid Science: Soft Colloids*. Vol. 5. Elsevier, 2005.
- [110] Emily Ma et al. “A new imaginary term in the 2nd order nonlinear susceptibility from charged interfaces.” In: *The Journal of Physical Chemistry Letters* 12.24 (2021), pp. 5649–5659. DOI: 10.1021/acs.jpcllett.1c01103.
- [111] Emily Ma et al. “Stern and diffuse layer interactions during ionic strength cycling.” In: *The Journal of Physical Chemistry C* 125.32 (2021), pp. 18002–18014. DOI: 10.1021/acs.jpcc.1c04836.
- [112] Ioan-Bogdan Magdau and Thomas F. Miller III. “Machine learning solvation environments in conductive polymers: Application to ProDOT-2Hex with solvent swelling.” In: *Macromolecules* 54.7 (2021), pp. 3377–3387.
- [113] Frederick Manby et al. “entos: A quantum molecular simulation package.” In: (2019).
- [114] R.-N. Manjunath, Vikas Khatkar, and Bijoy Kumar Behera. “Investigation on seawater ageing of pet-epoxy composites: An ecological and sustainable approach for marine applications.” In: *Journal of Polymers and the Environment* 28 (2020), pp. 2289–2300.
- [115] Dmitry V. Matyushov. “Energetics of electron-transfer reactions in soft condensed media.” In: *Accounts of Chemical Research* 40 (2007), pp. 294–301.
- [116] Thomas F. Miller III et al. “Designing polymer electrolytes for safe and high capacity rechargeable lithium batteries.” In: *Accounts of Chemical Research* 50.3 (2017), pp. 590–593.
- [117] Nicola Molinari, Jonathan P. Mailoa, and Boris Kozinsky. “General trend of a negative Li effective charge in ionic liquid electrolytes.” In: *The Journal of Physical Chemistry Letters* 10.10 (2019), pp. 2313–2319.
- [118] Akihiro Morita. *Theory of Sum Frequency Generation Spectroscopy*. Vol. 97. Springer, 2018.
- [119] Akihiro Morita and James T. Hynes. “A theoretical analysis of the sum frequency generation spectrum of the water surface. II. Time-dependent approach.” In: *The Journal of Physical Chemistry B* 106.3 (2002), pp. 673–685.
- [120] M. Nakano et al. “Collective bulk carrier delocalization driven by electrostatic surface charge accumulation.” In: *Nature* 487.7408 (2012), pp. 459–462.

- [121] Ievgen I. Nedrygailov et al. “On the significance of thermoelectric and thermionic emission currents induced by chemical reactions catalyzed on nanofilm metal–semiconductor heterostructures.” In: *Journal of Vacuum Science & Technology A: Vacuum, Surfaces, and Films* 31.2 (2013), p. 021101.
- [122] Naoki Nitta et al. “Li–ion battery materials: present and future.” In: *Materials Today* 18 (2015), pp. 252–264.
- [123] Abraham Nitzan and Mark A. Ratner. “Conduction in polymers: Dynamic disorder transport.” In: *The Journal of Physical Chemistry* 98.7 (1994), pp. 1765–1775.
- [124] Rodrigo Noriega et al. “A general relationship between disorder, aggregation and charge transport in conjugated polymers.” In: *Nature Materials* 12.11 (2013), pp. 1038–1044.
- [125] Paul E. Ohno et al. “Phase-referenced nonlinear spectroscopy of the  $\alpha$ -quartz/water interface.” In: *Nature Communications* 7.1 (2016), pp. 1–5.
- [126] Benjamin A. Paren et al. “Percolated ionic aggregate morphologies and decoupled ion transport in precise sulfonated polymers synthesized by ring-opening metathesis polymerization.” In: *Macromolecules* 53.20 (2020), pp. 8960–8973.
- [127] Changyong Park et al. “Hydration and distribution of ions at the mica-water interface.” In: *Physical Review Letters* 97.1 (2006), p. 016101.
- [128] Junwoo Park et al. “Identification of droplet-flow-induced electric energy on electrolyte–insulator–semiconductor structure.” In: *Journal of the American Chemical Society* 139.32 (2017), pp. 10968–10971.
- [129] Junwoo Park et al. “Investigation on resistivity-dependent behavior of carbon-composite-based paintable ionovoltaic device.” In: *ACS Applied Electronic Materials* 1.7 (2019), pp. 1059–1064.
- [130] Junwoo Park et al. “Ion specificity on electric energy generated by flowing water droplets.” In: *Angewandte Chemie International Edition* 57.8 (2018), pp. 2091–2095.
- [131] Bryan D. Paulsen et al. “Organic mixed ionic–electronic conductors.” In: *Nature Materials* 19.1 (2020), pp. 13–26.
- [132] E. Peled and S. Menkin. “Review—SEI: Past, Present and Future”. In: *Journal of The Electrochemical Society* 164.7 (2017), A1703–A1719.
- [133] Matt K. Petersen et al. “A computationally efficient treatment of polarizable electrochemical cells held at a constant potential.” In: *The Journal of Physical Chemistry C* 116.7 (2012), pp. 4903–4912.

- [134] Simone Pezzotti, Daria Ruth Galimberti, and Marie-Pierre Gaigeot. “Deconvolution of BIL-SFG and DL-SFG spectroscopic signals reveals order/disorder of water at the elusive aqueous silica interface.” In: *Physical Chemistry Chemical Physics* 21.40 (2019), pp. 22188–22202.
- [135] Simone Pezzotti et al. “What the diffuse layer (DL) reveals in non-linear SFG spectroscopy.” In: *Minerals* 8.7 (2018), p. 305.
- [136] Morgane Pfeiffer-Laplaud and Marie-Pierre Gaigeot. “Adsorption of singly charged ions at the hydroxylated (0001)  $\alpha$ -quartz/water interface.” In: *The Journal of Physical Chemistry C* 120.9 (2016), pp. 4866–4880.
- [137] Matthew B. Pinson and Martin Z. Bazant. “Theory of SEI formation in rechargeable batteries: Capacity fade, accelerated aging and lifetime prediction.” In: *Journal of The Electrochemical Society* 160.2 (2012), A243–A250.
- [138] Achilleas Pipertzis et al. “Polymerized ionic liquids with polythiophene backbones: self-assembly, thermal properties, and ion conduction.” In: *Macromolecules* 51.16 (2018), pp. 6440–6450.
- [139] Achilleas Pipertzis et al. “What determines the glass temperature and dc-conductivity in imidazolium-polymerized ionic liquids with a polythiophene backbone?” In: *Macromolecules* 53.9 (2020), pp. 3535–3550.
- [140] Steve Plimpton. “Fast parallel algorithms for short-range molecular dynamics.” In: *Journal of Computational Physics* 117.1 (1995), pp. 1–19.
- [141] Yuanshuai Qin et al. “Constant electricity generation in nanostructured silicon by evaporation-driven water flow.” In: *Angewandte Chemie* 132.26 (2020), pp. 10706–10712.
- [142] G. Ramos-Sanchez et al. “Computational studies of interfacial reactions at anode materials: Initial stages of the solid-electrolyte-interphase layer formation”. In: *Journal of Electrochemical Energy Conversion and Storage* 13.3 (2016), p. 031002.
- [143] Mark A. Ratner, Patrik Johansson, and Duward F. Shriver. “Polymer electrolytes: ionic transport mechanisms and relaxation coupling.” In: *MRS Bulletin* 25.3 (2000), pp. 31–37.
- [144] Mark A. Ratner and D. F. Shriver. “Polymer Ionics.” In: *MRS Bulletin* 14.09 (1989), pp. 39–51.
- [145] Mark A. Ratner and Duward F. Shriver. “Ion transport in solvent-free polymers.” In: *Chemical Reviews* 88.1 (1988), pp. 109–124.
- [146] Dakota Rawlings et al. “Li<sup>+</sup> and oxidant addition to control ionic and electronic conduction in ionic liquid functionalized conjugated polymers.” In: *Chemistry of Materials* (2021). DOI: 10.1021/acs.chemmater.1c01811.

- [147] M. Rami Reddy and M. Berkowitz. “The dielectric constant of SPC/E water.” In: *Chemical Physics Letters* 155.2 (1989), pp. 173–176.
- [148] Stewart . Reed, Oliver J. Lanning, and Paul A. Madden. “Electrochemical interface between an ionic liquid and a model metallic electrode.” In: *The Journal of Chemical Physics* 126.8 (Feb. 2007), pp. 084704–14.
- [149] Stewart K. Reed, Paul A. Madden, and Aristides Papadopoulos. “Electrochemical charge transfer at a metallic electrode: A simulation study.” In: *The Journal of Chemical Physics* 128.12 (Mar. 2008), p. 124701.
- [150] Benjamin Rehl et al. “New insights into  $\chi^{(3)}$  measurements: comparing non-resonant second harmonic generation and resonant sum frequency generation at the silica/aqueous electrolyte interface.” In: *The Journal of Physical Chemistry C* 123.17 (2019), pp. 10991–11000.
- [151] Chun-Lai Ren, Issei Nakamura, and Zhen-Gang Wang. “Effects of ion-induced cross-linking on the phase behavior in salt-doped polymer blends.” In: *Macromolecules* 49.1 (2015), pp. 425–431.
- [152] Jonathan Rivnay et al. “Organic electrochemical transistors.” In: *Nature Reviews Materials* 3.2 (2018), pp. 1–14.
- [153] Michael Rubinstein and Ralph H. Colby. *Polymer Physics*. OUP Oxford, 2003.
- [154] Jason Rugolo and Michael J. Aziz. “Electricity storage for intermittent renewable sources.” In: *Energy Environmental Science* 5 (5 2012), pp. 7151–7160.
- [155] Jean-Paul Ryckaert, Giovanni Ciccotti, and Herman J. C. Berendsen. “Numerical integration of the cartesian equations of motion of a system with constraints: molecular dynamics of n-alkanes.” In: *Journal of Computational Physics* 23.3 (1977), pp. 327–341.
- [156] Gabriel E. Sanoja et al. “Ion transport in dynamic polymer networks based on metal–ligand coordination: effect of cross-linker concentration.” In: *Macromolecules* 51.5 (2018), pp. 2017–2026.
- [157] Brett M. Savoie, Michael A. Webb, and Thomas F. Miller III. “Enhancing cation diffusion and suppressing anion Ddiffusion via Lewis-acidic polymer electrolytes.” In: *The Journal of Physical Chemistry Letters* 8.3 (2017), pp. 641–646.
- [158] Laura Scalfi et al. “A semiclassical Thomas–Fermi model to tune the metallicity of electrodes in molecular simulations.” In: *The Journal of Chemical Physics* 153.17 (2020), p. 174704.
- [159] Nicole S. Schausser et al. “Decoupling bulk mechanics and mono-and multivalent ion transport in polymers based on metal–ligand coordination.” In: *Chemistry of Materials* 30.16 (2018), pp. 5759–5769.

- [160] Nicole S. Schauer et al. “The role of backbone polarity on aggregation and conduction of ions in polymer electrolytes.” In: *Journal of the American Chemical Society* 142.15 (2020), pp. 7055–7065.
- [161] Philip Schmode et al. “The key role of side chain linkage in structure formation and mixed conduction of ethylene glycol substituted polythiophenes.” In: *ACS Applied Materials & Interfaces* 12.11 (2020), pp. 13029–13039.
- [162] Kjell Schroder et al. “The effect of fluoroethylene carbonate as an additive on the solid electrolyte interphase on silicon lithium-ion electrodes.” In: *Chemistry of Materials* 27.16 (2015), pp. 5531–5542.
- [163] Lars Seyfert et al. “Verification of the flexoelectric effect in PET polymer films for EH applications.” In: *Active and Passive Smart Structures and Integrated Systems XIV*. Vol. 11376. International Society for Optics and Photonics. 2020, 113761T.
- [164] A. Shayeghi et al. “Adsorption of Acetonitrile, benzene, and benzonitrile on Pt(111): Single crystal adsorption calorimetry and density functional theory.” In: *The Journal of Physical Chemistry C* 121.39 (2017), pp. 21354–21363.
- [165] Yuen-Ron Shen. “The Principles of Nonlinear Optics.” In: *New York* (1984).
- [166] Bobo Shi et al. “Polarization charge: Theory and applications to aqueous interfaces.” In: *The Journal Of Chemical Physics* 144.16 (2016), p. 164702.
- [167] J Ilja Siepmann and Michiel Sprik. “Influence of surface topology and electrostatic potential on water/electrode systems.” In: *The Journal of Chemical Physics* 102.1 (1995), pp. 511–524.
- [168] David E. Smith and Liem X. Dang. “Computer simulations of NaCl association in polarizable water.” In: *The Journal of Chemical Physics* 100.5 (1994), pp. 3757–3766.
- [169] Chang Yun Son and Zhen-Gang Wang. “Ion transport in small-molecule and polymer electrolytes.” In: *The Journal of Chemical Physics* 153.10 (2020), p. 100903.
- [170] Johanna K Stark, Yi Ding, and Paul A Kohl. “Dendrite-free electrodeposition and reoxidation of lithium-sodium alloy for metal-anode battery.” In: *Journal of The Electrochemical Society* 158.10 (2011), A1100–6.
- [171] Otto Stern. “Zur theorie der elektrolytischen doppelschicht.” In: *Zeitschrift für Elektrochemie und angewandte physikalische Chemie* 30.21-22 (1924), pp. 508–516.
- [172] John M. Stubbs, Jeffrey J. Potoff, and J. Ilja Siepmann. “Transferable potentials for phase equilibria. 6. United-atom description for ethers, glycols, ketones, and aldehydes.” In: *The Journal of Physical Chemistry B* 108.45 (2004), pp. 17596–17605.

- [173] Liumin Suo et al. ““Water-in-salt” electrolyte enables high-voltage aqueous lithium–ion chemistries.” In: *Science* 350.6263 (2015), pp. 938–943.
- [174] Qunwei Tang and Peizhi Yang. “The era of water-enabled electricity generation from graphene.” In: *Journal of Materials Chemistry A* 4.25 (2016), pp. 9730–9738.
- [175] Jean-Marie Tarascon and Michael Armand. “Issues and challenges facing rechargeable lithium batteries”. In: *Nature* 414.6861 (2001), pp. 359–367.
- [176] Joao P.-G. Tarelho et al. “Graphene-based materials and structures for energy harvesting with fluids—A review.” In: *Materials Today* 21.10 (2018), pp. 1019–1041.
- [177] Katharina Thanner et al. “Artificial solid electrolyte interphases for lithium metal electrodes by wet processing: The role of metal salt concentration and solvent choice.” In: *ACS Applied Materials & Interfaces* 12.29 (2020), pp. 32851–32862.
- [178] Mukul D. Tikekar et al. “Design principles for electrolytes and interfaces for stable lithium–metal batteries.” In: *Nature Energy* 1 (2016), pp. 1–7.
- [179] Jeff Tollefson. “Car industry: charging up the future.” In: *Nature news* 456.7221 (2008), pp. 436–440.
- [180] Yoichi Tominaga and Kenta Yamazaki. “Fast Li–ion conduction in poly(ethylene carbonate)-based electrolytes and composites filled with TiO<sub>2</sub> nanoparticles.” In: *Chemical Communications* 50.34 (2014), pp. 4448–4450.
- [181] Frank H. J. Van der Heyden et al. “Electrokinetic energy conversion efficiency in nanofluidic channels.” In: *Nano letters* 6.10 (2006), pp. 2232–2237.
- [182] Alberto Varzi et al. “Challenges and prospects of the role of solid electrolytes in the revitalization of lithium metal batteries.” In: *Journal of Materials Chemistry A* 4 (2016), pp. 17251–17259.
- [183] Jenel Vatamanu, Oleg Borodin, and Grant D Smith. “Molecular dynamics simulation studies of the structure of a mixed carbonate/LiPF<sub>6</sub> electrolyte near graphite surface as a function of electrode potential.” In: *The Journal of Physical Chemistry C* 116.1 (2011), pp. 1114–1121.
- [184] Pallavi Verma, Pascal Maire, and Petr Novák. “A review of the features and analyses of the solid electrolyte interphase in Li–ion batteries”. In: *Electrochimica Acta* 55.22 (2010), pp. 6332–6341.
- [185] Rodolphe Vuilleumier et al. “Extension of Marcus picture for electron transfer reactions with large solvation changes.” In: *Journal of the American Chemical Society* 134 (2011), pp. 2067–2074.
- [186] Staffan Wall. “The history of electrokinetic phenomena.” In: *Current Opinion in Colloid & Interface Science* 15.3 (2010), pp. 119–124.

- [187] Muqin Wang et al. “Effect of LiFSI concentrations to form thickness- and modulus-controlled SEI layers on lithium metal anodes.” In: *The Journal of Physical Chemistry C* 122.18 (2018), pp. 9825–9834.
- [188] Zhenxing Wang et al. “Evaluation of the constant potential method in simulating electric double-layer capacitors.” In: *The Journal of Chemical Physics* 141.18 (Nov. 2014), p. 184102.
- [189] Zhong Lin Wang et al. “New wave power.” In: *Nature* 542.7640 (2017), pp. 159–160.
- [190] Michael A. Webb et al. “Chemically specific dynamic bond percolation model for ion transport in polymer electrolytes.” In: *Macromolecules* 48.19 (2015), pp. 7346–7358.
- [191] Michael A. Webb et al. “Systematic computational and experimental investigation of lithium–ion transport mechanisms in polyester-based polymer electrolytes.” In: *ACS Central Science* 1.4 (2015), pp. 198–205.
- [192] Xing Wei and Yuen-Ron Shen. “Motional effect in surface sum-frequency vibrational spectroscopy.” In: *Physical Review Letters* 86.21 (2001), p. 4799.
- [193] Yu-Chieh Wen et al. “Unveiling microscopic structures of charged water interfaces by surface-specific vibrational spectroscopy.” In: *Physical Review Letters* 116.1 (2016), p. 016101.
- [194] Adam P. Willard et al. “Water at an electrochemical interface—a simulation study.” In: *Faraday Discussions* 141 (2009), pp. 423–441.
- [195] Shichuan + Xi et al. “Energy conversion via metal nanolayers in a wavetank.” In: *in preparation* (2021).
- [196] Yihan Xiao et al. “Understanding interface stability in solid-state batteries.” In: *Nature Reviews Materials* 5.2 (2020), pp. 105–126.
- [197] Kang Xu. “Electrolytes and interphases in Li–ion batteries and beyond”. In: *Chemical reviews* 114 (2014), pp. 11503–11618.
- [198] Mengjin Xu et al. “A theoretical study of structure-solubility correlations of carbon dioxide in polymers containing ether and carbonyl groups.” In: *Phys. Chem. Chem. Phys.* 13 (47 2011), pp. 21084–21092.
- [199] Qingmin Xu et al. *Solid electrolyte interphase (SEI) application on anode of fluoride ion/shuttle batteries*. US Patent App. 16/702,327. June 2020. URL: <https://patents.google.com/patent/US20200185776A1/en>.
- [200] Takayuki Yamamoto et al. “Room-temperature fluoride shuttle batteries based on a fluorohydrogenate ionic liquid electrolyte.” In: *ACS Applied Energy Materials* 2.9 (2019), pp. 6153–6157.
- [201] Chong Yan et al. “Dual-layered film protected lithium metal anode to enable dendrite-free lithium deposition.” In: *Advanced Materials* 30.25 (2018), p. 1707629.

- [202] Shanshan Yang et al. “Mechanism of electric power generation from ionic droplet motion on polymer supported graphene.” In: *Journal of the American Chemical Society* 140.42 (2018), pp. 13746–13752.
- [203] Svetlana V. Yanina and Kevin M. Rosso. “Linked reactivity at mineral-water interfaces through bulk crystal conduction.” In: *Science* 320.5873 (2008), pp. 218–222.
- [204] In-Chul Yeh and Max L. Berkowitz. “Ewald summation for systems with slab geometry.” In: *The Journal of Chemical Physics* 111.7 (1999), pp. 3155–3162.
- [205] Jun Yin et al. “Generating electricity by moving a droplet of ionic liquid along graphene.” In: *Nature Nanotechnology* 9.5 (2014), pp. 378–383.
- [206] Jun Yin et al. “Waving potential in graphene.” In: *Nature Communications* 5.1 (2014), pp. 1–6.
- [207] Zhiao Yu, Yi Cui, and Zhenan Bao. “Design principles of artificial solid electrolyte interphases for lithium-metal anodes.” In: *Cell Reports Physical Science* 1.7 (2020), p. 100119.
- [208] Michael J. Zachman et al. “Cryo-STEM mapping of solid–liquid interfaces and dendrites in lithium–metal batteries.” In: *Nature* 560.7718 (2018), p. 345.
- [209] Francisco Zaera. “Probing liquid/solid interfaces at the molecular level.” In: *Chemical reviews* 112.5 (2012), pp. 2920–2986.
- [210] Markus Zahn. “Point charge between two parallel grounded planes.” In: *American Journal of Physics* 44 (1976), pp. 1132–1134.
- [211] Zihao Zhai et al. “Metal-free synthesis of boron-doped graphene glass by hot-filament chemical vapor deposition for wave energy harvesting.” In: *ACS Applied Materials & Interfaces* 12.2 (2019), pp. 2805–2815.
- [212] Heng Zhang et al. “Single lithium-ion conducting solid polymer electrolytes: advances and perspectives.” In: *Chemical Society Reviews* 46.3 (2017), pp. 797–815.
- [213] Zhuhua Zhang et al. “Emerging hydrovoltaic technology.” In: *Nature nanotechnology* 13.12 (2018), pp. 1109–1119.
- [214] Fei Zhao et al. “Materials for solar-powered water evaporation.” In: *Nature Reviews Materials* 5.5 (2020), pp. 388–401.
- [215] Hui Zhao et al. “A polymerized vinylene carbonate anode binder enhances performance of lithium–ion batteries.” In: *Journal of Power Sources* 263 (2014), pp. 288–295.
- [216] Qing Zhao et al. “Designing solid-state electrolytes for safe, energy-dense batteries.” In: *Nature Reviews Materials* 5.3 (2020), pp. 229–252.

- [217] Qing Zhao et al. “Solid-state polymer electrolytes with in-built fast interfacial transport for secondary lithium batteries.” In: *Nature Energy* 4.5 (2019), pp. 365–373.
- [218] Jianming Zheng et al. “Electrolyte additive enabled fast charging and stable cycling lithium metal batteries.” In: *Nature Energy* 2.3 (2017), pp. 17012–8.
- [219] Qi Zheng et al. “Optimizing ion transport in polyether-based electrolytes for lithium batteries.” In: *Macromolecules* 51.8 (2018), pp. 2847–2858.